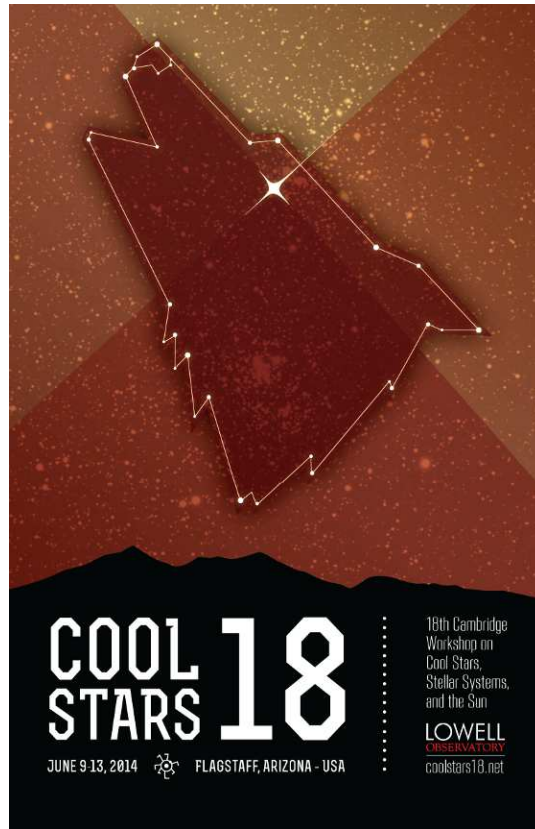


*18th Cambridge Workshop on Cool Stars, Stellar Systems, and the Sun
Proceedings of Lowell Observatory (9-13 June 2014)
Edited by G. van Belle & H. Harris*



**Proceedings of the 18th Cambridge Workshop on Cool Stars,
Stellar Systems and the Sun**

Proceedings Draft, version 2014-08-05

Contents

1	Foreward	11
2	The Transition Between X-ray Emission Regimes in the M34 Open Cluster	13
3	Lithium Abundance and Rotation in the Pleiades and M34 Open Clusters	21
4	Line Bisector Variability in the Sun as a Star	29
5	Stars with and without planets: Where do they come from?	35
6	Preparation of the CARMENES Input Catalogue: Low- and High-resolution Spectroscopy of M dwarfs	43
7	Convection in Cool Stars, as Seen Through <i>Kepler's</i> Eyes	53
8	Solar Cycle Dependency of Sun-as-a-Star Photospheric Spectral Line Profiles	61
9	Short-term Activity in Young Solar Analogs	71
10	Preparation of the CARMENES Input Catalogue: Multiplicity of M dwarfs from tenths of arcseconds to hundreds of arcminutes	77
11	Stellar Spectroscopy during Exoplanet Transits: Dissecting fine structure across stellar surfaces	85
12	Hot Stars With Cool Companions	97
13	Potential magnetic field extrapolation in binary star systems	103
14	Probing Rotational Dynamo Extremes: X-ray and Optical Spectroscopy of the 0.5 Day Period Eclipsing Binary, HD 79826	111
15	The long and the short of it: timescales for stellar activity	119
16	The coolest 'stars' are free-floating planets	125

17 Dynamical Masses of Pre-Main-Sequence Binary Systems	133
18 Star-planet interactions	139
19 Determining the stellar spin axis orientation	159
20 Predicting the Extreme-UV and Lyman- α Fluxes Received by Exoplanets from their Host Stars	167
21 The extension of the corona in classical T Tauri stars	175
22 X-Shooter Medium Resolution Brown Dwarfs Library	179
23 First results of the TIGRE chromospheric activity survey	193
24 Molecular outflows driven by young brown dwarfs and VLMS. New clues from IRAM interferometer observations	199
25 Preparation of the CARMENES Input Catalogue: Mining public archives for stellar parameters and spectra of M dwarfs with master thesis students	203
26 New Results from the GALEX Nearby Young-Star Survey	213
27 M dwarfs search for pulsations and flare studies within Kepler GO program	217
28 Solar cycle 24 UV radiation: lowest since more than 6 decades	221
29 The Surface Brightness Contribution of II Peg: A Comparison of TiO Band Analysis and Doppler Imaging	227
30 UCAC4 Nearby Star Survey: A Search for Our Stellar Neighbors	233
31 Characterizing the Parents: Exoplanets Around Cool Stars	239

Participants List

Fred Adams (Univ. Michigan, fca@umich.edu)
Vladimir Airapetian (NASA/GSFC, vladimir.airapetian@nasa.gov)
Thomas Allen (University of Toledo, tom.sco@gmail.com)
Kimberly Aller (University of Hawaii, kaller@ifa.hawaii.edu)
Katelyn Allers (Bucknell University, k.allers@bucknell.edu)
Francisco Javier Alonso Floriano (Universidad Complutense, fjalonso@ucm.es)
Julian David Alvarado-Gomez (ESO, jalvarad@eso.org)
Catarina Alves de Oliveira (European Space Agency, calves@sciops.esa.int)
Marin Anderson (Caltech, mmanders@astro.caltech.edu)
Guillem Anglada-Escude (Queen Mary, London, guillem.anglada@gmail.com)
Ruth Angus (University of Oxford, ruth.angus@astro.ox.ac.uk)
Megan Ansdell (University of Hawaii, mansdell@ifa.hawaii.edu)
Antoaneta Antonova (Sofia University, tony@phys.uni-sofia.bg)
Daniel Apai (University of Arizona, apai@arizona.edu)
Costanza Argiroffi (Univ. of Palermo, argi@astropa.unipa.it)
Pamela Arriagada (DTM, CIW, parriagada@carnegiescience.edu)
Kyle Augustson (High Altitude Observatory, kyle.augustson@gmail.com)
Ian Avilez (Lowell Observatory, iavilez@lowell.edu)
Sarah Ballard (University of Washington, sarahba@uw.edu)
Daniella Bardalez Gagliuffi (UCSD, daniella@physics.ucsd.edu)
Sydney Barnes (Leibniz Inst Astrophysics, sbarnes@aip.de)
Eddie Baron (Univ. of Oklahoma, baron@ou.edu)
Gibor Basri (UC Berkeley, basri@berkeley.edu)
Fabienne Bastien (Vanderbilt University, fabienne.a.bastien@vanderbilt.edu)
Juan Carlos Beamin (PUC chile / ESO, jcbeamin@astro.puc.cl)
Benjamin Beeck (MPS, beeck@mps.mpg.de)
Carolina Bergfors (University College London, c.bergfors@ucl.ac.uk)
Alexander Berkner (University of Hamburg, aberkner@hs.uni-hamburg.de)
Luca Bertello (NSO, lbertello@nso.edu)
Will Best (University of Hawaii, wbest@ifa.hawaii.edu)
Emily Bevins (Lowell Observatory, ekbevins@gmail.com)
Beth Biller (University of Edinburgh, beth.biller@gmail.com)
Alexander Binks (Keele University, a.s.binks@keele.ac.uk)
Catie Blazek (Lowell Observatory, catie@lowell.edu)
John Bochanski (Haverford College, bochanski@gmail.com)
Isabelle Boisse (LAM (Marseille, France), isabelle.boisse@lam.fr)
Rosaria Bonito (UNIPA-INAF-OAPa, sbonito@astropa.unipa.it)
Simon Borgniet (IPAG, Simon.Borgniet@obs.ujf-grenoble.fr)
Brendan Bowler (Caltech, bpbowler@caltech.edu)
Tabetha Boyajian (Yale, tabetha.boyajian@yale.edu)
Cesar Briceo (CTIO, cbriceno@ctio.noao.edu)
Nancy Brickhouse (CfA, nbrickhouse@cfa.harvard.edu)

Alexander Brown (University of Colorado, Alexander.Brown@colorado.edu)
Timothy Brown (LCOGT, tbrown@lcogt.net)
Matthew Browning (Exeter, browning@astro.ex.ac.uk)
Allan Sacha Brun (CEA AIM Paris Saclay, sachabrun@cea.fr)
Ryan Buckingham (NAU/Lowell Observatory, ryanB@nau.edu)
Esther Buenzli (MPIA Heidelberg, buenzli@mpia.de)
Adam Burgasser (UCSD, aburgasser@ucsd.edu)
Ben Burningham (Univ. of Hertfordshire, UK, b.burningham@herts.ac.uk)
Derek Buzasi (FGCU, dbuzasi@fgcu.edu)
Andrew Cameron (University of St Andrews, acc4@st-andrews.ac.uk)
Dongtao Cao (Yunnan Observatories, CAS, dtcao@ynao.ac.cn)
Joleen Carlberg (Carnegie DTM, jcarlberg@dtm.ciw.edu)
Kenneth Carpenter (NASA's GSFC, Kenneth.G.Carpenter@nasa.gov)
Thorsten A. Carroll (AIP Potsdam, tcarroll@aip.de)
Brad Carter (Uni Southern Queensland, brad.carter@usq.edu.au)
Luca Casagrande (Australian National Univ., luca.casagrande@anu.edu.au)
Paul Wilson Cauley (Rice University, pwc1@rice.edu)
Heather Cegla (Queen's University Belfast, h.cegla@qub.ac.uk)
Julio Chaname (Univ Catolica, Chile, jchaname@astro.puc.cl)
Ann Marie Cody (IPAC/Caltech, amc@ipac.caltech.edu)
Ofer Cohen (Harvard-Smithsonian CfA, ocohen@cfa.harvard.edu)
Remo Collet (Australian National Univ., remo.collet@anu.edu.au)
Neil Cook (Hertfordshire, neil.james.cook@gmail.com)
Christopher Corbally (Vatican Observatory, corbally@as.arizona.edu)
Miriam Cortes (UCM, micortes@ucm.es)
Kevin Covey (Lowell Observatory, kcovey@lowell.edu)
Kelle Cruz (Hunter College & AMNH, kellecruz@gmail.com)
Manfred Cuntz (Univ. of Texas, Arlington, cuntz@uta.edu)
Jason Curtis (Penn State, jlc600@psu.edu)
Michael Cushing (University of Toledo, michael.cushing@utoledo.edu)
Sebastian Daemgen (University of Toronto, daemgen@astro.utoronto.ca)
Conard Dahn (U. S. Naval Observatory, dahn@nofs.navy.mil)
James Davenport (University of Washington, jrad@astro.washington.edu)
Claire Davies (University of St Andrews, cd54@st-andrews.ac.uk)
Cassy Davison (Georgia State Univ, davison@chara.gsu.edu)
Elisa De Castro (U. Complutense de Madrid, elisacas@ucm.es)
Bart De Pontieu (Lockheed, bdp@lmsal.com)
Robert De Rosa (ASU/University of Exeter, rjderosa@asu.edu)
Niall Deacon (MPIA, deacon@mpia.de)
Casey Deen (MPIA, deen@mpia.de)
Sebastien Deheuvels (IRAP (Toulouse), sebastien.deheuvels@irap.omp.eu)
Laetitia Delrez (University of Lige, ldelrez@ulg.ac.be)
Carsten Denker (Leibniz Inst Astr Potsdam, cdenker@aip.de)
Stephen Desch (ASU, steve.desch@asu.edu)
Jason Dittmann (Harvard, jdittmann@cfa.harvard.edu)
Amy Dobson (Keele University, a.l.dobson@keele.ac.uk)
Aaron Dotter (ANU, aaron.dotter@gmail.com)
Caitlin Doughty (University of Washington, cchristinedoughty@gmail.com)

Stephanie Douglas (Columbia University/AMNH, stephaniedouglas@gmail.com)
Emily Drabek-Maunder (Imperial College London, e.drabek-maunder@imperial.ac.uk)
Dainis Dravins (Lund Observatory, Sweden, dainis@astro.lu.se)
Xavier Dumusque (Harvard Smithsonian CfA, xdumusque@cfa.harvard.edu)
Edward Dunham (Lowell Observatory, dunham@lowell.edu)
Andrea Dupree (Center for Astrophysics, dupree@cfa.harvard.edu)
Trent Dupuy (University of Texas, tdupuy@gmail.com)
Kathleen Eastwood (Northern Arizona U, kathy.eastwood@nau.edu)
Suzan Edwards (Smith College, sedwards@smith.edu)
Ricky Egeland (Montana State University, regeland@physics.montana.edu)
David Elliott (JPL (retired), dellott3@charter.net)
Taran Esplin (Penn State, tle918@psu.edu)
Jacqueline Faherty (Carnegie DTM, jfaherty17@gmail.com)
Gregory Feiden (Uppsala University, gregory.feiden@physics.uu.se)
Francis Fekel (Tennessee State Univ., fekel@evans.tsuniv.edu)
Joe Filippazzo (City University of New Yo, jcfilippazzo@gmail.com)
Ettore Flaccomio (INAF-Osservatorio Astronomico di Palermo, ettoref@astropa.inaf.it)
Scott Fleming (STScI / CSC, fleming@stsci.edu)
Ettore Floacomino (INAF, ettoref@astropa.inaf.it)
Lisa Foley (Lowell Observatory, lifo@lowell.edu)
Colin Folsom (IRAP, cfolsom@irap.omp.eu)
Jonathan Gagn (U. de Montreal / Caltech, jonathan.gagne.1@gmail.com)
Cezary Galan (NCAC PAS, Warsaw, Poland, cgalan@camk.edu.pl)
Victor Garcia (Vanderbilt / Lowell, eugenio.v.garcia@gmail.com)
Cecilia Garraffo (Harvard-Smithsonian CfA, cgarraffo@cfa.harvard.edu)
Liz Gehret (Lowell Observatory, thelovelyladyliz@hotmail.com)
Christopher Gelino (NExSci/Caltech, cgelino@ipac.caltech.edu)
Luan Ghezzi (Harvard University, lghezzi@cfa.harvard.edu)
Mark Giampapa (NSO, giampapa@nso.edu)
Gordon Gibb (University of St Andrews, gpsg@st-andrews.ac.uk)
Ed Gillen (University of Oxford, ed.gillen@astro.ox.ac.uk)
John Gizis (University of Delaware, gizis@udel.edu)
Laurent Gizon (MPG, gizon@mps.mpg.de)
Ana Ines Gomez de Castro (UCM, aig@ucm.es)
Philippe Gondoin (European Space Agency, pgondoin@rssd.esa.int)
Richard Gray (Appalachian State Univ, grayro@appstate.edu)
Jean-Mathias Griessmeier (CNRS, jean-mathias.griessmeier@cnrs-orleans.fr)
Cecilia Guerra (Universidad de Guanajuato, cguerra@astro.ugto.mx)
Kevin Gullikson (University of Texas, kgulliks@astro.as.utexas.edu)
Hans Moritz Gnther (Harvard-Smithsonian CfA, hguenther@cfa.harvard.edu)
Jeffrey Hall (Lowell Observatory, jch@lowell.edu)
Gregg Hallinan (Caltech, gh@astro.caltech.edu)
Kevin Hardegree-Ullman (University of Toledo, khardeg@rockets.utoledo.edu)
Mattie Harrington (Lowell Observatory, mharrington@lowell.edu)
Hugh Harris (US Naval Observatory, hch@nofs.navy.mil)

Suzanne Hawley (University of Washington, slhawley@uw.edu)
 Raphaelle Haywood (University of St Andrews, rdh4@st-andrews.ac.uk)
 Leslie Hebb (Hobart & William Smith, hebb@hws.edu)
 Elodie Hbrard (IRAP, elodie.hebrard@irap.omp.eu)
 Aren Heinze (Stony Brook University, ariheinze@hotmail.com)
 Neda Hejazi (York University, nedahej@yorku.ca)
 Krzysztof Helminiak (Subaru Telescope, NAOJ, xysiek@naoj.org)
 lynne hillenbrand (caltech, lah@astro.caltech.edu)
 Natalie Hinkel (San Francisco State Uni, natalie.hinkel@gmail.com)
 Kay Hiranaka (Hunter College, GC, AMNH, oookay@gmail.com)
 Volkmar Holzwarth (KIS, Freiburg, Germany, volkmar.holzwarth@kis.uni-freiburg.de)
 Derek Homeier (CRAL/ENS-Lyon, derek.homeier@ens-lyon.fr)
 Daniel Huber (NASA Ames, daniel.huber@nasa.gov)
 David Huenenmoedrder (MIT, dph@space.mit.edu.)
 Gaitee Hussain (ESO, ghussain@eso.org)
 Panagiotis Ioannidis (Hamburger Sternwarte, pioannidis@hs.uni-hamburg.de)
 Jonathan Irwin (SAO, jirwin@cfa.harvard.edu)
 David Jaimes (Columbia University, jaimes@astro.columbia.edu)
 Kenneth Janes (Boston University, janes@bu.edu)
 Hannah Jang-Condell (University of Wyoming, hjangcon@uwyo.edu)
 Moira Jardine (University of St Andrews, mmj@st-andrews.ac.uk)
 James Jenkins (Universidad de Chile, jjenkins@das.uchile.cl)
 James Jenkins (U. Chile, jjenkins@das.uchile.cl)
 Eric Jensen (Swarthmore College, ejensen1@swarthmore.edu)
 Viki Joergens (MPIA Heidelberg, viki@mpia.de)
 Christopher Johns-Krull (Rice University, cmj@rice.edu)
 Lehtinen Juhana (Helsinki, jyri.j.lehtinen@helsinki.fi)
 Melodie Kao (Caltech, mkao@caltech.edu)
 Theodora Karalidi (Steward Observatory, tkaralidi@email.arizona.edu)
 Joel Kastner (Rochester Inst. of Tech., jhk@cis.rit.edu)
 Kendra Kellogg (Western University, kkellogg@uwo.ca)
 Bokyoung Kim (Ewha Womans University, bkkim315@gmail.com)
 Marcin Kiraga (Warsaw University Obs., kiraga@astrouw.edu.pl)
 Oleg Kochukhov (Uppsala University, oleg.kochukhov@physics.uu.se)
 Rainer Koehler (MPIA Heidelberg, koehler@mpia-hd.mpg.de)
 Rachel Koncewicz (Oxford, konce@thphys.ox.ac.uk)
 Sohei Kondo (Kyoto Sangyo Univ., kondosh@cc.kyoto-su.ac.jp)
 Taisiya Kopytova (MPIA, kopytova@mpia.de)
 Heidi Korhonen (FINCA, Turku University, heidi.h.korhonen@utu.fi)
 Andreas Korn (Uppsala University, andreas.korn@physics.uu.se)
 Nadiia Kostogryz (KIS Freiburg Germany, kostogryz@kis.uni-freiburg.de)
 Adam Kowalski (NASA/GSFC, adam.f.kowalski@nasa.gov)
 Kaitlin Kratter (University of Arizona, kkratter@email.arizona.edu)
 Adam Kraus (UT - Austin, alk@astro.as.utexas.edu)
 Tereza Krejcova (Hamburg Observatory, tereza.krejcova@hs.uni-hamburg.de)
 Arunas Kucinskas (Vilnius University, arunas.kucinskas@tfai.vu.lt)
 Manfred Kueker (AIP Potsdam, mkueker@aip.de)

Radostin Kurtev (Valparaiso University, radostin.kurtev@uv.cl)
Oleksii Kuzmychov (KIS Freiburg Germany, oleksii@kis.uni-freiburg.de)
Sairam Lalitha (TIFR, lalithasairam@gmail.com)
Antonino Lanza (INAF, nlanza@oact.inaf.it)
Alexis Lavail (Uppsala University, alexis.lavail@physics.uu.se)
Samantha Lawler (University of Victoria, lawler@uvic.ca)
Jyri Lehtinen (University of Helsinki, jyri.j.lehtinen@helsinki.fi)
John Leibacher (NSO, jleibacher@nso.edu)
Sebastien Lepine (Georgia State University, slepine@chara.gsu.edu)
Anna-Lea Lesage (University Leiden, lesage@strw.leidenuniv.nl)
Sara Lindgren (Uppsala university, sara.lindgren@physics.uu.se)
Michael Line (UC-Santa Cruz, mrline@ucsc.edu)
Jeffrey Linsky (University of Colorado, jlinsky@jila.colorado.edu)
Michael Liu (University of Hawaii, liumicha@hawaii.edu)
Joe Llama (University of St Andrews, joe.llama@st-andrews.ac.uk)
Nicolas Lodieu (IAC Tenerife, Spain, nlodieu@iac.es)
Sarah Logsdon (UCLA, slogsdon@astro.ucla.edu)
Miguel ngel Lpez Garca (U. Complutense de Madrid, miglopez@ucm.es)
Javier Lopez-Santiago (UCM, jalopez@ucm.es)
Richard Lovelace (Cornell University, lovelace@astro.cornell.edu)
Robert Loyd (University of Colorado, robert.loyd@colorado.edu)
Philip Lucas (U Hertfordshire, p.w.lucas@herts.ac.uk)
Jacob Lustig-Yaeger (UC Santa Cruz, jlustigy@ucsc.edu)
Julie Lutz (University of Washington, jlutz@astro.washington.edu)
Christene Lynch (University of Iowa, christene-lynch@uiowa.edu)
Gregory Mace (UCLA, gmace@astro.ucla.edu)
Suvrath Mahadevan (Penn State, suvrath@astro.psu.edu)
Carlo Felice Manara (ESO, cmanara@eso.org)
Elena Manjavacas (MPIA, Heidelberg, manjavacas@mpia.de)
Andrew Mann (University of Texas, amann@astro.as.utexas.edu)
MARK MARLEY (NASA, mark.s.marley@nasa.gov)
Stephen Marsden (Uni Southern Queensland, Stephen.Marsden@usq.edu.au)
Emily Martin (UCLA, emartin@astro.ucla.edu)
Titos Matsakos (University of Chicago, titos.matsakos@uchicago.edu)
Kyle McCarthy (University of Kentucky, kyle.mccarthy@uky.edu)
Matthew McJunkin (CU Boulder, matthew.mcjunkin@colorado.edu)
Travis Metcalfe (Space Science Institute, travis@spsci.org)
Stanimir Metchev (Western Univ - Canada, smetchev@uwo.ca)
Marco Mittag (Hamburger Sternwarte, mmittag@hs.uni-hamburg.de)
Zaira Modroo-Berdias (IAA-CSIC, zaira@iaa.es)
Subhanjoy Mohanty (Imperial College London, s.mohanty@imperial.ac.uk)
Jean-Louis Monin (IPAG-Universit Grenoble,
Jean-Louis.Monin@obs.ujf-grenoble.fr)
David Montes (UCM - Dpto Astrofisica, dmontes@ucm.es)
Benjamin Montet (Caltech / Harvard, btm@astro.caltech.edu)
Dylan Morgan (Boston University, dpmorg@bu.edu)
Julien Morin (Univ. Montpellier, julien.morin@univ-montp2.fr)
Caroline Morley (UC Santa Cruz, cmorley@ucsc.edu)

Claire Moutou (CFHT, moutou@cfht.hawaii.edu)
 Simon Murphy (University of Heidelberg, murphy@ari.uni-heidelberg.de)
 Robert Mutel (University of Iowa, robert-mutel@uiowa.edu)
 Harold Nations (College of S. Nevada, harold.nations@csn.edu)
 James Neff (NSF & CofC, neffj@cofc.edu)
 Nicholas Nelson (Los Alamos National Lab, njnelson@lanl.gov)
 Elisabeth Newton (Harvard, enewton@cfa.harvard.edu)
 Alejandro Nunez (Columbia University, alejandro@astro.columbia.edu)
 Neal Riain (Trinity College Dublin, oriainn@tcd.ie)
 Masashi Omiya (PD, omiya.m@geo.titech.ac.jp)
 Douglas O'Neal (Keystone College, douglas.oneal@keystone.edu)
 Daniela Opitz (UNSW, daniela.opitz@student.unsw.edu.au)
 Ilaria Pascucci (U Arizona/LPL, pascucci@lpl.arizona.edu)
 Rahul Patel (Stony Brook University, rahul.patel.1@stonybrook.edu)
 Karla Pea Ramrez (Univ. Catlica de Chile, kpena@astro.puc.cl)
 Volker Perdelwitz (Hamburg Observatory,
 volker.perdelwitz@hs.uni-hamburg.de)
 Vctor Pereira Blanco (U. Complutense de Madrid, vpereirablanca@ucm.es)
 Greg Perugini (Burlington County College, gperugin@bcc.edu)
 Alexei Pevtsov (National Solar Observatory, apevtsov@nso.edu)
 Tiffany Pewett (Georgia State University, pewett@astro.gsu.edu)
 Ignazio Pillitteri (INAF- O.A.Pa. - ITALY, ignazio.pillitteri@gmail.com)
 John Pineda (Caltech, jspineda@astro.caltech.edu)
 Nikolai Piskunov (Uppsala University, piskunov@astro.uu.se)
 Katja Poppenhaeger (Harvard-Smithsonian CfA,
 kpoppenhaeger@cfa.harvard.edu)
 Lisa Prato (Lowell Observatory, lprato@lowell.edu)
 David Principe (Rochester Inst. of Tech., daveprincipe@astro.rit.edu)
 Andreas Quirrenbach (LSW Heidelberg, A.Quirrenbach@lsw.uni-heidelberg.de)
 Doug Rabin (NASA Goddard, douglas.rabin@nasa.gov)
 Jacqueline Radigan (STScI, radigan@stsci.edu)
 Stefanie Raetz (ESA/ESTEC SRE-S Noordwijk, sraetz@rssd.esa.int)
 Abhijith Rajan (ASU/SESE, abhijithrajan@asu.edu)
 Luisa Rebull (Caltech, rebull@ipac.caltech.edu)
 Bo Reipurth (University of Hawaii, reipurth@ifa.hawaii.edu)
 Victor Reville (CEA AIM Paris Saclay, victor.reville@cea.fr)
 Basmah Riaz (Uni. of Hertfordshire, b.riaz@herts.ac.uk)
 Emily Rice (CUNY/AMNH, emily.rice@csi.cuny.edu)
 Andrew Riddle (Univ. of Texas at Austin, ajriddle@astro.as.utexas.edu)
 Adric Riedel (Hunter College/AMNH, adric.riedel@gmail.com)
 Elisabetta Rigliaco (University of Arizona/LPL, rigliaco@lpl.arizona.edu)
 Tyler Robinson (NASA Ames Research Center, tyler.d.robinson@nasa.gov)
 Jan Robrade (Hamburger Sternwarte, jrobrade@hs.uni-hamburg.de)
 Jan Robrade (University of Hamburg, jrobrade@hs.uni-hamburg.de)
 David Rodriguez (Universidad de Chile, drodrigu@das.uchile.cl)
 Cristina Rodriguez-Lopez (IAA-CSIC (Spain), crl@iaa.es)
 Rachael Roettenbacher (University of Michigan, rmroett@umich.edu)
 Barbara Rojas (CAUP, babs@astro.up.pt)

Marina Romanova (Cornell University, Asc266@cornell.edu)
Lisa Rosn (Uppsala University, lisa.rosen@physics.uu.se)
Steven Saar (SAO, ssaar@cfa.harvard.edu)
Giuseppe Germano Sacco (INAF-Arcetri, gsacco@arcetri.inaf.it)
Johannes Sahlmann (ESA, Johannes.Sahlmann@esa.int)
Jon Saken (Marshall University, saken@marshall.edu)
Jason Sanborn (Lowell Observatory, jaisen1@lowell.edu)
Victor J. Sanchez Bejar (IAC, vbejar@iac.es)
Didier Saumon (Los Alamos National Lab, dsaumon@lanl.gov)
Gail Schaefer (Georgia State University, schaefer@chara-array.org)
Katharine Schlesinger (RSAA, katharine.schlesinger@anu.edu.au)
Joshua Schlieder (MPIA Heidelberg, schlieder@mpia-hd.mpg.de)
Sarah Schmidt (Ohio State University, sarahjaneschmidt@gmail.com)
Tobias Schmidt (Hamburg Observatory, tobi@astro.uni-jena.de)
Paul Schmidtke (Arizona State University, paul.schmidtke@asu.edu)
Adam Schneider (University of Toledo, aschneid10@gmail.com)
Klaus-Peter Schrder (Univers. Guanajuato, kps@astro.ugto.mx)
Wyke See (University of St Andrews, wcvs@st-andrews.ac.uk)
Hakan Volkan Senavci (Ankara University, volkan.senavci@gmail.com)
Paul Shankland (US Naval Observatory, pds@nofs.navy.mil)
Alexander Shapiro (PMOD/WRC, alexander.shapiro@pmodwrc.ch)
Sergiy Shelyag (Monash University, sergiy.shelyag@monash.edu)
Evgenya Shkolnik (Lowell Observatory, shkolnik@lowell.edu)
Adam Showman (University of Arizona, showman@lpl.arizona.edu)
Denis Shulyak (Goettingen University, denis.shulyak@gmail.com)
Victor Silva Aguirre (Aarhus University, victor@phys.au.dk)
Michal Simon (Stony Brook University, michal.simon@stonybrook.edu)
David Sing (University of Exeter, sing@astro.ex.ac.uk)
Andy Skemer (University of Arizona, askemer@as.arizona.edu)
Rodolfo Smiljanic (CAMK/Poland, rsmiljanic@ncac.torun.pl)
Sarah Smith (Lowell Observatory, sms633@nau.edu)
Chris Sneden (University of Texas, chris@verdi.as.utexas.edu)
Garrett Somers (The Ohio State University, somers.38@osu.edu)
Federico Spada (AIP Potsdam, fspada@aip.de)
Craig Stark (University of St Andrews, crs21@st-andrews.ac.uk)
Summer Starrfield (Arizona State University, starrfield@asu.edu)
John Stauffer (Spitzer Science Center, stauffer@ipac.caltech.edu)
Shelly Stearns (Lowell Observatory, suzannetackitt@gmail.com)
Henricus Stempels (Uppsala University, Eric.Stempels@physics.uu.se)
David Stooksbury (The University of Georgia, stooks@engr.uga.edu)
Klaus Strassmeier (AIP, Potsdam, kstrassmeier@aip.de)
Antoine Strugarek (U. de Montral, strugarek@astro.umontreal.ca)
John Subasavage (U. S. Naval Observatory, jsubasavage@nofs.navy.mil)
Jonathan Swift (Caltech, jsswift@astro.caltech.edu)
Suzanne Tackitt (Lowell Observatory, suzannetackitt@gmail.com)
xianyu tan (LPL, xianyut@lpl.arizona.edu)
Angelle Tanner (Mississippi State, at876@msstate.edu)
Susan Terebey (Cal State LA, sterebe@calstatela.edu)

Ryan Terrien (Penn State, rct151@psu.edu)
Paola Testa (Harvard-Smithsonian CfA, ptesta@cfa.harvard.edu)
Christopher Theissen (Boston University, ctheisse@bu.edu)
Chris Tinney (UNSW Australia, c.tinney@unsw.edu.au)
Jonathan Tottle (Imperial College London, j.tottle11@imperial.ac.uk)
Regner Trampedach (SAC, Aarhus Univ., art@phys.au.dk)
Alexandra Tritschler (NSO, ali@nso.edu)
Jake Turner (University of Virginia, jt6an@virginia.edu)
Jeffrey Valenti (STScI, valenti@stsci.edu)
Adriana Valio (Mackenzie University, adrivalio@gmail.com)
Gerard van Belle (Lowell Observatory, gerard@lowell.edu)
Laura Venuti (IPAG, Grenoble, Laura.Venuti@obs.ujf-grenoble.fr)
Aline Vidotto (University of Geneva, Aline.Vidotto@unige.ch)
Jacqueline Villadsen (Caltech, jrv@astro.caltech.edu)
Kaspar von Braun (MPIA, braun@mpia.de)
Frederick Vrba (U.S. Naval Observatory, fjr@no.navy.mil)
Lucianne Walkowicz (Princeton University, l.m.walkowicz@gmail.com)
George Wallerstein (University of Washington, wall@astro.washington.edu)
Frederick Walter (Stony Brook University, frederick.walter@stonybrook.edu)
Ji Wang (Yale University, ji.wang@yale.edu)
Kimberly Ward-Duong (Arizona State University, kwardduo@asu.edu)
Sven Wedemeyer-Boehm (University of Oslo, svenwe@astro.uio.no)
Kolby Weisenburger (Boston University, kolbylyn@bu.edu)
Andrew West (Boston University, aawest@bu.edu)
Peter Williams (Harvard, pwilliams@cfa.harvard.edu)
Peter Todd Williams (Agilent Technologies, Inc, peter.todd.williams@gmail.com)
Jennifer Winters (Georgia State Univ., winters@astro.gsu.edu)
Robert Wittenmyer (UNSW, rob@phys.unsw.edu.au)
Scott Wolk (Harvard-Smithsonian CfA, swolk@cfa.harvard.edu)
Uwe Wolter (University of Hamburg, uwolter@hs.uni-hamburg.de)
Martin Woodard (NWRA, mfw@nwra.com)
Duncan Wright (UNSW, duncan.wright@unsw.edu.au)
Ya-Lin Wu (University of Arizona, yalinwu@email.arizona.edu)
Rakesh Yadav (MPI for Sol. Sys. Res., yadav@mps.mpg.de)
Hao Yang (University of Arizona, haoyang@email.arizona.edu)
Jennifer Yee (Harvard-Smithsonian CfA, jyee@cfa.harvard.edu)
Chadwick Young (Nicholls State University, chad.young@nicholls.edu)
Kaisa Young (Nicholls State University, kaisa.young@nicholls.edu)
Hyein Yu (Ewha W. University, yuhyein@gmail.com)
Robert Zavala (US Naval Observatory, bzavala@no.navy.mil)
Xi Zhang (University of Arizona, xiz@lpl.arizona.edu)
ZengHua Zhang (IAC, zenghuazhang@gmail.com)



CS18 bags full of goodies awaiting the conference.

Chapter 1

Foreward

Gerard van Belle¹

¹*Lowell Observatory, 1400 West Mars Hill Road, Flagstaff, Arizona, USA
86001*

Some inspiring, insightful text goes here.



Gerard van Belle opens up the Cool Stars 18 meeting.

Chapter 2

The Transition Between X-ray Emission Regimes in the M34 Open Cluster

Ph. Gondoin

European Space Agency, ESTEC - Postbus 299, 2200 AH Noordwijk, The Netherlands

Abstract. I report on a correlation between the saturated and non-saturated regimes of X-ray emission and the rotation sequences that have been observed in the M34 open cluster from extensive rotation periods surveys. An interpretation of this correlation in term of a transition between different dynamo regimes in the early stage of evolution on the main sequence is proposed.

1. Introduction

The present paper summarises the results of a study of the X-ray coronal emission in the M34 open cluster. M34 (NGC 1039) is located at a distance of about 470 pc (Jones et al. 1996). Its metallicity is close to solar (Schuler et al. 2003). Its age between 177 Myr (Meynet et al. 1993) and 251 Myr (Ianna & Schlemmer 1993) is intermediate between that of the Pleiades (~ 125 Myrs) and that of the Hyades (~ 625 Myrs).

While stars in the Pleiades rotate at rates between 0.2 and 10 days (Hartman et al. 2010), stars in the Hyades are in general much slower rotators (Delorme et al. 2011). During the ~ 500 Myrs time interval that separates these two clusters, late-type stars such as those present in M34 thus undergo significant changes in their surface rotation rate. These changes are the visible signature of modifications of their internal rotation profiles. These, in turn, could affect the dynamo processes that operate in their interiors, possibly altering the level

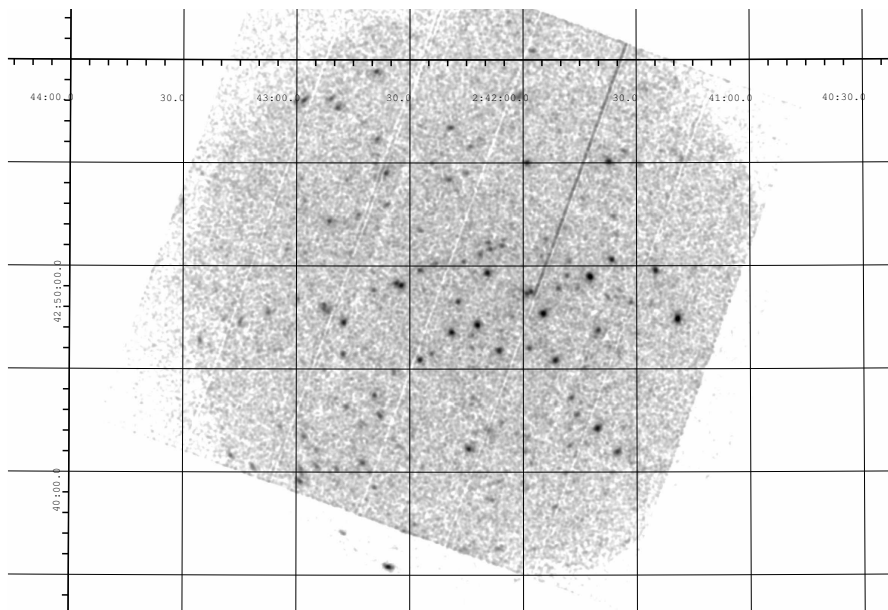


Figure 1.: Combined MOS1, MOS2, and PN image of NGC 1039 in the 0.5 to 4.5 keV band.

of magnetic activity in their outer atmospheres. The purpose of the study was to look for the X-ray signatures of such possible modifications.

2. Observations

M34 was observed with the EPIC pn and the two EPIC MOS cameras on board the *XMM – Newton* space observatory (Jansen et al. 2001). The EPIC pn and MOS exposure times were 42 ksec and 39 ksec, respectively (see Fig. 1). A “thick” aluminum filter was used in front of the cameras to reject visible light from the stars. Detection was made of 189 X-ray sources that are listed in the *XMM – Newton* Serendipitous Source Catalog (Watson et al. 2009).

The X-ray data were complemented with recent measurement results of stellar rotation periods. The *XMM – Newton* X-ray source list was first correlated with the list of 83 kinematic and photometric late-type M34 cluster members with known rotation periods established by Meibom et al. (2011). It was then correlated with the results of a time series photometric survey of M34 in the V- and i- bands reported by Irwin et al. (2006). Finally, the list was correlated with the list of 55 solar-type stars in M34, whose rotation periods were derived from differential photometry by James et al. (2010). In total, 41 stellar members of the M34 open cluster have been found that have known rotational periods and for which X-ray emission has been detected.

X-ray fluxes were derived from the source count rates using energy conversion factors (ECF). These ECFs were calculated using the Portable, Interactive, Multi-Mission Simulator (Mukai 1993) in the 0.5-4.5 keV range for optically thin plasmas with temperatures comparable to those found in the spectral fitting of active stellar coronae (Gondoin 2006). The absorbing hydrogen column density

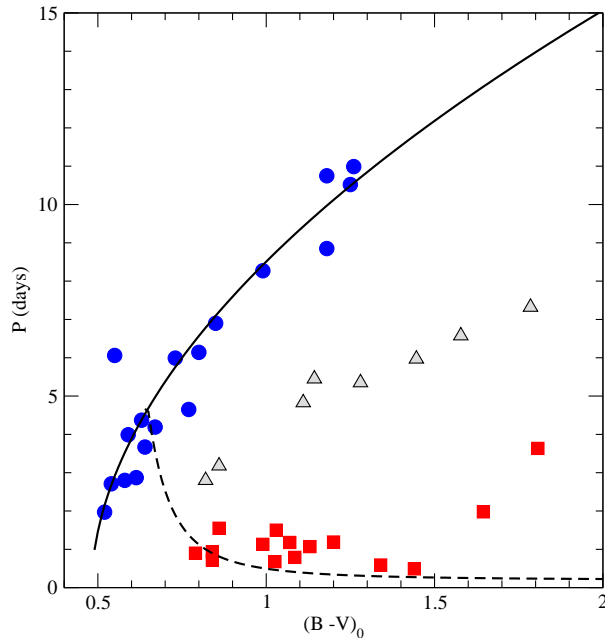


Figure 2.: Rotation periods vs. $(B-V)_0$ indices of the M34 sample stars. The solid line represents the I sequence defined by Barnes (2007). The dashed line represents the C sequence determined by Meibom et al.(2011). M34 stars represented as blue circles and red squares were classified as I and C sequence stars, respectively. Grey triangles represent gap stars assumed to be evolving from the C to the I sequence.

towards M34 was estimated from the reddening correction $E_{B-V} = 0.07$ (Canterna et al. 1979) to about $3.4 \times 10^{20} \text{ cm}^{-2}$. For absorbing hydrogen column densities lower than 10^{21} cm^{-2} , the energy conversion factor of the EPIC pn camera equipped with a thick filter in the 0.5-4.5 keV band is flat and well approximated by $\text{ECF} = 3.7 \times 10^{11} \text{ counts erg}^{-1} \text{ cm}^2$ for plasma temperatures in the range $(4-25) \times 10^6 \text{ K}$ (Gondoin 2006). The X-ray fluxes were then converted into stellar X-ray luminosities assuming a distance of 470 pc (Jones et al. 1996).

3. Analysis

The X-ray luminosities of F5 through M5 main-sequence stars relative to their bolometric luminosities have been found to depend on their Rossby numbers (Patten & Simon 1996); (Randich 2000). This number ($Ro = P_{\text{rot}} / \tau_c$) is an important indicator in hydromagnetic dynamo theory that measures the extent to which rotation can induce both helicity and differential rotation, which are considered essential for a solar-type dynamo. While the stellar rotation period P_{rot} can be directly measured, τ_c is sometimes derived from the mixing-length

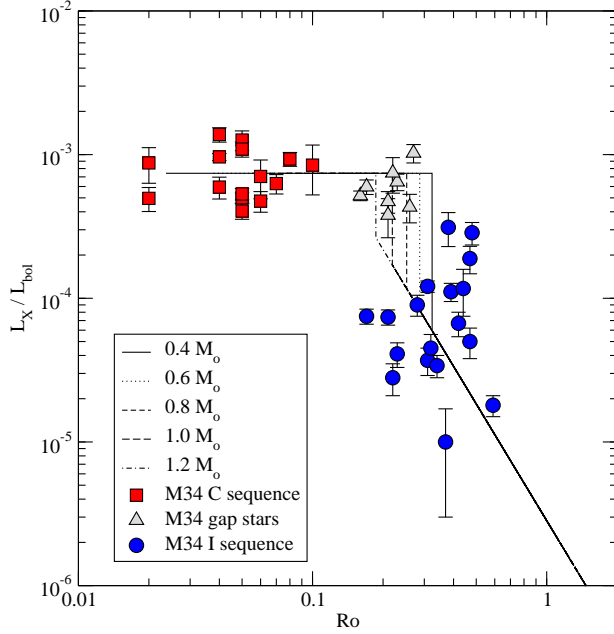


Figure 3.: X-ray to bolometric luminosity ratio vs Rossby number of the sample stars compared with a model of X-ray activity evolution (Gondoin 2013) for stars with masses between 0.4 and $1.2 M_{\odot}$ having an initial period of rotation of 1.1 days on the ZAMS.

theory (Kim & Demarque 1996) and usually empirically determined. A relationship between stellar mass and convective turnover time was recently derived by Wright et al. (2011) that is valid over the range $0.09 M_{\odot} < M < 1.36 M_{\odot}$. It is scaled such that values of τ_c for solar-mass stars match those of Noyes et al. (1984) for the Sun. This relationship was used to estimate the Rossby numbers of the sample stars.

Young stars tend to group into two main sub-populations that lie on narrow sequences in diagrams where the measured rotation periods of the members of a stellar cluster are plotted against their $B - V$ colors (Barnes 2003); (Meibom et al. 2009). One sequence, called the I sequence, consists of stars that form a diagonal band of increasing period with increasing $B - V$ color. In young clusters, another sequence of ultra-fast rotators called the C sequence, is also observed, bifurcating away from the I sequence towards shorter rotation periods. Some stars lie in the intervening gap between the I and C sequences.

Figure 2 shows the rotational periods P_{rot} of the sample stars as a function of their reddening corrected $(B - V)_0$ indices. It also displays the rotational isochrones of the I and C sequences. Their functional forms were first introduced by Barnes (2003a). For the I sequence, I used the form subsequently modified by Barnes (2007) in line with the gyrochronology analysis of M34 performed by

(Meibom et al. 2011). The proximity of the M34 data points to these curves was used to determine their membership to the C and I sequences or the gap between them.

Figure 3 displays the X-ray to bolometric luminosity ratio vs Rossby number diagram of the M34 sample stars, distinguishing members of the I sequence, of the C sequence and of the gap. It shows a correlation between the X-ray emission regimes and rotation sequence classification. Indeed, members of the C sequence have small Rossby numbers ($Ro < 0.1$) and X-ray to bolometric luminosity ratios close to the 10^{-3} saturation level. Members of the I sequence, in contrast, have larger Rossby numbers ($Ro \geq 0.17$) and X-ray to bolometric luminosity ratios significantly smaller than the saturation limit.

Gap stars occupy an intermediary position in the L_X/L_{bol} vs. Ro diagrams. On the one hand, gap stars have Rossby number ($Ro \geq 0.17$) in the same range as those of some I sequence stars. They would therefore be expected to operate in a non-saturated regime of X-ray emission. On the other hand, their X-ray to bolometric luminosity ratio is similar to those of C sequence stars, i.e., close to the saturation level.

4. Discussion

A correlation between rotation sequences (see Fig. 2) and X-ray emission regimes (see Fig.3) is observed among main sequence stars in the M34 open cluster. A steep transition in the L_X/L_{bol} ratio is detected between the C sequence and gap stars that emit close to the 10^{-3} saturation level, and the I sequence stars, whose L_X/L_{bol} ratio is significantly lower. The L_X/L_{bol} ratio is a lower limit of the ratio between the surface magnetic flux and the outer convective flux (Gondoin 2012). A decrease of this ratio around $Ro \approx 0.14 - 0.4$ is thus indicative of a drop in dynamo efficiency.

Independently from any specific model of stellar rotation evolution, the clustering of main-sequence stars in M34 into fast and slow rotation sequences in period vs colour index diagrams, and the low density of stars in the gap indicate that stars spend less time in this part of the diagram than on the C and I sequences. The transition from the C to the I sequence thus constitutes an evidence for a brief phase of strong surface rotation deceleration among some of the late-G and K type stars in M34. Such a decay is most likely due to rotational braking by stellar wind. If the magnetic field lines that sling charged particles from the wind into space are rooted in the photosphere, the convective envelope rotation should be decelerated by the wind torque more efficiently than the radiative core which is kept in rapid rotation by the conservation of angular momentum. Young stars shall thus develop a strong gradient in angular velocity at the base of the convection zone. Such a gradient is an essential ingredient for the generation of an interface dynamo at the base of the convection zone (Spruit 2002).

According to a scenario described in Gondoin (2013), the correlation between rotation sequences and X-ray emission regimes would thus result from the co-existence of two dynamo processes among M34 stars, i.e. a boundary-layer interface dynamo and a convective envelope turbulent dynamo. This last process dominates in rapidly rotating C sequence stars. As the shear between the fast spinning radiative interior and the convective envelope increases during the transition of gap stars from the C to the I sequence, another process strengthens

in which dynamo action occurs in the boundary region between the radiative core and the convective envelope. This dynamo process relies on differential rotation, but also induces important redistributions of angular momentum. As the stars reach the I sequence and the rotation of their convective envelope decays, the turbulent dynamo is quenched and the interface dynamo becomes dominant, decreasing progressively at later stages of evolution when rotation dies away.

Acknowledgements. I am grateful to the Organising Committees of the "Cool Stars 18" workshop for allowing me to present this work.

References

- Barnes, S. A. 2003, *ApJ*, 586, 464
- Barnes, S. A. 2007, *ApJ*, 669, 1167
- Brown, B. P., Browning, M. K., Brun, A. S. et al. 2008, *AJ*, 689, 1354
- Canterna, R., Crawford, D. L., & Perry, C. L. 1979, *PASP*, 91, 263
- Delorme, P., Cameron, A. C., Hebb, L. et al. 2011, in the proceedings of the 16th Cambridge Workshop on Cool Stars, Stellar Systems, and the Sun. ASP Conference Series, Vol. 448, p. 841.
- Fisher, G., Longcope, D., Metcalf, T. et al. 1998, *ApJ*, 508, 885
- Gondoin, P. 2006, *A&A*, 454, 595
- Gondoin, P. 2012, *A&A*, 546, A117
- Gondoin, P. 2013, *A&A*, 556, A14
- Hartman, J. D., Bakos, G. ., Kovcs, G., & Noyes, R. W. 2010, *MNRAS*, 408, 475
- Ianna, P. A., & Schlemmer, D. M. 1993, *AJ*, 105, 209
- Irwin, J., Aigrain, S., Hodgkin, S. et al. 2006, *MNRAS*, 370, 954
- James, D. J., Barnes, S. A., Meibom, S. et al. 2010, *A&A*, 515, A100
- Jansen, F., Lumb, D., Altieri, B., et al. 2001, *A&A*, 365, L1
- Jones, B. F., & Prosser, C. F. 1996, *AJ*, 111,1193
- Kim, Y., & Demarque, P. 1996, *ApJ*, 457, 340
- Meibom, S., Mathieu, R. D., & Stassun, K. G. 2009, *ApJ*, 695, 679
- Meibom, S., Mathieu, R. D., Stassun, K. G. et al. 2011, *ApJ*, 733, 115
- Meynet, G., Mermilliod, J., & Maeder, A. 1993, *A&AS*, 98, 477
- Mukai, K. 1993, *Legacy* 3, 21-31
- Noyes, R. W., Hartmann, L. W., Baliunas, S. L., et al. 1984, *ApJ*, 279, 763
- Patten, B. M., & Simon, T. 1996, *ApJS*, 106, 489
- Randich, S. 2000, in ASP Conf. Ser. 198, *Stellar Clusters and Association: Convection, Rotation and Dynamos*, 401
- Schuler, S. C., King, J. R., Fischer, D. A., et al. 2003, *AJ*, 125, 2085
- Spruit, H., C. 2002, *A&A*, 381, 923
- Watson, M. G., Schrder, A. C., Fyfe, D., et al. 2009, *A&A*, 493, 339
- Wright, N. J., Drake, J. J., Mamajek, E. E., & Henry, G. W. 2011, *ApJ*, 743, 48



Our Cool Stars 18 ‘Great Debaters’, Martin Asplund and Marc Pinsonneault.



Natalie Hinkel covered the details of her Hypatia database.

Chapter 3

Lithium Abundance and Rotation in the Pleiades and M34 Open Clusters

Ph. Gondoin

European Space Agency, ESTEC - Postbus 299, 2200 AH Noordwijk, The Netherlands

Abstract. K-type stars of similar effective temperatures in clusters younger than about 250 Myrs are characterised by a wide dispersion in lithium abundance whose origin is not understood.

Photometric monitoring programs indicate that young stars tend to group into two main populations that lie on narrow sequences in diagrams where the measured rotation periods of the members of a stellar cluster are plotted against their (B - V) colours.

I report on the results of a study that investigated the dependence of lithium abundance with effective temperature distinguishing stars that belong to different rotation sequences in the Pleiades and M34 open clusters.

1. Introduction

Photometric monitoring programs have produced a large number of rotation period measurements in open clusters, including the Pleiades (Hartman et al. 2010) and M34 (Meibom et al. 2011). These measurements have shown (Barnes 2003) that members of young stellar clusters tend to group on narrow sequences in diagrams where the measured rotation periods are plotted against masses or $B - V$ colour indices. I revisited the connection between Li abundance and rotation in the Pleiades and M34 open clusters in light of these new rotation rate measurements (Gondoin 2014).

2. Li abundances and stellar rotation periods measurements

2.1 The Pleiades

Recently, Hartman et al. (2010) conducted an extensive photometric time-series survey of the Pleiades based on the membership list of Stauffer et al. (2007). Rotation periods were measured on 368 stars with $0.4 \leq M/M_{\odot} \leq 1.3$. I cross-matched these data with lithium abundance measurements in the Pleiades retrieved by King et al. (2000). The colour indices of the resulting 64 sample stars are in the range $0.5 < (B-V)_0 < 1.33$ which corresponds to late-F, G, and early-K spectral types and to masses between 0.7 and 1.3 M_{\odot} . All these stars have reached the main sequence since their Kelvin-Helmholtz contraction timescales is shorter than their age of about 100–150 Myrs (Stauffer 2010).

2.2 The M34 open cluster

Lithium abundances in M34 were derived by Jones et al. (1997) from a high resolution spectroscopy study of stars with high membership probabilities. I correlated these data with the list of 83 kinematic and photometric late-type M34 cluster members with known rotation periods established by Meibom et al. (2011), with the results of a time series photometric survey of M34 reported by Irwin et al. (2006), and with the list of 55 solar-type stars in M34, whose rotation periods were derived from differential photometry by James et al. (2010). In total, 23 stellar members of the M34 open cluster have been found that have known rotational periods and Li abundances. Their colour indices in the range $0.55 < (B-V)_0 < 1.23$ and age estimate between 177 Myrs (Meynet et al. 1993) and 251 Myrs (Ianna & Schlemmer 1993) indicate that these stars have reached the main sequence.

3. Analysis

3.1 Classification into rotation sequences

Observations of main sequence stars with G and K spectral types in young open clusters (~ 100 -200 Myrs) show clear evidence for two distinct sequences of fast and slow rotators in period vs mass or $(B-V)$ colour index diagrams (Hartman et al. 2010). These rotation sequences are called hereafter the C and the I sequence along the paradigm advanced by Barnes (2003).

Figure 1 (bottom) plots the rotational periods P of the M34 sample stars as a function of their reddening corrected $(B-V)_0$ indices. It also displays functional forms of the I and C sequences that were first introduced by Barnes (2003). For the I sequence, I used the form subsequently modified by Barnes (2007) in line with the gyrochronology analysis of M34 performed by Meibom et al. (2011). From the data point positions relative to these curves, the M34 sample stars were classified as lying on the C sequence, on the I sequence, or in the gap between these two sequences.

Hartman et al. (2010) compared the mass-period diagrams, which are equivalent to colour-period diagrams, of the Pleiades and four other open clusters with similar ages. They noted that the mass-period diagram of the Pleiades is remarkably similar to that seen by Meibom et al. (2009) for the M35 open cluster which gyro-age ranges from 134 Myrs to 161 Myrs. Figure 1 (top) shows the colour-

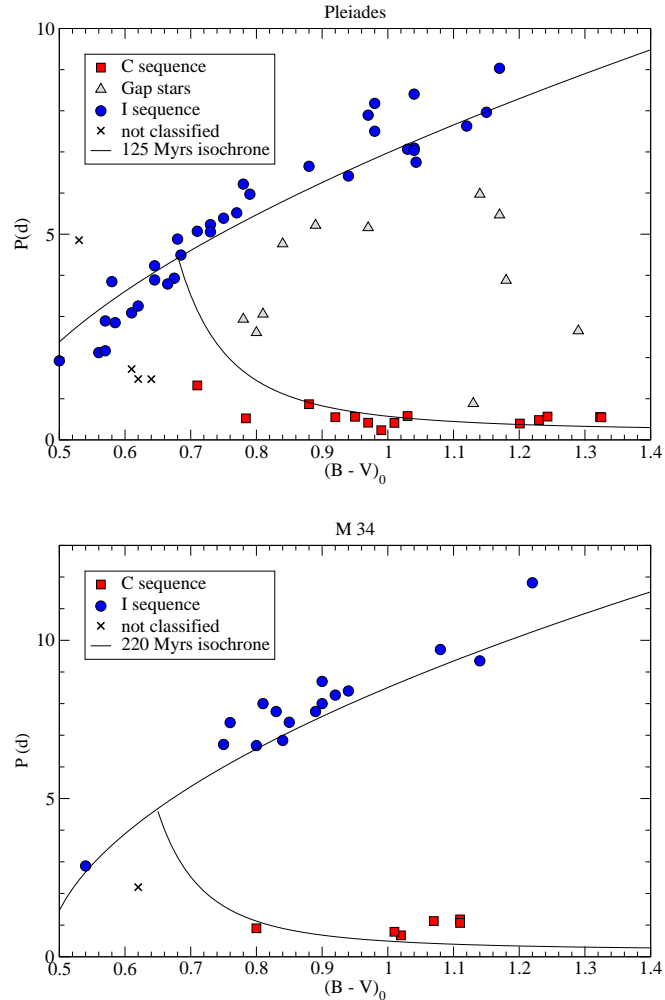


Figure 1.: Rotation periods of the Pleiades (top) and M34 (bottom) sample stars as a function of their $(B-V)_0$ colour indices compared with C and I isochrones.

period diagram of the Pleiades sample stars with known Li abundances. It also displays functional forms of the I and C rotation isochrones derived from the gyrochronology analysis of M35 performed by Meibom et al. (2009). I classified the Pleiades sample stars as members of the C sequence, of the I sequence or of the gap based on their proximity to the 125 Myrs C and I isochrones.

Four stars in the Pleiades and one star in M34 with $(B-V)_0 < 0.7$ could not be classified and are marked by crosses in Fig. 1. These blue and bright objects are most likely close binaries in which the active component is locked into high rotation by synchronisation with the orbital period due to tidal effects.

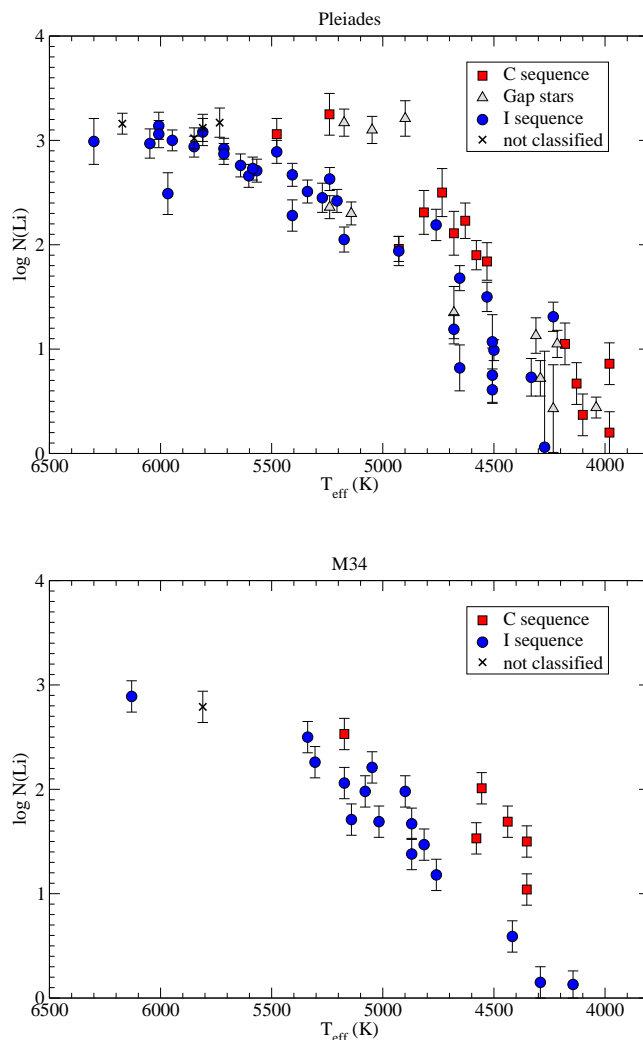


Figure 2.: Lithium abundance vs effective temperature for the Pleiades (top) and M34 (bottom) sample stars.

3.2 Lithium abundance and rotation

The lithium abundances of the Pleiades and M34 sample stars are plotted as a function of their effective temperatures in Fig. 2. The lithium abundance decreases with effective temperature by nearly three orders of magnitude between 6000 K and 4000 K. This well-known decay is expected from standard models of stellar evolution that predict the attrition of Li as a function of stellar mass, and age. According to these models, pre-main sequence stars with low masses evolving down the Hayashi track develop high enough temperatures at the base of their convection zone for energetic protons to destroy Li there, thereby depleting their

surface Li abundance. Reversely, little Li depletion is expected for stars reaching the zero-age main sequence (ZAMS) as A, F, or G dwarfs (Pinsonneault 1997). Since Li depletion ceases as the surface convection zone recedes toward the surface and its base cools, standard models of stellar evolution also predicts that no further Li depletion occurs on the main-sequence for A, F, and G dwarfs (Proffitt et al. 1989); (Deliyannis et al. 1990); (Swenson 1990), whereas K and M dwarfs should continue to deplete Li as they evolve beyond the ZAMS. This prediction is consistent with Fig. 2. Indeed, G-type stars have similar Li abundance in the Pleiades and M34 while K-type stars have in average lower Li abundance in the older M34 cluster. This comparison is justified since the two clusters have similar metallicities (Schuler et al. 2003); (Taylor 2008).

However, standard models also predict that ${}^7\text{Li}$ depletion in a star is a unique function of age, mass, and metallicity. Figure 2, in contrast, shows that stars with the same T_{eff} in the Pleiades or in M34 have significantly different Li abundances. The scatter in the star-to-star Li abundance is particularly large in the 5500–4000 K temperature range as noted by Jones et al. (1997) in M34 and by Soderblom et al. (1993a), Jones et al. (1996), and King et al. (2000) in the Pleiades. A comparison of the observed scatter in Li abundances with the estimated uncertainties indicates that this spread is statistically significant. Furthermore, Fig. 2 shows that, at any given temperature below 5500 K, C sequence and gap stars in the Pleiades have significantly higher lithium abundances than I sequence stars with the same effective temperature.

4. Discussion

Independently from any specific model of stellar rotation evolution, the clustering of young main-sequence stars into fast and slow rotation sequences in period vs colour index diagrams, their later evolution through the gap towards a single sequence, and the low density of stars in the gap indicate that stars spend less time in this part of the diagram than on the C and I sequences. The transition from the C to the I sequence thus constitutes an evidence for a brief phase of strong surface rotation deceleration among rapidly rotating late-G and K type stars in their early phase of evolution on the main sequence.

The fact that the transition from the C to the I rotation sequence in the Pleiades and M34 is correlated with a drop in Li abundance suggests that the associated decay of the rotation rate is accelerating the depletion of lithium in young late-G and K-type stars. Rotational braking by stellar winds is the commonly accepted explanation for the decay of stellar rotation on the main sequence. Since the magnetic field lines that sling charged particles from the wind into space are rooted in the photosphere, the wind torque is expected to decelerate the envelope rotation while the conservation of angular momentum should keep the radiative core in rapid rotation. Gap stars in young open clusters should thus develop a large shear at the base of their convection zone that triggers various instabilities. Studies indicate that these instabilities drive mass motions or gravity waves that redistribute angular momentum and mix the stellar material enhancing light-element depletion (Chaboyer et al. 1995); (Charbonnel & Talon 2005); (Talon 2008).

The dispersion in surface Li abundance observed among K stars in young open clusters could thus result from an acceleration of the Li depletion in rapidly

rotating K stars due to shear instabilities at the bottom of the convection zone during a brief episode of strong rotational braking by stellar wind in their early evolution on the main sequence. This scenario explains that no lithium dispersion is observed in the Hyades and Praesaepe star clusters (Soderblom et al. 1993b) since, by the age of these clusters (~ 700 Myrs), observations show a clear convergence in the angular momentum evolution of all F, G, and K dwarfs towards a single sequence of slow rotators. All the stars have by then experienced a strong rotational braking that accelerated Li depletion and the coolest stars ($T_{\text{eff}} < 5000$ K) have fully depleted their lithium.

Acknowledgements. I am grateful to the Organising Committees of the "Cool Stars 18" workshop for allowing me to present this work.

References

- Barnes, S. A. 2003, ApJ, 586, 464
- Barnes, S. A. 2007, ApJ, 669, 1167
- Chaboyer, B., Demarque, P., & Pinsonneault, M. H. 1995, ApJ, 441, 876
- Charbonnel, C. & Talon, S. 2005, Science, Vol. 309, Iss. 5744, p. 2189
- Deliyannis, C. P., Demarque, P., & Kawaler, S. D. 1990, ApJS, 73, 21
- Gondoin, P. 2014, A&A, 566, A72
- Hartman, J. D., Bakos, G. ., Kovcs, G., & Noyes, R. W. 2010, MNRAS, 408, 475
- Ianna, P. A., & Schlemmer, D. M. 1993, AJ, 105, 209
- Irwin, J., Aigrain, S., Hodgkin, S. et al. 2006, MNRAS, 370, 954
- James, D. J., Barnes, S. A., Meibom, S. et al. 2010, A&A, 515, A100
- Jones, B. F., Shetrone, M., Fischer, D., & Soderblom, D. R. 1996, AJ, 112, 186
- Jones, B. F., Fischer, D., Shetrone, M., & Soderblom, D. R. 1997, AJ, 114, 352
- King, J. R., Krishnamurthi, A., & Pinsonneault, M. H. 2000, AJ, 119, 859
- Meibom, S., Mathieu, R. D., & Stassun, K. G. 2009, ApJ, 695, 679
- Meibom, S., Matthieu, R. D., Stassun, K. G. et al. 2011, ApJ, 733, 115
- Meynet, G., Mermilliod, J., & Maeder, A. 1993, A&AS,, 98, 477
- Pinsonneault, M. 1997, ARA&A, 35, 557
- Proffitt, C. R. & Michaud, G. 1989, ApJ, 346, 976
- Schuler, S. C., King, J. R., Fischer, D. A., et al. 2003, AJ, 125, 2085
- Soderblom, D. R., Jones, B. F., Balachandran, S. et al. 1993a, AJ, 106, 1059
- Soderblom, D. R., Fedele, S. B., Jones, B. F. et al. 1993b AJ, 106, 1080
- Stauffer, J. R., Hartmann, L. W., Fazio, G. G., et al. 2007, ApJS, 172, 663
- Stauffer, J. R. 2010, in Star Clusters in the Era of Large Survey, Proceedings of Symposium 5 of JENAM, A. Moitinho & J. A. Alves eds., p. 155
- Swenson, F. J., Faulkner, J., Rogers, F. J., & Iglesias, C. A. 1994, ApJ, 425, 286
- Talon, S. 2008, Memorie della Societa Astronomica Italiana, 79, 569
- Taylor, B. J. 2008, AJ, 136, 1388



Moira Jardine shows the way with stellar activity timescales.



Emily Rice and Lil' Brown Dwarf taking a break.

Chapter 4

Line Bisector Variability in the Sun as a Star

Mark Giampapa¹, Luca Bertello¹ & Alexei Pevtsov¹

¹*National Solar Observatory, Tucson, Arizona, USA 85726-6732*

Abstract. We utilize spectra obtained with the Integrated Sunlight Spectrometer (ISS) instrument of the NSO SOLIS facility on Kitt Peak, AZ to perform a preliminary study of the variability of line asymmetries in the Mn I line at 539.5 nm and the nearby Fe I line at 539.3 nm, respectively. We derive the line bisector for these photospheric features from daily spectra of the Sun as a star acquired since January 2007, and characterize the variability of a measure of bisector amplitude with the solar cycle. A simple two-component model of the solar magnetic field is investigated as a possible origin for the variation in line depth with time of the magnetically sensitive Mn I feature.

1. Introduction

The intrinsic asymmetry in spectral lines in the Sun and late-type stars arises from the velocity-brightness correlation between hotter and brighter upward (blueshifted) moving granules and downward (redshifted) flowing plasma in the intergranular lanes (Gray 1988). Thus, natural line asymmetries are a diagnostic of the nature of global velocity fields in the solar-stellar atmosphere as seen in spatially integrated spectra.

We utilize spectra obtained with the Integrated Sunlight Spectrometer (ISS) – an instrument of the NSO SOLIS (*Synoptic Long-term Investigation of the Sun*) facility on Kitt Peak, Arizona – to conduct a preliminary investigation of the variability of line asymmetries in selected solar photospheric lines since 2007. The SOLIS facility with its suite of instruments is described by Keller et al. (2003). Additional details about ISS observations are given by Bertello et al.

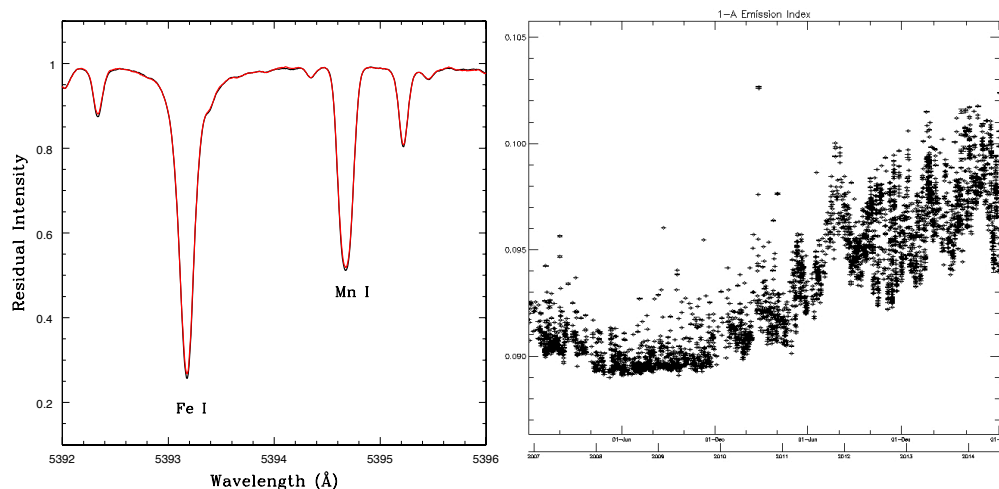


Figure 1.: The spectral region of the Fe I and Mn I lines (*left*). The spectrum is from 3 May 2009 (solid black line). Overplotted (dashed red line) is the spectrum from 3 May 2014. Note the slight filling in of the line cores in the spectrum from 2014 (dashed-red). The Ca II K time series for the 1-Å core emission index in the Sun observed as a star is displayed for reference (*right*). The spectral resolution is about $R = 300,000$

(2011). The ISS spectra discussed herein were calibrated according to procedures described by Pevtsov et al. (2014). We display in Fig. 1 spectra obtained in the region of interest during the extended solar minimum in 2009 and the current rise toward the maximum of Cycle 24 in 2014. Also shown for reference is the time series of the 1 Å index in the core of the Ca II K line. We adopt the line bisector as a measure of the line asymmetry and calculate its velocity span, or amplitude, in the Mn I line at 539.47 nm and the nearby Fe I feature at 539.32 nm, respectively. We discuss general features of the variability of the profiles with the solar cycle of activity. We also refer the reader to Bertello et al. (2014; these Proceedings) for a complementary discussion of variations in photospheric line parameters in the Sun as a star.

2. Line Bisector Construction

We followed the approach described by Povich et al. (2001) in their analysis of stellar line bisectors in the spectra of hosts of exoplanet systems. Specifically, we start with the point nearest the central wavelength position and then step up the blue side of the profile point by point. We determine the line center position through a spline fit to the (relatively broad) core. The line bisector was derived by using points on the blue side of the profile without any interpolation and performing a linear interpolation between wavelength positions on the red side at the same relative intensity. We then determined the midpoint of the corresponding segment with the bisector constructed by connecting the midpoints of all the line segments. This procedure typically yielded a bisector consisting of 21 points in these high-resolution solar spectra.

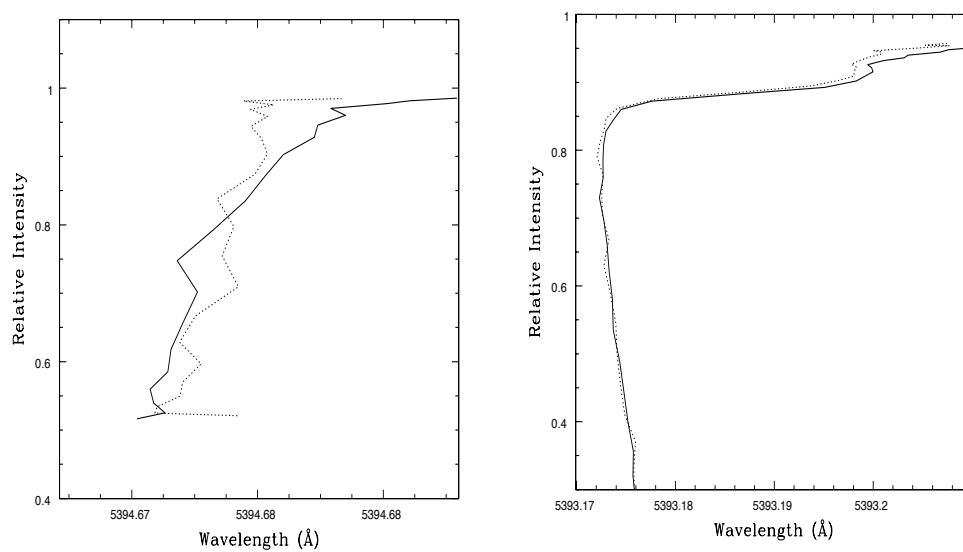


Figure 2.: The line bisectors corresponding to the photospheric lines in Figure 1. (*Left*) Bisectors for the Mn I line. The solid line is the bisector from the 2009 spectrum obtained during the extended minimum of Cycle 23 while the dashed line is the bisector acquired in 2014 during the current Cycle 24 rise to maximum. (*Right*) Similarly but for the Fe I feature. Note the relative complexity of the bisector for the Mn I line and its apparent variation from solar minimum to solar maximum. By contrast, the Fe I line exhibits comparatively little change

Examples of line bisectors for the Mn I line and the Fe I feature displayed in Fig. 1, respectively, are given in Fig. 2. Bisectors of both lines exhibit the characteristic "C-shape" arising from the velocity-brightness correlation of granular motions. However, the Mn I bisector is characterized by a complex structure with less of an overall C-shape in 2014 compared to that from 2009. Livingston et al. (1999) have attributed the reduced velocity span of the C-shape to magnetic effects on the velocity field in the line formation region. By contrast, the Fe I bisector is more smooth and exhibits little variation from solar minimum to the current maximum.

Given the complexity of the Mn I bisector, we adopted the approach of Povich et al. (2001) in deducing the velocity span by calculating an average velocity displacement from line center utilizing three evaluation points at relative intensities (0.60, 0.75, 0.90). By adopting the average of three evaluation points, the uncertainties in individual velocity spans are minimized. This method yielded a time series of bisector amplitudes derived from 1,704 near-daily spectra obtained from 2007 January – 2014 May. The Lomb-Scargle periodogram of the time series of velocity spans did not yield any significant peaks at solar rotation periods. Thus, variations in the bisector amplitude are not dominated by major active region complexes that could be expected to exhibit a rotational modulation signal, analogous to that seen in the Ca II K line. Therefore, the line bisector amplitude must be affected by a longer-period variation in the background global solar magnetic field (in the region of line formation). The implicit assumption in this supposition is that variability in the line bisector is due primarily to magnetic field-induced effects and not purely hydrodynamical effects.

3. Two-component Magnetic Model of Line Profile Variations

The variation in the core relative intensity is likely a manifestation of the interplay between enhanced heating and Zeeman sensitivity arising from the increase in the globally averaged magnetic flux with the solar-stellar cycle. This effect can be reproduced by simple single-component thermal models. We present an additional perspective that recognizes that enhanced heating occurs in the presence of magnetic fields combined with a consideration of the magnetic sensitivity of, in this case, the Mn I 539.467 nm line, which is characterized by an effective Landé g -factor of 1.857 (indicative of moderate magnetic sensitivity). Following Giampapa et al. (1983), we adopt a two-component model where the observed stellar profile is a combination of profiles from quiet (nonmagnetic) and active (magnetic) regions weighted by the filling factor of active regions, or

$$M(\lambda) = (1 - f)Q(\lambda) + Af[Z(\lambda - \Delta_H) + Z(\lambda + \Delta_H)] + BfZ(\lambda),$$

where M is the observed profile, Q is the reference quiet profile, Z is the unsplit profile, and A and B are constants that depend on the line-of-sight to the field lines. In this approach we have approximated the hyperfine splitting in the Mn I line with a simple Zeeman triplet representation. The Zeeman splitting is given by $\Delta_H = 4.7 \times 10^{-13} gH\lambda^2$ in units of Å, where H is the magnetic field in Gauss and g is the effective Landé g -factor. Upon Fourier transforming with k as the transform variable and averaging over all possible line-of-sight angles we obtain

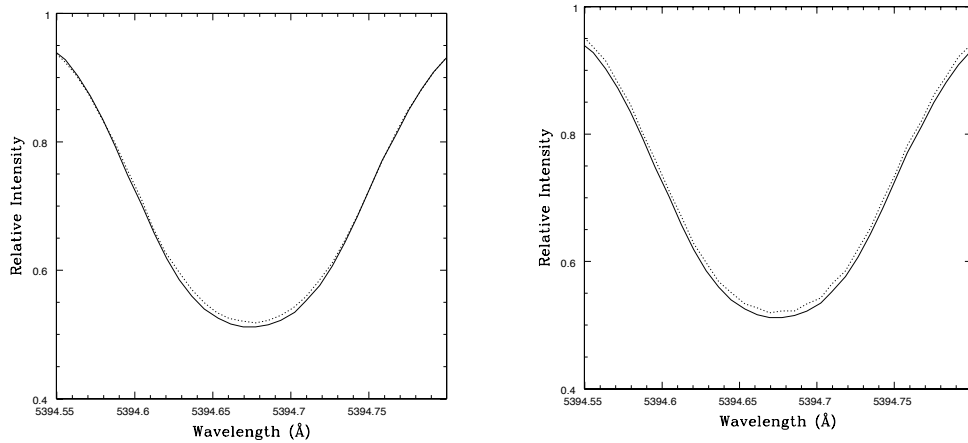


Figure 3.: (*Left*) The observed Mn I line profiles recorded during the Cycle 23 minimum (solid) and the current Cycle 24 rise to maximum (dashed). The slight filling in of the line core with increasing globally averaged chromospheric activity is evident in these high signal-to-noise spectra. (*Right*) The same Mn I profile from solar minimum (solid) along with the line profile resulting from the application of a simple two-component model (*dashed*) as described below

$$g(k) = (1 - f) + \frac{1}{4} \frac{M}{Q} f [1 + 3 \cos(\Delta_H k)] .$$

Multiplying the transform of the solar-minimum Mn I profile by the function $g(k)$ and inverse transforming yields the dashed profile in the right panel of Fig. 3, where we adopted a filling factor $f = 0.3$ and a field strength of $H = 500$ G. The similarity of the resulting profile derived from the application of the above model to the quiescent profile is consistent, at least qualitatively, with the results of Vitas et al. (2009). In particular, these investigators claim on the basis of extensive modeling that the sensitivity of the Mn I 539.47 nm line to activity is due entirely to its hyperfine structure. The nearby Fe I 539.317 nm line with an effective Landé g-factor of 1.5 also is sensitive to magnetic fields. The above model could be equally applied to this feature to account for the slight change in core depth noted in Fig. 1. However, the marked difference in the line bisector shapes between the Mn I and the Fe I 539.317 nm lines (Fig. 2) would seem to reinforce the conclusion by Vitas et al. (2009) that it is the hyperfine structure of the Mn I line in the presence of magnetic fields that is the dominant factor in the determination of changes in the line profile shape in the spatially integrated spectrum of the Sun as a star. Our simplified approach is illustrative of the additional perspectives that can be obtained on the variation of magnetically sensitive lines with atmospheric heating and the associated magnetic field regions.

Acknowledgements. We thank the organizers of the 18th “Cool Stars” Workshop for a productive and enjoyable meeting. This work utilizes SOLIS data obtained by the NSO Integrated Synoptic Program (NISP). NISP is managed by the National Solar Observatory, which is operated by the Association of Universities for Research in Astronomy, Inc., under a cooperative agreement with the National Science Foundation.

References

- Bertello, L., Pevtsov, A., Giampapa, M. & Marble, A. 2014, Proc. Lowell Observ. (9-13 June 2014)
- Bertello, L., Pevtsov, A. A., Harvey, J. W., & Toussaint, R. M. 2011, Solar Phys., 272, 229
- Golub, L., Giampapa, M. S., & Worden, S. P. 1983, ApJ, 268, L121
- Gray, D. F. 1988, Lectures on Spectral-Line Analysis: F, G, and K Stars (Arva: Ontario)
- Keller, C. U., Harvey, J. W., & Giampapa, M. S. 2003, SPIE Proc., 4853, 194
- Livingston, W., Wallace, L., Huang, Y., & Moise, E. 1999, High Resolution Solar Physics: Theory, Observations, and Techniques, ed. T. R. Rimmele, K. S. Balasubramaniam & R. R. Radick, ASP Conf. Ser. 183, 494
- Pevtsov, A. A., Bertello, L., & Marble, A. R. 2014, Astronomische Nachrichten, 335, 21
- Povich, M. S., Giampapa, M. S., Valenti, J. A., et al. 2001, AJ, 121, 1136
- Vitas, N., Viticchiè, B., Rutten, R. J., & Vögler, A. 2009, A&A, 499, 301

Chapter 5

Stars with and without planets: Where do they come from?

V. Zh. Adibekyan¹, J. I. González Hernández^{2,3}, E. Delgado Mena¹,
S. G. Sousa^{1,2,4}, N. C. Santos^{1,4}, G. Israelian^{2,3}, P. Figueira¹, S.
Bertran de Lis^{2,3}

¹*Centro de Astrofísica da Universidade do Porto, Rua das Estrelas,
4150-762 Porto, Portuga*

²*Instituto de Astrofísica de Canarias, 38200 La Laguna, Tenerife, Spain*

³*Departamento de Astrofísica, Universidad de La Laguna, 38206 La
Laguna, Tenerife, Spain*

⁴*Departamento de Física e Astronomia, Faculdade de Ciências da
Universidade do Porto, Portugal*

Abstract. A long and thorough investigation of chemical abundances of planet-hosting stars that lasted for more than a decade has finally bore fruit. We explore a sample of 148 solar-like stars to search for a possible correlation between the slopes of the abundance trends versus condensation temperature (known as the T_c slope) both with stellar parameters and Galactic orbital parameters in order to understand the nature of the peculiar chemical signatures of these stars and the possible connection with planet formation. We find that the T_c slope correlates at a significant level (at more than 4σ) with the stellar age and the stellar surface gravity. We also find tentative evidence that the T_c slope correlates with the mean galactocentric distance of the stars (R_{mean}), suggesting that stars that originated in the inner Galaxy have fewer refractory elements relative to the volatile ones. We found that the chemical peculiarities (small refractory-to-volatile ratio) of planet-hosting stars is merely a reflection of their older age and their inner

Galaxy origin. We conclude that the stellar age and probably Galactic birth place are key to establish the abundances of some specific elements.

1. Introduction

Dozen of studies during the last decade explored the connection between stellar and planetary properties. Naturally, this connection is found to be bidirectional: stellar properties play an important role on planet formation and evolution (e.g. stellar metallicity-giant planet frequency - Gonzalez (1997); Santos et al. (2001)), and the planet formation may have an impact on stellar properties (e.g. extra depletion of lithium in planet-hosting stars - Israelian et al. (2009); Delgado Mena et al. (2014)).

After the first planets discovered, astronomers have been also trying to understand if the stars hosting planets are chemically peculiar (in terms of individual elements) and even to search for chemical signatures of planet formation on the hosting stars atmospheres. For the first part the most significant result was recently obtained by Adibekyan et al. (2012a,b) who found that most of the metal-poor planet hosts are enhanced in α -elements. For the second part (chemical imprints of planet formation) the results are still feeding a lively debate.

Several studies suggested that the chemical abundance trend with the condensation temperature, T_c , is a signature of terrestrial planet formation (e.g. Meléndez et al. 2009; Ramírez et al. 2009). In particular, that the Sun shows "peculiar" chemical abundances because of the presence of the terrestrial planets in our solar system (Meléndez et al. 2009). Although these conclusions have been strongly debated in other studies (e.g. González Hernández et al. 2010, 2013, hereafter GH10,13), the main reason of the observed chemical peculiarities was not identified.

Here we explore the origin of the trend observed between $[X/H]$ (or $[X/Fe]$) and T_c using a sample of 148 solar-like stars from GH10,13. The more detailed analysis and complete results are presented in Adibekyan et al. (2014).

2. Data

Our initial sample is a combination of two samples of solar analogs (95 stars) and "hot" analogs (61 stars) taken from GH10,13. We have cross-matched this sample with the Geneva-Copenhagen Survey sample (GCS- Nordström et al. 2004), for which Casagrande et al. (2011) provides the Galactic orbital parameters, the space velocity components, and the ages of 148 of the stars considered in our study¹. Fifty-seven of these stars are planet hosts, while for the remaining 91 no planetary companion has been detected up to now.

¹Throughout the paper, BASTI expectation ages are used as suggested by Casagrande et al. (2011).

The stellar atmospheric parameters and the slopes of the $\Delta[X/Fe]_{SUN-star}$ versus T_c were derived using very high-quality HARPS spectra². Twenty-five elements from C ($Z = 6$) to Eu ($Z = 63$) have been used for this analysis. These slopes are corrected for the Galactic chemical evolution trends as discussed in GH10,13.

The stars in the sample have effective temperatures $5604 K \leq T_{eff} \leq 6374 K$, metallicities $-0.29 \leq [Fe/H] \leq 0.38$ dex, and surface gravities $4.14 \leq \log g \leq 4.63$ dex. Throughout the paper we defined solar analogs as stars with; $T_{eff} = 5777 \pm 200$ K; $\log g = 4.44 \pm 0.20$ dex; $[Fe/H] = 0.0 \pm 0.2$ dex. Fifteen out of 58 solar analogs in this sample are known to be orbited by planets.

3. Correlations with T_c slope

We searched for possible correlations between the T_c slope and, in turn, atmospheric parameters, and also Galactic orbital parameters and age, in order to understand which is/are the main factor(s) possibly responsible for the abundance trends with T_c .

3.1 T_c slope against stellar parameters and age

After a detailed analysis, we found that the T_c trend strongly relates (at more than 4σ) with the surface gravity and stellar age (see Figure 1): old stars are more depleted in refractory elements (smaller refractory-to-volatile ratios) than their younger counterparts. At the same time we found no significant correlation of the T_c slope with other stellar parameters.

Since for FGK dwarf stars in the main sequence one does not expect significant changes in their atmospheric chemical abundances with age, we are led to believe that the observed correlation is likely to reflect the chemical evolution in the Galaxy. We note that this is the simplest assumption we can make based on our limited current knowledge of stellar evolution, and we caution the reader that there might be other effects that could severely affect the composition of stars as a function of age .

3.2 T_c slope and Galactic orbital parameters

Moving one step further, we found a tentative evidence that the T_c slopes correlate also with the mean galactocentric distance of the stars (R_{mean}), which we use as a proxy of the birth radii (see Figure 2)³. This trend is indicating that stars which have originated in the inner Galaxy have less refractory elements relative to the volatiles. This result qualitatively agrees with the recent observations of Galactic abundance gradients by Lemasle et al. (2013), where the authors used young Galactic Cepheids for the gradient derivations.

²Zero slope means solar chemical composition, and a positive slope corresponds to a smaller refractory-to-volatile ratio compared to the Sun.

³Several studies have shown that the mean of the apo- and pericentric distances, R_{mean} , are good indicators of the stellar birthplace (e.g. Grenon 1987; Edvardsson et al. 1993)

3.3 T_c slope and planets

Following our definition of solar analogs, we found that the average of the T_c slope for planet hosting solar analogs is greater (0.012 ± 0.31) than that of their non-host counterparts (-0.16 ± 0.34). The Kolmogorov-Smirnov (K-S) statistics predict the ≈ 0.21 probability (P_{KS}) that these two subsamples came from the same underlying distribution for T_c slope. At the same time, the same statistics predict a $P_{KS} \approx 0.20$ probability that they stem from the same underlying age distributions. The latter can be seen in Figure 1: most of the planet-hosting stars tend to be relatively old (> 5 Gyr). Moreover, planet host and non-host samples show a different distribution of $R_{mean} - P_{KS} \approx 0.007$. As can also be seen in Figure 2, 66% planet hosts have R_{mean} smaller than 7.5 kpc (where slopes are usually high) and only 37% of stars without detected planets have similarly low R_{mean} values. Clearly the two subsamples are not consistent with respect to the mean galactocentric distance and age. Interestingly, Haywood (2009) has already shown that (giant) planet host stars tend to have smaller R_{mean} and probably originate in the inner disk, which follow the same direction as our findings.

These results suggest that the difference in T_c slopes observed for solar analogs with and without planets is then probably due to the differences in their “birth places” and birth moment.

4. Conclusion

Our findings lead us to two interesting conclusions i) The solar analogues with planets in the solar neighborhood mostly come from the inner Galaxy (because of still unknown reason) and ii) the age and galactic birth place are the main factors responsible for the abundance ratio of refractory to volatile elements in the stars.

Acknowledgements. This work was supported by the European Research Council/European Community under the FP7 through Starting Grant agreement number 239953. V.Zh.A., S.G.S., and E.D.M are supported by grants SFRH/BPD/70574/2010, SFRH/BPD/47611/2008, and SFRH/BPD/76606/2011 from the FCT (Portugal), respectively. NCS also acknowledges support in the form of a Investigador FCT contract funded by FCT/MCTES (Portugal) and POPH/FSE (EC). G.I., S.B.L, and J.I.G.H. acknowledge financial support from the Spanish Ministry project MINECO AYA2011-29060, and J.I.G.H. also received support from the Spanish Ministry of Economy and Competitiveness (MINECO) under the 2011 Severo Ochoa Program MINECO SEV-2011-0187. PF is supported by the FCT and POPH/FSE (EC) through an Investigador FCT contract with application reference IF/01037/2013 and POPH/FSE (EC) by FEDER funding through the program ”Programa Operacional de Factores de Competitividade - COMPETE.

References

- Adibekyan, V. Z., Delgado Mena, E., Sousa, S. G., et al. 2012, *A&A*, 547, A36
- Adibekyan, V. Z., Santos, N. C., Sousa, S. G., et al. 2012, *A&A*, 543, A89
- Adibekyan, V. Z., González Hernández, J. I., Delgado Mena, E., et al. 2014, *A&A*, 564, L15

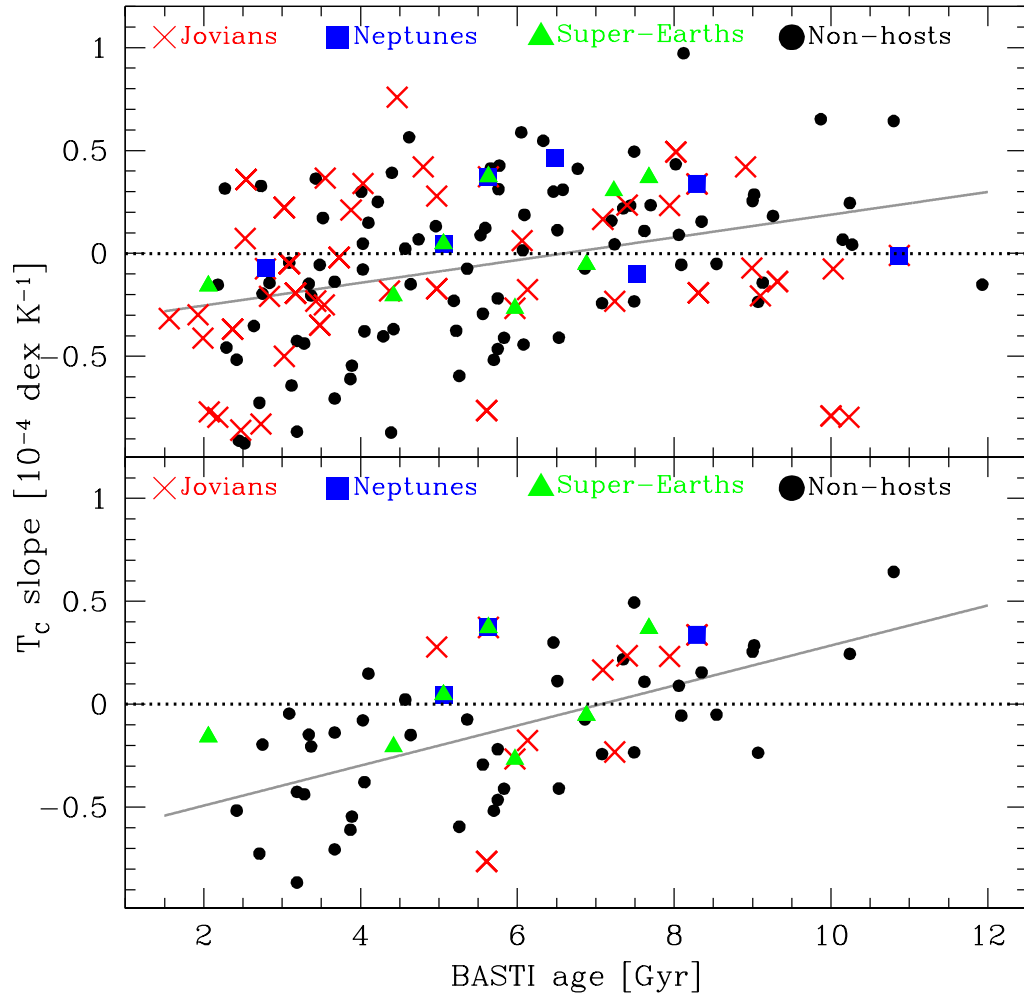


Figure 1.: T_c slopes versus ages for the full sample (*top*) and for the solar analogs (*bottom*). Gray solid lines provide linear fits to the data points.

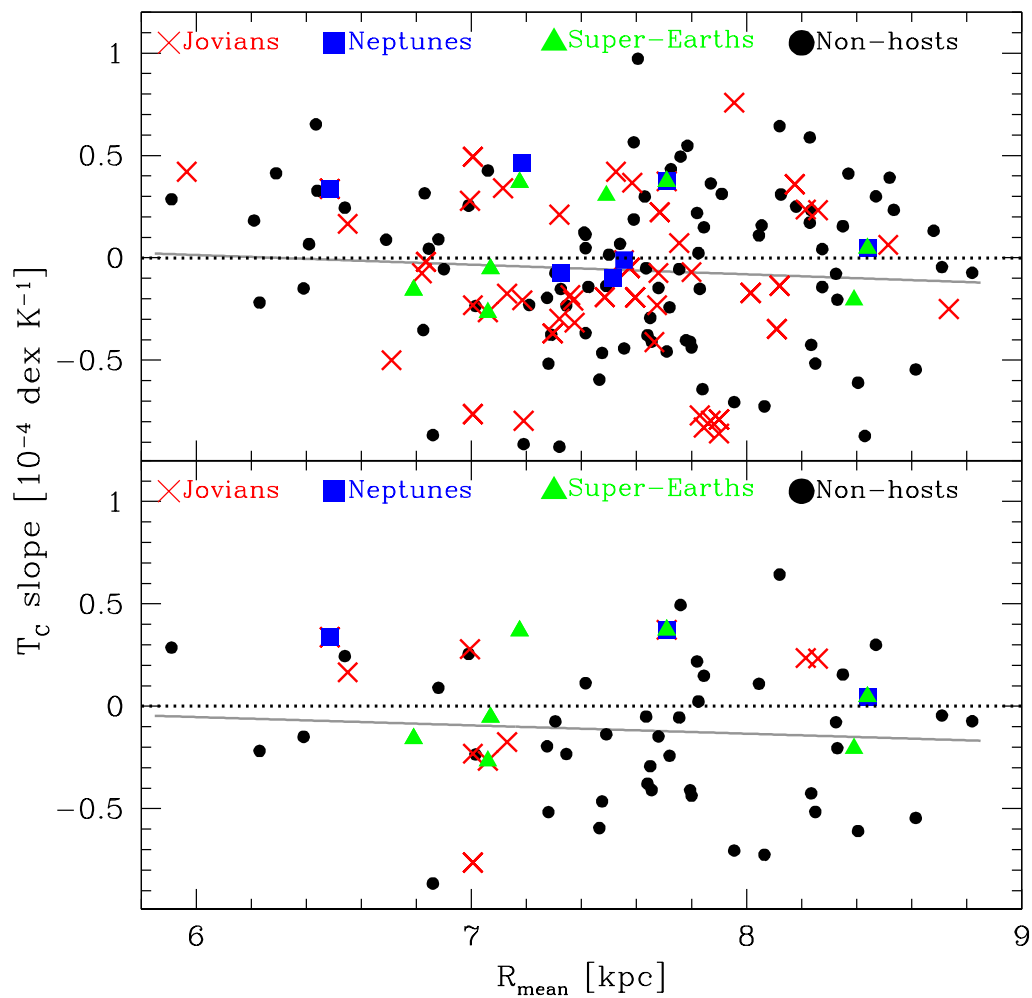


Figure 2: T_c slopes versus R_{mean} for the full sample (top) and for the solar analogs (bottom). Gray solid lines provide linear fits to the data points.

- Casagrande, L., Schönrich, R., Asplund, M., et al. 2011, *A&A*, 530, A138
- Delgado Mena, E., Israelian, G., González Hernández, J. I., et al. 2014, *A&A*, 562, A92
- Edvardsson, B., Andersen, J., Gustafsson, B., et al. 1993, *A&A*, 275, 101
- Gonzalez, G. 1997, *MNRAS*, 285, 403
- González Hernández, J. I., Israelian, G., Santos, N. C., et al. 2010, *ApJ*, 720, 1592
- González Hernández, J. I., Delgado-Mena, E., Sousa, S. G., et al. 2013, *A&A*, 552, A6
- Grenon, M. 1987, *Journal of Astrophysics and Astronomy*, 8, 123
- Haywood, M. 2009, *ApJ*, 698, L1
- Israelian, G., Delgado Mena, E., Santos, N. C., et al. 2009, *Nature*, 462, 189
- Lemasle, B., François, P., Genovali, K., et al. 2013, *A&A*, 558, A31
- Meléndez, J., Asplund, M., Gustafsson, B., & Yong, D. 2009, *ApJ*, 704, L66
- Nordström, B., Mayor, M., Andersen, J., et al. 2004, *A&A*, 418, 989
- Ramírez, I., Meléndez, J., & Asplund, M. 2009, *A&A*, 508, L17
- Santos, N. C., Israelian, G., & Mayor, M. 2001, *A&A*, 373, 1019

Chapter 6

Preparation of the CARMENES Input Catalogue: Low- and High-resolution Spectroscopy of M dwarfs

F. J. Alonso-Floriano¹, D. Montes¹, J. A. Caballero², A. Klutsch^{1,3},
S. Jeffers⁴, A. Reiners⁴, M. Zechmeister⁴, A. Lamert⁴,
V. M. Passegger⁴, R. Mundt⁵, P. J. Amado⁶, Z. M. Berdiñas⁶,
E. Casal⁶, M. Cortés-Contreras¹, J. C. Morales^{7,8}, I. Ribas⁷,
C. Rodríguez-López⁶, A. Quirrenbach⁹

¹*Departamento de Astrofísica, Facultad de Física, Universidad
Complutense de Madrid, E-28040 Madrid, Spain*

²*Centro de Astrobiología (CSIC-INTA), Campus ESAC, PO Box 78,
E-28691 Villanueva de la Cañada, Madrid, Spain*

³*Osservatorio Astrofisico di Catania, Via S. Sofia 78, 95123, Catania, Italy*

⁴*Institut für Astrophysik (IAG), Friedrich-Hund-Platz 1, D-37077
Göttingen, Germany*

⁵*Max-Planck-Institut für Astronomie, (MPIA), Königstuhl 17, D-69117
Heidelberg, Germany*

⁶*Instituto de Astrofísica de Andalucía (CSIC), Glorieta de la Astronomía
s/n, E-18008 Granada, Spain*

⁷*Institut de Ciències de l'Espai (CSIC-IEEC), Campus UAB, Facultat
Ciències, E-08193, Barcelona, Spain*

⁸*LESIA Observatoire de Paris, 61 Avenue de l'Observatoire, 75014, Paris,
France*

⁹*Landessternwarte (LSW), Zentrum für Astronomie der Universität
Heidelberg, Königstuhl 12, D-69117 Heidelberg, Germany*

Abstract. The identification of the most promising targets for exoplanet hunting is a crucial first step to ensure an efficient use of the CARMENES

guaranteed time. To achieve this, we obtained low-resolution ($R \sim 1500$) spectra of 752 M (and late K) dwarfs mostly fainter than $J = 9$ mag with CAFOS. For all of them, we derived spectral types with 0.5 subtypes accuracy. We also studied metallicity and surface gravity through spectral indices, and activity from $pEW(H\alpha)$. Next, we observed over 600 M dwarfs at higher resolution ($R = 30\,000\text{--}48\,000$) with FEROS, CAFE and HRS. We determined rotational velocities, $v \sin i$ ($\pm 0.2\text{--}0.5 \text{ km s}^{-1}$), and radial velocities, V_r ($\pm 0.1\text{--}0.2 \text{ km s}^{-1}$), of the observed stars. From our observations, we identified high-activity, low-metallicity and low-gravity stars, single- and double-lined spectroscopic binaries and, specially, fast rotators, which should be discarded from any target list for exoplanet searches. Here we present preliminary results.

1. The CARMENES Input Catalogue

CARMENES¹ is an exoplanet survey instrument being built by a collaboration of several Spanish and German institutions and the Calar Alto Observatory. Its main goal is to find exoearths around M dwarfs by the radial velocity technique (Quirrenbach et al. 2012).

CARMENCITA is the CARMENES Input Catalogue. It contains almost 2 200 M dwarfs from a number of references (Reid et al. 1995, 2002; Hawley et al. 1996; Gizis et al. 2002; Bochanski et al. 2005; Caballero 2007; Gatewood & Coban 2009; Lépine et al. 2009; Lépine & Gaidos 2011; Johnson et al. 2010; Irwin et al. 2011; Avenhaus et al. 2012; Deacon et al. 2012; Newton et al. 2014). This catalogue includes information on spectral type, photometry, multiplicity, $v \sin i$, activity, X-ray, etc., and helps us to select the 300 brightest, latest, less active, single M dwarfs observable from Calar Alto that will be monitored during CARMENES guaranteed time. Since many stars lack some of that information, we fill that gap by compiling it from the literature or by measuring it by ourselves. The first step of our preparatory observations was to take accurate low-resolution spectroscopy of M dwarf candidates with not well determined spectral types, as a complement to current spectroscopic surveys (Lépine et al. 2013; Gaidos et al. 2014). The second step was to take high-resolution imaging (Cortés-Contreras et al. 2014) and spectroscopy in order to discard binaries, fast rotators with high $v \sin i$ and very active M dwarfs.

2. Low-resolution spectroscopy

From November 2011 to April 2013, we used the CAFOS spectrograph at the 2.2 m Calar Alto telescope to observe 752 M (and late K) stars, including standard stars. With a spectral resolution $R \sim 1\,500$, a wavelength range of 4 300–8 300 Å and a signal-to-noise larger than 50 near $H\alpha$, we covered the whole main features of M dwarfs in the optical. The processing of the spectra, including instrumental response correction, was done with IRAF. We determined spectral

¹<http://carmenes.caha.es>

types, measured $pEW(H\alpha)$, studied gravity sensitive features and calculated the Lépine et al. (2007) metallicity-sensitive index ζ .

For spectral typing, we defined a grid of 19 “prototype” and 52 “standard” stars from K3.0 V to M8.0 V (Fig. 1). We derived spectral types based on 31 spectral indices (e.g., Kirkpatrick et al. 1991; Reid et al. 1995; Martín et al. 1996) and from best-fit and χ^2 matches (Klutsch et al. 2012). Uncertainties were of only 0.5 subtypes.

We used the $pEW(H\alpha)$ measurements to study the influence of activity on the spectral types indices and identify possibly accreting stars (White & Basri 2003; Barrado y Navascués & Martín 2003). We picked up unidentified giant stars with the ratio C (Na I $\lambda\lambda 8183, 8195 \text{ \AA}$; Kirkpatrick et al. 1991; Fig. 2) and subdwarf candidates with the ζ index (Fig. 3) All the results outlined in this section, including the spectral typing for more than 700 M dwarfs, will be presented in a forthcoming paper (Alonso-Floriano et al. in prep.).

3. High-resolution spectroscopy

We are using FEROS at the MPG 2.2 m La Silla telescope (Fig. 4), CAFE at the 2.2 m Calar Alto telescope and HRS at the Hobby Eberly Telescope for obtaining high-resolution ($R \sim 30\,000\text{--}48\,000$) spectra of M dwarfs. We are measuring rotational and radial velocities (Fig. 5), with accuracies of 0.2–0.5 and 0.1–0.2 km s^{-1} , respectively, and $pEW(H\alpha)$ s for over 600 M dwarfs. Some of them are new spectroscopic binaries, based on their double peaks in cross-correlation functions (CCFs; Fig. 6).

Acknowledgments. Based on observations made at the 2.2 m telescope of the Centro Astronómico Hispano-Alemán (CAHA) at Calar Alto, operated jointly by the Max-Planck Institut für Astronomie and the Instituto de Astrofísica de Andalucía (CSIC), and at the MPG/ESO 2.2-m telescope at the La Silla Paranal Observatory under programmes 090.A-9003(A), 090.A-9029(A), 091.A-9004(A), 092.A-9005(A) and 093.A-9001(A). Also based on observations at the Hobby-Eberly Telescope (HET), which is a joint project of the University of Texas at Austin, the Pennsylvania State University, Stanford University, Ludwig-Maximilians-Universität München, and Georg-August-Universität Göttingen. Financial support was provided by the Spanish Ministerio de Ciencia e Innovación under grants AYA2011-30147-C03-02 and AYA2011-30147-C03-03.

References

- Avenhaus, H., Schmidt, H. M., & Meyer, M. R. 2012, A&A, 548, A105
- Barrado y Navascués, D., & Martín, E. L. 2003, AJ, 126, 2997
- Bochanski, J. J., Hawley, S. L., Reid, I. N., et al. 2005, AJ, 130, 1871
- Caballero, J. A. 2007, ApJ, 667, 520
- Cortés-Contreras, M., Béjar, V. J. S., Caballero, J. A. et al. 2014, this volume
- Deacon, N. R., Liu, M. C., Magnier, E. A., et al. 2012, ApJ, 757, 100

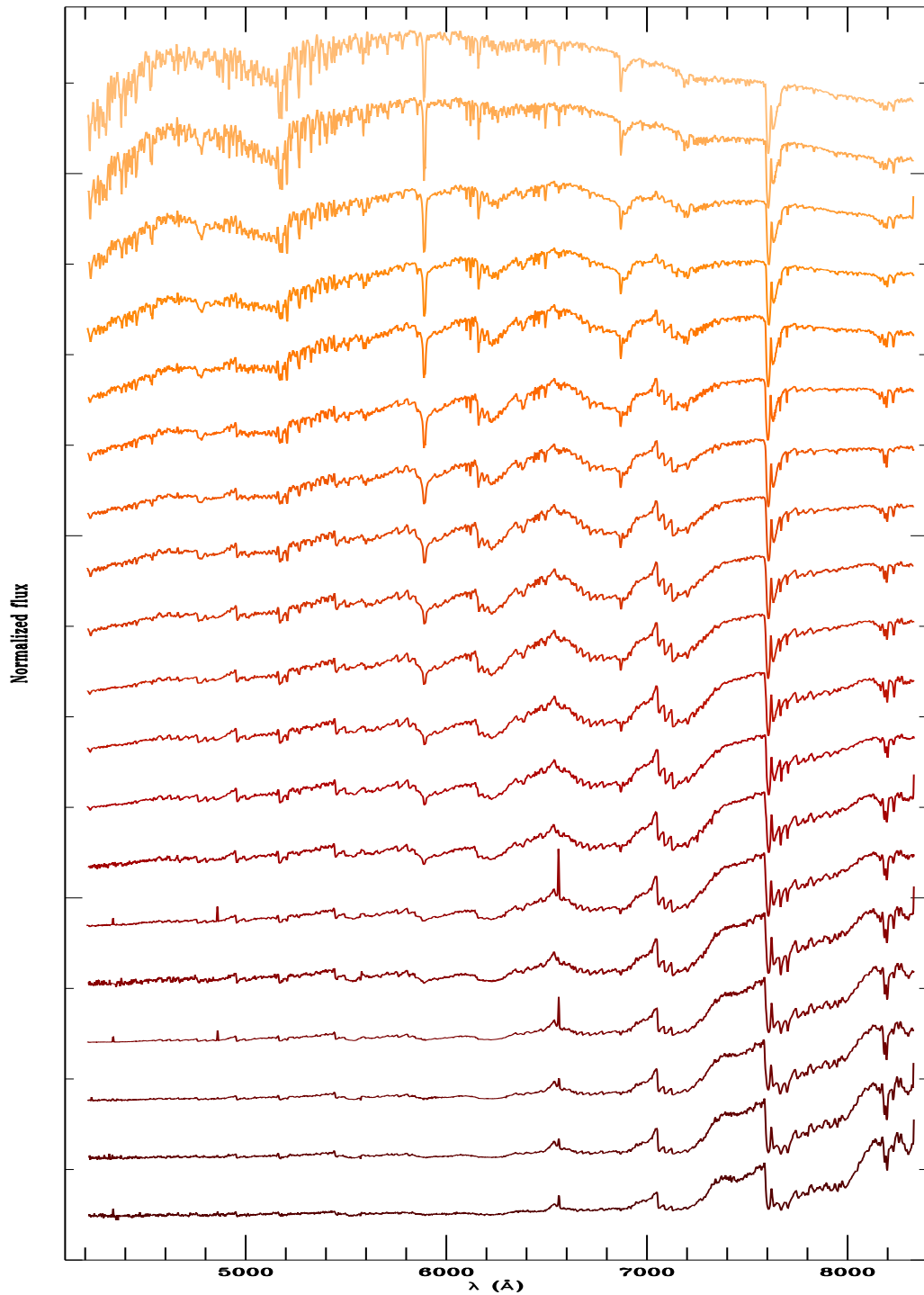


Figure 1.: CAFOS spectra of our prototype stars. From top to bottom: HD 50281 (K3 V), 61 Cyg A (K5 V), η Cas B (K7 V), HD 79210 (M0.0 V), BD+45 2743 (M0.5 V), GX And (M1.0 V), HD 36395 (M1.5 V), GJ 2066 (M2.0 V), Ross 905 (M2.5 V), HD 173739 (M3.0 V), Luyten's star (M3.5 V), V1352 Ori (M4.0 V), GJ 1256 (M4.5 V), V388 Cas (M5.0 V), LP 469-067 (M5.5 V), CN Leo (M6.0 V), DX Cnc (M6.5 V), vB 8 (M7.0 V) and V1298 Aql (M8.0 V).

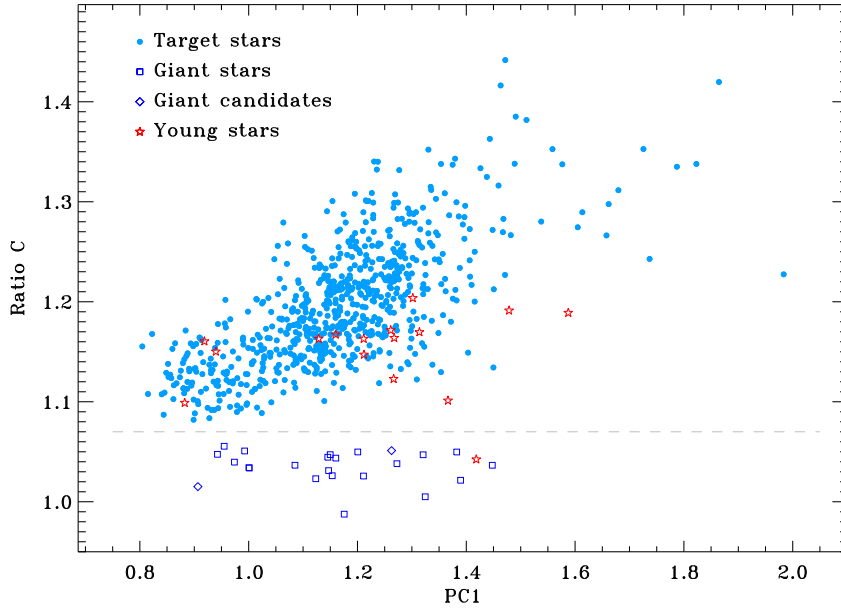


Figure 2.: Ratio C vs. PC1 diagram. The PC1 index is a spectral type proxy. A T Tauri star (open red star) and all objects below the dashed line (open squares and rhombs) have very low surface gravities typical of giant stars.

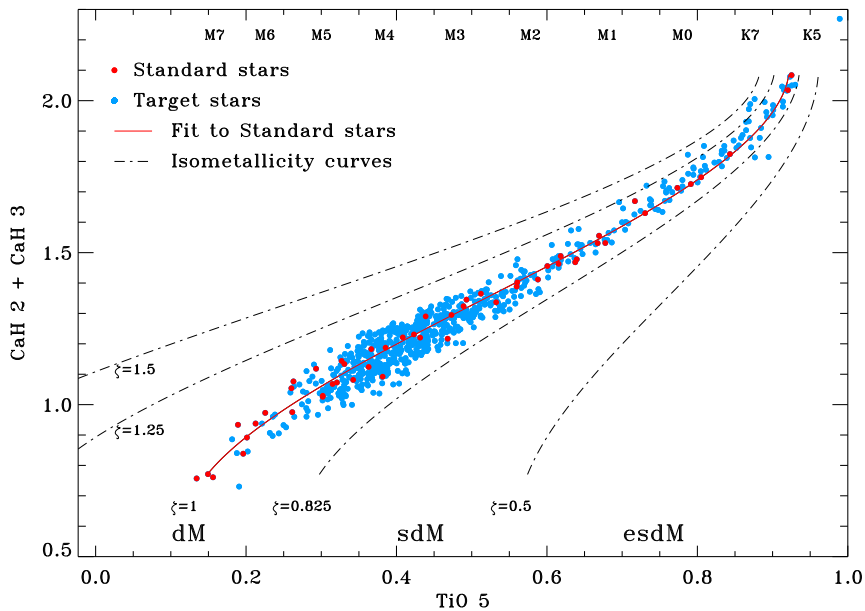


Figure 3.: CaH bands vs. TiO5 diagram. The stars under the “isometallicity curve” $\zeta=0.825$ are low-metallicity candidates.

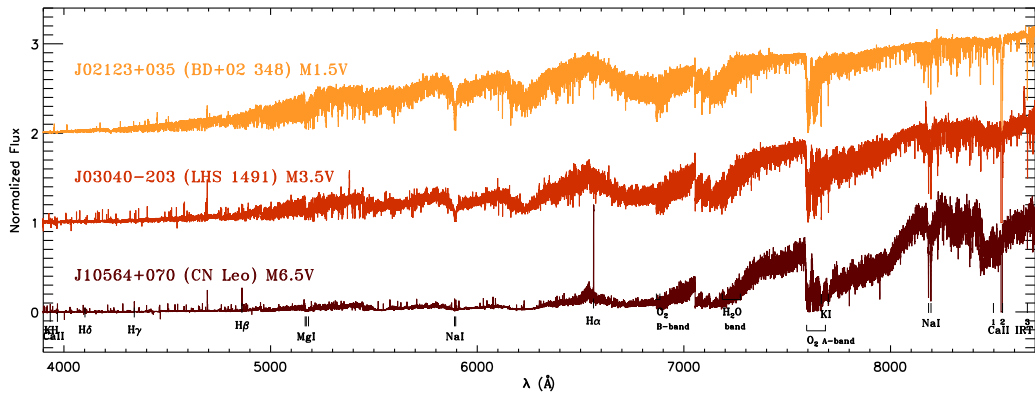


Figure 4.: Three representative examples of spectra taken with FEROS. The main optical lines and telluric bands are indicated.

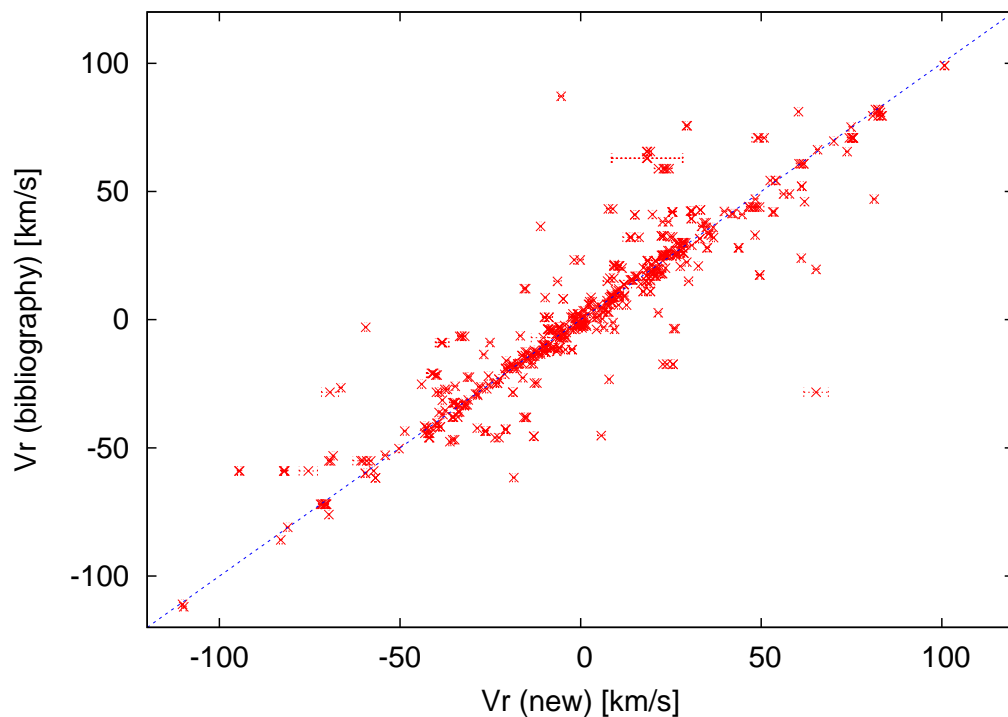


Figure 5.: Radial velocity values from the bibliography compared with our radial velocity measurements. The blue dashed line is the one-to-one line. Error bars are showed

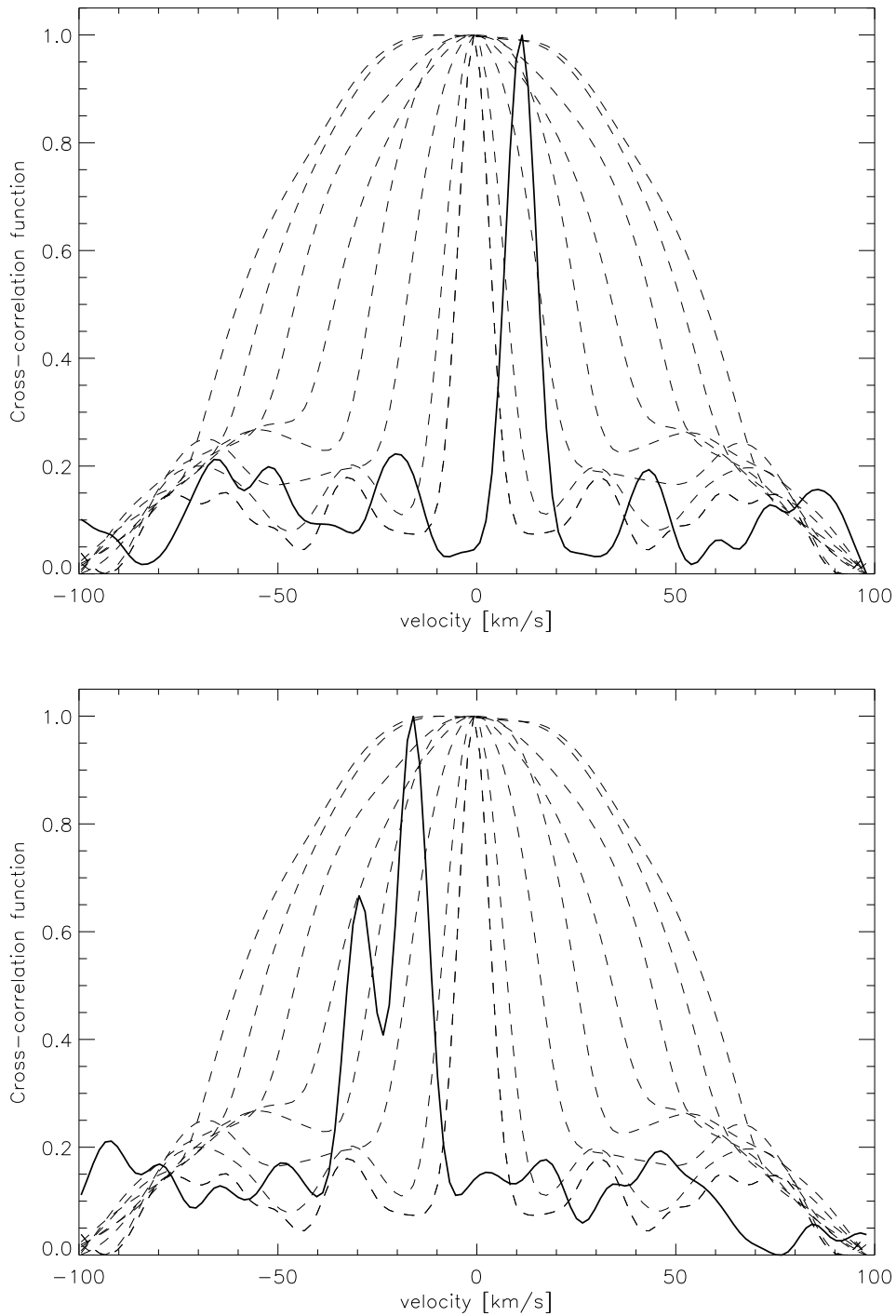


Figure 6.: Cross-correlation functions. Top: Slow rotator star. Bottom: New double-lined spectroscopic binary. Dashed lines are CCFs for several $v \sin i$ values obtained from the artificially broadened of the template spectrum. The solid lines are the CCF of the target star, shifted by its own radial velocity.

- Gaidos, E., Mann, A. W., Lépine, S., et al. 2014, MNRAS, in press (arXiv:1406.7353)
- Gatewood, G., & Coban, L. 2009, AJ, 137, 402
- Gizis, J. E., Reid, I. N., & Hawley, S. L. 2002, AJ, 123, 3356
- Hawley, S. L., Gizis, J. E., & Reid, I. N. 1996, AJ, 112, 2799
- Irwin, J., Berta, Z. K., Burke, C. J., et al. 2011, ApJ, 727, 56
- Johnson, J. A., Aller, K. M., Howard, A. W., et al. 2010, PASP, 122, 905
- Kirkpatrick, J. D., Henry, T. J., & McCarthy, D. W., Jr. 1991, ApJS, 77, 417
- Klutsch, A., Alonso-Floriano, F. J., Caballero, J. A., et al. 2012, SF2A-2012: Proceedings of the Annual meeting of the French Society of Astronomy and Astrophysics, 357
- Lépine, S., Rich, R. M., & Shara, M. M. 2007, ApJ, 669, 1235
- Lépine, S., Thorstensen, J. R., Shara, M. M., et al. 2009, AJ, 137, 4109
- Lépine, S., & Gaidos, E. 2011, AJ, 142, 138
- Lépine, S., Hilton, E. J., Mann, A. W., et al. 2013, AJ, 145, 102
- Martín, E. L., Rebolo, R., & Zapatero Osorio, M. R. 1996, ApJ, 469, 706
- Newton, E. R., Charbonneau, D., Irwin, J., et al. 2014, AJ, 147, 20
- Quirrenbach, A., Amado, P. J., Seifert, W., et al. 2012, SPIE Proceeding, 8446, E0R
- Reid, I. N., Hawley, S. L., & Gizis, J. E. 1995, AJ, 110, 1838
- Reid, I. N., Gizis, J. E., & Hawley, S. L. 2002, AJ, 124, 2721
- Schlieder, J. E., Lépine, S., Rice, E., et al. 2012, AJ, 143, 114
- White, R. J., & Basri, G. 2003, ApJ, 582, 1109

Chapter 7

Convection in Cool Stars, as Seen Through *Kepler*'s Eyes

Fabienne A. Bastien^{1, 2}

¹*Vanderbilt University, 1807 Station B, Nashville, TN 37235, USA*

²*Current Affiliation: Hubble Fellow, Pennsylvania State University, 525 Davey Lab, University Park, PA 16803, USA*

Abstract. Stellar surface processes represent a fundamental limit to the detection of extrasolar planets with the currently most heavily-used techniques. As such, considerable effort has gone into trying to mitigate the impact of these processes on planet detection, with most studies focusing on magnetic spots. Meanwhile, high-precision photometric planet surveys like CoRoT and *Kepler* have unveiled a wide variety of stellar variability at previously inaccessible levels. We demonstrate that these newly revealed variations are not solely magnetically driven but also trace surface convection through light curve “flicker.” We show that “flicker” not only yields a simple measurement of surface gravity with a precision of ~ 0.1 dex, but it may also improve our knowledge of planet properties, enhance radial velocity planet detection and discovery, and provide new insights into stellar evolution.

1. Introduction

Most planets are observed only indirectly, through their influence on their host star. The planet properties we infer therefore strongly depend on how well we know those of the stars. Our ability to determine the surface gravity ($\log g$) of field stars, however, is notoriously limited: broadband photometry, while efficient, yields errors of ~ 0.5 dex; spectroscopy suffers from well known degeneracies between $\log g$, T_{eff} and metallicity (Torres et al. 2010) while having $\log g$ errors of 0.1–0.2 dex (Ghezzi et al. 2010); and asteroseismology, the gold standard for

stellar parameter estimation with $\log g$ errors of ~ 0.01 dex (Chaplin et al. 2011, 2014), is time and resource intensive and, particularly for dwarfs, is limited to the brightest stars.

Meanwhile, high precision photometric surveys like CoRoT and *Kepler* have surveyed over $\sim 200\,000$ Sun-like stars in their hunt for exoplanets, revealing stellar variations that have previously only been robustly observed in the Sun and a handful of bright Sun-like stars — and also variations that were previously unknown but, as we show, encode a simple measure of stellar $\log g$. In what follows, I describe our analysis of the newly unveiled high frequency photometric variations, which we term “flicker” (or F_8) and which enable us to measure $\log g$ with an accuracy of ~ 0.1 dex. I summarize our work thus far in using F_8 to study granulation in Sun-like stars, to examine the impact of granulation in radial velocity planet detection, and to improve size estimates of transiting exoplanets.

2. Photometric “Flicker:” a Tracer of Granulation and a Simple Measure of Stellar Surface Gravity

Using light curves from NASA’s *Kepler* mission, we discovered that stellar $\log g$ reveals itself through F_8 a measure of photometric variations on timescales of < 8 hr — and may hence be used to measure $\log g$ with errors of ~ 0.1 dex, even for stars too faint for asteroseismology (Bastien et al. 2013, Fig. 1). The measurement of $\log g$ from F_8 only requires the discovery light curves, and this measurement not only yields a result with an accuracy that rivals spectroscopy, it also does so very quickly and efficiently, requiring only a simple routine that can be executed by anyone in just a few seconds per star.

In Bastien et al. (2013), we ascribed F_8 to granulation power, which is known to depend on the stellar $\log g$ (Kjeldsen & Bedding 2011; Mathur et al. 2011). Recent independent simulations and asteroseismic studies have examined the expected photometric manifestations of granulation (Samadi et al. 2013a,b; Mathur et al. 2011), nominally through the Fourier spectrum from which it can be difficult to extract the granulation signal. We used the simulations to predict the granulation-driven F_8 , and we find excellent agreement with our observed F_8 , demonstrating that the F_8 is indeed granulation-driven (Cranmer et al. 2014). We also determined an empirical correction to the granulation models, particularly for F stars which have the shallowest convective outer layers. Indeed, our results suggest that these models must include the effects of the magnetic suppression of convection in F stars in order to reproduce the observations. This work can ultimately help to develop our technique of granulation asteroseismology, enabling the precise determination of a larger number of stellar, and hence planetary, parameters.

3. Stellar “Flicker” Suggests Larger Radii for Bright *Kepler* Planet Host Stars

The speed and efficiency with which one can determine accurate $\log g$ solely with the discovery light curves translates directly into a rapid assessment of the distribution of bulk planet properties — in particular, with greater accuracy and fewer telescopic and computational resources than similar studies (Batalha et al.

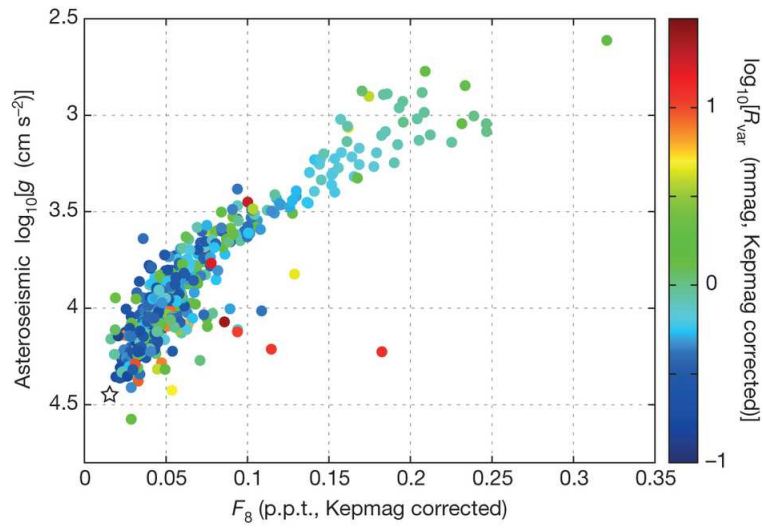


Figure 1.: Stellar surface gravity manifests in a simple measure of brightness variations. Asteroseismically determined $\log g$ shows a tight correlation with F_8 . Color represents the amplitude of the stars’ brightness variations; outliers tend to have large brightness variations. Excluding these outliers, a cubic-polynomial fit through the Kepler stars and through the Sun (large star symbol) shows a median absolute deviation of 0.06 dex and a r.m.s. deviation of 0.10 dex. To simulate how the solar $\log g$ would appear in data we use to measure $\log g$ for other stars, we divide the solar data into 90-d “quarters”. Our F_8 – $\log g$ relation measured over multiple quarters then yields a median solar $\log g$ of 4.442 with a median absolute deviation of 0.005 dex and a r.m.s. error of 0.009 dex (the true solar $\log g$ is 4.438). From Bastien et al. (2013).

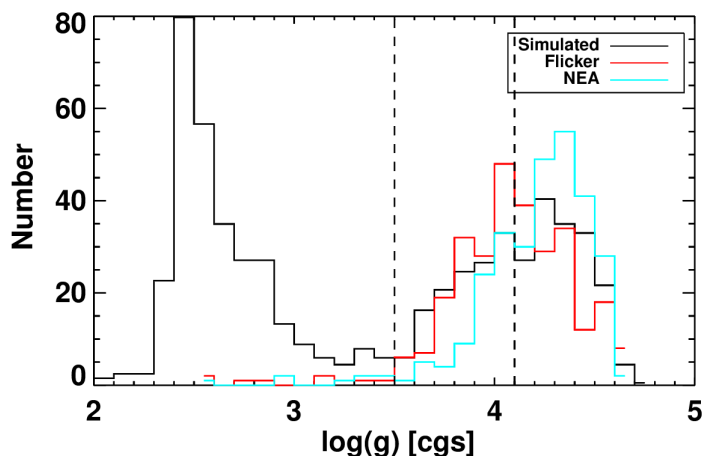


Figure 2.: Distributions of $\log g$ for the TRILEGAL simulated sample (black) and KOI host stars with F_8 -based $\log g$ (red) and broadband photometry/spectroscopy-based $\log g$ (“NEA”; cyan curve). We limit the T_{eff} range here to 4700–6500 K, for which the *Kepler* targets should be representative of the field. Vertical lines indicate the range of $\log g$ corresponding to subgiants. We find that F_8 reproduces the expected underlying distribution, and, in particular, recovers the expected population of subgiants, while the NEA parameters are preferentially pushed towards the main sequence. Adapted from Bastien et al. (2014b).

2013; Burke et al. 2014) that of necessity relied on broadband photometric measurements to determine stellar properties. We therefore applied our F_8 technique to a few hundred bright (*Kepler* magnitudes between 8 and 13) planet candidates in the *Kepler* field, and we find that these stars are significantly more evolved than previous studies suggest (Bastien et al. 2014b). As a result, the planet radii are 20–30% larger than previously estimated. In addition, we find that the high proportion of subgiants we derive (48%) is consistent with predictions from galactic models of the underlying stellar population (45%), whereas previous analyses heavily bias stellar parameters towards the main sequence and hence yield a low subgiant fraction (27%; Figs. 2,3).

We expand upon this work by tailoring our initial F_8 relation to be more directly useful to the exoplanet community by deriving a relationship between F_8 and stellar density (Kipping et al. 2014). This relation, which can yield the stellar density with an uncertainty of $\sim 30\%$, can help to constrain exoplanet eccentricities and enable the application of techniques like astrodensity profiling to hundreds of exoplanet host stars in the *Kepler* field alone.

4. RV Jitter in Magnetically Inactive Stars is Linked to High Frequency “Flicker” in Light Curves

RV planet detection, particularly of small planets, requires precise Doppler measurements, and only a few instruments are able to achieve the precision needed to observe them. Key to the success of RV planet campaigns is the avoidance of “RV

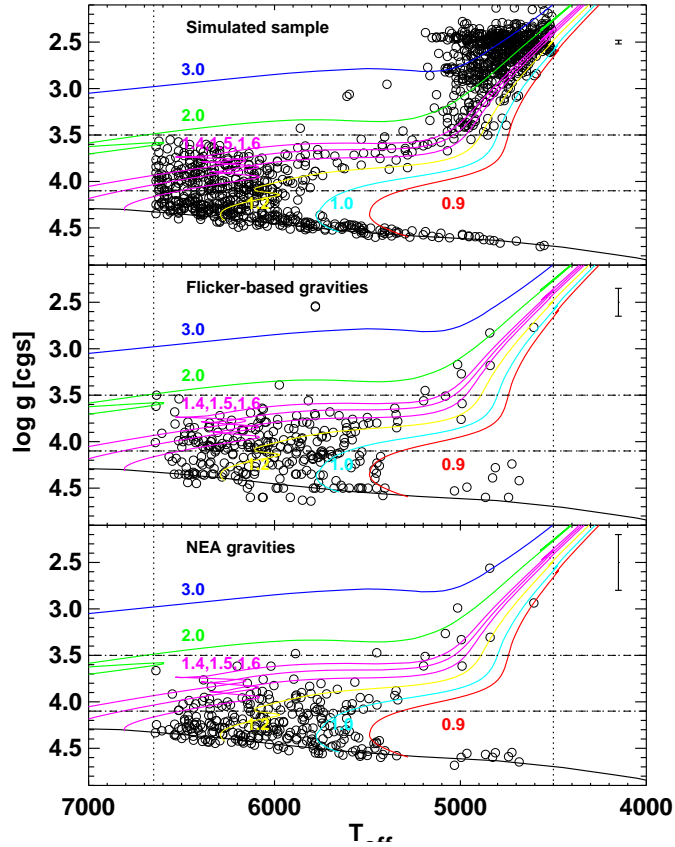


Figure 3.: H-R diagram of KOI host stars with $\log g$ derived from F_8 (middle) and broadband photometry/spectroscopy (bottom), and as predicted by a TRILEGAL (Girardi et al. 2005) simulation (top). Colored curves represent the theoretical evolutionary tracks (masses labeled in M_{\odot}). Vertical lines demarcate the range of stellar T_{eff} considered in this study. The horizontal lines demarcate the range of $\log g$ for subgiants ($3.5 < \log g < 4.1$). A representative error bar on $\log g$ for each stellar sample is in the upper right of each panel. We find that the F_8 -based $\log g$ distribution more closely matches expectation than previous $\log g$ measurements, particularly in the subgiant domain, perhaps because F_8 involves no main-sequence prior on the F_8 -based $\log g$ values. From Bastien et al. (2014b).

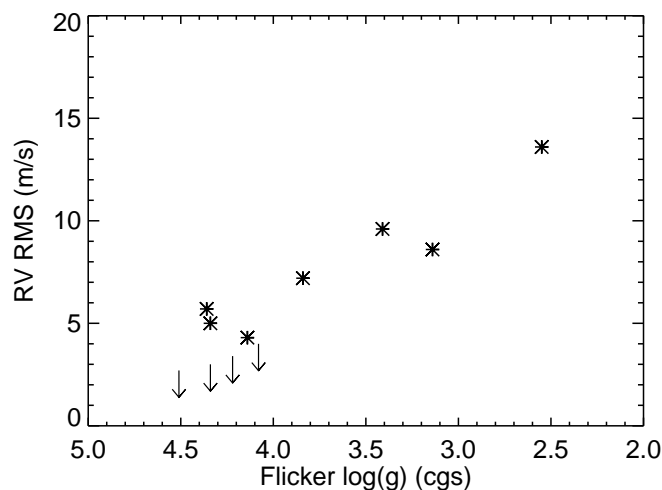


Figure 4.: Comparison between RV jitter (RV RMS) and F_8 -based $\log g$: RV jitter shows a strong anti-correlation with F_8 -based $\log g$, with a statistical confidence of 97% derived from a survival analysis. A similar trend was found by Wright (2005). F_8 measures granulation power (Bastien et al. 2013), indicating that the RV jitter of magnetically inactive stars is driven by convective motions on the stellar surface whose strength increases as stars evolve. Adapted from Bastien et al. (2014a).

loud” stars — those likely to exhibit large levels of RV jitter that can impede and sometimes even mimic planetary signals (Queloz et al. 2001). Most RV surveys therefore focus their attention on magnetically quiet stars, as magnetic spots tend to drive the largest amount of RV jitter. Nonetheless, magnetically inactive stars can exhibit unexpectedly high levels of RV jitter (Wright 2005; Galland et al. 2005), and even low jitter levels can impede the detection of small planets. The drivers of RV jitter in inactive stars remain elusive (Dumusque et al. 2011a,b; Boisse et al. 2012), continuing to plague RV planet detection and, in the case of F dwarfs, resulting in the outright avoidance of whole groups of notoriously RV noisy stars, even in transit surveys with large ground-based follow-up efforts like *Kepler* (Brown et al. 2011).

Given the breadth of stellar photometric behavior newly revealed by ultra-high precision light curves, and the new insights that they are giving into stellar surface processes, we compared different ways of characterizing this photometric behavior with RV jitter for all stars with both ultra-high precision light curves and high precision, long term RV monitoring (Bastien et al. 2014a). These stars have very low photometric amplitudes (less than 3 ppt), a previously unexplored regime of both photometric variability and RV jitter. We find that the RV jitter of these stars, ranging from 3 m s^{-1} to 135 m s^{-1} , manifests in the light curve Fourier spectrum, which we then use to develop an empirical predictor of RV jitter. We also find that spot models grossly under-predict the observed jitter by factors of 2–1000. Finally, we demonstrate that F_8 itself is a remarkably clean predictor of RV jitter in magnetically quiet stars (Fig. 4), suggesting that

the observed jitter is driven by convective motions on the stellar surface and is strongly tied to $\log g$.

5. Summary

We find that surface convection in cool stars manifests as the high frequency “flicker” observed in high precision, long time-baseline light curves, such as those from *Kepler*. We show that it yields a simple measure of stellar surface gravity and density, and we use it to place empirical constraints on granulation models. We use it to perform an ensemble analysis of exoplanet host stars, finding that the exoplanet radii are larger than previous studies suggested. Finally, we find that it is a clean predictor of RV jitter in magnetically inactive stars and can hence be used to identify promising targets for RV follow-up campaigns and RV planet searches.

More generally, we show that stellar variability — traditionally considered a major noise source and nuisance, particularly in exoplanet detection — can be used to enhance both exoplanet science and our understanding of stellar evolution.

Acknowledgements. I thank the Cool Stars 18 SOC for a great conference and for kindly inviting me to share my work. I would like to acknowledge funding support from a NASA Harriet Jenkins Pre-Doctoral Fellowship and helpful discussions with all those who have contributed to the results discussed here.

References

- Bastien, F. A., Stassun, K. G., Basri, G., & Pepper, J. 2013, *Nature*, 500, 427
- Bastien, F. A., Stassun, K. G., Pepper, J., et al. 2014, *AJ*, 147, 29
- Bastien, F. A., Stassun, K. G., & Pepper, J. 2014, *ApJ*, 788, L9
- Batalha, N. M., Rowe, J. F., Bryson, S. T., et al. 2013, *ApJS*, 204, 24
- Boisse, I., Bonfils, X., & Santos, N. C. 2012, *A&A*, 545, A109
- Brown, T. M., Latham, D. W., Everett, M. E., & Esquerdo, G. A. 2011, *AJ*, 142, 112
- Burke, C. J., Bryson, S. T., Mullally, F., et al. 2014, *ApJS*, 210, 19
- Cegla, H. M., Stassun, K. G., Watson, C. A., Bastien, F. A., & Pepper, J. 2014, *ApJ*, 780, 104
- Chaplin, W. J., Kjeldsen, H., Christensen-Dalsgaard, J., et al. 2011, *Science*, 332, 213
- Chaplin, W. J., Basu, S., Huber, D., et al. 2014, *ApJS*, 210, 1
- Cranmer, S. R., Bastien, F. A., Stassun, K. G., & Saar, S. H. 2014, *ApJ*, 781, 124
- Dressing, C. D., & Charbonneau, D. 2013, *ApJ*, 767, 95

- Dumusque, X., Udry, S., Lovis, C., Santos, N. C., & Monteiro, M. J. P. F. G. 2011, *A&A*, 525, A140
- Dumusque, X., Santos, N. C., Udry, S., Lovis, C., & Bonfils, X. 2011, *A&A*, 527, A82
- Galland, F., Lagrange, A.-M., Udry, S., et al. 2005, *A&A*, 443, 337
- Ghezzi, L., Cunha, K., Smith, V. V., et al. 2010, *ApJ*, 720, 1290
- Girardi, L., Groenewegen, M. A. T., Hatziminaoglou, E., & da Costa, L. 2005, *A&A*, 436, 895
- Kipping, D. M., Bastien, F. A., Stassun, K. G., et al. 2014, *ApJ*, 785, L32
- Kjeldsen, H., & Bedding, T. R. 2011, *A&A*, 529, L8
- Mathur, S., Hekker, S., Trampedach, R., et al. 2011, *ApJ*, 741, 119
- Petigura, E. A., Marcy, G. W., & Howard, A. W. 2013, *ApJ*, 770, 69
- Queloz, D., Henry, G. W., Sivan, J. P., et al. 2001, *A&A*, 379, 279
- Samadi, R., Belkacem, K., & Ludwig, H.-G. 2013, *A&A*, 559, A39
- Samadi, R., Belkacem, K., Ludwig, H.-G., et al. 2013, *A&A*, 559, A40
- Torres, G., Andersen, J., & Giménez, A. 2010, *A&A Rev.*, 18, 67
- Wright, J. T. 2005, *PASP*, 117, 657

Chapter 8

Solar Cycle Dependency of Sun-as-a-Star Photospheric Spectral Line Profiles

Luca Bertello¹, Alexei A. Pevtsov², Mark S. Giampapa¹, Andrew R. Marble¹

¹*National Solar Observatory, 950 North Cherry Ave., Tucson, Arizona, USA 85719*

²*National Solar Observatory, Sunspot, New Mexico, USA 88349*

Abstract. We investigate solar-cycle related changes in the profile of several photospheric spectral lines taken with the Integrated Sunlight Spectrometer (ISS) operating at the National Solar Observatory at Kitt Peak (Arizona). ISS, which is one of three instruments comprising the Synoptic Optical Long-term Investigations of the Sun (SOLIS) facility, is designed to obtain high spectral resolution ($R = 300,000$) observations of the Sun-as-a-star in a broad range of wavelengths (350 nm - 1100 nm). Daily measurements were obtained since December 2006, covering the decline of solar cycle 23 and the rising phase of cycle 24. We present time series of line parameters and discuss their correlation to indices of solar magnetic activity. Because of their different response to variations in the thermodynamic and magnetic structures of the solar atmosphere, the measured line shape parameters provide an excellent tool for disentangling thermal and magnetic effects occurring during different phases of the solar cycle. The results of this analysis may also help with developing a better understanding of magnetic cycles of activity in other solar-like stars.

1. Introduction

The diagnostic value of the Fraunhofer spectral lines to probe the conditions of the solar atmosphere was established a long time ago. Changes in the observed profile of these lines provide significant information about the velocity fields and properties of the magnetized plasma in the atmospheres of the Sun and other stars. For example, convective motions in the photospheres of the Sun/stars produce asymmetries in spectral lines because brightness differences are coupled to the flow velocities (e.g., Voigt 1956; Ridgway & Friel 1981). A standard metric for measuring the asymmetry of spectral lines is given by its bisector. The bisector is defined as the line half-way between points of equal intensity on the line profile. The details of bisector shapes vary across the H-R diagram (e.g., Gray 2005b). A curvature reminiscent of a distorted letter C is common for stars on the cool half of the H-R diagram, while bisectors for hotter stars have a reversed-C shape (Gray & Toner 1986; Gray 2005a).

Variations in the shape of magnetically sensitive lines can be used to detect changes in the thermodynamic properties of the plasma and global magnetic field (e.g. Fabbian et al. 2010; Livingston et al. 2007; Penza et al. 2004; Criscuoli et al. 2013). However, these changes are particularly difficult to detect in Sun-as-a-star and stellar observations due to the very small magnitude of these effects.

The Integrated Sunlight Spectrometer (ISS) operating at the National Solar Observatory at Kitt Peak (Arizona) is designed to obtain high spectral resolution ($R \cong 300,000$) observations of the Sun-as-a-star in a broad range of wavelengths (350 nm -1100 nm). Beginning December 1, 2006, the ISS has been taking daily observations in nine spectral bands centered at the CN head band at 388.40 nm, Ca II H at 396.85 nm, Ca II K at 393.37 nm, C I at 538.00, Mn I at 539.41 nm, H- α at 656.30 nm, Ca II at 854.19 nm, He I at 1083.02 nm, and NaD1 at 589.59 nm. Beginning January 7, 2008, C I 538.00 nm spectra superimposed with reference lines from an iodine vapor cell have been additionally included. Table 1 lists currently observed spectral lines.

Additional information about ISS, including transmission characteristics of the fiber optics, the instrument's block diagram, and its mechanical and optical layout are available from the SOLIS web site at <http://solis.nso.edu/ISSOverview.html>. Daily observations can be accessed from <http://solis.nso.edu/0/iss>.

Criscuoli et al. (2013) have investigated the effect of magnetic features on the shape of two Fe I magnetically sensitive lines (630.2 nm and 617.3 nm) using high-resolution spectro-polarimetric data acquired with the Interferometric Bidimensional Spectrometer (IBIS; Cavallini 2006) at the Dunn Solar Telescope (NSO at Sacramento Peak). Their results show that the central intensity of these lines is sensitive to both temperature and magnetic flux density variations, the full width at half maximum (FWHM) is mostly affected by magnetic field changes, and the equivalent width (EQW) is mostly sensitive to temperature. This implies that it is possible to disentangle magnetic from purely thermodynamic effects by comparing time series of these parameters. The objective of our investigation is to extend this idea to disk-integrated solar measurements and possibly determine a correlation between temporal variations in the solar global magnetic field and corresponding variations in line shape parameters. The outcome of this study may offer important clues about possible new approaches to determining the

Table 1.: Spectral bands measured by the ISS instrument

Spectral band	λ_0 , nm	$\Delta\lambda$, nm	$d\lambda/dx$, pm/pixel	Start date
CN	388.40	0.58	0.564	December 4, 2006
Ca II K	393.37	0.55	0.541	December 1, 2006
Ca II H	396.85	0.53	0.522	December 4, 2006
C I	538.00	0.84	0.824	December 4, 2006
C I (with iodine lines)	538.00	0.84	0.824	January 7, 2008
Mn I	539.41	0.83	0.816	December 4, 2006
NaD1	589.59	0.98	0.956	March 23, 2011
H-alpha	656.30	1.14	1.12	August 31, 2007
Ca II	854.19	1.61	1.58	December 13, 2006
He I	1083.02	1.65	1.61	December 4, 2006

Notes to Table 1.: Each spectral band is centered at λ_0 , with a bandwidth given by $\Delta\lambda$. The average linear dispersion over time, $d\lambda/dx$, is also given. The start date (fifth column) indicates the first day ISS began to observe in that particular spectral band.

magnetic field properties in other stars. We present here some very preliminary results from this investigation.

2. Data Analysis

For this study, we investigated the temporal behavior of a set of photospheric lines extracted from the ISS bands centered at C I 538.00 nm and Mn I 539.41 nm spectral lines. Figure 1 shows typical ISS observations taken in these two bands, where the lines investigated here are marked by a number. The set includes spectral lines of different strength and magnetic sensitivity, as listed in Table 2.

The wavelength- and flux-calibration of both the ISS C I and Mn I data were performed following the approach described in Pevtsov et al. (2014), using

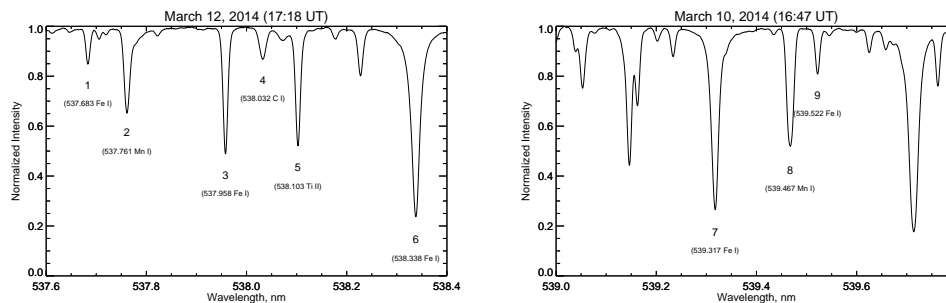


Figure 1.: ISS C I (left) and Mn I (right) bands. The spectral sampling is about $8.2 \text{ m}\text{\AA}$. The numbers refer to the spectral lines used in this study and their properties are listed in Table 2.

Table 2.: List of spectral lines

no.	λ_0 (nm)	Elem.	Transition	Low EP (eV)	High EP (eV)	g_{eff}	I_{core}	EQW (mÅ)
1	537.6833	Fe I	$b^1D_{22} - v^3P_1^{\circ}$	4.29	6.60	0.750	0.85	13
2	537.7612	Mn I	$z^4P_{5/2}^{\circ} - e^4S_{3/2}$	3.83	6.12	1.300	0.65	45
3	537.9579	Fe I	$b^1G_{24} - z^1H_5^{\circ}$	3.69	6.00	1.000	0.49	56
4	538.0323	C I	$^1P_1^{\circ} - ^1P_1$	7.68	9.99	1.000	0.87	26
5	538.1026	Ti II	$b^2D_{3/2} - z^2F_{5/2}^{\circ}$	1.57	3.87	0.900	0.52	56
6	538.3379	Fe I	$z^5G_5^{\circ} - e^5H_6$	4.31	6.61	1.083	0.23	204
7	539.3174	Fe I	$z^5D_3^{\circ} - e^5D_4$	3.24	5.54	1.500	0.26	153
8	539.4672	Mn I	$a^6S_{5/2} - z^8P_{7/2}^{\circ}$	0.00	2.30	1.857	0.51	74
9	539.5218	Fe I	$z^5G_2^{\circ} - g^5F_1$	4.45	6.74	0.500	0.81	20

Notes to Table 2.: λ_0 is the reference wavelength, the central intensity I_{core} is the median value determined from all the ISS measurements, and EQW is the equivalent width. The effective Landé factor g_{eff} was computed using the formula given in Landi Degl'Innocenti (1982), while the other quantities are from the National Institute of Standards and Technology (NIST) website (<http://www.nist.gov/pml/data/asd.cfm>).

the NSO Fourier Transform Spectrometer (FTS; Wallace, Hinkle & Livingston 2007) spectral atlas as a reference. In brief, a second order (i.e., linear dispersion) wavelength solution was obtained by cross-correlating the regions of the ISS and FTS spectra with absorption features. Simultaneously, a third order flux-calibration curve was fit via least-squares minimization of the spectra within continuum windows between those features.

For each line listed in the table we extracted from the observed profile a set of parameters and studied their behavior with respect to the solar cycle of activity. The parameters are: FWHM, EQW, core intensity (I_{core}), and line asymmetry. The bisector of a spectral line is routinely used to characterize its asymmetry. For this study, we used the wavelength position of the bisector at three different relative intensity levels (25%, 50%, and 75% from the core intensity). The core intensity is determined from a 9-point quadratic fit of the bottom of the profile, while the FWHM and bisector were computed via cubic spline interpolation at the proper intensity levels. The EQW is determined by numerically integrating

$$\text{EQW} = \int (1 - I_{\lambda}) d\lambda$$

over a selected wavelength range of interest centered on the line core, and with the assumption that the continuum intensity is equal to one. Since we are interested in relative variations of EQW, the actual extension of this range is not critical. Finally, it is important to point out that, because of the adopted calibration, the central wavelength positions of these lines is constrained to be the same as those of the FTS spectrum used as a reference. That is, these central wavelength positions will not change with time.

3. Results

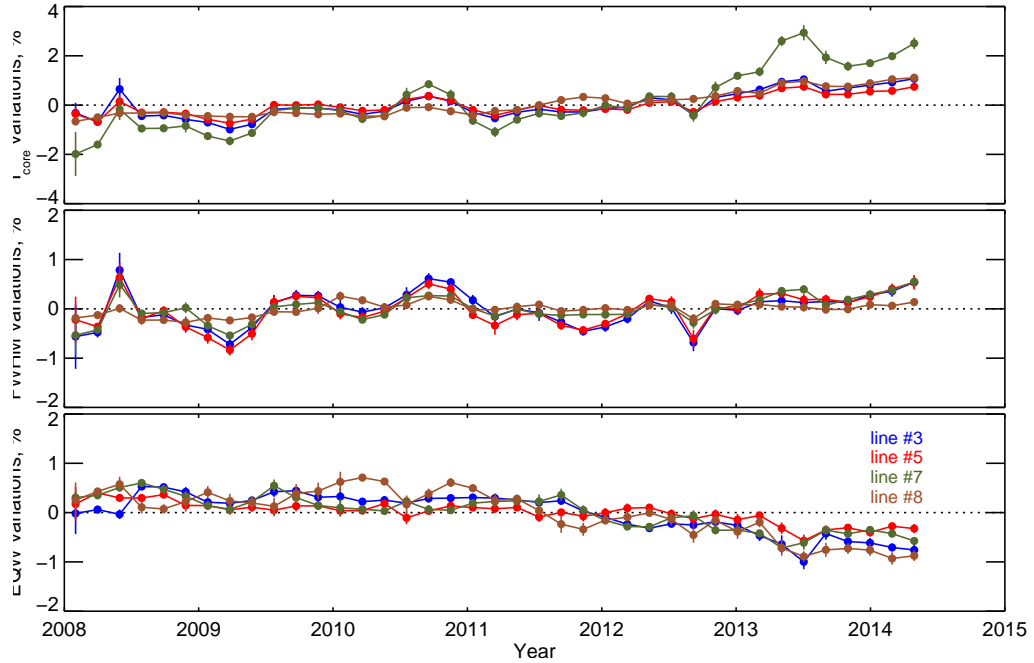


Figure 2.: Variations in core residual intensity (I_{core}), FWHM, and equivalent width (EQW) for four of the nine spectral lines investigated in this study. Data were averaged in 60-day intervals, and the variations are computed with respect to the median value of the original time series. The error bars are $3\text{-}\sigma$ of the mean.

Figure 2 shows the variations with the cycle of solar activity of three of the four line parameters investigated. For clarity, we plot here only the results for some of the strongest lines in the set. These lines exhibit a systematic increase in I_{core} of about 4-5% (e.g., line #7) and a systematic decrease in EQW of about 1% during the rising phase of cycle 24. On the other hand, the FWHM does not present any significant long-term trends with the cycle of activity. Shallow lines (e.g., #1, #4, and #9), not shown here, exhibit very little or insignificant variations in these parameters. One interesting feature shown in Figure 2 is the presence of an annual modulation in the I_{core} and FWHM time series, quite visible during the period $\sim 2008 - 2011$.

This modulation seems to be in phase with the annual variation of the B_0 angle - the heliographic latitude of the centre of the solar disk - as shown in Figure 3, suggesting that it may be caused by the Earth's orbital motion around the Sun. This effect is more prominent during periods of minimal solar activity when the poloidal field is the major magnetic contributor affecting the line shape and at times of extreme B_0 angle values (when one of the Sun's poles is observed). Once the overall level of magnetic activity rises and the toroidal field becomes predominant, the activity moves to lower latitudinal bands and the sensitivity to variations in the B_0 angle is strongly reduced. The fact that the annual variations disappear after 2011 indicates that these variations are of solar origin, and not

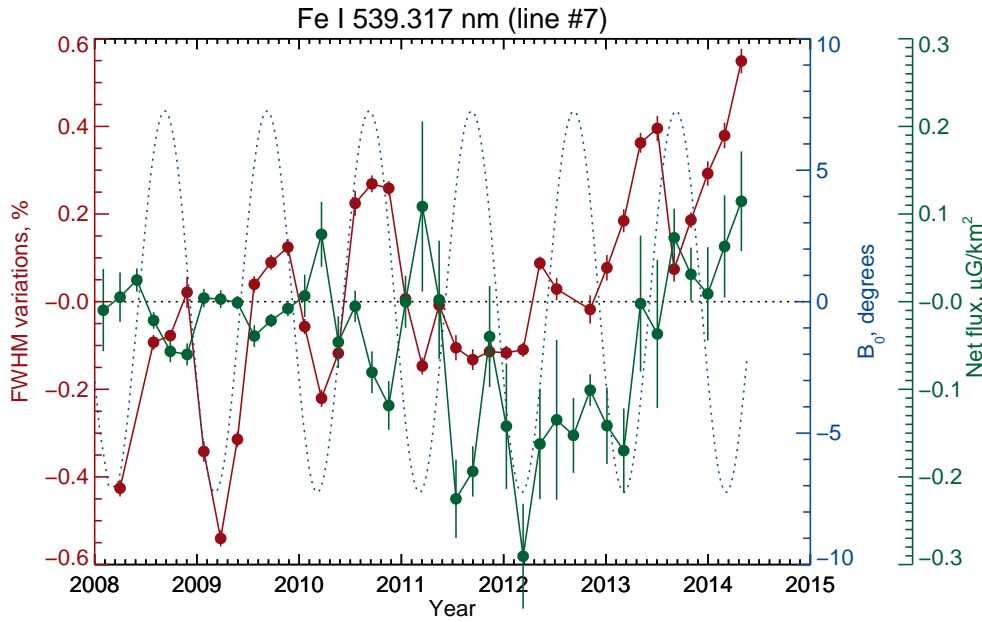


Figure 3.: Comparison between variations in the FWHM of one of the strongest lines used in this investigation (red points) and the net magnetic flux computed at 630.15 nm from SOLIS Vector Spectromagnetograph observations (green points). Data were averaged in 60-day intervals, and the error bars for both sets of points are the standard deviation of the mean. Also shown in blue, as a reference, are the variations of the heliographic latitude of the central point of the solar disk (B_0).

caused by the Earth's orbital motion. The rise in solar activity can explain the quasi-systematic increase in FWHM after 2011. To further validate this idea, we also plot in Figure 3 the average values of the net magnetic flux computed from daily SOLIS VSM full-disk magnetograms taken in the Fe I 630.15 nm spectral line for the same period of time covered by the ISS observations. Although not quite as evident as for the case of the FWHM, the net magnetic flux exhibits a similar modulation around zero during the years 2008 to 2011. After 2011, the net flux is mostly negative until it reverses its sign around the middle of 2013. The good overall agreement between the behavior of the FWHM and the net magnetic flux is another indication that some of the line shape parameters investigated here, as measured by the ISS instrument, are very sensitive to variations in the solar global magnetic field.

Figure 4 shows the results from the analysis of the line bisector. All the lines investigated here preserve their asymmetry during the cycle of activity up to about a 50% level of their residual intensity. A slight change of asymmetry (fraction of mÅ) is detected at higher intensity levels. Some of these changes may be due to the contamination of nearby telluric lines that typically have seasonal variations. However, there is a clear systematic change in asymmetry close to the continuum occurring around the middle of 2011. The change in sign

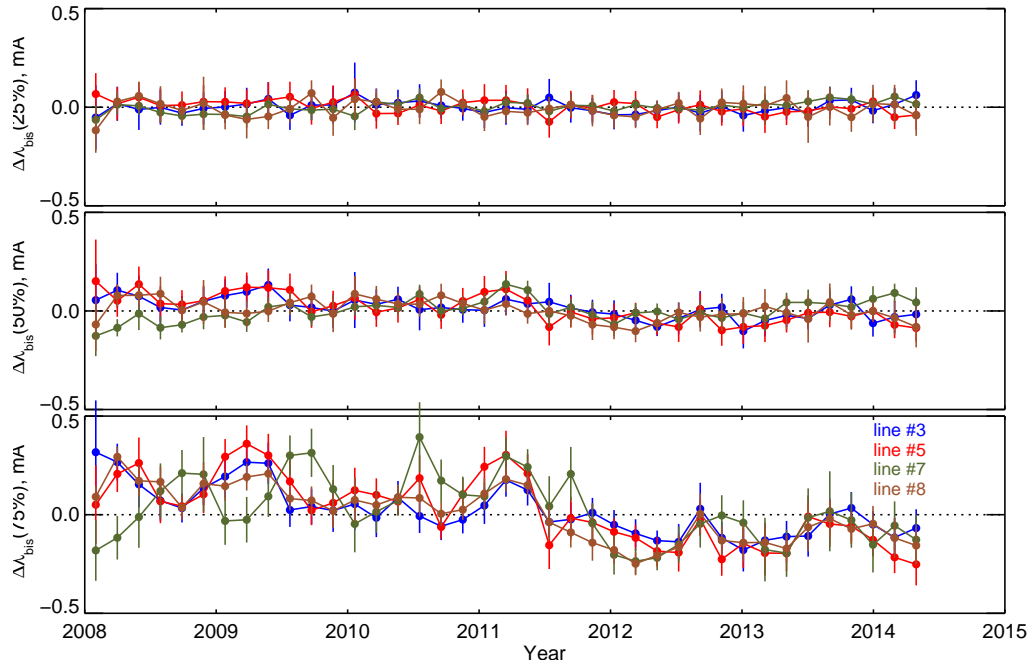


Figure 4.: Variations in the line bisector for the same four lines discussed in Figure 2. The wavelength position of the line bisector is computed at three different relative intensity levels: $I_i = f_i(1 - I_{\text{core}}) + I_{\text{core}}$, with $f_i = \{0.25, 0.50, 0.75\}$. Corresponding variations are computed from the formula $\Delta\lambda_{\text{bis}}(I_i, t) = \lambda_{\text{bis}}(I_i, t) - \text{median}(\lambda_{\text{bis}}(I_i, t))$. Data are averaged in 60-day intervals.

of $\Delta\lambda_{\text{bis}}(75\%)$, from positive to negative, indicates that the line profiles tend to become more symmetric with the overall increase in solar activity.

Of the pool of spectral lines examined in this study, the Mn I 539.467 nm line is one that has received considerable attention in the past (e.g. Livingston & Wallace 1987; Malanushenko et al. 2004; Livingston et al. 2007). This spectral line presents an unusual sensitivity to solar activity, due, most likely, to its excessive hyperfine structure (Vitas et al. 2009). For example, Livingston & Wallace (1987) have noted that the EQW of this line correlates quite well with the chromospheric Ca II K core intensity during the period 1976 to 1985. Figure 5 show a very similar trend with the solar cycle between the intensity variations in the core of Mn I 539.467 nm and the Ca II K 1-Å emission index. While Fig. 5 would appear to suggest that the variations in Mn I are a direct result of chromospheric heating, Vitas et al. (2009) pointed out that variability in the Mn I 539.467 nm line is in fact dominated by magnetic concentrations that constitute on-disk network and plage combined with the its Zeeman sensitivity but is not affected by chromospheric heating. Therefore, the correlation in Fig. 5 is the result of the separate correlations of the Ca II K core and the Mn I core, respectively, with magnetic field strength and area coverage.

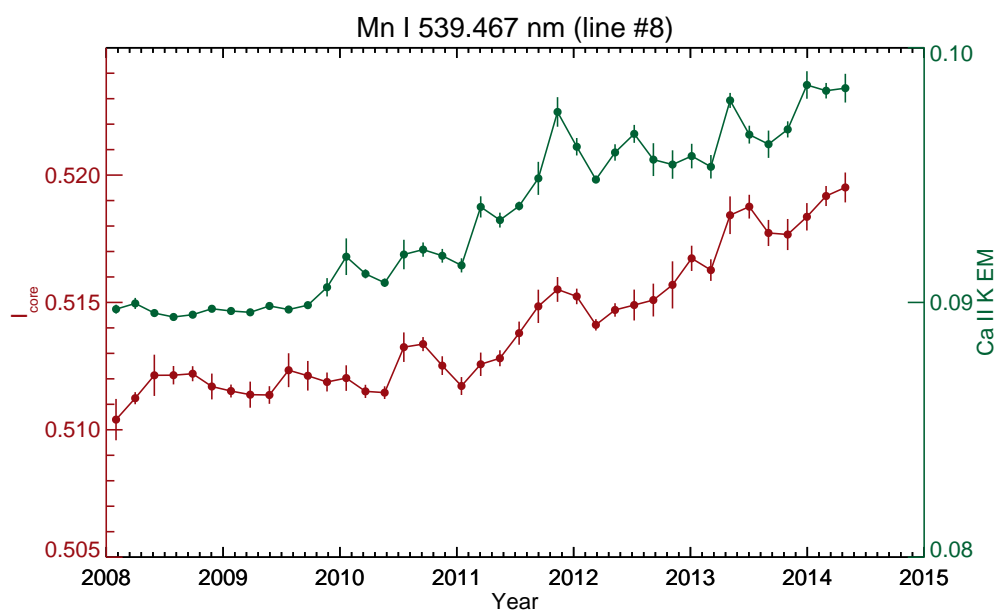


Figure 5.: Intensity variations in the core of Mn I 539.467 nm and their correlation with the chromospheric ISS Ca II K 1-Å emission index (EM). Error bars in both sets are 3 standard deviations of the mean value. The good correlation between these two parameters indicates that the core of this line is a good proxy for monitoring chromospheric activity in the Sun and, maybe, in solar-like stars.

4. Conclusions

Shallow lines show very little or insignificant variations in the line core relative intensity with respect to the cycle of solar activity, while stronger lines exhibit a systematic increase of about 4-5% (e.g. line #7). The EQW shows a systematic decrease of about 1% for the strongest lines during the rising phase of cycle 24. This dependency of the line profile parameters on the magnetic field is consistent with the results published in Criscuoli et al. (2013). The analysis of the line bisectors indicates that all the lines maintain their asymmetry during the cycle of activity, at least up to the 50% level of their residual intensity. A slight change of asymmetry (fraction of mÅ) is detected at relative intensity levels closer to the continuum.

During the period $\sim 2008-2011$, the variations in FWHM are quite well correlated with the variations in B_0 and anticorrelated with the net magnetic flux. This is mainly because of the contribution of the polar fields. After ~ 2012 , the FWHM increases with the rising level of solar activity. One line from our set, Mn I 539.467 nm, exhibits properties in its core intensity that are very similar to the behavior of the 1-Å emission index of the well studied Ca II K chromospheric line. Finally, from a visual inspection of the top panel of Figure 2, we note that the strong spectral line Fe I 539.3174 nm (line #7) shows the largest variations in its core intensity among all the lines investigated by this study.

Acknowledgements. The authors thank the organizers of the 18th "Cool Stars" Workshop for their hospitality. This work utilizes SOLIS data obtained by the NSO Integrated Synoptic Program (NISP), managed by the National Solar Observatory, which is operated by the Association of Universities for Research in Astronomy (AURA), Inc. under a cooperative agreement with the National Science Foundation.

References

- Cavallini, F. 2006, *Solar Phys.*, 236, 415
- Criscuoli, S., Ermolli, I., Uitenbroek, H., & Giorgi, F. 2013, *ApJ*, 763, 144
- Fabbian, D., Khomenko, E., Moreno-Insertis, F., & Nordlund, Å. 2010, *ApJ*, 724, 1536
- Gray, D. F. 2005a, *PASP*, 117, 711
- Gray, D. F. 2005b, "The Observation and Analysis of Stellar Photospheres, 3rd Edition, by D.F. Gray. ISBN 0521851866
- Gray, D. F., & Toner, C. G. 1986, *ApJ*, 310, 277
- Landi Degl'Innocenti, E. 1982, *Solar Phys.*, 77, 285
- Livingston, W., & Wallace, L. 1987, *ApJ*, 314, 808
- Livingston, W., Wallace, L., White, O. R., & Giampapa, M. S. 2007, *ApJ*, 657, 1137
- Malanushenko, O., Jones, H. P., & Livingston, W. 2004, in *Multi-Wavelength Investigations of Solar Activity*, ed. A. V. Stepanov, E. E. Benevolenskaya & A. G. Kosovichev, *IAU Symp.*, 223, 645
- Penza, V., Caccin, B., & Del Moro, D. 2004, *A&A*, 427, 345
- Pevtsov, A. A., Bertello, L., & Marble, A. R. 2014, *Astronomische Nachrichten*, 335, 21
- Ridgway, S. T., & Friel, E. D. 1981, *IAU Colloq. 59: Effects of Mass Loss on Stellar Evolution*, 89, 119
- Vitas, N., Viticchiè, B., Rutten, R. J., Voumlgler, A. 2009, *A&A*, 499, 301
- Voigt, H.-H. 1956, *Zeitschrift für Astroph.*, 40, 157
- Wallace, L., Hinkle, K., & Livingston, W. 2007, *Advances in Solid State Physics*

Chapter 9

Short-term Activity in Young Solar Analogs

Christopher J. Corbally¹, Richard O. Gray², Jon M. Saken³, Ryan A. Lambert²

¹*Vatican Observatory Research Group, University of Arizona, Tucson, AZ 85721-0065, USA*

²*Department of Physics and Astronomy, Appalachian State University, Boone, NC 26808, USA*

³*Department of Physics and Physical Science, Marshall University, Huntington, WV 25755, USA*

Abstract. Knowing the chromospheric and magnetic activity in Young Solar Analogs (YSAs) gives us an insight into the conditions in the early solar system when life was establishing a foothold on the earth. To complement an 8-year history of monitoring 31 YSAs on long and medium timescales, a program of high-cadence, high signal-to-noise spectroscopy started in 2013. Initial, spectacular results for flares are presented, together with flickering.

1. Introduction

The Young Solar Analogs (YSAs) Project is designed to answer a number of fundamental questions about the early Sun. Did the early Sun exhibit a sunspot cycle? How did the early Sun vary on time scales from minutes to years? How did the solar flux across the visible spectrum vary with solar activity? To answer these questions we are monitoring 31 young (0.3-1.5 Gyr) solar-type stars (F8-K2) both photometrically and spectroscopically.

The monitoring has been going on for eight years with telescopes at the Dark Sky Observatory, NC. Its long- and medium-duration phenomena are presented, with methods, in the Gray et al. (2014) and Saken et al. (2014) papers in these same Cool Stars 18 proceedings.

High-cadence spectroscopic observations, on timescales of minutes to hours, complement the above monitoring. These observations started in early 2013 at VATT, a 1.8-m telescope situated on Mt. Graham, AZ, where they are being carried out with VATTSpec. The camera is a 2688x512 pixel, back illuminated STA0520A CCD. An Hg-Ar comparison lamp is used for wavelength calibrations. With a 1200 g/mm grating, VATTSpec delivers for these YSA stars spectra of high signal-to-noise at a rate of one every 1 or 2 minutes, having a resolution of 1Å in the region containing Ca II K & H and the G-band. These features detect, respectively, chromospheric activity and large-scale magnetic structure changes in the photosphere on timescales of minutes to hours. We shall be addressing the question of the energy output and frequency of flares on a subset (10) of our program stars. Here initial, spectacular results for flares are shown, together with flickering.

2. Flares

A powerful white-light flare in HD 76218 near the end of the 2011/12 season is shown in three photometric bands observed at the Dark Sky Observatory (Figure 1). The mid-flare was detected in the piggy-back data, but it appears that the robotic telescope picked up the end of the flare. Typical precisions in the Johnson bands are 0.005-0.007 mag.

Spectroscopic observations with the VATT of HD 82885 for one hour a night for four separate nights captured a flare on the second night (Figure 2). S_2 is VATTs instrumental version of chromospheric activity, based on Ca II K & H. It will be calibrated with the Mount Wilson S_{MW} index after sufficient observations have been made on different nights of Mount Wilson stars (Baliunas et al. 1995).

In a similar way, a flare for HD 101501, with an abrupt onset but this time with a slower and nearly linear decay, was captured on the third night of observations with the VATT (Figure 3).

3. Flickering

Figure 4 shows the instrumental S_2 variations for three active YSA stars over as long a period as possible during a single night, i.e., up to 7 hours. One inactive star, HD 207978, was observed on the same night as the observations for HD 130322. It is included in the lower-left plot for a control. This plot represents monitoring over about half an hour and, while its MJD scale is appropriately short, it has the same S_2 range as the others. The scatter in S_2 is ± 0.0004 , indicating the very small instrumental error achieved.

HD 16673, upper left, showed little variation, save a slight decline in activity level. However, the right-hand pair of stars enjoyed considerable flickering, with scatters in S_2 of ± 0.0016 for HD 76218 and ± 0.0015 for HD 130322. The flickering amplitude for HD 76218 even increased. Long-term data from our monitoring suggests this star, which in Figure 1 had almost a superflare, is returning to an uniform distribution of spots with longitude on its surface.

Micro-variability, or flickering, in stars is not well-understood, though it is ascribed to variations in surface granulation. It is receiving considerable interest since it occurs on timescales similar to exoplanet transits and can mask the signal

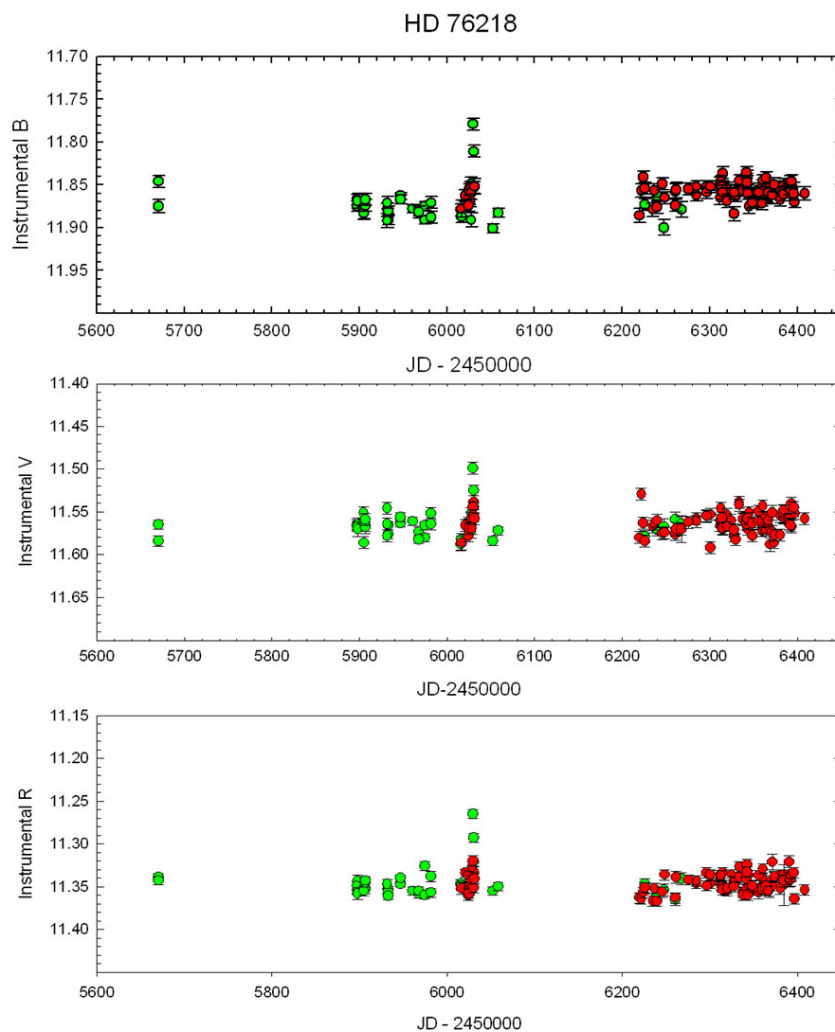


Figure 1.: Photometric observations in three bands of a powerful white-light flare in HD 76218. Data from the piggy-back photometer are the green symbols, the robotic data the red.

from these (e.g., Aigrain et al. 2004). We are continuing this high-cadence, many hours monitoring on VATT for a subset of 10 YSAs.

Acknowledgements. We gratefully acknowledge support from NSF Grant AST-1109158, and support from the Vatican Observatory Foundation.

References

- Aigrain, S., Favata, F., & Gilmore, G. 2004, *A&A*, 414, 1139
- Baliunas, S. L., Donahue, R. A., Soon, W. H., et al. 1995, *ApJ*, 438, 269

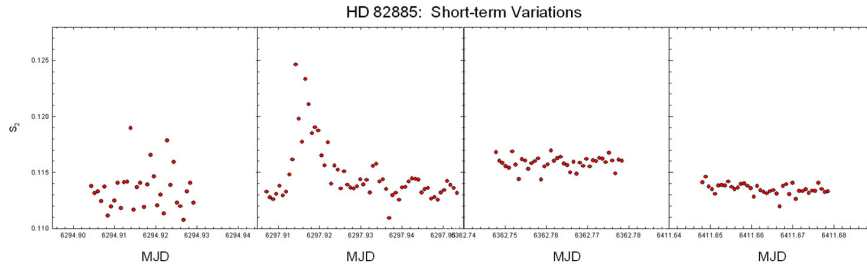


Figure 2.: VATT's short-term spectroscopic Ca II K & H observations of HD 82885 capture, on the second night, a flare with an abrupt onset and decay.

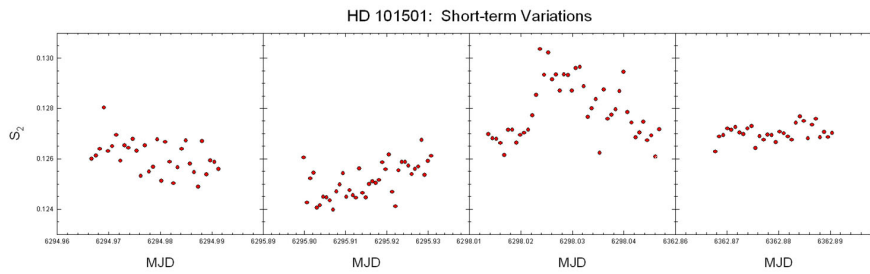


Figure 3.: Similar to Figure 2 but for a flare on the third night for HD 101501.

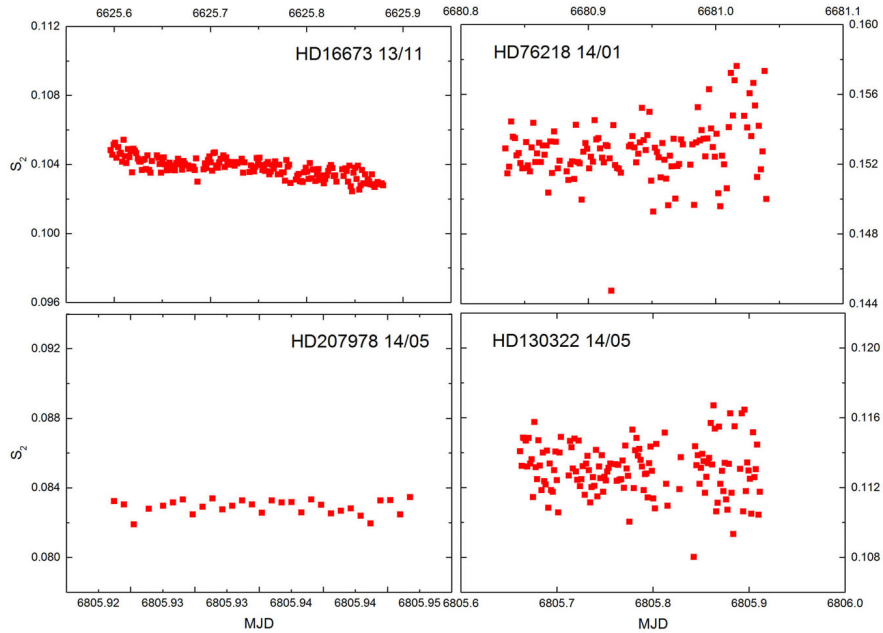


Figure 4.: VATTs short-term spectroscopic observations of three active and one inactive star, HD 207978

Gray, R.O., Saken, J.M., Corbally, C.J., Briley, M.M., Fuller, V.A., Lambert, R.A., Newsome, I.M., & Childers, M.J. 2014, *The Young Solar Analogs Project*, in 18th Cambridge Workshop on Cool Stars, Stellar Systems, and the Sun, Proceedings of Lowell Observatory, eds G. van Belle & H. Harris

Saken, J.M., Gray, R.O., Corbally, C.J., & Briley, M.M. 2014, *The Young Solar Analogs Project: Observations & Analysis*, in 18th Cambridge Workshop on Cool Stars, Stellar Systems, and the Sun, Proceedings of Lowell Observatory, eds. G. van Belle & H. Harris

Chapter 10

Preparation of the CARMENES Input Catalogue: Multiplicity of M dwarfs from tenths of arcseconds to hundreds of arcminutes

M. Cortés Contreras¹, J. A. Caballero³, V. J. S. Béjar², B. Gauza²,
D. Montes¹, F. J. Alonso-Floriano¹, I. Ribas⁴, A. Reiners⁵,
A. Quirrenbach⁶, P. J. Amado⁷

¹*Departamento de Astrofísica, Facultad de Física, Universidad
Complutense de Madrid, E-28040 Madrid, Spain*

²*Centro de Astrobiología (CSIC-INTA), Campus ESAC, PO Box 78,
E-28691 Villanueva de la Cañada, Madrid, Spain*

³*Instituto de Astrofísica de Canarias, Vía Lactea s/n, E-38205 La Laguna,
Tenerife, Spain, and Dept. Astrofísica, Universidad de La Laguna (ULL),
E-38206 La Laguna, Tenerife, Spain*

⁴*Institut de Ciències de l'Espai (CSIC-IEEC), Campus UAB, Facultat
Ciències, Torre C5 - parell - 2a planta, E-08193 Bellaterra, Barcelona,
Spain*

⁵*Institut für Astrophysik (IAG), Friedrich-Hund-Platz 1, D-37077
Göttingen, Germany*

⁶*Landessternwarte (LSW), Zentrum für Astronomie der Universität
Heidelberg, Königstuhl 12, D-69117 Heidelberg, Germany*

⁷*Instituto de Astrofísica de Andalucía (CSIC), Glorieta de la Astronomía
s/n, E-18008 Granada, Spain*

Abstract. With the help of CARMENCITA, the CARMENES Cool dwarf
Information and daTa Archive, we investigate the multiplicity of M dwarfs in

the solar neighbourhood observable from Calar Alto to prepare and characterize the final sample of CARMENES stars. Our multiplicity study covers a wide range in projected physical separations, from 0.5 to 55 000 au. The inner range is covered with a lucky-imaging survey of 385 M dwarfs with FastCam at the 1.5 m Telescopio Carlos Sánchez, complemented with a literature search. We explore visual or physical companions from 0.15 to 18 arcsec around our targets. These observations are important to discard very close companions that may induce spurious variations in the radial velocity of the primary and mimic the presence of planets. The outer range is covered with a detailed analysis of Washington Double Stars catalogue data and optical images taken by us with TCP and CAMELOT at the 0.8 m IAC80 telescope, and an astrometric study of all-sky public images and catalogues. We review the main results of our searches and derive the multiplicity of M dwarfs at close and wide physical separations.

1. Introduction

The CARMENES instrument is a next-generation radial-velocity instrument optimized for planet searches of mid- to late-type M dwarfs for the 3.5 m telescope at the Calar Alto Observatory, which is being built by a consortium of several Spanish and German institutions (Quirrenbach et al. 2012).

CARMENCITA is a comprehensive database of almost 2 200 M stars that contains information on all relevant properties of the potential targets, such as spectral type, photometry, multiplicity, $v \sin i$ activity, X-ray, etc., useful to select the least-active, brightest, latest M dwarfs with no companions at less than 5 arcsec (a separation at which the flux of any visual or physical companion could affect the radial-velocity measurement of the main target) observable from Calar Alto. To this purpose, we take high-resolution imaging and spectroscopy in order to identify and discard very close binaries, fast rotators and very active stars. In particular, in this proceeding, we look for unknown resolved binaries with new high- and low-resolution imaging and virtual observatory data.

2. Lucky imaging of close pairs with FastCam at 1.5 m TCS

FastCam is a lucky imaging instrument with a pixel scale of 42.3 mas/pix at the 1.5 m Telescopio Carlos Sánchez (TCS) at the Observatorio del Teide (Oscoz et al. 2008) used to obtain *I*-band imaging of 385 mid- to late-M dwarfs on 19 nights since Oct 2011 to May 2014. For each target, we took 10 000 frames of 50 ms. We aligned and combined all of them, as well as the best 1, 10 and 50 % raw frames, using the brightest pixel (Fig. 1).

About 69 % of the targets were single, 21 % had confirmed or probable physical companions in the range 0.15–17.70 arcsec and the remaining 10 % had possible background sources or artifacts that needed extra analysis. We provide new astrometric epochs for over 70 pairs (of which two are discordant with published values) and discover eight new pairs. Twenty physical companion candidates (including three new) have estimated periods shorter than 10 years.

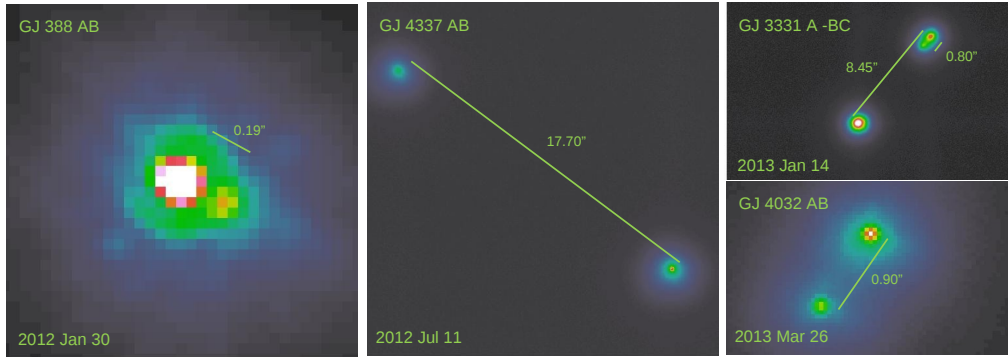


Figure 1.: FastCam I-band images. Left panel: close pair in the quadruple AD Leo system (GJ 388). Middle and top right panels: previously known triple M-dwarf systems G 190-028 (GJ 4337) and BD-21 1074 (GJ 3331). Bottom right panel: possible physical companion of G 183-010 (GJ 4032).

3. Imaging of wide pairs with TCP (and CAMELOT) at 0.8 m IAC80

With the Tromsø CCD Photometer (TCP, 0.537 arcsec/pix) and the Cámara Mejorada Ligera del Observatorio del Teide (CAMELOT, 0.304 arcsec/pix) we observed in *R*-band 54 pair candidates with at least one M dwarf during a semester in 2012 (Fig. 2). After a comprehensive astrometric analysis, we confirm the physical binding of 52 pairs for which we provide projected physical separations, individual masses, reduced orbital periods and binding energies (Cortés-Contreras et al., in prep.).

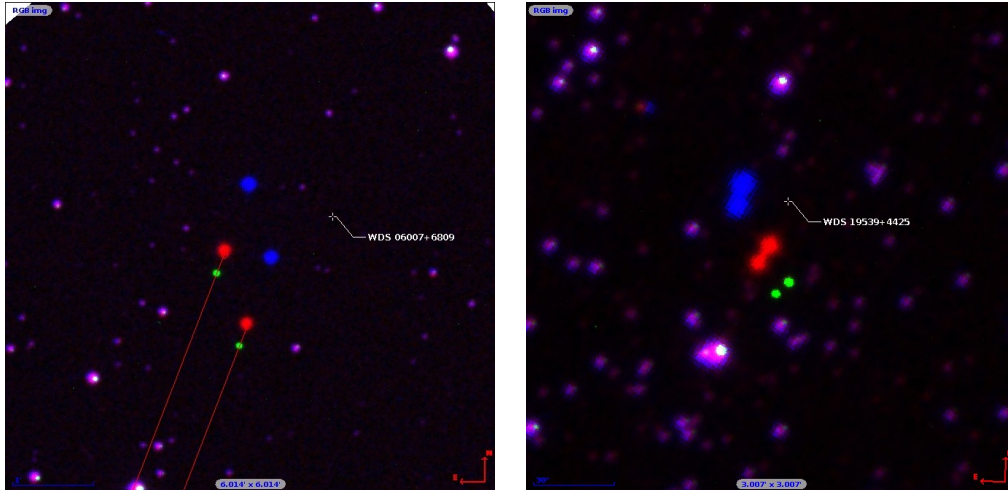


Figure 2.: False-color composite images of two high proper-motion pairs, LP 057–041 AB and V1581 Cyg AB (blue: POSS-I 1950, red: POSS-II 1990, green: IAC80 2012). The right pair shows a clear relative movement, which is useful to track orbital variations.

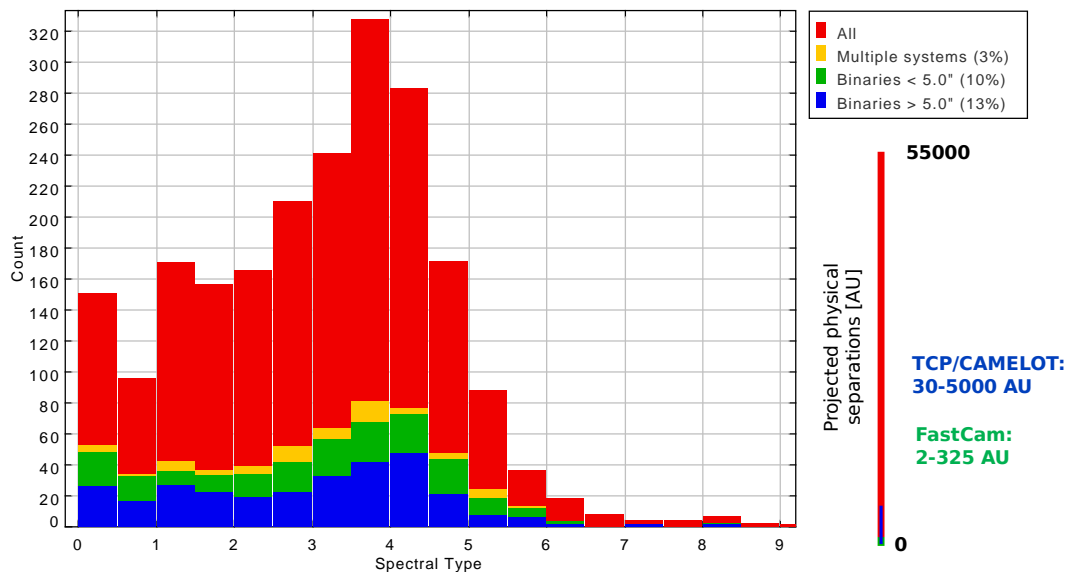


Figure 3.: Spectral type distribution of close and wide binaries and multiple systems. The colored vertical bar to the right indicates the projected physical separations coverage of the instruments used in this study and of the sample.

4. The CARMENCITA sample

4.1 Multiplicity

Projected physical separations covered with FastCam, TCP and CAMELOT are in the range 2–5 000 au (Fig. 3). Accounting also for previously known pairs (Giclas et al. 1978; Luyten 1997; Beuzit et al. 2004), the total multiplicity fraction of the more than 2100 M dwarfs of CARMENCITA is 26 %, in agreement with given values in similar works (Janson et al. 2012, 2014; Jódar et al. 2012).

4.2 Parameters

For all multiples in CARMENCITA separated by over 5 arcsec, we measured angular separations. Closer angular separations were taken from the Washington Double Star catalogue or other sources. For those stars without parallax determination, we estimated spectro-photometric distances (d) from our own M_J -spectral type relation derived from 2MASS photometry, parallactic measurements from *Hipparcos* and spectral types determined mostly by Alonso-Floriano et al. in prep.

We computed projected physical separations (s) in the range from 0.5 to 55 000 au. Only 55 systems have $s < 10$ au and just seven have $s > 10 000$ au. Masses (M_1 , M_2) of the components were estimated with the NextGen models from Baraffe et al. 1998, assuming a typical age interval of $\tau \sim 1$ –5 Gyr. Gravitational potential energies (U_g^*) and periods (P) were estimated from the total mass $M_1 + M_2$ (Fig. 4). While there are no ultra-fragile systems in our sample (Caballero 2009; Dhital et al. 2012), there are however some interesting close pairs for which one could easily derive dynamical masses.

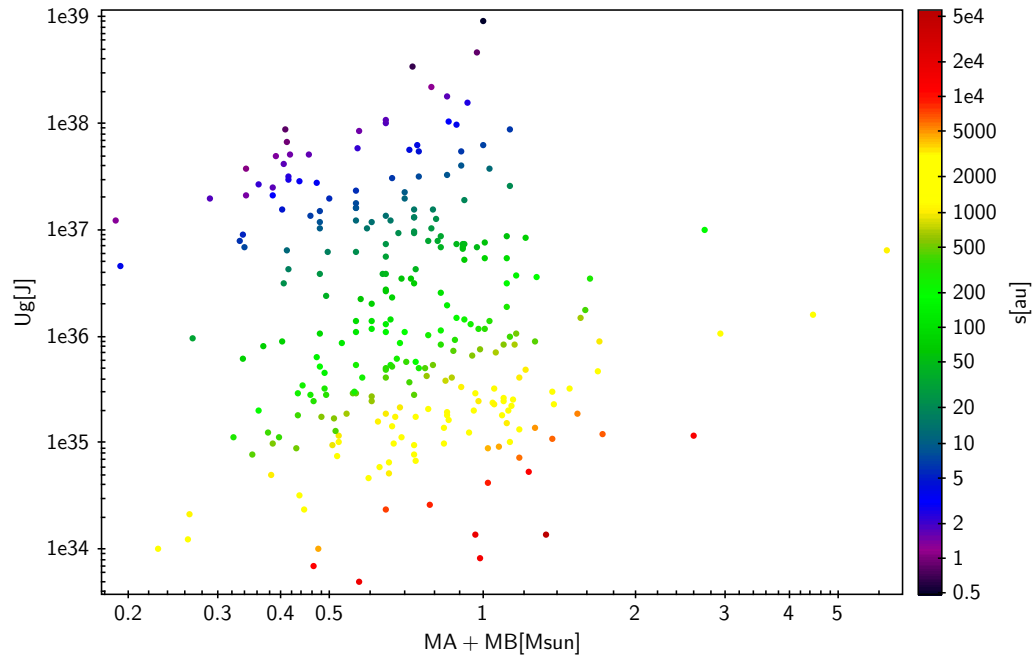


Figure 4.: Binding energy vs. total mass in logarithmic scale of a representative sample of CARMENCITA M-dwarf multiple systems. There is a U_g^* threshold at -10^{33} J. The right color bar indicates projected physical separations, also in logarithmic scale.

Acknowledgements. This proceeding is based on observations made with the TCS and IAC80 telescopes operated on the island of Tenerife by the IAC in the Spanish Observatorio del Teide. Financial support was provided by the Spanish Ministerio de Ciencia e Innovación under grants AYA2011-30147-C03-02 and AYA2011-30147-C03-03.

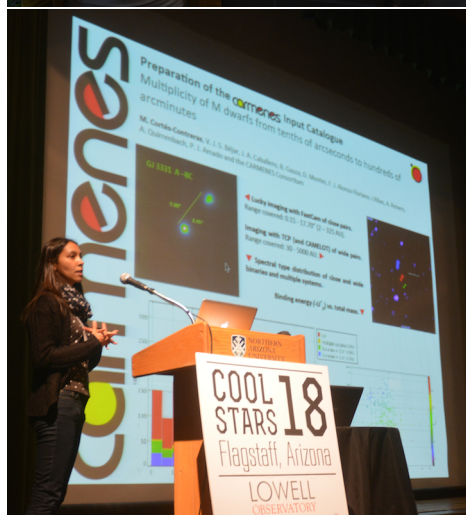
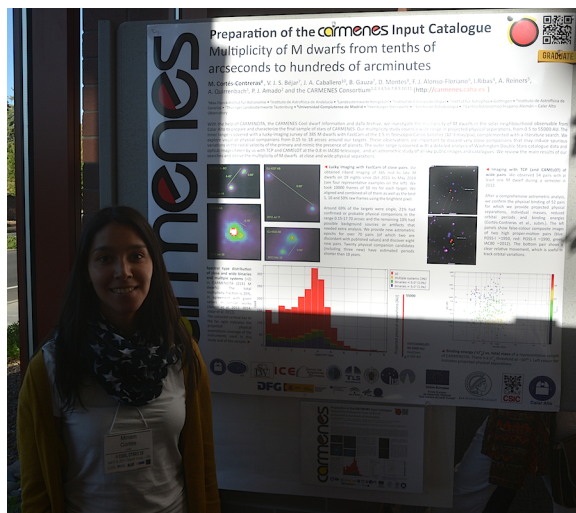


Figure 5.: Miriam Cortés in front of her CARMENES poster during the CS18 meeting (left) and during the poster pop-up presentation of the splinter session: "Portraying The Hosts: Stellar Science From Planet Searcher" (right)

References

- Alonso-Floriano, F. J., Morales, J. C., Caballero, J. A. et al. in prep.
- Baraffe, I., Chabrier, G. Allard, F., Hauschildt, P. H. 1998, A&A, 337, 403
- Beuzit, J.-L., Ségransan, D., Forveille, T. et al. 2004, A&A, 425, 997
- Caballero, J. A. 2009, A&A, 507, 251
- Cortés-Contreras, M., Béjar, V. J. S., Caballero, J.A. et al. in prep.
- Dhital, S., Stassun, K. G., West, A. A. 2012, AAS, 219, 132.05
- Giclas, H. L., Burnham, R., Thomas, N. G. 1978, LowOB, 8, 89

Janson, M., Hormuth, F. Bergfors, C. et al. 2012, ApJ, 754, 44

Janson, M., Bergfors, C., Brandner, W. et al. 2014, ApJ, 789, 102

Jódar, E., Pérez-Garrido, A., Díaz-Sánchez, A. et al. 2013, MNRAS, 429, 859

Luyten, W. .J. 1997, yCat, 1130

Oscos, A., Rebolo, R., López, R. et al. 2008, SPIE, 7014, E137O

Quirrenbach, A., Amado, P. J., Seifert, W., et al. 2012, SPIE Proceeding, 8446, E0R

Chapter 11

Stellar Spectroscopy during Exoplanet Transits: Dissecting fine structure across stellar surfaces

Dainis Dravins¹, Hans-Günter Ludwig², Erik Dahlén¹, Hiva Pazira^{1,3}

¹*Lund Observatory, Box 43, SE-22100 Lund, Sweden*

²*Zentrum für Astronomie der Universität Heidelberg, Landessternwarte
Königstuhl, DE-69117 Heidelberg, Germany*

³*Department of Astronomy, AlbaNova University Center, SE-10691
Stockholm, Sweden*

Abstract. Differential spectroscopy during exoplanet transits permits to reconstruct spectra of small stellar surface portions that successively become hidden behind the planet. The center-to-limb behavior of stellar line shapes, asymmetries and wavelength shifts will enable detailed tests of 3-dimensional hydrodynamic models of stellar atmospheres, such that are required for any precise determination of abundances or seismic properties. Such models can now be computed for widely different stars but have been feasible to test in detail only for the Sun with its resolved surface structure. Although very high quality spectra are required, already current data permit reconstructions of line profiles in the brightest transit host stars such as HD 209458 (G0 V).

1. Context

Three-dimensional and time-dependent hydrodynamic simulations are now established as realistic descriptions for the convective photospheres of various classes of

stars, and must be applied in any more precise determinations of chemical abundances, oscillation properties, or atmospheric structure. Such models can now be produced for stars with widely different properties, ranging from white dwarfs to red supergiants, and with all sorts of metallicities (Freytag et al. 2012; Magic et al. 2013; Tremblay et al. 2013); Fig. 1. Although, in principle, such simulations do not have freely tunable physical parameters, their complexity implies that they must apply various physical, mathematical, and numerical approximations to be manageable. Such models do well reproduce the details of solar spectral line profiles as well as the fine structure (granulation) observed across the solar surface, its time evolution, as well as its interaction with magnetic fields. However, the verification (or falsification) of such models is more challenging for other stars, where surface structures cannot be spatially resolved.

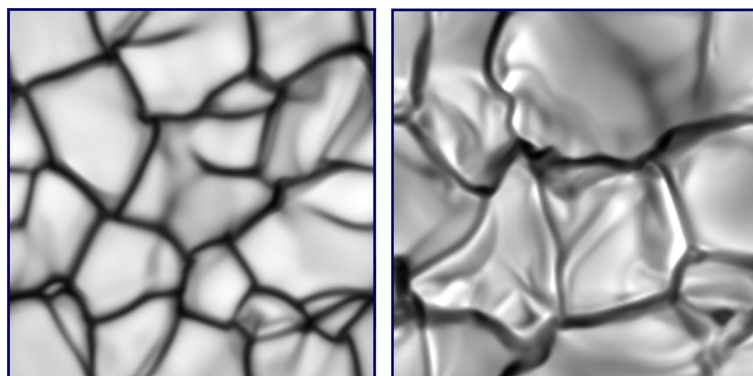


Figure 1.: Simulations of 3-dimensional hydrodynamics in stellar atmospheres: Examples of emergent intensity during granular evolution on the surface of a 12,000 K white dwarf (left) and a 3,800 K red giant. The areas differ by many orders of magnitude: $7 \times 7 \text{ km}^2$ for the white dwarf, and $23 \times 23 R_{\odot}^2$ for the giant. It has become possible to model widely different stars, but the observational means for verifying such simulations remain limited, except for the Sun.

Using the output from such simulations as temporally and spatially varying model atmospheres, synthetic spectral line profiles can be computed as temporal and spatial averages over the simulation sequence (Beck et al. 2013; Holzreuter & Solanki 2013; Pereira et al. 2013). Details of the atmospheric structure and dynamics are reflected in the exact profiles of photospheric absorption lines and in their center-to-limb variations. Line asymmetries and wavelength shifts originate from the statistical bias of an often greater number of [spectrally blueshifted] photons from hot and rising surface elements (granules) than from the cooler and sinking ones. Center-to-limb changes depend on the relative amplitudes of horizontal and vertical velocities, whose Doppler shifts contribute differently to the line broadening. These changes also depend on the amount of ‘corrugation’ across the stellar surfaces: if those are ‘smooth’ (in the optical-depth sense), convective blueshifts should decrease from disk center towards the limb, since vertical convective velocities become perpendicular to the line of sight, and the horizontal velocities that contribute Doppler shifts appear symmetric. However, stars with ‘hills’ and ‘valleys’ should show an increasing blueshift towards the limb, where one will predominantly see the approaching (thus blueshifted) velocities on the slopes of the ‘hills’ facing the observer. The depth dependence

of atmospheric properties causes dependences on parameters such as the line’s oscillator strength, its excitation potential, ionization level, and the wavelength region. Obviously, such types of spectral data could open up stellar surface structure to rather detailed observational study (Dravins & Nordlund 1990; Dravins et al. 2005).

2. Stellar physics from exoplanet transits

Exoplanet transits offer a possibility to disentangle spectra from small portions across the stellar surface. During transit, an exoplanet hides successive segments of the stellar disk and differential spectroscopy between epochs outside transit, and those during different transit phases, provide spectra of those particular surface segments that were then hidden behind the planet (Fig. 2). If the planet would happen to cross a starspot, even spatially resolved spectra (with their magnetic signatures) of such stellar surface features could become attainable, provided sufficient spectral fidelity can be reached. Knowing the precise ‘background’ stellar spectrum at different disk positions, also measurements of exoplanet atmospheres during transit would be better constrained.

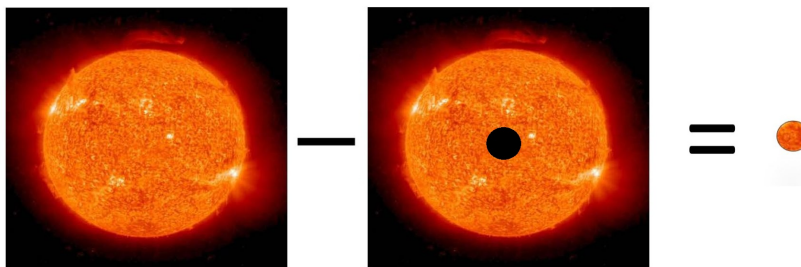


Figure 2.: The difference between the flux recorded outside, and during exoplanet transit, yields the signal of the temporarily hidden stellar surface segment.

Although the method is straightforward in principle, it is observationally very challenging since exoplanets cover only a tiny fraction of the stellar disk (no more than $\sim 1\%$ for main-sequence stars). If a desired signal-to-noise in the reconstructed spectrum would be on order $S/N = 100$, say, extracted from only $\sim 1\%$ of the total stellar signal, that would require a S/N in the latter on the order of 10,000 or more. This may appear daunting, but the method actually turns out to be (at least marginally) feasible for the brightest exoplanet host stars already with current spectrometers (e.g., UVES on VLT). In the near future one can expect it to become more potent; both because ongoing exoplanet surveys are likely to find brighter planet hosts, and because forthcoming higher-performance spectrometers (e.g., PEPSI on LBT or ESPRESSO on VLT) will enable such studies for also fainter and rarer stellar types.

3. Synthetic spectral lines from 3-D modeling

Examples of synthetic spectral lines computed from CO⁵BOLD models (Freytag et al. 2012) illustrate what types of signatures to expect (Figs. 3-4). The sim-

ulations are made for a certain spatial area on the star, and run for sufficiently many timesteps, so that the output is statistically stable. Spectral line profiles are then computed for each spatial location across the simulation area, for each timestep, and for different inclination angles to produce representative spatial and temporal averages for different center-to-limb positions. Since such spectroscopic measures are insensitive to (modest amounts of) spatial smearing, they can be compared to observations with modest spatial resolution; already spectra from a small number of center-to-limb positions will provide unique information.

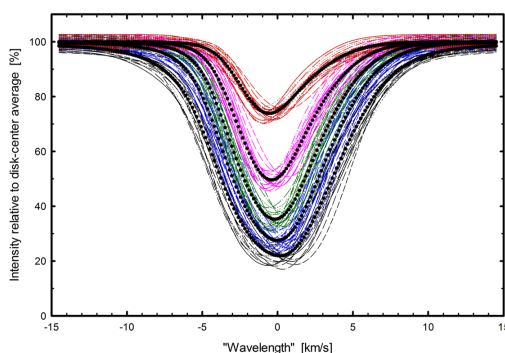


Figure 3.: Synthetic Fe I lines at stellar disk center ($\mu = \cos \theta = 1.0$) from a CO ⁵BOLD model of a giant star with approximate spectral type K0 III ($T_{eff} = 5000$ K, $\log g$ [cgs] = 2.5). Thin lines are averages over the spatial simulation area for each of 20 timesteps; bold curves are their temporal averages. Five different line strengths are shown; $\lambda = 620$ nm, $\chi = 3$ eV.

Fig. 3 illustrates some characteristic features of spectral lines formed in convective atmospheres. The lines generally become asymmetric and wavelength-shifted and these effects depend on line-strength; e.g., the weaker lines display a stronger convective blueshift. Fig. 4 shows other dependences, now also including that on excitation potential, and the position across the stellar disk. Clearly, such data encode a wealth of information.

4. Synthetic spectral lines across stellar disks

We now examine what types of spectral-line signatures one may expect across stellar disks. Fig. 5 shows a center-to-limb sequence for synthetic line profiles in a main-sequence star with solar metallicity, and $T_{eff} = 6800$ K, including the line bisectors (on an expanded scale). Close to disk center, there is a sudden change in the bisector shape near continuum intensity, the curve suddenly turning to the blue, i.e. a ‘blueward hook’. This has been previously observed for the F-type star Procyon and theoretically traced to the extended Lorentzian wings of the stronger, saturated, and blueshifted line components. Their contribution in one flank of the spatially averaged line also affects the intensity in the opposite flank, in contrast to Gaussian-like components, whose absorption disappears over a short wavelength distance. The steeper temperature gradients in the rising and blueshifted granules produce stronger absorption lines, which therefore tend to first saturate and develop Lorentzian damping wings in those spatial lo-

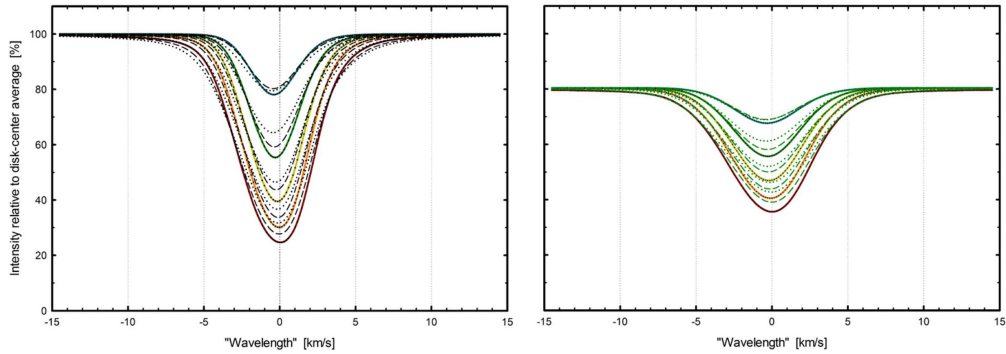


Figure 4.: Synthetic time-averaged photospheric Fe I lines for a solar model. Left: Disk center ($\mu = \cos \theta = 1.0$); five different line strengths, each for the three excitation potentials $\chi = 1, 3,$ and 5 eV. Right: Same for disk position $\mu = \cos \theta = 0.59$. The decreased intensity reflects the limb darkening at $\lambda=620$ nm while increased linewidths reflect that average horizontal velocities are greater than vertical ones, contributing more Doppler broadening towards the limb.

cations; Allende Prieto et al. (2002). Such signatures thus reveal differences in line-formation conditions in different inhomogeneities across the stellar surface.

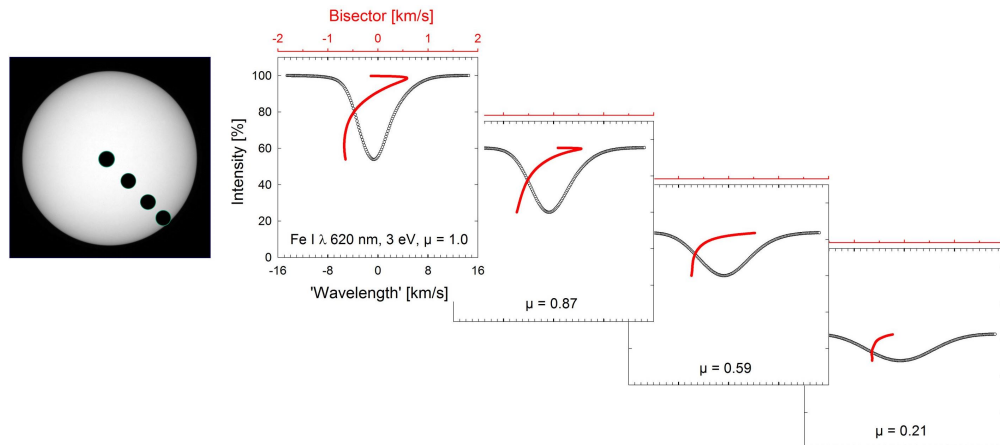


Figure 5.: Sequence of synthetic Fe I line profiles across the stellar disk, computed from a CO 5 BOLD model of a main-sequence star of solar metallicity, $T_{eff} = 6800$ K. The line asymmetries and wavelength shifts are shown by the bisectors.

5. Simulated line changes during exoplanet transit

As already noted, the spectrophotometric fidelity required for the corresponding observations is quite challenging. An examination of various options in retrieving spatially resolved stellar spectra suggests that a ratio method appears to be the one least sensitive to systematic and random noise. Fig. 6 shows the expected line-profile ratios during (half of) an exoplanet transit across the stellar equator. The red solid curves show the ratios of line profiles relative to that outside transit.

This simulation sequence from a CO⁵BOLD model is for an Fe I line (λ 620 nm, $\chi = 3$ eV) during the transit by a ‘bloated’ Jupiter-size exoplanet moving in a prograde orbit across the stellar equator, covering 2% of this main-sequence star with solar metallicity, $T_{\text{eff}} = 6300$ K, rotating with $V = 5$ km s⁻¹.

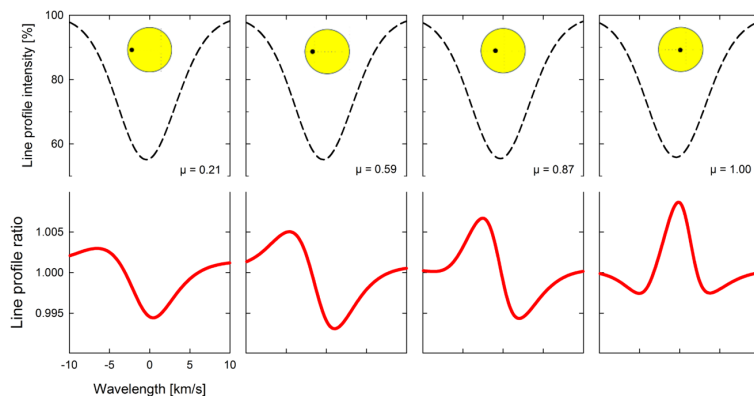


Figure 6.: Simulated line changes during the first half of an exoplanet transit across the equator of a $T_{\text{eff}} = 6800$ K main-sequence star. Red: Ratios of line profiles relative to the profile outside transit.

5.1 Simulated Rossiter-McLaughlin Effect

There are other measures that can be observed during a transit, e.g., the change of the star’s apparent radial velocity. This ‘Rossiter-McLaughlin effect’ occurs because the exoplanet successively hides different portions of a rotating star with locally either blue- or redshifted Doppler components, tipping the disk-averaged wavelength slightly towards longer or shorter values.

Fig. 7 shows the Rossiter-McLaughlin effect simulated for the same model as that for Fig. 6. The concept of ‘wavelength’ (not unique for asymmetric spectral lines) is here defined as fits of Gaussian functions to the synthetic line profiles. The values are negative (i.e., shorter than laboratory values) because of the convective blueshift. It can also be noted that the curves before and after mid-transit ($\mu = \cos \theta = 0.21, 0.59, 0.87$) are not exact mirror images of one another due to intrinsic stellar line asymmetries.

Exoplanet transit geometry

The geometry of the exoplanet transit must be known in order to fully interpret any observed line-profile variations (only in rare cases will the transit occur along the stellar equator). This can be constrained through the Rossiter-McLaughlin effect, enabling the planet’s position and path across the stellar disk to be determined; e.g., Torres et al. (2008).

6. Observations with current facilities

The demanding signal-to-noise requirements (e.g., the line-ratio amplitudes seen in Fig. 6 have amplitudes of only 0.5%) limit usable data to the very highest-fidelity spectra from high-resolution spectrometers at very large telescopes. Al-

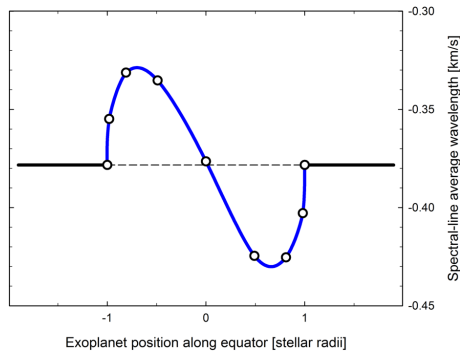


Figure 7.: Simulated Rossiter-McLaughlin effect for a $T_{eff} = 6800$ K star rotating with equatorial velocity $= 5 \text{ km s}^{-1}$, and a transiting planet covering 2% of the stellar disk. The spectral-line ‘wavelengths’ were here obtained as Gaussian fits to the synthetic (and asymmetric) line profiles.

though very many transiting planets are known, realistic targets include only such where the exoplanet is large (Jupiter-size or bigger) and the star among the brightest hosts found so far. Of course, these are the very objects of which extensive observations have been carried out in order to characterize the exoplanet and its atmosphere, and where numerous spectra are available in observatory archives. For some dozen such candidates, many hundreds of archive spectra were retrieved from several different observatories and examined for their suitability within the present project. The particular data shown in the following figures originate from one observation night with the UVES spectrometer (Dekker et al. 2000) on the VLT Kueyen telescope of ESO on Paranal as part of an investigation of the atmosphere of the exoplanet HD 209458b, for which other results were documented in Albrecht et al. (2009) and Snellen et al. (2011). The nominal random signal-to-noise values, as computed by the ESO data pipeline, reached values exceeding 500 in the centers of the best-exposed echelle orders. Exposure times were 400 seconds during and outside the three-hour transit, with nominal spectral resolution $\lambda/\Delta\lambda \approx 65,000$. This is a large planet (‘bloated hot Jupiter’, with $R = 1.38 R_{Jup}$), covering some 1.5 % of the stellar surface, close to the maximum for a solar-type main-sequence star. Exoplanets are not expected to get much larger, but some might well be found around smaller red (or even white) dwarfs, which would make these studies easier (but at the cost of a lower relative spatial resolution on the star).

Fig. 8 shows preliminary data for reconstructed $H\beta$ line profiles on various positions across the disk of HD 209458. The star is close to the Sun in spectral type (G0 V, sometimes also classified as F9 V; $T_{eff} = 6100$ K, $\log g [\text{cgs}] = 4.50$; $[\text{Fe}/\text{H}] = 0$; $V_{rot} = 4.5 \text{ km s}^{-1}$, and $\sin i = 1$ if the star rotates in the same plane as its transiting planet). The solid curve shows the spectrum outside transit, obtained as an average over numerous recordings, and the dashed curves show the extracted spectrum behind the exoplanet during various phases of the transit: longer-dashed during earlier parts, and shorter-dashed curves from later parts of the transit. As can be seen, the line gradually shifts towards longer wavelengths, as appropriate for a planet in a prograde orbit. In a sense, this is

the spatially resolved version of the Rossiter-McLaughlin effect, directly revealing the magnitude of the stellar rotational velocity vector.

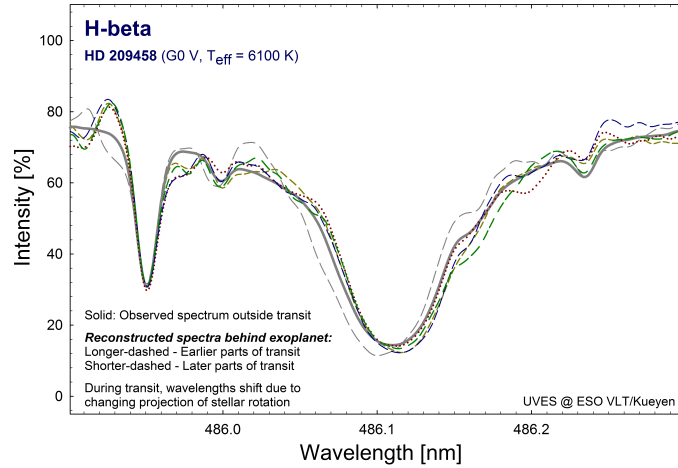


Figure 8.: Reconstructed $H\beta$ profiles for different positions across the disk of HD 209458 using spectra recorded with the UVES spectrometer at ESO/VLT.

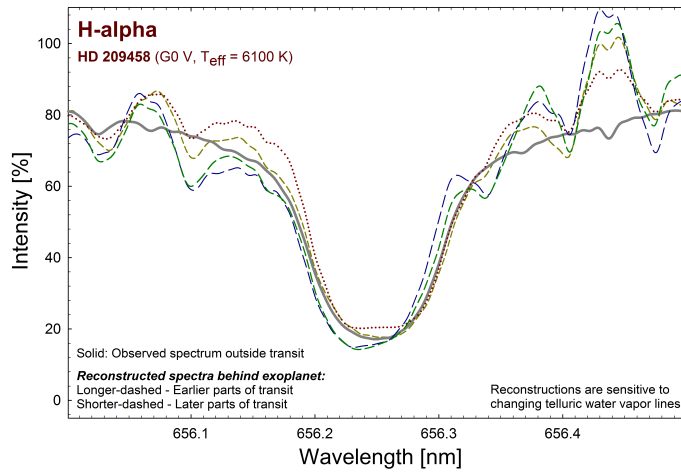


Figure 9.: Reconstructed $H\alpha$ profiles across the disk of HD 209458. The apparent ‘emission’ in the longward part is an artifact from varying telluric water vapor lines during the hours of transit and outside it.

Fig. 9 shows analogous reconstructions around the $H\alpha$ line. Besides the same sequence of gradually shifting signatures of stellar rotation, this illustrates another challenge in such reconstructions. Around λ 656.5 nm, some spurious ‘emission’ appears. This was identified as an artifact originating from variations in the strength of telluric water vapor lines during the several hours of transit and the period outside it. The reconstruction obtains that line profile, which is required to make its intensity-weighted summation with the observed transit profile, equal to the profile from outside transit. Already a small change of telluric line strengths between the transit and out-of-transit epochs implies that

the deduced spectrum from behind the exoplanet must carry all this change. Since it carries only a small weight corresponding to its tiny area coverage, this spectrum must then be significantly modified to account for it all. Even if water vapor effects are most prominent in the red part of the spectrum (like here around $H\alpha$), this exemplifies the need to control systematic errors.

Strong chromospheric lines such as these Balmer ones do not obtain their widths from photospheric motions, and their relative center-to-limb changes are expected to be rather smaller than for photospheric ones. A further aspect is that these strong lines are also those where some contribution from the extended atmosphere of the exoplanet may be expected. However, their large widths makes them less challenging to reconstruct, which is the reason why they were chosen for these first data samples. A somewhat narrower line is represented by the Na I D doublet (also studied in the context of the exoplanet atmosphere). Its greater intensity gradients makes it more susceptible to noise, with the photometric limitations illustrated in Figures 10 and 11. The average profiles for earlier and later parts of the transit do again clearly show the stellar rotation signature with amplitude on order 5 km s^{-1} , consistent with rotational estimates from full-disk photospheric line broadening. The sequences in Figure 11 of the ratios of successive 400-second exposures to the reference spectrum from outside transit illustrate how line profile changes can be followed during transit well above the noise level seen in out-of-transit spectra, however not by a very large margin. The pattern of stable differences in the transit spectra are believed to originate from differences in telluric water-vapor lines between the hours of transit and the times of recording out-of-transit spectra.

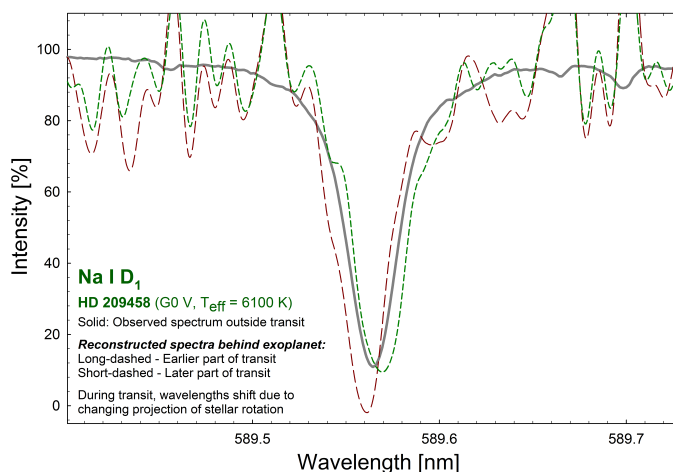


Figure 10.: Reconstructed Na I D₁ profiles across the disk of HD 209458. The noise level in current UVES spectra starts to become marginal for these narrower Na I D lines. Shown are average profiles for earlier and later parts of the transit.

These examples show that: (i) Already with data from existing facilities, it is feasible to reconstruct stellar line profiles from tiny portions of a stellar disk although (ii) for *individual* single lines, observed during only one transit, the very high signal-to-noise level required permits this to be done only for the broadest and strongest chromospheric ones. At these S/N levels, also close attention has to be paid to possible sources of systematics, such as variable telluric absorption in

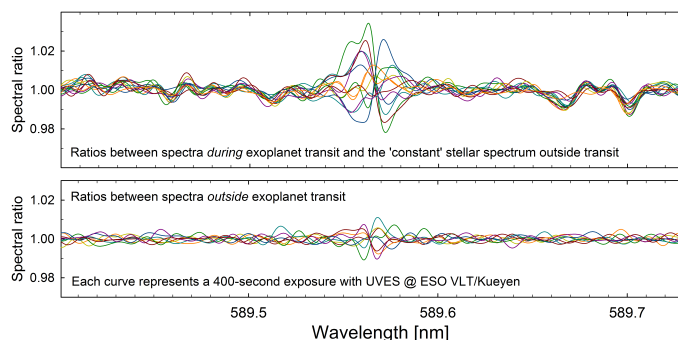


Figure 11.: Spectral fidelity around Na I D₁: Successive exposures compared to the reference spectrum from outside transit. Line profile changes can be followed during the exoplanet transit (top) with the noise level illustrated by analogous data outside transit (bottom). Changes during the observing night in telluric line-strengths are believed to cause the stable ratio patterns outside the Na I line.

some spectral regions, the stability of spectrometer calibration, of its software routines, and other.

The longer-term aim is to retrieve narrow photospheric line profiles, such as shown in Figure 5. Although, with current facilities and current stellar targets, this appears not practical for *individual* spectral lines, it may well be possible taking advantage of the multitude of physically similar ones (an option not available for the strong but few and mutually different chromospheric lines). However, already from just Fe I, the visual spectrum of solar-type stars contains on the order of 1000 measurable photospheric lines, of which perhaps one half can be classified as reasonably ‘unblended’. These can then be subdivided into perhaps five groups of differently strong ones, with ~ 100 lines per group. For lines with similar formation conditions, their profiles are shaped in a similar fashion and the information content in their line profiles is basically redundant. Thus, a suitable averaging of lines in such groups must be able to increase the data amount by a factor of ~ 100 , correspondingly reducing the noise level. There is a requirement of sufficiently high spectral resolution but not necessarily of a very small stellar rotational velocity. Even if the lines appear rotationally broadened and blended in the integrated disk spectrum, their spatially resolved reconstructions will have no such broadening. Such averaging over numerous – different but physically similar – lines has been made for the solar spectrum (Dravins 2008), permitting to identify also subtle patterns of line asymmetries, otherwise hidden in noise for individual lines. Work in this direction is currently in progress.

7. Future observations

As demonstrated above, retrieval of stellar spectral lines from small portions across stellar disks is feasible already with current facilities, and for current stellar targets. Both of these parameters are about to change in the near future, likely offering much improved possibilities for spatially resolved stellar spectroscopy.

One limiting parameter comes from the photometric noise that can be reached with existing telescopes and instruments. The data shown above originated from observations with the ESO 8.2 m VLT Kueyen telescope, with its UVES spectrometer entrance slit opened up to 0.5 arcseconds to maximize photometric precision at the cost of spectral resolution. Such a compromise was dictated by the limited brightness of the target star, HD 209458, of visual magnitude $V = 7.6$. Although brighter transiting planet hosts are currently not known (e.g., HD 189733, K0 V, is of a similar magnitude), numerous surveys are in progress or being planned, both from ground and from space, to survey brighter stars for possible exoplanet transits. This is a highest-priority activity for exoplanet studies since the possibilities for exoplanet characterization likewise are strongly dependent on the host star brightness. Given the known statistics of exoplanet occurrence, it is highly likely that suitable transiting planets will soon be found around also brighter hosts. Once a target star of visual magnitude $V = 5$, say, is found, that will improve the signal by one order of magnitude.

Another limiting parameter comes from the telescope + spectrometer combination. Here, very promising developments are in progress (Dravins 2010). The PEPSI spectrometer (Strassmeier et al. 2004, 2008) is in the process of becoming operational at the Large Binocular Telescope with its two 8.4 m apertures. Offering extended spectral coverage with resolutions $\lambda/\Delta\lambda$ up to 320,000, this has fully sufficient performance to reveal photospheric line asymmetries and other signatures of stellar photospheric structure and dynamics of convection. Also in progress is the ESPRESSO spectrometer for the combined focus of the four VLT unit telescopes of ESO on Paranal (Pepe et al. 2013, 2014). Observing time for such studies is virtually guaranteed since the detailed spectroscopy of exoplanets during transit of bright stars is also one of the highest-priority projects of exoplanet research, and the data required for stellar analyses will be obtained concurrently. In the somewhat more distant future, we can look forward to the proposed HIRES instrument at E-ELT, the European Extremely Large Telescope (Maiolino et al. 2013). This may not reach higher spectral resolution than its predecessors, but the order-of-magnitude increase in the telescope's collecting area should enable to reach also fainter and rarer stars, perhaps metal-poor, chemically peculiar and magnetically special ones.

Acknowledgements. This study used data obtained from the ESO Science Archive Facility, originating from observations made with ESO Telescopes at the La Silla Paranal Observatory under program ID: 077.C-0379(A) by Snellen, Collier, Cameron, and Horne. At Lund Observatory, contributions to the examination of archival spectra from different observatories were made also by Tiphaine Lagadec and Joel Wallenius. HGL acknowledges financial support by the Sonderforschungsbereich SFB881 “The Milky Way System” (subprojects A4 and A5) of the German Research Foundation (DFG).

References

- Albrecht, S., Snellen, I., de Mooij, E., & Le Poole, R. 2009, IAU Symp., 253, 520
- Allende Prieto, C., Asplund, M., García López, R. J., & Lambert, D. L. 2002, ApJ, 567, 544

- Beck, C., Fabbian, D., Moreno-Insertis, F., Puschmann, K. G., & Rezaei, R. 2013, *A&A*, 557, A109; corrigendum *A&A*, 559, 1
- Dekker, H., D'Odorico, S., Kaufer, A., Delabre, B., & Kotzlowski, H. 2000, *Proc. SPIE* 4008, 534
- Dravins, D. 2008, *A&A*, 492, 199
- Dravins, D. 2010, *Astron. Nachr.*, 331, 535
- Dravins, D., & Nordlund, Å. 1990, *A&A*, 228, 184
- Dravins, D., Lindegren, L., Ludwig, H.-G., & Madsen, S. 2005, in *ESA SP-560, 13th Cambridge Workshop Cool Stars*, ed. F. Favata et al., 113
- Freytag, B., Steffen, M., Ludwig, H.-G., et al. 2012, *J. Comp. Phys.*, 231, 919
- Holzreuter, R., & Solanki, S. K. 2013, *A&A*, 558, A20
- Magic, Z., Collet, R., Asplund, M., et al. 2013, *A&A*, 557, A26
- Maiolino, R., Haehmelt, M., Murphy, M. T., et al. 2013, *arXiv:1310.3163*
- Pepe, F., Cristiani, S., Rebolo, R., et al. 2013, *ESO Messenger*, 153, 6
- Pepe, F., Molaro, P., Cristiani, S., et al. 2014, *Astron. Nachr.*, 335, 8
- Pereira, T. M. D., Asplund, M., Collet, R., et al. 2013, *A&A*, 554, A118
- Snellen, I., Albrecht, S., de Mooij, E., & Poole, R. L. 2011, *Astron. Soc. Pacific Conf. Ser.*, 450, 39
- Strassmeier, K. G., Pallavicini, R., Rice, J. B., & Andersen, M. I. 2004, *Astron. Nachr.*, 325, 278
- Strassmeier, K. G., Woche, M., Ilyin, I., et al. 2008, *Proc. SPIE* 7014, 70140N
- Torres, G., Winn, J. N., & Holman, M. J. 2008, *ApJ*, 677, 1324
- Tremblay, P.-E., Ludwig, H.-G., Freytag, B., Steffen, M., & Caffau, E. 2013, *A&A*, 557, A7

Chapter 12

Hot Stars With Cool Companions

Kevin Gullikson¹, Adam Kraus¹, Sarah Dodson-Robinson²

¹*University of Texas, 2515 Speedway, STOP C1400, Austin, TX 78712*

²*University of Delaware, 217 Sharp Lab, Newark, DE 19716*

Abstract.

Young intermediate-mass stars have become high-priority targets for direct-imaging planet searches following the recent discoveries of planets orbiting e.g. HR 8799 and Beta Pictoris. Close stellar companions to these stars can affect the formation and orbital evolution of any planets, and so a census of the multiplicity properties of nearby intermediate mass stars is needed. Additionally, the multiplicity can help constrain the important binary star formation physics. We report initial results from a spectroscopic survey of 400 nearby A- and B-type stars. We search for companions by cross-correlating high resolution and high signal-to-noise ratio echelle spectra of the targets stars against model spectra for F- to M-type stars. We have so far found 18 new candidate companions, and have detected the spectral lines of the secondary in 4 known spectroscopic binary systems. We present the distribution of mass-ratios for close companions, and find that it differs from the distribution for wide ($a \gtrsim 100$ AU) intermediate-mass binaries, which may indicate a different formation mechanism for the two populations.

1. Introduction

Recent radial-velocity searches for massive planets orbiting $1-2M_{\odot}$ subgiant “retired A-stars” (Johnson et al. 2011) have indicated that intermediate-mass stars may be more likely to host planets than solar-type and low-mass stars. This finding, in combination with the direct-imaging detections of massive planets on

very wide orbits around young A-type stars (e.g. Marois et al. 2008, 2010; Lagrange et al. 2010), has spurred an increased interest in intermediate-mass stars as potential planet hosts. Especially interesting are the *young* intermediate-mass stars, where a planet on a wide orbit will be bright enough to be directly imaged and characterized. However, since stellar multiplicity increases with mass (Zinnecker & Yorke 2007) and decreases with age (Duchêne & Kraus 2013), the same young intermediate-mass stars that are attractive targets for planet searches may very often host a close *stellar* companion that can impact the planet formation process. Since close companions that may not be resolvable by current imaging systems are likely to have the largest impact on planet formation, a spectroscopic multiplicity survey of nearby intermediate-mass stars is needed.

The multiplicity of A- and B-type stars can also help constrain the binary star formation mechanism and the relevant physics involved during and after the formation of the secondary. The dominant mode of binary star formation is thought to be molecular core fragmentation (Boss & Bodenheimer 1979; Boss 1986; Bate et al. 1995) in which a collapsing cloud of gas fragments into two or more stars. The ratio of masses is set largely by the turbulent power spectrum, density structure, angular momentum, and magnetic field in the pre-stellar core. Low-mass stars may also form directly via gravitational instabilities (Kratter & Matzner 2006; Stamatellos & Whitworth 2011) in the massive disk surrounding a forming intermediate-mass star. This alternate formation scenario will only act within ~ 100 AU, and may create an observationally distinguishable inner mass-ratio distribution. Observational studies of the multiplicity, mass-ratio distribution and separation distribution in a population of stars provide a benchmark against which future star formation models and simulations must agree.

The intermediate-mass binary population has been well-mapped for wide orbits ($a \gtrsim 50$ AU) with imaging studies in the young Scorpius-Centaurus OB associations (Kouwenhoven et al. 2007) and recently for field A-star primaries (De Rosa et al. 2014). These studies have both found a preference for binary systems with low mass-ratios q ($q \equiv M_s/M_p$, where M_s and M_p are the secondary and primary mass, respectively), and are consistent with a power law $f(q) \sim q^\Gamma$ with $\Gamma = -0.4$. While there does not appear to be a difference between close and wide binary systems for solar-type and low-mass primaries (Reggiani & Meyer 2013), there is some evidence that intermediate-mass binaries have a flatter mass-ratio distribution inside ~ 100 AU (De Rosa et al. 2014). This radius is the same order of magnitude as a circumstellar disk, and seems to imply that the disk around an intermediate-mass protostar plays a more crucial role in binary formation and evolution than it does for solar-type and low-mass stars. It may be a sign that disk fragmentation is capable of producing a distinct population of binary companions when there is enough disk mass, or could be an effect of increased or preferential accretion onto the secondary star if it forms near the gas-rich disk.

Most of the systematic studies searching for companions to intermediate-mass stars to date have used imaging, and so miss low-mass companions within a few tens of AU from the primary star. Thus, a spectroscopic study is necessary to derive the true mass-ratio distribution for close binary systems and compare it to that of wide binary systems. We have begun such a survey, using high signal-to-noise ratio (S/N) echelle spectra to directly detect the spectral lines of secondary stars orbiting 400 nearby Main Sequence A- and B-type stars.

2. Observations and Methods

We have observed 292 of a total sample of 400 A- and B-type stars. The sample was chosen from the Simbad database, and includes all main-sequence A- and B-stars with $v \sin i > 80 \text{ km s}^{-1}$, $m_V < 6$, and no spectral peculiarities. We have observed these stars with the CHIRON spectrograph on the 1.5m telescope at Cerro Tololo Interamerican Observatory, the Tull coude spectrograph on the 2.7m telescope at McDonald Observatory, and the High Resolution Spectrograph on the Hobby Eberly Telescope at McDonald Observatory. The data were bias-subtracted, flat-fielded, and extracted with the optimal extraction method using standard IRAF tasks. The extracted spectra were wavelength-calibrated using Th-Ar lamps taken the same night as the data. All three instruments are visible echelle spectrographs with similar resolution and wavelength ranges.

After extraction, the data were corrected for telluric absorption lines using the TelFit package (Gullikson et al. 2014). Several frames were taken for each star, and each frame was telluric-corrected separately to better account for the changing airmass and atmospheric conditions over the course of the exposures. The corrected frames for each target were added together before further analysis, resulting in spectra with a typical peak S/N ratio per pixel of 500.

As a final pre-processing step, we removed the rotationally broadened spectral lines of the primary star by fitting a cubic Savitzky-Golay (Savitzky & Golay 1964) smoothing spline with a window size of $0.8v \sin i$, where the $v \sin i$ came from the most recent literature value in the Simbad database. The factor of 0.8 was chosen to give the best fit to the data while leaving the high frequency components intact. We divided the data by the smoothing spline, in effect passing it through a high-pass filter.

To search for companions, we cross-correlated the processed spectra against the following grid of Phoenix model spectra (Hauschildt & Baron 2005)

- $3000K < T_{\text{eff}} < 7000K$, in 100 K steps
- $-0.5 < [\text{Fe}/\text{H}] < +0.5$, in 0.5 dex steps
- $\log g = 4.5$
- $v \sin i = 10, 20, 30, 40 \text{ km s}^{-1}$

Figure 1 demonstrates the cross-correlation method for a secondary star that is just barely detectable “by eye,” but is unambiguously detected in the cross-correlation function. This method can detect fainter companions which are not visible in the spectrum but are evident in the cross-correlation function; by injecting artificial signals into the data, we have found that companions with $T_{\text{eff}} \gtrsim 3500 \text{ K}$ (spectral types earlier than about M2-M3) are detectable in most of our data.

3. Preliminary Results and Discussion

After searching for companions in all of our data to date, we have found 18 new candidate companions, and have detected the spectral lines of the secondary in 4 previously single-lined spectroscopic binaries. Since the new detections require follow-up observations to confirm, we do not report them here. However, we list

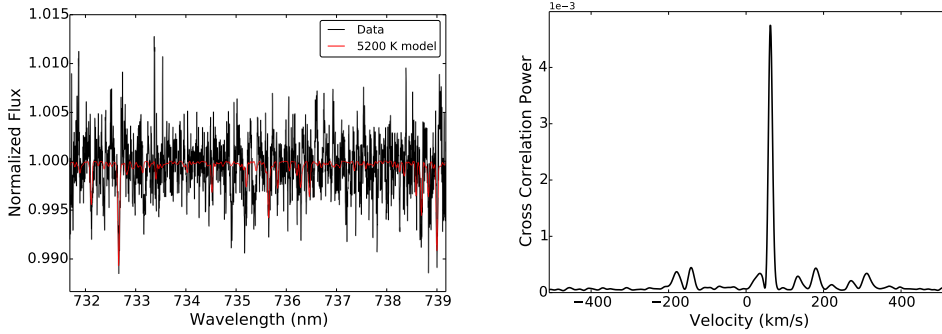


Figure 1.: Example of the cross-correlation based technique described in section 2. *Left:* One order of a spectrum of HIP 32607, an A8V star. The observed spectrum is in black, with a 5200 K model spectrum in red. Some of the spectral lines of the secondary are barely visible in the spectrum, most notably the line near 732.7 nm. *Right:* The cross-correlation function of all orders of the same observation against the same 5200 K model. The strong peak indicates a clear detection of the secondary.

the companions to known single-lined binaries in Table 1. Since we only have single-epoch data for these stars, we cannot fit an orbital solution. We report the spectral type of the secondary star in Table 1, which is determined from the temperature which gives the most significant cross-correlation function detection.

Star Name	Primary Spectral Type	Secondary Spectral Type
HIP 106786	A7V	G7
HIP 32607	A8V	K0
HIP 109521	A5V	K2
HIP 22833	A3V	G9

We also show the mass-ratio distribution that we derive from the candidates so far detected in Figure 2. To determine the mass of the secondaries, we first find the temperature that gives the most significant cross-correlation function peak. That temperature is the best match to the observed spectrum, and so we take it as the true temperature of the candidate companion star. We then interpolate Baraffe stellar evolutionary tracks (Baraffe et al. 1998) at the age of the system to find the secondary star mass. Masses for the primary stars come from main sequence relationships. We do not have ages for most of our sample at this time, and use the main sequence lifetime of the primary star for the system age. Doing so will tend to slightly overestimate the mass of the secondary; however, since we chose only main sequence targets, we don't expect the age to change by much more than a factor of 2 and so the secondary masses should not be significantly affected in most cases. In the near future, we intend to use the observed spectra to measure the effective temperature, gravity, and metallicity of the primary stars, and use that information to better constrain the age of the system and mass of the primary star.

The mass ratio distribution we show in Figure 2 is consistent with a flat distribution, similar to the results that De Rosa et al. (2014) find for field A-type stars inside 125 AU. Notably, a Kolmogorov-Smirnov test shows that it is

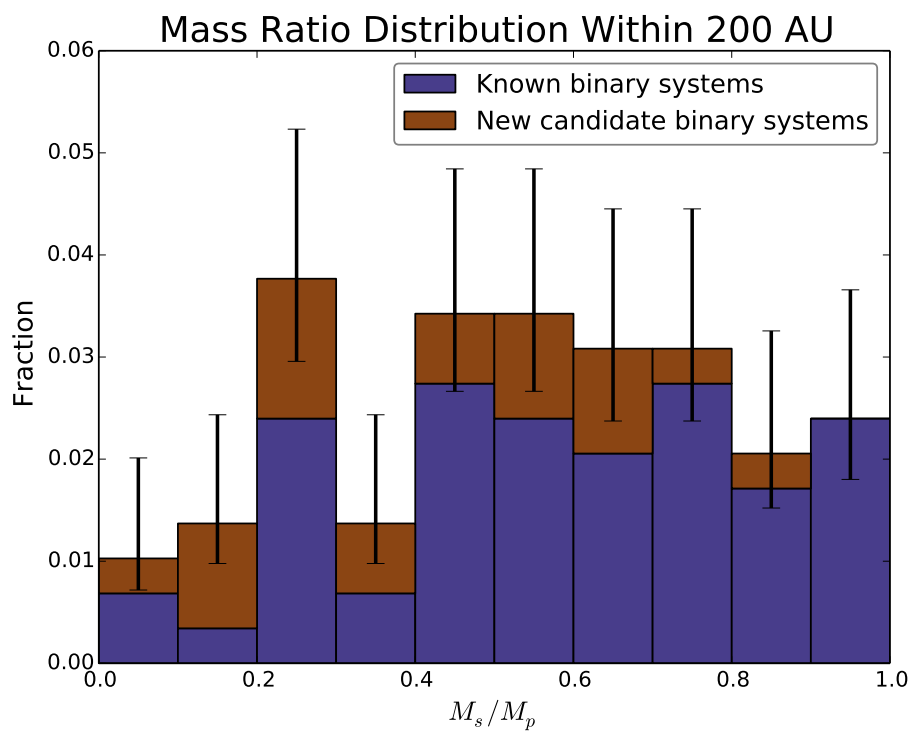


Figure 2.: Mass-ratio distribution for the stars we have so far observed. The distribution is complete down to $q \sim 0.15$, and includes both known and new binary systems. The 1σ binomial confidence interval is shown for each bin.

inconsistent with a power law with slope $\Gamma = -0.4$ ($p = 7.4 \times 10^{-6}$). These results seem to indicate that disk physics are important in forming intermediate-mass binaries systems.

Acknowledgements. This research has made use of the SIMBAD database, operated at CDS, Strasbourg, France. This project was funded by a UT Austin Hutchinson fellowship to Kevin Gullikson and start-up funding to Sarah Dodson-Robinson from the University of Texas.

References

- Baraffe, I. et al. 1998, *A&A*, 337, 403
- Bate, M. R., Bonnell, I. A., & Price, N. M. 1995, *MNRAS*, 277, 362
- Boss, A. P. 1986, *ApJS*, 62, 519
- Boss, A. P. & Bodenheimer, P. 1979, *ApJ*, 234, 289
- De Rosa, R. J. et al. 2014, *MNRAS*, 437, 1216
- Duchêne, G. & Kraus, A. 2013, *ARA&A*, 51, 269
- Gullikson, K., Dodson-Robinson, S., & Kraus, A. 2014, ArXiv e-prints
- Hauschildt, P. & Baron, E. 2005, *Memorie della Societa Astronomica Italiana Supplementi*, 7, 140
- Johnson, J. A. et al. 2011, *ApJS*, 197, 26
- Kouwenhoven, M. B. N. et al. 2007, *A&A*, 474, 77
- Kratter, K. M. & Matzner, C. D. 2006, *MNRAS*, 373, 1563
- Lagrange, A.-M. et al. 2010, *Science*, 329, 57
- Marois, C. et al. 2008, *Science*, 322, 1348
- Marois, C. et al. 2010, *Nature*, 468, 1080
- Reggiani, M. & Meyer, M. R. 2013, *A&A*, 553, A124
- Savitzky, A. & Golay, M. J. E. 1964, *Analytical Chemistry*, 36, 1627
- Stamatellos, D., & Whitworth, A. 2011, *European Physical Journal Web of Conferences*, 16, 5001
- Zinnecker, H. & Yorke, H. W. 2007, *ARA&A*, 45, 481

Chapter 13

Potential magnetic field extrapolation in binary star systems

Volkmar Holzwarth¹, Scott G. Gregory²

¹*Kiepenheuer-Institut für Sonnenphysik, Schöneckstr. 6, 79104 Freiburg, Germany*

²*School of Physics & Astronomy, University of St Andrews, St Andrews KY16 9SS, UK*

Abstract. For several decades the potential field source surface (PFSS) approximation has proven helpful in the description of the large-scale coronal magnetic fields of the Sun and of cool single stars. Here, we extend the PFSS technique to systems with two objects, to investigate the magnetic field structure of close binary stars. We describe the deviation of the two-centre extrapolation technique and demonstrate its applicability in the case of the close pre-main sequence binary system V4046 Sgr. Our results reveal a joint magnetosphere with complex field structures connecting both stellar components. The binary extrapolation method is also applicable to the case of magnetic interaction between a host star and a close-in hot Jupiter.

1. Introduction

Magnetic fields have a decisive influence on the structural, dynamical and thermal properties of the coronae of cool stars. Since even in the case of the Sun direct observations of coronal magnetic fields are difficult to accomplish, extrapolation methods are frequently used to infer them from magnetic field distributions observed in the photosphere. Introduced by Schatten et al. (1969) for the case of the Sun, the potential field source surface (PFSS) extrapolation technique has since been used numerous times to describe the magnetospheres and wind zones of cool

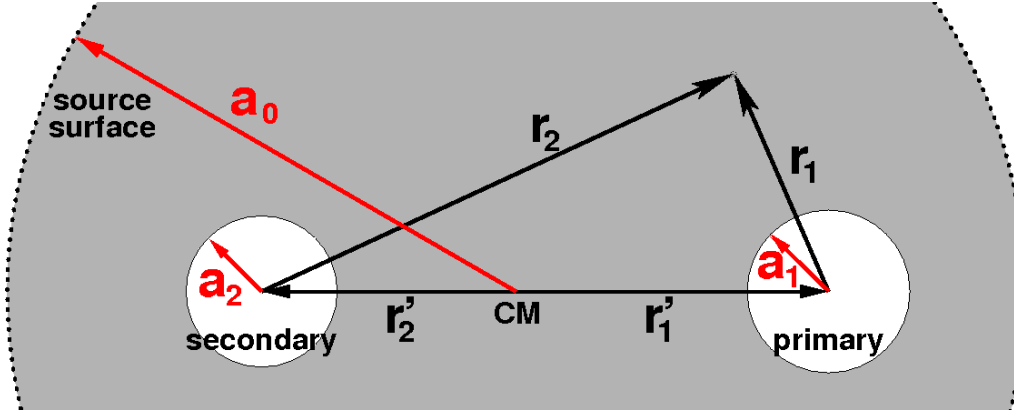


Figure 1.: Schematic binary system. The region of interest (grey) is bounded at the outside by the source surface (dotted line) and inside by the stellar surfaces.

stars. It accounts for the existence of stellar winds through the assumption of magnetic fields becoming purely radial at some distance above the photosphere. Albeit more sophisticated extrapolation methods have been developed since (e.g., Wiegmann & Sakurai 2012, and references therein), the PFSS approach remains significant, since the resulting magnetic field represents the stable, lowest-energy state of the magnetosphere which is consistent with boundary conditions given in the photosphere.

We extend the PFSS technique to close binary stars and demonstrate the applicability of the new method with the case of the close PMS binary V4046 Sgr, for which magnetic surface maps for both stellar components have been reconstructed based on Zeeman-Doppler imaging observations (Donati et al. 2011). Our extrapolation method is applicable also to star-planet and planet-moon systems, and easily expandable to N-body systems.

2. Binary field extrapolation technique

We consider a binary system consisting of a primary star, S_1 , with radius a_1 located (with respect to the center of mass, CM) at point \vec{r}'_1 and a secondary star, S_2 with radius a_2 at point \vec{r}'_2 . The source surface S_0 , with radius a_0 and centred in CM, marks the location at which the magnetic field becomes purely radial through the effect of winds from both stellar components. In the case of the Sun, a standard value is $a_0 = 2.5 R_\odot$ (e.g. Schatten et al. 1969), whereas for single stars the position of the source surface is empirically determined through, for example, through a comparison of reconstructed emission measures with empirical values based on X-ray observations (Jardine et al. 2002).

The region of interest, shaded grey in Fig. 1, is taken to be current free. The magnetic field, $\vec{B} = -\nabla\Psi$, is therefore given by the gradient of a scalar potential function, Ψ , which, owing to the solenoidal condition $\nabla \cdot \vec{B} = 0$, satisfies the Laplace equation, $\nabla^2\Psi = 0$. The joint magnetosphere of the binary system is thus determined by solving the Laplace equation, subject to boundary conditions specified on the surfaces of both stellar components and on the source surface.

The potential Ψ is expanded in terms of regular and irregular solid spherical harmonics (SSH),

$$R_l^m(\vec{r}) = (-1)^m \frac{r^l}{(l+m)!} P_l^m(\cos \theta) e^{im\phi} \quad (13.1)$$

$$S_l^m(\vec{r}) = (-1)^m \frac{(l-m)!}{r^{l+1}} P_l^m(\cos \theta) e^{im\phi}, \quad (13.2)$$

respectively (Steinborn & Ruedenberg 1973), around the origins \vec{r}'_k of the spheres S_k , where we take into account that $\vec{r} = \vec{r}'_k + \vec{r}_k$ (see Fig. 1):

$$\Psi(\vec{r}) = \sum_{l,m} c_{lm}^{(0)} R_l^m(\vec{r}_0) + \sum_{l,m,k>0} c_{lm}^{(k)} S_l^m(\vec{r}_k) \quad (13.3)$$

The second term on the right hand side of Eq. (13.3) comprises the magnetic moments of the two stellar components, whereas the the first term contains the magnetic moments arising from the boundary condition at the source surface; in mathematical terms, the later is realised through the assumption of mirror sources located beyond the source surface, which in concert with the magnetic moments of the two stars result in a radial magnetic field at S_0 .

The boundary conditions at S_1, S_2 , and S_0 specify expansion coefficients, $c_{lm}^{(k)}$. For their determination, we make use of SSH translation theorems (e.g. Steinborn & Ruedenberg 1973),

$$R_l^m(\vec{r}_1 + \vec{r}_2) = \sum_{\lambda,\mu} (R|R)_{\lambda l}^{\mu m}(\vec{r}_1) R_\lambda^\mu(\vec{r}_2) = \sum_{\lambda,\mu} R_{l-\lambda}^{m-\mu}(\vec{r}_1) R_\lambda^\mu(\vec{r}_2) \quad (13.4)$$

$$S_l^m(\vec{r}_> + \vec{r}_<) = \sum_{\lambda,\mu} (S|R)_{\lambda l}^{\mu m}(\vec{r}_>) R_\lambda^\mu(\vec{r}_<) = \sum_{\lambda,\mu} (-1)^{\lambda-\mu} S_{l+\lambda}^{m-\mu}(\vec{r}_>) R_\lambda^\mu(\vec{r}_<) \quad (13.5)$$

$$S_l^m(\vec{r}_> + \vec{r}_<) = \sum_{\lambda,\mu} (S|S)_{\lambda l}^{\mu m}(\vec{r}_<) S_\lambda^\mu(\vec{r}_>) = \sum_{\lambda,\mu} (-1)^{\lambda+\mu-l-m} R_{\lambda-l}^{m-\mu}(\vec{r}_<) S_\lambda^\mu(\vec{r}_>) \quad (13.6)$$

which describe the contribution of a magnetic moment (l, m) of an expansion to the magnetic moment (λ, μ) of a translated expansion shifted by translation vector \vec{r}_1 . Note that in the case of irregular SSH, one has to distinguish between regions which are closer, Eq. (13.5), and further, Eq. (13.6), away from the shifted centre of expansion than the applied translation vector, that is $|\vec{r}_<| < |\vec{r}_>|$.

The contributions of the stellar magnetic moments to the expansion of the potential function on the source surface are described through Eq. (13.6), that is

$$\Psi(\vec{r}_0)|_{S_0} = \sum_{l,m} c_{lm}^{(0)} R_l^m(\vec{r}_0) + \sum_{l,m,k>0} c_{lm}^{(k)} S_l^m(\vec{r}'_0 - \vec{r}'_k + \vec{r}_0) \quad (13.7)$$

$$= \sum_{l,m} c_{lm}^{(0)} R_l^m(\vec{r}_0) + \sum_{l,m,k>0} c_{lm}^{(k)} \sum_{\lambda,\mu} (S|S)_{\lambda l}^{\mu m}(\vec{r}'_{k0}) S_\lambda^\mu(\vec{r}_0) \quad (13.8)$$

with $\vec{r}'_{k0} = \vec{r}'_0 - \vec{r}'_k$. The boundary condition of magnetic fields being purely radial implies $\Psi(\vec{r}_0)|_{S_0} = \text{const.}$ For the sake of simplicity, we set $\Psi(\vec{r}_0)|_{S_0} = 0$, which yields the determining equations for the coefficients

$$c_{lm}^{(0)} = -\frac{1}{a_0^{2l+1}} \sum_{l',m',k>0} (S|S)_{l'l}^{mm'}(\vec{r}'_{k0}) c_{l'm'}^{(k)} \quad (13.9)$$

in terms of the stellar magnetic moments $c_{l'm'}^{(k)}$, $k > 0$.

Inserting Eq. (13.9) and Eqs. (13.4-13.5) in Eq. (13.3) yields the expansion of the potential on the surface S_j of stellar component j :

$$\Psi(\vec{r}_j)|_{S_j} = \sum_{l,m} c_{lm}^{(j)} S_l^m(\vec{r}_j) + \sum_{\lambda,\mu,j \neq k > 0} c_{\lambda\mu}^{(jk)} R_\lambda^\mu(\vec{r}_j) \quad (13.10)$$

Whereas the first term on the right side of Eq. (13.10) accounts for the contributions of the magnetic moments of star j , the second term, with the new coefficients

$$c_{\lambda\mu}^{(jk)} = - \sum_{l',m'} c_{l'm'}^{(j)} W_{\lambda l'}^{\mu m'}(\vec{r}'_{0j}, \vec{r}'_{j0}, a_0) \quad (13.11)$$

$$+ \sum_{l,m,k \neq j} c_{lm}^{(k)} [(S|R)_{\lambda l}^{\mu m}(\vec{r}'_{kj}) - W_{\lambda l}^{\mu m}(\vec{r}'_{0j}, \vec{r}'_{k0}, a_0)] \quad (13.12)$$

subsumes the contributions of both magnetic moments of the companion star and influence of binary winds (i.e. the source surface). In Eq. (13.12), the abbreviation

$$W_{l_R l_S}^{m_R m_S}(\vec{r}_R, \vec{r}_S, a) = \sum_{l,m} (R|R)_{l_R l}^{m_R m}(\vec{r}_R) (S|S)_{l_S l}^{m m_S}(\vec{r}_S) \frac{1}{a^{2l+1}} \quad (13.13)$$

has been introduced. The boundary conditions on the stellar surfaces are given by maps of the radial magnetic field component. The coefficients, $B_{l'm'}^{(j)}$, resulting from the expansion of these maps in terms of spherical harmonics, determine the magnetic moments $c_{lm}^{(j)}$:

$$B_{l'm'}^{(j)} = \frac{l'+1}{a_j^{l'+2}} c_{l'm'}^{(j)} + l' a_j^{l'-1} \sum_{l,m} W_{l'l}^{m'm}(\vec{r}'_{0j}, \vec{r}'_{j0}, a_0) c_{lm}^{(j)} - l' a_j^{l'-1} \sum_{k \neq j, l, m} [(S|R)_{l'l}^{m'm}(\vec{r}'_{kj}) - W_{l'l}^{m'm}(\vec{r}'_{0j}, \vec{r}'_{k0}, a_0)] c_{lm}^{(k)} \quad (13.14)$$

In the case of a binary system, a solution of the linear system of equations

$$\begin{pmatrix} B_{l',m'}^{(1)}/a_1^{l'-1} \\ B_{l',m'}^{(2)}/a_2^{l'-1} \end{pmatrix} = \begin{pmatrix} \mathcal{M}_{\infty\infty} & \mathcal{M}_{\infty\epsilon} \\ \mathcal{M}_{\epsilon\infty} & \mathcal{M}_{\epsilon\epsilon} \end{pmatrix} \begin{pmatrix} c_{l,m}^{(1)} \\ c_{l,m}^{(2)} \end{pmatrix} \quad (13.15)$$

with

$$\mathcal{M}_{\parallel} = \begin{cases} \delta_{l'l'} \delta_{mm'} (l'+1) a_j^{-(2l'+1)} + l' W_{l'l}^{m'm}(\vec{r}'_{0j}, \vec{r}'_{j0}, a_0) & , \quad j = k \\ -l' (S|R)_{l'l}^{m'm}(\vec{r}'_{kj}) + l' W_{l'l}^{m'm}(\vec{r}'_{0j}, \vec{r}'_{k0}, a_0) & , \quad j \neq k \end{cases} \quad (13.16)$$

determines the expansion coefficients and, thus, the structure of the joint magnetosphere.

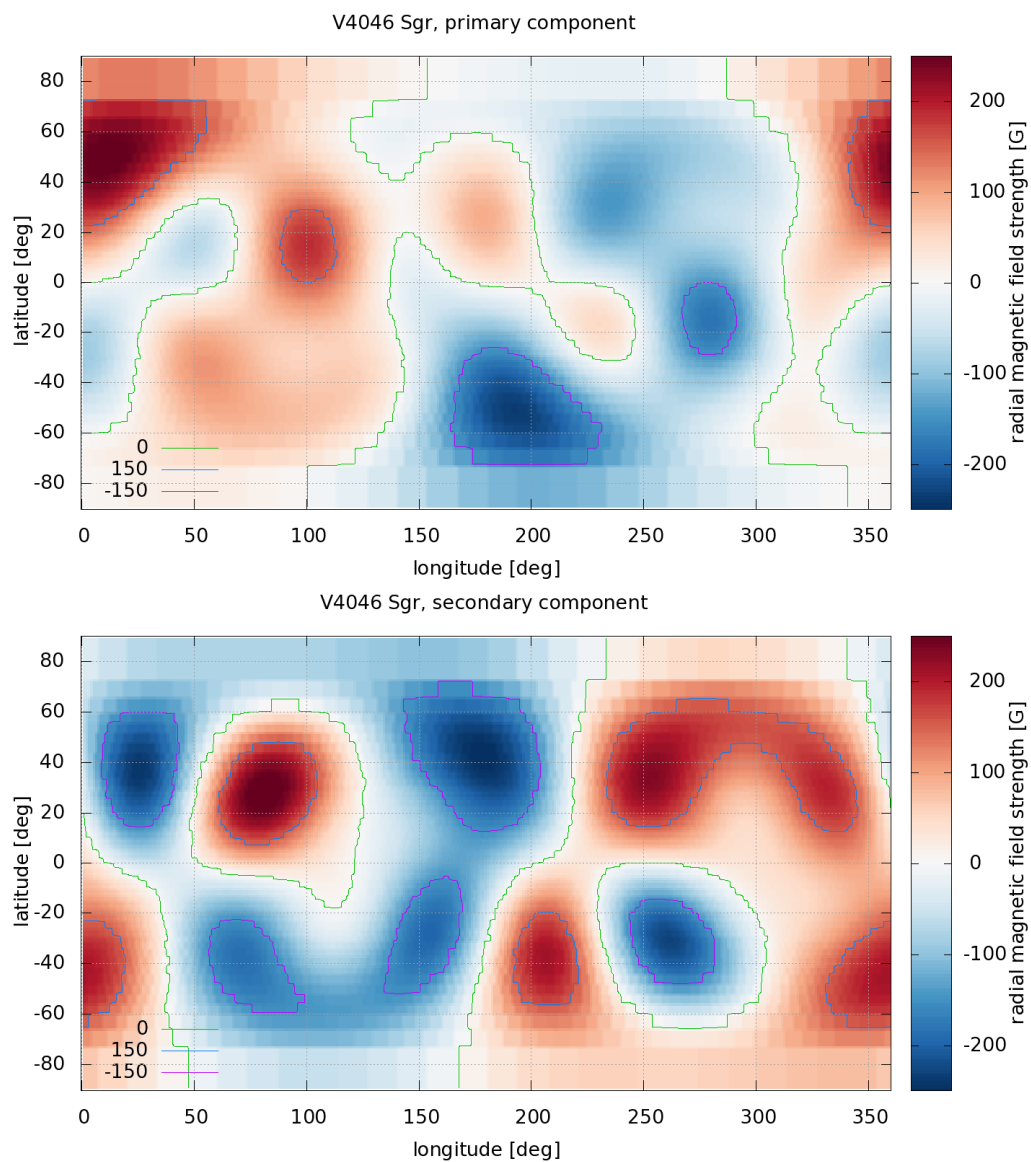


Figure 2.: Surface distributions of the radial magnetic field strength on the primary (top) and secondary (bottom) component of the pre-MS binary V4046 Sgr, reconstructed from Zeeman-Doppler imaging observations (Donati et al. 2011).

3. Example: V4046 Sgr

We demonstrate the applicability of our method through the reconstruction of the joint magnetosphere of the young (~ 13 Myr) pre-main sequence binary V4046 Sgr. Figure 2 shows surface maps of the radial magnetic field strength of both stellar components, based on spectropolarimetric observations using ES-PaDONs at the CFHT in 2009 (Donati et al. 2011; Gregory et al. 2014).

The system parameters (cf. Fig. 1) used for the reconstruction of the magnetosphere are given in Table 1. The source surface radius of a binary system is, as

surface S_k	k	position $x'_k [R_\odot]$	radius $a_k [R_\odot]$
source	0	0	10.0
primary	1	4.3	1.12
secondary	2	-4.5	1.04

Table 1.: Parameter combination for the potential magnetic field extrapolation of V4046 Sgr, shown in Fig. 3; positions, $\vec{r}'_k = (x'_k, 0, 0)^T$, along the x -axis are relative to centre of mass, CM, of binary system (Fig. 1).

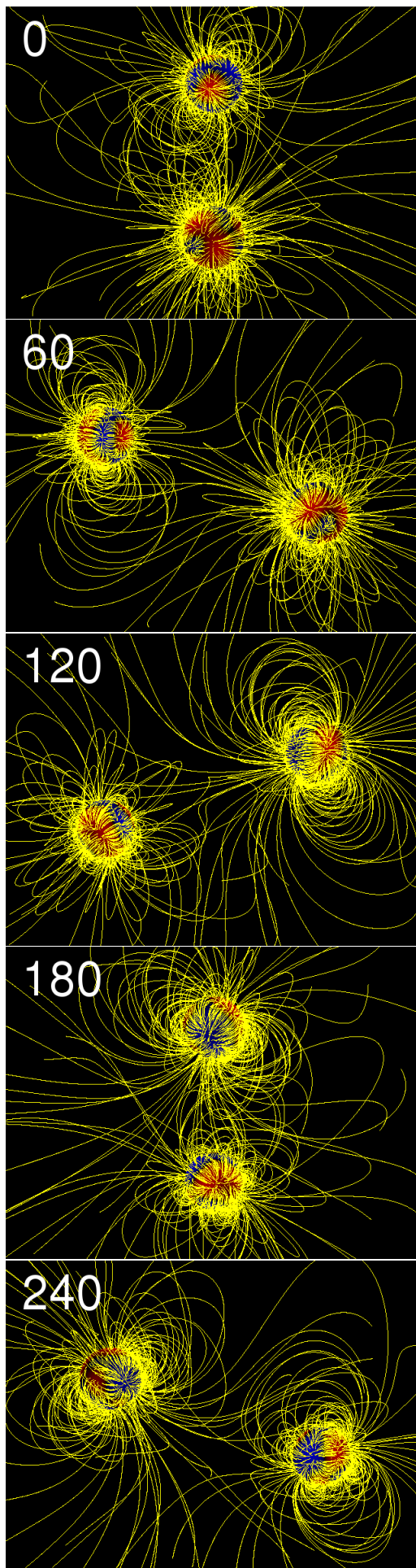
yet, observationally unconstrained, so that $a_0 = 10 R_\odot$ is somewhat arbitrarily. This value has been chosen based on the assumption that, for the hemispheres pointing away from the companion, the source surface is in a similar distance as for respective single star models.

Our reconstruction reveals complex magnetic field structures in the binary system (Fig. 3). The magnetic field in the vicinity of each star is dominated by tilted dipoles, somewhat modified by the influence of higher magnetic moments. Of particular interest are magnetic field structures connecting both stellar components; some 'S'-shaped field lines can be identified which inter-connect the dayside hemisphere of one component with the night side of the other.

4. Discussion

Close, late-type binary stars, such as RS CVn and BY Dra systems, are among the most active stellar objects we know. Their combination of rapid rotation and convective motions entails pronounced magnetic activity signatures which are discernible from the visible to the X-ray spectral range. The interpretation of, e.g., the amount and variability of coronal X-ray emission or the location of high-energetic flaring, requires, however, some notion of the magnetic field underlying their atmospheres. To this end, we extend the PFSS technique to close binaries to provide, in conjunction with Zeeman-Doppler imaging observations of photospheric magnetic fields, approximations of their joint magnetospheres.

More advanced (e.g. non-linear force-free field) extrapolation techniques are frequently applied locally, for instance to active regions on the Sun, where high-resolution observations permit to set up sophisticated boundary conditions. In the stellar case, however, the less-demanding PFSS approach seems adequate, because detailed observations of small-scale magnetic field distributions are unavailable. Disregarding electric currents and dissipation mechanisms, the PFSS approximation provides the lowest-energy, and therefore stable, state of the global field configuration. This allows us to address question related to the distribution



of open, closed, and inter-connecting magnetic flux on the surfaces of binary stars, the inter-binary field structure and locations of activity, and on the mass transfer along connecting field lines. Our preliminary results for V4046 Sgr reveal, for instance, complex field structures which connect different hemispheres of both stellar components.

Our method of potential magnetic field extrapolation is applicable to detached binary star systems, single stars with exoplanets, and single stars with asymmetric winds (i.e. an off-centred source surface). Objects which deviate significantly from spherical geometry such as semi-detached or contact systems are currently excluded, since any rotational or tidal deformations are neglected. Yet an extension of our method to systems with $k_{\max} > 2$ objects is straightforward, so that it can easily be applied to N-body problems involving potential fields of different kind, such as source-free magnetic, electric, or gravitational fields.

Acknowledgements. SGG acknowledges support from the Science & Technology Facilities Council (STFC) via an Ernest Rutherford Fellowship [ST/J003255/1].

References

- Donati, J.-F., Gregory, S. G., Montmerle, T., et al. 2011, MNRAS, 417, 1747
- Gregory, S. G., Holzwarth, V. R., Donati, J.-F., et al. 2014, European Physical Journal Web of Conferences, 64, 8009
- Jardine, M., Wood, K., Collier Cameron, A., Donati, J.-F., & Mackay, D. H. 2002, MNRAS, 336, 1364
- Schatten, K. H., Wilcox, J. M., & Ness, N. F. 1969, Solar Phys., 6, 442
- Steinborn, E. O., & Ruedenberg, K. 1973, Advances in Quantum Chemistry, 7, 1
- Wiegmann, T., & Sakurai, T. 2012, Living Reviews in Solar Physics, 9, 5

Chapter 14

Probing Rotational Dynamo Extremes: X-ray and Optical Spectroscopy of the 0.5 Day Period Eclipsing Binary, HD 79826

David P. Huenemoerder¹, Joy S. Nichols², David DePalma², David Garcia-Alvarez³, Norbert S. Schulz¹

¹*MIT Kavli Institute for Astrophysics and Space Research*

²*Harvard-Smithsonian Center for Astrophysics*

³*Instituto de Astofísica de Canarias*

Abstract. The highly modulated optical light curve of HD 79826 (spectral types G5+M5) was discovered in the *Chandra* guide-star light curves, indicating a period of about 0.5 days, a strong and migrating distortion wave, and a shallow eclipse. We subsequently obtained simultaneous *Chandra* high resolution X-ray spectra and optical photometry, along with contemporaneous ground-based photometry and spectra. X-ray rotational or eclipse modulation was totally obscured by X-ray variability and flares. X-ray spectra are characterized by coronal emission near the saturation limit of $L_x/L_{\text{bol}} = 10^{-3}$. Optical spectra show extremely rotationally broadened features, variable with orbital phase. Optical light curves show the modulation to be not only rapidly migrating in phase, but also of variable amplitude. We characterize the X-ray emission through measurements of line widths, velocities, and fluxes, and provide coronal plasma models. This star is near

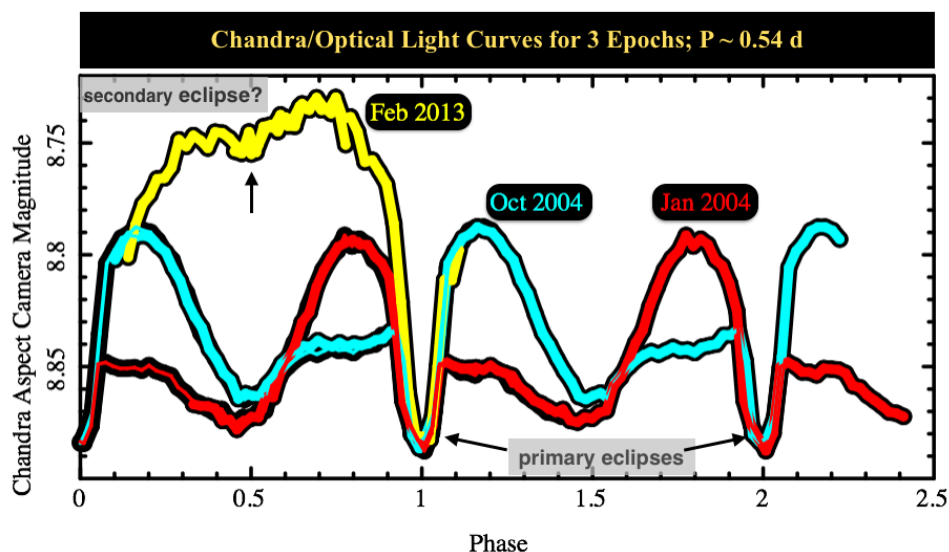


Figure 1.: *Chandra* aspect camera optical light curves of HD 79826. The cyan and red curves each cover more than two cycles (data have *not* been replicated for phases greater than 1.0).

or at the limits of dynamo saturation, and since it is partially eclipsing, has potential to be well characterized in terms of fundamental stellar parameters.

1. *Chandra* Optical Light Curves

HD 79826 was discovered to be a short period eclipsing variable with a rapidly migrating distortion (spot) wave in the *Chandra* Variable Guide Star Catalog^a of ?. In 2004 it was observed twice for over two cycles each time. In 2013, it was observed both as a guide star and as the primary X-ray target of the *Chandra* High Energy Grating Spectrometer (HETG). Figure 1 shows three *Chandra* optical light curves indicating the primary eclipse and the rapidly changing distortion wave.

An estimate of the system geometry and basic parameters are shown in Figure 2, based on the observed period and nominal spectral types.

2. *Chandra*/HETG X-ray Light Curves

The X-ray light curves were derived from the February 2013 *Chandra*/HETG observations of HD 79826 (observation identifiers 15272 and 15612) in which the star was also used as an aspect camera guide star. Light curves were extracted from

^a<http://cxc.harvard.edu/vguide>

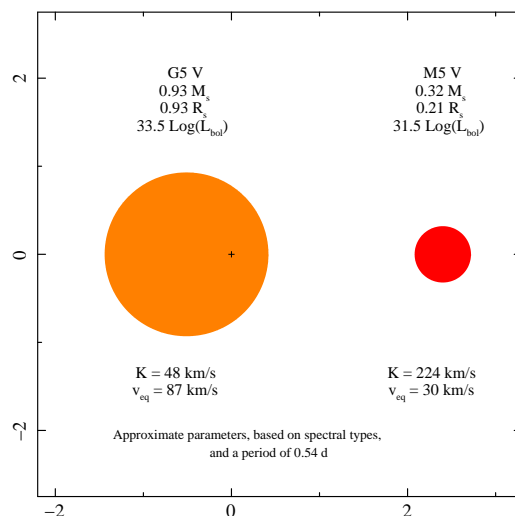


Figure 2.: Approximate binary system geometry and parameters, based on nominal spectral types and the observed period. Axes' units are in solar radii.

the HETG first order events in soft, hard, and full bands^b The *Chandra*/HETG X-ray light curves show strong variability. However, this is primarily due to a strong flare, seen not only in the sharp jump in count rate, but also in a hardness ratio. Figure 3 shows the HETG light curves. The flare, unfortunately, occurred right through primary eclipse, hiding any modulation of coronal emission by the secondary. Figure 4 shows the phased simultaneous X-ray and optical light curves.

3. X-ray Spectra

The *Chandra*/HETG X-ray spectrum is typical of coronal emission with a host of H- and He-like emission lines of abundant elements, as well as Fe-L lines. Figure 5 shows mean flux for the two observations. A 3-temperature component APEC ?? model follows the data very well. The lines show no width or shift in excess of instrumental resolution, indicating that the primary (G5 V) star dominates the X-ray emission. ($\Delta v = 25 \pm 35 \text{ km s}^{-1}$; $FWHM < 280 \text{ km s}^{-1}$).

The higher flux HETG spectrum is characteristic of stellar and solar flares in the sharp rise in count rate with slower decay, as well as in spectral changes indicative of high temperature plasmas, namely an enhanced short-wavelength continuum ($2 - 10 \text{ \AA}$) and strong lines of highly ionized iron. Figure 6 shows the flare and low-state spectra. Discrete 3-temperature plasma model fits to the flare and low-state spectra yield the temperature and emission measure which show

^bCurves were extracted using the “aglc” package; <http://space.mit.edu/cxc/analysis/aglc/>.

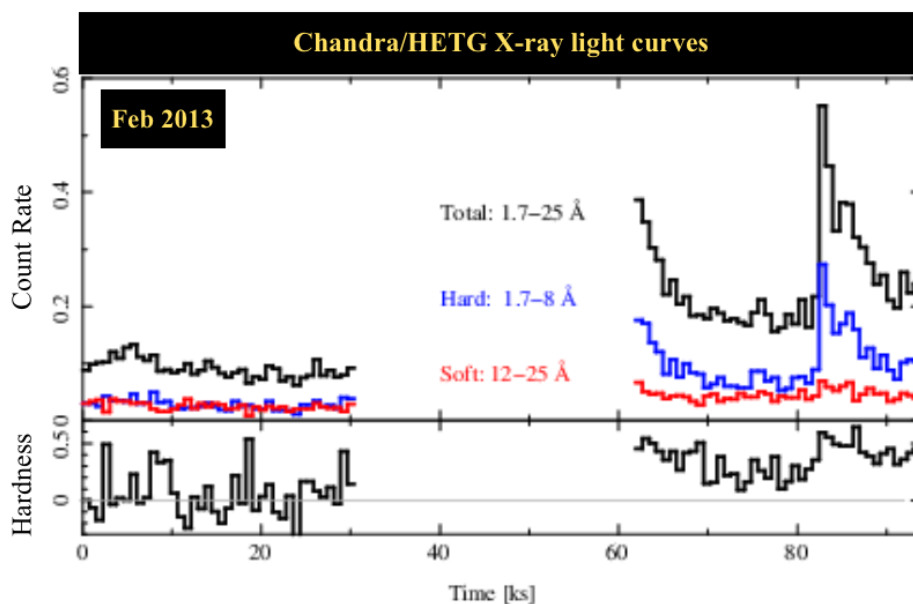


Figure 3.: X-ray light curves from HETG events. The time is from the start of the first observation, and the count rate is for the sum of the HEG and MEG first orders. Black (top curve) is the full HETG band, blue (middle curve) a hard band, and red (lower) a soft band. The lower panel shows a hardness ratio, defined as $(hard - soft)/(hard + soft)$.

(Figure 6, right panel) the large enhancement in high temperature plasma typical of flares.

4. Optical Spectra

We have obtained high resolution optical spectra, monitored contemporaneously with the X-ray spectra. Figure 7 shows two examples from the series, showing the $H\alpha$ and $H\beta$ regions. Lines are highly broadened, as expected for rapidly rotating stars. We will model these spectra by fitting templates and will derive radial and rotational velocities and relative intensity weights, and thereby improve the binary systems basic parameters.

5. Relevance

Compared to other coronally active stars, HD 79826 is among the most active, being near or at the saturation limit, and showing no sign of “supersaturation” at the shortest periods. Being a detached (probably) and eclipsing binary, it can provide an important benchmark at the extreme limit of stellar magnetic dynamos. Figure 8 shows the location of the HD 79826 among other stars.

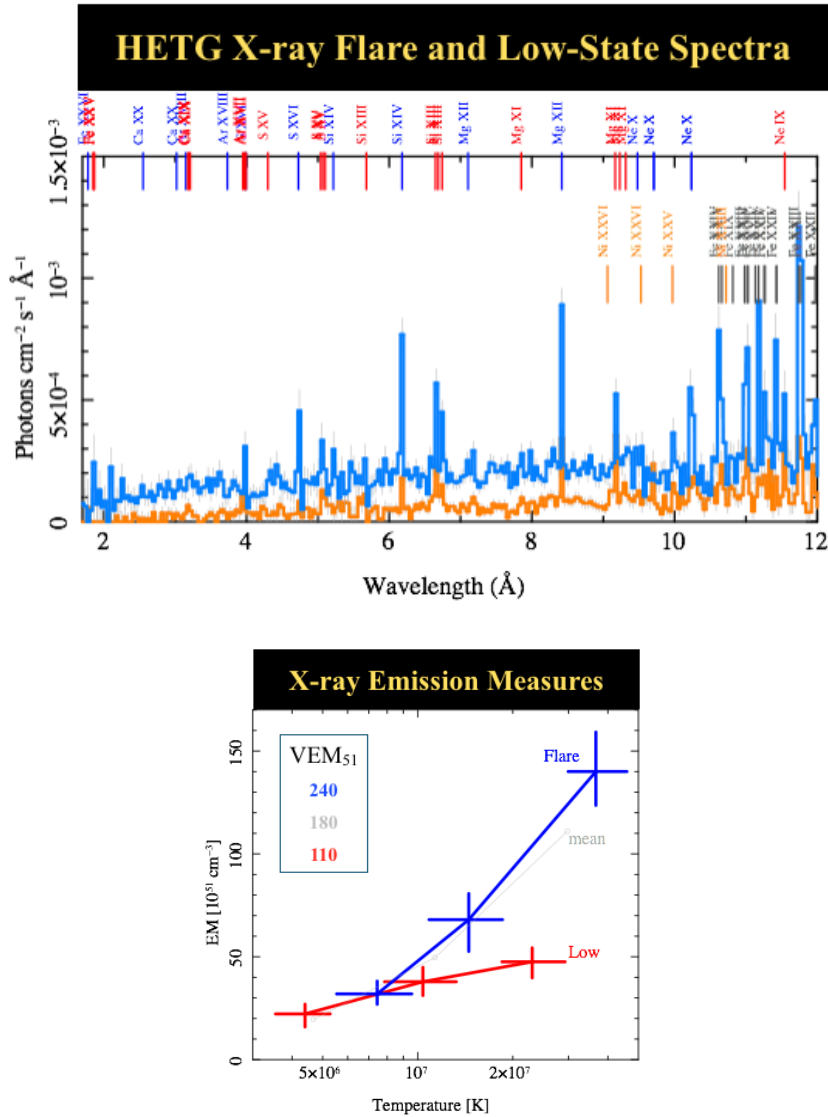


Figure 6.: On the top is the HETG spectrum during the flares (blue; observation shown in dark gray in Figure 4) and the low-state spectrum (orange; black in Figure 4). The bottom panel shows the temperatures and emission measures of 3-temperature APEC model fits to the flare (blue) and low (red) states. The inset table in the bottom panel gives integrated emission measures for each state (other values for comparison: Capella (moderate activity): 50, and II Peg (high activity): 800).

Acknowledgements: This work was supported by NASA through the Smithsonian Astrophysical Observatory (SAO) contract SV3-73016 for the Chandra X-Ray Center and Science Instruments.

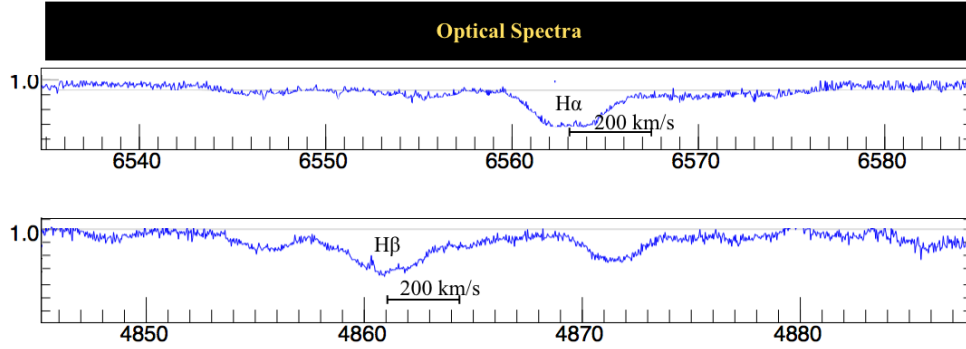


Figure 7.: Example H α (top) and H β spectra obtained contemporaneously with the X-ray spectra. Lines are very broad. A bar of length 200 km s^{-1} is shown for reference, which is the approximate maximum velocity separation of the two components, though it may be difficult to detect the fainter M5 star's signature.

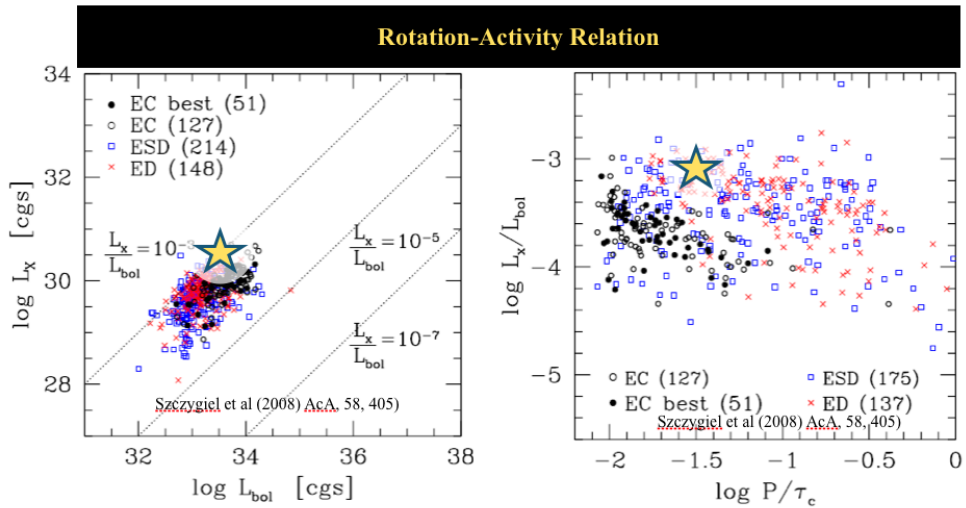


Figure 8.: The location of HD 79826 is shown (big yellow star) on the distribution of other active stars, from ?. In the right-hand panel, the x -axis is the Rossby number, the ratio of the rotational period, P , to convective turnover time, τ_c .

Chapter 15

The long and the short of it: timescales for stellar activity

Jardine, M.¹, Vidotto, A.², Llama, J.¹, See, V.¹, Gibb, G.³

¹*SUPA, School of Physics and Astronomy, North Haugh, St Andrews, Fife, KY16 9SS, UK*

²*Observatoire de Genève, Université de Genève, Chemin des Mailletes 51, Versoix, 1290, Switzerland*

³*School of Mathematics and Statistics, North Haugh, St Andrews, Fife, KY16 9SS, UK*

Abstract. Stellar activity varies on a range of timescales, from the long-term decrease due to stellar spindown, through the shorter timescales of magnetic cycles and the rapid fluctuations of flares and coronal mass ejections. All of these are influenced by the mass of the star. This governs the nature of the dynamo that generates magnetic field in the stellar interior and determines the observed large-scale magnetic structure. Stellar mass also governs the processes (such as differential rotation) that transport flux across stellar surfaces and drive coronal evolution and dynamics. In this review I will discuss recent progress in these areas and consider the impact that stellar activity on all these timescales may have on exoplanetary systems.

1. Introduction

Stellar activity varies on a range of time scales, from the long timescale of stellar evolution, through the shorter variations of stellar cycles, to the rapid energy release seen in flares and mass ejections. On the longest timescales, stars spin down as they age and their activity decays as a result. Rather like people, stars, when they are young, are more dynamic - they are certainly more active and rotate faster. Unlike people however, stars tend to lose mass as they age. More

importantly, they lose angular momentum. Thus an active and dynamic youth is replaced by a more sedate middle age, characterised by slow rotation and more predictable behaviour.

1.1 The long timescale of angular momentum loss

Stars achieve this transformation by losing angular momentum in a hot, magnetically-channeled wind (Weber & Davis 1967). Angular momentum is removed at a rate given by

$$-\dot{J} = \frac{8\pi}{3\mu_0} \frac{\Omega}{u_A} (B_0 r_\star^2)^2$$

and therefore depends on the stellar angular velocity Ω , the Alfvén speed u_A , and magnetic flux $B_0 r_\star^2$ threading the surface. If the wind is thermally driven, then the Alfvén speed can be replaced by the sound speed. If we further assume a linear dynamo, such that $B \propto \Omega$, then we can recover the Skumanich braking law (Skumanich 1972). Of course the original formulation of this expression was based on only 3 data points, and we can do much better nowadays. Studies of rotation rates of stars in young open clusters (Irwin et al. 2011) show a very characteristic behaviour as a function of time. Initially the stellar rotation rate is held constant by the presence of a disk, but once the disk is dissipated, the star spins up as it contracts. This generates an increasingly strong magnetic field, and hence an increasingly powerful wind that carries away angular momentum and spins the star down.

Over the timescale of this spin down, however, planets may form and evolve around the star. In order to see this timescale in context, we can look at what was happening in the solar system while the Sun was evolving in this way.

1.2 Solar system evolution

In the earliest phases, from 1 to 10 My, the gas giants formed (see Fig. 1). These planets therefore formed when the Sun was at its most active. The rocky planets formed later, sometime before around 100 My. Some time later, two catastrophic events happened in the solar system. The first was that Mars, being a small planet that cooled quickly, lost its internal convection and hence its magnetic field (Acuña et al. 2001). Planetary magnetic fields protect the atmosphere of the planet from the impact of the solar wind, and Mars lost its atmosphere not very long after this (Kulikov et al. 2007). The second catastrophic event was the Late Heavy Bombardment that showered to the inner solar system with impacts.

The very earliest evidence that we have the presence of the Earth’s magnetic field comes from measurements taken in very ancient rocks (Tarduno et al. 2010). We don’t know at what point the Earth began generating a magnetic field that could protect its atmosphere, but this is the earliest measurement that we have. It was still some time yet however before the Earth developed an oxygen rich atmosphere that signified the presence of life.

This brief history of the solar system emphasises how many different processes were taking place in the newly forming planets, while the Sun was steadily becoming less active. Had the Sun been a lower mass star, however, its rotational evolution would have been much slower, and therefore it would have maintained

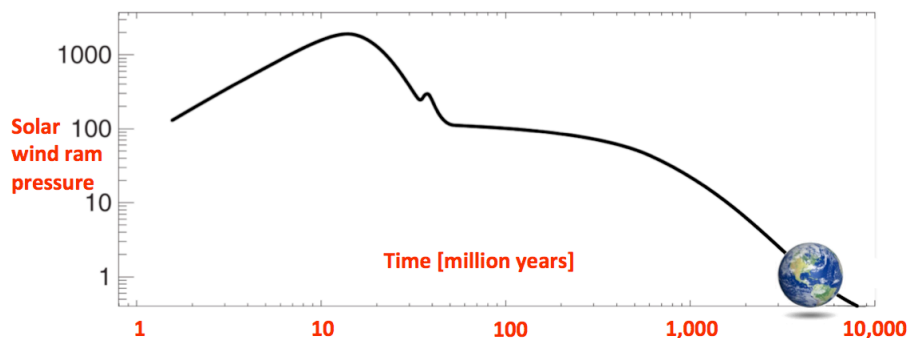


Figure 1.: Ram pressure of the solar wind (scaled to the present-day value) as a function of time (adapted from Holzwarth & Jardine 2007).

a high level of activity for much longer, posing a greater threat to any planets that might form around it (Khodachenko et al. 2007).

1.3 The expanding waistlines of exoplanetary magnetospheres

We can investigate the impact of stellar activity on planets by using some simple but transparent stellar wind models. See et al (2014, submitted) have recently used both a thermal model (Parker 1958) and one due to Cranmer & Saar that is rather more sophisticated, but which can still be run on a laptop, without the need of high-performance computing (Cranmer & Saar 2011). They determined, for an Earth-like planet placed in the habitable zone of a star, what the size of the planet’s magnetosphere would be. Using the scaling between chromospheric activity and age, they demonstrated the expansion of planetary magnetospheres with age. They found that most solar-like stars have magnetospheres whose sizes lie within the historical range expected for the Earth. This is in contrast to what is expected for M dwarfs, and suggests that for these low mass stars, planets simply have to wait a long time before the star has spun down sufficiently to allow the planet to maintain an Earth-sized magnetosphere (Vidotto et al. 2013, 2014).

1.4 Testing our assumptions about stellar dynamos

We are now in a position to test some of the assumptions that went into the Skumanich model. Using average values of the large-scale magnetic field determined from Zeeman Doppler imaging, Vidotto et al. (2014) have demonstrated that these observed magnetic fields follow a linear dynamo law. Interestingly, the technique of Zeeman broadening, which is sensitive to both the large and small scale fields, shows the same scaling. This may suggest that both the large and small scales of stellar magnetic fields share the same dynamo mechanism. A plot of the observed X-ray luminosity of these stars as a function of Rossby number and average field strength (see Fig. 2), shows a tight correlation at low luminosities and a broad plateau at high luminosities. The X-ray luminosity scales nearly linearly with the magnetic flux, as found by Pevtsov et al. (2003) from Zeeman broadening measurements.

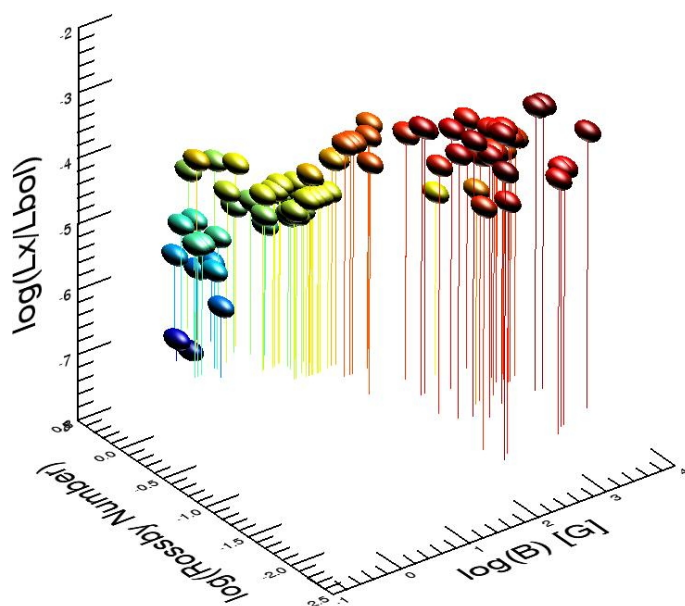


Figure 2.: X-ray luminosity as a function of Rossby number and the average value of the large-scale magnetic field (based on Vidotto et al, 2014).

1.5 Taking the shorter view of activity timescales

On shorter timescales still, magnetic activity can vary because of the stellar cycle. One very well studied example is Tau Boo for which a full magnetic reversal has been observed (Donati et al. 2008; Fares et al. 2009). An MHD wind model based on the observed magnetic field shows that the mass loss rate and X-ray flux vary little through the cycle, but the angular momentum loss rate varies by a factor of two (Vidotto et al. 2012). In the case of Tau Boo, the orbiting planet is tidally locked, such that its orbital period is the same as the stellar rotation period, and hence the planet always orbits over the same longitude of the star. In contrast, the orbiting planet in the HD 189733 system has an orbital period that is faster than the stellar rotation period, and hence the planet moves through different parts of the stellar wind and corona as it orbits. As a result, the bowshock formed when the stellar wind impacts on the exoplanetary magnetosphere is expected to vary both in geometry and strength throughout the planetary orbit (Llama et al. 2013). As shown by Llama et al, this may lead to a UV transit whose depth and shape and can change from one observation to the next (Ben-Jaffel & Ballester 2013; Bourrier et al. 2013; Bourrier & Lecavelier des Etangs 2013).

1.6 Flares and coronal mass ejections

Rapid changes in stellar magnetic activity are seen through X-ray and white light flares, and hence also possibly (although much more difficult to observe) coronal mass ejections. The timescale for these processes is influenced by the surface drivers, i.e. the processes that transport magnetic flux. These include diffusion, meridional flow, and differential rotation. In the case of the Sun, the most rapid timescale is the differential rotation. We now know that differential rotation varies with stellar mass, such that low mass stars, which have deep convective

zones, rotate almost as solid bodies. Stars more massive than the Sun, which have shallower convective zones, show a higher differential rotation (Reiners 2006). In order to explore how this variation in differential rotation might influence the timescales for coronal activity, we have performed a simple experiment (Gibb et al. 2014, in press). We consider a single bipole evolving in response to surface transport processes. Using a magnetofictional approach, we determine the time taken to form a flux rope, and thereafter, the time for that flux rope to be ejected. We find that the formation time scales as the geometric mean of the timescales for diffusion and differential rotation, such that

$$\tau_{form} \simeq \sqrt{\tau_{Diffrot}\tau_{Diffusion}}.$$

This reflects the two processes that dominate this phase of evolution. The lifetime on the other hand, scales simply as the timescale for differential rotation, such that

$$\tau_{life} \simeq \tau_{Diffrot}.$$

This suggests that stars more massive than the Sun, whose differential rotation is more rapid than the solar value, might have rapidly-evolving coronae. This raises the interesting question: on these stars is there is time for prominences to form, and hence for coronal mass ejections to enhance the winds of the stars in the same way as we see on the Sun?

1.7 The hidden face of stellar activity

While these coronal mass ejections may be very important from the point of view of habitability of exoplanets, and the erosion of exoplanetary atmospheres, they are extremely difficult to observe. We do not, for example, know if all stars share the same relationship between the energy in coronal mass ejections and the energy in flares that we see on the Sun. Aarnio et al. (2012, 2013) use the solar scaling to estimate the angular momentum that might be carried away in these mass ejections on young stars. They suggest that this process may have a significant contribution after about 1 million years. In a related piece of work, Drake et al. (2013) use the solar scaling to estimate the energy carried away in coronal mass ejections in very active stars. They show that such a scaling would predict an unfeasibly large energy content, and hence suggest that the solar scaling breaks down for very active stars. Certainly, estimates of mass loss rates from a range of stars, using the enhanced absorption in the hydrogen wall of stellar astrospheres, suggests that the most X-ray bright stars do not have correspondingly powerful winds (Wood et al. 2002).

It seems that for some time yet, the question of the many timescales for standard activity will continue to challenge us.

Acknowledgements. Our thanks go to the organisers of Cool Stars 18 for a great meeting.

References

- Aarnio, A. N., Matt, S. P., & Stassun, K. G. 2012, *ApJ*, 760, 9
 Aarnio, A. N., Matt, S. P., & Stassun, K. G. 2013, *Astronomische Nachrichten*, 334, 77

- Acuña, M. H., Connerney, J. E. P., Wasilewski, P., et al. 2001, *JGR*, 106, 23403
- Ben-Jaffel, L., & Ballester, G. E. 2013, *A&A*, 553, A52
- Bourrier, V., Lecavelier des Etangs, A., Dupuy, H., et al. 2013, *A&A*, 551, A63
- Bourrier, V., & Lecavelier des Etangs, A. 2013, *A&A*, 557, A124
- Cranmer, S. R., & Saar, S. H. 2011, *ApJ*, 741, 54
- Donati, J.-F., Moutou, C., Farès, R., et al. 2008, *MNRAS*, 385, 1179
- Drake, J. J., Cohen, O., Yashiro, S., & Gopalswamy, N. 2013, *ApJ*, 764, 170
- Fares, R., Donati, J.-F., Moutou, C., et al. 2009, *MNRAS*, 398, 1383
- Irwin, J., Berta, Z. K., Burke, C. J., et al. 2011, *ApJ*, 727, 56
- Khodachenko, M. L., Ribas, I., Lammer, H., et al. 2007, *Astrobiology*, 7, 167
- Kulikov, Y. N., Lammer, H., Lichtenegger, H. I. M., et al. 2007, *Space Sci.Rev.*, 129, 207
- Llama, J., Vidotto, A. A., Jardine, M., et al. 2013, *MNRAS*, 436, 2179
- Parker, E. N. 1958, *Physical Review*, 109, 1874
- Pevtsov, A. A., Fisher, G. H., Acton, L. W., et al. 2003, *ApJ*, 598, 1387
- Reiners, A. 2006, *A&A*, 446, 267
- Skumanich, A. 1972, *ApJ*, 171, 565
- Tarduno, J. A., Cottrell, R. D., Watkeys, M. K., et al. 2010, *Science*, 327, 1238
- Vidotto, A. A., Fares, R., Jardine, M., et al. 2012, *MNRAS*, 423, 3285
- Vidotto, A. A., Jardine, M., Morin, J., et al. 2013, *A&A*, 557, A67
- Vidotto, A. A., Jardine, M., Morin, J., et al. 2014, *MNRAS*, 438, 1162
- Vidotto, A. A., Gregory, S. G., Jardine, M., et al. 2014, *MNRAS*, 441, 2361
- Weber, E. J., & Davis, L., Jr. 1967, *ApJ*, 148, 217
- Wood, B. E., Müller, H.-R., Zank, G. P., & Linsky, J. L. 2002, *ApJ*, 574, 412

Chapter 16

The coolest 'stars' are free-floating planets

V. Joergens^{1,2}, M. Bonnefoy³, Y. Liu⁴, A. Bayo¹, S. Wolf⁵

¹*Max-Planck Institut für Astronomie, Königstuhl 17, 69117 Heidelberg, Germany*

²*Institut für Theoretische Astrophysik, Zentrum für Astronomie der Universität Heidelberg, Albert-Ueberle-Str. 2, 69120 Heidelberg, Germany*

³*Institut de Planétologie et d'Astrophysique de Grenoble, UMR 5274, Grenoble, 38041, France*

⁴*Purple Mountain Observatory & Key Laboratory for Radio Astronomy, Chinese Academy of Sciences, Nanjing 210008, China*

⁵*Institut für Theoretische Physik und Astrophysik, Universität Kiel, Leibnizstr. 15, 24118 Kiel, Germany*

Abstract. We show that the coolest known object that is probably formed in a star-like mode is a free-floating planet. We discovered recently that the free-floating planetary mass object OTS 44 (M9.5, ~ 12 Jupiter masses, age ~ 2 Myr) has significant accretion and a substantial disk. This demonstrates that the processes that characterize the canonical star-like mode of formation apply to isolated objects down to a few Jupiter masses. We detected in VLT/SINFONI spectra that OTS 44 has strong, broad, and variable Paschen β emission. This is the first evidence for active accretion of a free-floating planet. The object allows us to study accretion and disk physics at the extreme and can be seen as free-floating analog of accreting planets that orbit stars. Our analysis of OTS 44 shows that the mass-accretion rate decreases continuously from stars of several solar masses down to free-floating planets. We determined, furthermore, the disk mass (10 Earth masses) and further disk properties of OTS 44 through modeling its SED including Herschel far-IR data. We find that objects between 14 and 0.01 solar masses have the

same ratio of the disk-to-central-mass of about 1%. Our results suggest that OTS 44 is formed like a star and that the increasing number of young free-floating planets and ultra-cool T and Y field dwarfs are the low-mass extension of the stellar population.

1. Introduction

We have witnessed in the last decade the detection of free-floating substellar objects with increasingly lower masses and cooler temperatures that reach the canonical planetary regime of a few Jupiter masses and a few hundred Kelvin. Examples are free-floating planetary mass objects in star-forming regions (e.g., Zapatero Osorio et al. 2000) and ultracool Y dwarfs in the field (e.g., Cushing et al. 2011). One of the main open questions in the theory of star formation is: How do these free-floating planetary-like objects - and brown dwarfs in general - form? A high-density phase is necessary for the gravitational fragmentation to create very small Jeans-unstable cores. Proposed scenarios to prevent a substellar core in a dense environment from accreting to stellar mass are ejection of the core through dynamical interactions (e.g., Reipurth & Clarke 2001) or photo-evaporation of the gas envelope through radiation of a nearby hot star (e.g., Whitworth & Zinnecker 2004). Also suggested was the formation of brown dwarfs by disk instabilities in the outer regions of massive circumstellar disks (e.g., Stamatellos & Whitworth 2009). Alternatively, brown dwarfs could form in a more isolated mode by direct collapse. For example, filament collapse (e.g., Inutsuka & Miyama 1992) might form low-mass cores that experience high self-erosion in outflows and become brown dwarfs (Machida et al. 2009). A key to understanding star and brown dwarf formation is to observationally define the minimum mass that the canonical star-like mode of formation can produce by detecting and exploring the main features characteristic of this process, such as disks, accretion, outflows, and orbiting planets, for the lowest-mass objects.

The first indications for the existence of free-floating planetary mass objects came from observations in the very young σ Orionis cluster (Zapatero Osorio et al. 2000). While it is difficult to establish the membership to σ Ori and, therefore, the age and mass, some very promising candidates were detected. An example is S Ori 60, for which mid-IR excess indicates a young age (Luhman et al. 2008a). Other candidates, however, turned out not to be members of the cluster, such as S Ori 70 (Burgasser et al. 2004; Peña Ramirez, this volume). The coolest known free-floating objects are Y dwarfs, of which 17 are spectroscopically confirmed to date (Cushing et al. 2014). While we can expect many planetary mass objects among Y dwarfs, the age and mass of these nearby field objects are in most cases unknown. The first confirmed Y dwarf, WISE 1828+2650 (Cushing et al. 2011), was suggested to have a temperature and mass of only about 300 K and 3-6 M_{Jup} , respectively, although there are indications that the temperature might be significantly larger (Dupuy & Kraus 2013). Very recently a remarkably cold and low-mass object was detected in the very near vicinity of our Sun: WISE 0855-0714 at a distance of 2.2 pc has a proposed temperature and mass of 250 K and 3-10 M_{Jup} , respectively (Luhman 2014). Nearby objects that do allow constraints on their age and, therefore, mass are members of young moving groups (see also Faherty, this volume). One of them, PSO J318.5-22, was recently detected to be

a planetary-mass member of β Pic. Depending on the assumed age for β Pic its mass is estimated to $6.5 M_{\text{Jup}}$ (age: 12 Myr) and $8.4 M_{\text{Jup}}$ (21 Myr), respectively (Liu et al. 2013; Allers, this volume).

To address the question how free-floating planets form, we observed OTS 44, the lowest mass known member of the Chamaeleon I star-forming region (Cha I, ~ 2 Myr, 160 pc). OTS 44 was first identified as a brown dwarf candidate in a deep near-IR imaging survey (Oasa et al. 1999) and later confirmed as very low-mass substellar object of spectral-type M9.5 based on low-resolution near-IR and optical spectra (e.g. Luhman et al. 2004). Its mass was estimated using near-IR spectra to lie in or very close to the planetary regime (~ 6 - $17 M_{\text{Jup}}$, Bonnefoy et al. 2013) with an average rounded value of $12 M_{\text{Jup}}$.

2. OTS 44 - a 12 Jupiter mass object with a substantial disk

Mid-IR photometry of OTS 44 by Spitzer/IRAC and MIPS (Luhman et al. 2008b) indicated the presence of circumstellar material surrounding OTS 44. Recently, the disk of OTS 44 was detected at far-IR wavelength by Herschel/PACS (Harvey et al. 2012). We re-analyzed the Herschel flux measurement (Joergens et al. 2014) and find a slightly smaller value for OTS 44 than Harvey et al. (2012).

We modeled the SED of OTS 44 based on flux measurements from the optical to the far-IR using the radiative transfer code MC3D (Wolf 2003). We employ a passive-disk model consisting of a central substellar source surrounded by a parameterized flared disk in which dust and gas are well mixed and homogeneous throughout the system. We assume dust grains of astronomical silicate (62.5%) and graphite (37.5%) with minimum and maximum grain sizes of $0.005 \mu\text{m}$ and $0.25 \mu\text{m}$, respectively. As there are model degeneracies between different disk parameters, we conducted a Bayesian analysis to estimate the validity range for each parameter. See Joergens et al. (2013) for details. Fig. 1 shows the SED and the best-fit disk model of OTS 44 based on the re-analysis of the Herschel fluxes (Joergens et al. 2014). We find that OTS 44 has a highly flared disk ($\beta > 1.3$) with a disk mass of $3.25 \times 10^{-5} M_{\odot}$, i.e. about $10 M_{\text{Earth}}$.

3. OTS 44 - a 12 Jupiter mass object with significant accretion

We took near-IR J-band spectra (1.1 - $1.4 \mu\text{m}$) of OTS 44 with SINFONI at the VLT at a medium spectral resolution ($R = \lambda/\Delta\lambda \sim 2000$, Bonnefoy et al. 2013). We discovered a strong, broad, and variable Paschen β ($\text{Pa}\beta$) emission line of OTS 44 in these spectra (Joergens et al. 2013), as shown in Fig. 2 (left, middle). Furthermore, a prominent $\text{H}\alpha$ emission line is visible in the optical spectrum of Luhman (2007) as shown in the right panel of Fig. 2. Both of these Hydrogen emission lines exhibit a broad profile with velocities of $\pm 200 \text{ km s}^{-1}$ or more. We determined the equivalent width (EW) of both lines. The $\text{H}\alpha$ line has a symmetrically shaped profile with an EW of -141 \AA , demonstrating that OTS 44 is actively accreting. The profile of the $\text{Pa}\beta$ line is significantly variable between the two observing epochs separated by a few days (EW of -7 and -4 \AA).

We determined the mass accretion rate of OTS 44 based on the $\text{H}\alpha$ line by assuming that the $\text{H}\alpha$ emission is entirely formed by accretion processes. We derived an $\text{H}\alpha$ line luminosity $\log L_{\text{H}\alpha}$ (L_{\odot}) of -6.16 for OTS 44 and applied the

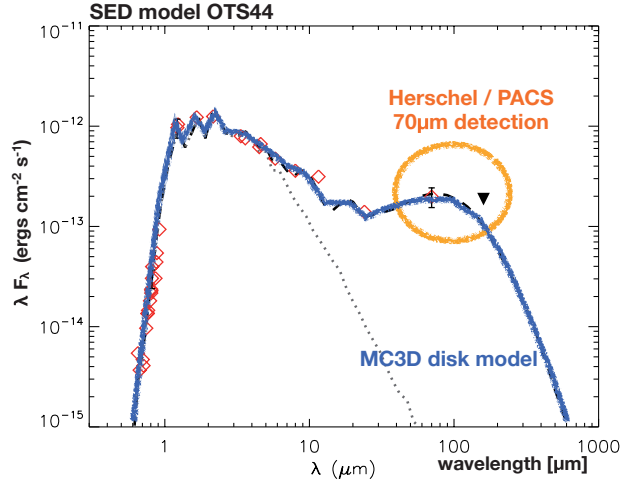


Figure 1.: SED of OTS 44. Shown are photometric measurements (red diamonds) an upper limit for the $160\ \mu\text{m}$ flux (black triangle), the best-fit SED model (blue thick line), and the input BT-Settl photosphere model (gray dotted line). This is a slightly revised version of the SED model of OTS 44 in Joergens et al. (2013) using a revised Herschel flux measurement (Joergens et al. 2014).

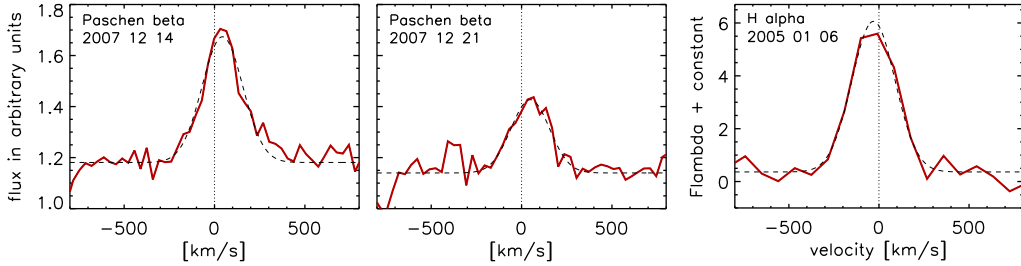


Figure 2.: $\text{Pa}\beta$ emission of OTS 44 in VLT/SINFONI spectra (left, middle) and $\text{H}\alpha$ emission of OTS 44 in a MAGELLANI/IMACS spectrum (right). The dashed lines are Gaussian fits to the profiles. From Joergens et al. (2013).

empirical relation between the $\text{H}\alpha$ line and accretion luminosity of Fang et al. (2009), which is based on $\log L_{\text{H}\alpha}$ (L_{\odot}) ranging between -1 and -6. We estimate an mass accretion rate of OTS 44 of $7.6 \times 10^{-12} M_{\odot} \text{yr}^{-1}$.

4. Conclusions

We have discovered strong, broad, and variable $\text{Pa}\beta$ emission of the young very low-mass substellar object OTS 44 (M9.5) in VLT/SINFONI spectra, which is evidence for active accretion of a planetary mass object (Joergens et al. 2013). We determined the properties of the disk that surrounds OTS 44 through MC3D radiative transfer modeling of flux measurements from the optical to the far-IR including Herschel data (Joergens et al. 2013, 2014). We found that OTS 44 has a highly flared disk ($\beta > 1.3$) with a mass of $3.25 \times 10^{-5} M_{\odot}$, i.e. about $10 M_{\text{Earth}}$. We also investigated the $\text{H}\alpha$ line of OTS 44 in a MAGELLANI/IMACS spectrum

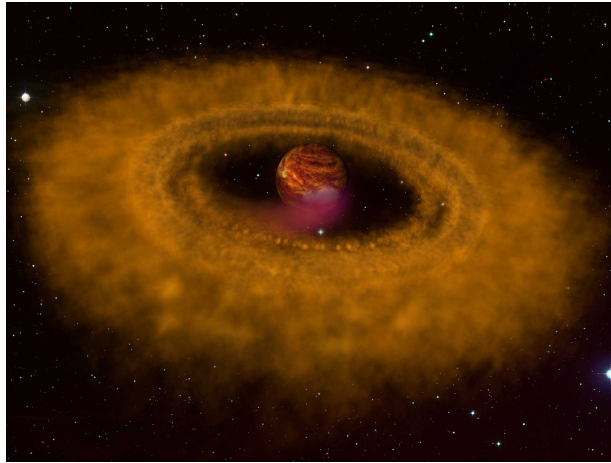


Figure 3.: Artist’s view of the accreting and disk-bearing free-floating planetary mass object OTS 44. Credit: MPIA / A. M. Quetz.

spectrum and found strong $H\alpha$ emission with an EW of -141 \AA indicative of active accretion. Both the $\text{Pa}\beta$ and $H\alpha$ emission lines of OTS 44 have broad

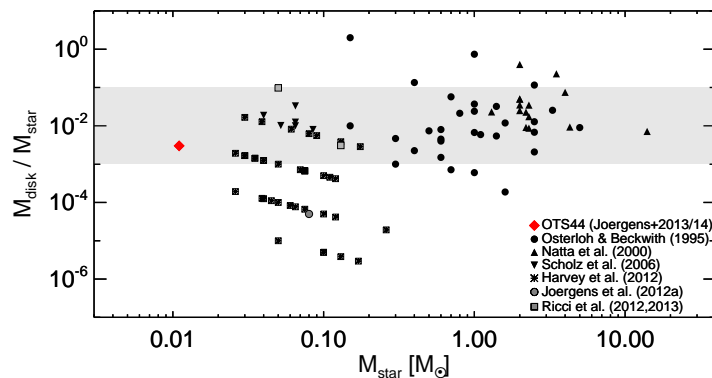


Figure 4.: Relative disk mass versus central mass of stars and brown dwarfs including OTS 44 (red diamond). Slightly revised version of similar plot from Joergens et al. (2013).

profiles with the wings extending to velocities of about $\pm 200 \text{ km s}^{-1}$. The $\text{Pa}\beta$ emission is significantly variable on timescales of a few days, indicating variability in accretion-related processes of OTS 44. We estimated the mass accretion rate of OTS 44 to $7.6 \times 10^{-12} \text{ yr}^{-1}$ by using the $H\alpha$ line. A mass accretion rate based on the $\text{Pa}\beta$ line gives a significantly higher value, and we speculate that part of the $\text{Pa}\beta$ emission might come from other processes related to accretion, such as outflows. Furthermore, in the course of studying OTS 44, we fitted a photospheric BT-Settl model to its optical and near-IR SED and derived a lower effective temperature and higher extinction than was previously found (Luhman 2007).

We have presented the first detection of $\text{Pa}\beta$ emission for a free-floating object below the deuterium-burning limit. Our analysis of $\text{Pa}\beta$ and $H\alpha$ emission of OTS 44 demonstrates that free-floating objects of a few Jupiter masses can be

active accretors. OTS 44 can be seen as free-floating analog of recently detected accreting planetary mass companions that orbit stars (e.g., Bowler et al. 2011, Zhou et al. 2014) and it plays a key role in the study of disk evolution and accretion physics in an extremely low-gravity and -temperature environment. Furthermore, OTS 44 (M9.5) is the lowest-mass object to date for which the disk mass is determined based on far-IR data. Also interesting in this context is the mm-detection of an M9 dwarf (Scholz et al. 2006). Our detections therefore extend the exploration of disks and accretion during the T Tauri phase down to the planetary mass regime. Plotting the relative disk masses of stars and brown dwarfs including OTS 44 (Fig. 4) shows that the ratio of the disk-to-central-mass of about 10^{-2} found for objects between $0.03 M_{\odot}$ and $14 M_{\odot}$ is also valid for OTS 44 at a mass of about $0.01 M_{\odot}$. Furthermore, the mass accretion rate of OTS 44 is consistent with a decreasing trend from stars of several solar masses to substellar objects down to $0.01 M_{\odot}$ (Fig. 5). It is also obvious from this figure that OTS 44 has a relatively high mass accretion rate considering its small mass. These observations show that the processes that accompany canonical star formation, disks and accretion, are present down to a central mass of a few Jupiter masses. This suggests that OTS 44 is formed like a star and that the increasing number of young free-floating planets and ultra-cool T and Y field dwarfs are the low-mass extension of the stellar population.

Figure 6 illustrates how a very young free-floating planetary mass object of about 10 Jupiter masses, such as OTS 44, cools down while aging and becomes an L dwarf at about 10 Myr, similar to PSO J318.5-22, and a Y dwarf at ≥ 1 Gyr, similar to WISE 0855-0714. This illustration uses a plot of the evolution of the effective temperature by Burrows et al. (2001). While this might not be the most sophisticated evolutionary model to date and discrepancies with observations can be seen in the temperature (see caption of Fig. 6), it nevertheless shows very nicely the general picture of a substellar object shifting through spectral classes during its evolution.

Acknowledgements. We thank K. Luhman for providing the optical spectrum of OTS 44 and the ESO staff at Paranal for executing the SINFONI observations in service mode.

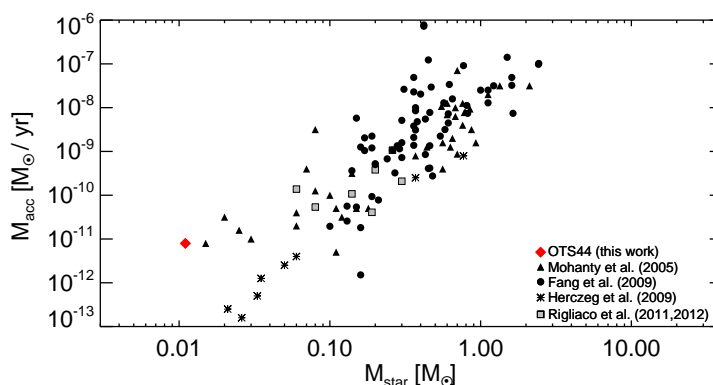


Figure 5.: Mass accretion rate versus central mass of stars and brown dwarfs including OTS 44 (red diamond). From Joergens et al. (2013).

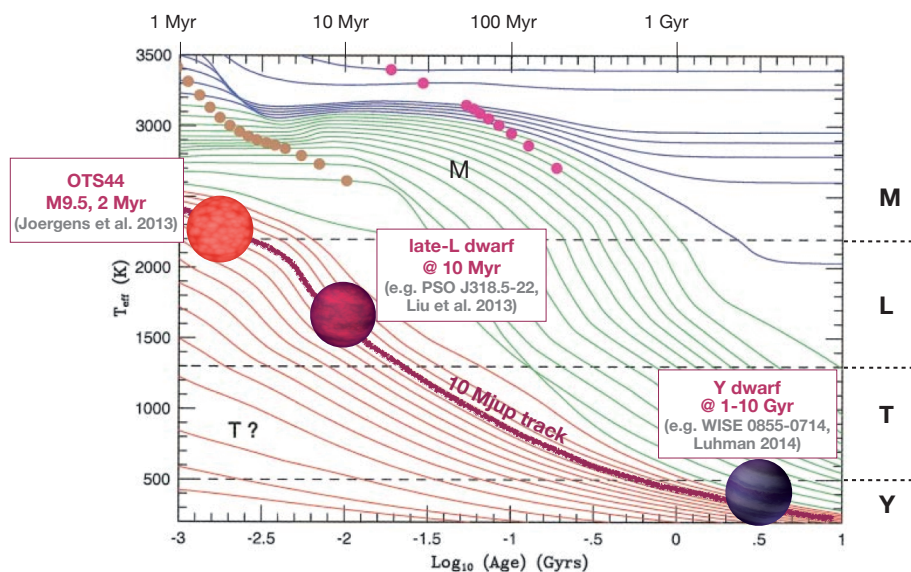


Figure 6.: OTS 44 will become a Y dwarf in 10^9 years. For this illustration of the evolution of the effective temperature of a very low-mass substellar object we used a plot of Burrows et al. (2001). Note that the model temperatures are hotter than the observationally determined temperatures, which are 1700 K for OTS 44, 1200 K for PSO J318.5-22, and 250 K for WISE 0855-0714.

References

- Allard, F., Homeier, D., Freytag, B., & Sharp, C. M. 2012, in EAS Publications Series, Vol. 57, ed. C. Reyle, C. Charbonnel, & M. Schultheis, 343
- Bonnefoy, M., Boccaletti, A., Lagrange, A.-M., et al. 2013, *A&A*, 555, A107
- Bowler, B. P., Liu, M. C., Kraus, A. L., Mann, A. W., & Ireland, M. J. 2011, *ApJ*, 743, 148
- Burgasser, A. J., Kirkpatrick, J. D., McGovern, M. R., et al. 2004, *ApJ*, 604, 827
- Burrows, A., Hubbard, W. B., Lunine, J. I., & Liebert, J. 2001, *Reviews of Modern Physics*, 73, 719
- Cushing, M. C., Kirkpatrick, J. D., Gelino, C. R., et al. 2011, *ApJ*, 743, 50
- Cushing, M. C., Kirkpatrick, J. D., Gelino, C. R., et al. 2014, *AJ*, 147, 113
- Delorme, P., Gagné, J., Malo, L., et al. 2012, *A&A*, 548, A26
- Dupuy, T. J., & Kraus, A. L. 2013, *Science*, 341, 1492
- Faherty, J. K., Rice, E. L., Cruz, K. L., Mamajek, E. E., & Núñez, A. 2013, *AJ*, 145, 2
- Fang, M., van Boekel, R., Wang, W., et al. 2009, *A&A*, 504, 461
- Harvey, P. M., Henning, T., Liu, Y., et al. 2012, *ApJ*, 755, 67

- Herczeg, G. J., Cruz, K. L., & Hillenbrand, L. A. 2009, *ApJ*, 696, 1589
- Joergens, V., Bonnefoy, M., Liu, Y., et al. 2013, *A&A*, 558, L7
- Joergens, V., Liu, Y., Bayo, A. et al. 2014, in prep.
- Liu, M. C., Magnier, E. A., Deacon, N. R., et al. 2013, *ApJ*, 777, L20
- Luhman, K. L., Peterson, D. E., & Megeath, S. T. 2004, *ApJ*, 617, 565
- Luhman, K. L., Adame, L., D'Alessio, P., et al. 2005, *ApJ*, 635, L93
- Luhman, K. L., D'Alessio, P., Calvet, N., et al. 2005, *ApJ*, 620, L51
- Luhman, K. L. 2007, *ApJS*, 173, 104
- Luhman, K. L., Hernández, J., Downes, J. J., Hartmann, L., & Briceño, C. 2008a, *ApJ*, 688, 362
- Luhman, K. L., Allen, L. E., Allen, P. R., et al. 2008b, *ApJ*, 675, 1375
- Luhman, K. L. 2014, *ApJ*, 786, L18
- Mohanty, S., Jayawardhana, R., & Basri, G. 2005, *ApJ*, 626, 498
- Natta, A., Grinin, V., & Mannings, V. 2000, *Protostars and Planets IV*, 559
- Oasa, Y., Tamura, M., & Sugitani, K. 1999, *ApJ*, 526, 336
- Osterloh, M., & Beckwith, S. V. W. 1995, *ApJ*, 439, 288
- Reipurth, B., & Clarke, C. 2001, *AJ*, 122, 432
- Ricci, L., Testi, L., Natta, A., Scholz, A., & de Gregorio-Monsalvo, I. 2012, *ApJ*, 761, L20
- Ricci, L., Isella, A., Carpenter, J. M., & Testi, L. 2013, *ApJ*, 764, L27
- Rigliaco, E., Natta, A., Randich, S., et al. 2011, *A&A*, 526, L6
- Rigliaco, E., Natta, A., Testi, L., et al. 2012, *A&A*, 548, A56
- Scholz, A., Jayawardhana, R., & Wood, K. 2006, *ApJ*, 645, 1498
- Stamatellos, D., & Whitworth, A. P. 2009, *MNRAS*, 392, 413
- Whitworth, A. P., & Zinnecker, H. 2004, *A&A*, 427, 299
- Wolf, S. 2003, *ApJ*, 582, 859
- Zapatero Osorio, M. R., Béjar, V. J. S., Martín, E. L., et al. 2000, *Science*, 290, 103
- Zhou, Y., Herczeg, G. J., Kraus, A. L., Metchev, S., & Cruz, K. L. 2014, *ApJ*, 783, L17

Chapter 17

Dynamical Masses of Pre-Main-Sequence Binary Systems

Rainer Köhler¹, Hector Hiss¹

¹*Max-Planck-Institut für Astronomie, Königstuhl 17, 69117 Heidelberg, Germany*

Abstract. We present results of our ongoing monitoring program for orbital motion of T Tauri binaries. Their companions were discovered in the 1990s. With projected separations of 15 – 42 AU, the expected orbital periods range from 60 to 250 years. We have collected observations using speckle interferometry, adaptive optics, and lucky imaging. About 16 companions have clearly moved since their discovery, about 10 of them show signs of curvature characteristic for orbital motion. For a few binaries, it is already possible to solve for a (very) preliminary orbit solution.

1. Introduction

The mass is probably the most important parameter for the structure and evolution of a star. For a pre-main-sequence (PMS) star, it is usually estimated by the star's location in the Hertzsprung-Russell diagram relative to theoretical model calculations of PMS evolution. Unfortunately, for stars less massive than $\sim 1.5 M_{\odot}$, these estimates vary depending on the calculations used (e.g. Simon 2008; Hillenbrand & White 2004).

Therefore, model-independent mass determinations are crucial for our understanding of stellar astrophysics. If we determine the orbit of a binary star with a known distance, we also get its mass. This is the only way to measure stellar masses directly, without relying on theoretical models. Binary stars are therefore valuable test cases for theoretical pre-main-sequence tracks.

In the 1990s, a number of multiplicity surveys among T Tauri stars have been performed, providing us with a sample of visual binaries with separations of $0.1 - 0.3''$ (Ghez et al. 1993; Leinert et al. 1993; Köhler & Leinert 1998). At distances of 140 pc and projected separations of $15 - 42$ AU, the expected orbital periods range from 60 to 250 years.

We are monitoring a number of close visual binaries in the star-forming region Taurus-Auriga, with the goal to determine their orbits and ultimately their masses.

2. Observations

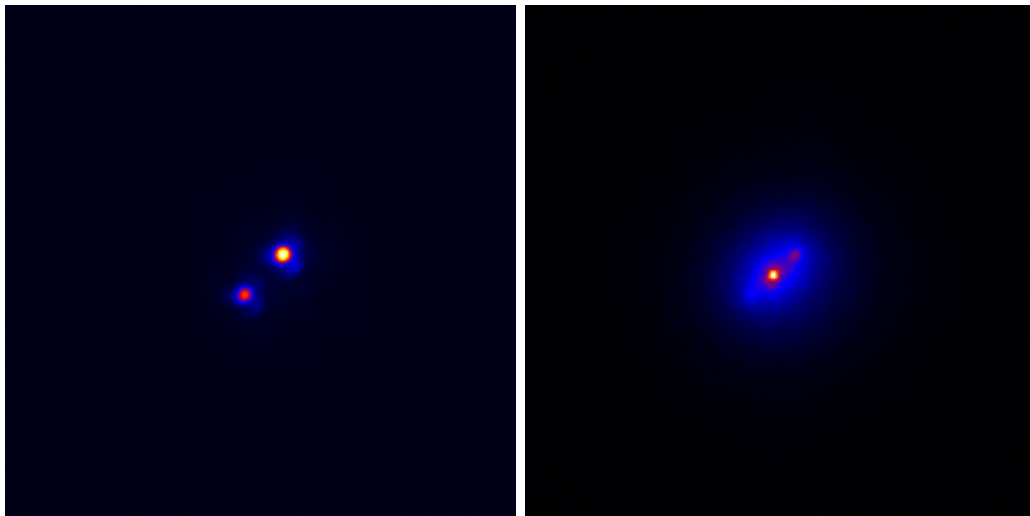


Figure 1.: Images of XZ Tau taken with NACO in the Ks-band in November 2006 (left) and with AstraLux through the SDSS z' filter in October 2013 (right). North is up, and East to the left. The separation of the two stars is about 0.3 arcsec. Note that the field of view of the two images is not the same.

For our monitoring program of close binaries, we used different telescopes and instruments:

- the adaptive optics (AO) system at the 3 m Shane Telescope of Lick observatory on Mount Hamilton, California (Bauman et al. 2002),
- the AO-system NAOS/Conica (NACO) at ESO’s 8 m Very Large Telescope on Paranal, Chile (Lenzen et al. 2003; Rousset et al. 2003),
- the lucky imaging camera AstraLux at the 2.2 m telescope on Calar Alto, Spain (Hormuth et al. 2008).

Figure 1 shows examples of the resulting images.

We paid particular attention to the astrometric calibration of the cameras. During each observing run, a field near the trapezium in the Orion Nebula Cluster was observed. The pixel positions of the cluster stars were compared to the

Table 1.: Period and mass estimates, based on circular orbit models

Name	Period estimate [years]	Mass estimate [M_{\odot}]
BD+26 718B	1200	1.3
FO Tau	170	0.8
FS Tau	3000	21
HD 284135	220	3.3
HK Tau G2	210	0.8
IS Tau	190	1.1
IW Tau	320	1.7
LkH α 332 G1	220	0.8
RX J0430.8+2113	72	59
RX J0444.4+1952	68	14
UZ Tau w	420	0.8
XZ Tau	1060	1.0

coordinates given in Close et al. (2012), which in turn are based on HST-positions of a few cluster stars. We computed the mean pixel scale and orientation of the detector from a global fit of all star positions. The scatter of values derived from star pairs were used to estimate the errors.

3. Results

Many of the close binary T Tauri stars in Taurus-Auriga show changes in their relative positions. However, none of the stars in our monitoring program has moved enough for a full orbit fit. In order to get an estimate for the binary periods, we fit circular orbits to the data. The fitting procedure is the same as described in, e.g., Köhler et al. (2013), except that only orbit models with eccentricity zero were used. The results for the cases where the fit converged are listed in table 1. Most of the mass estimates appear plausible, although our experience with incomplete orbit fits shows that more data can change the result by a factor of 2 or more.

Some of the the estimated masses (FS Tau, RX J0430.8+2113, and RX J0444.4+1952) do not agree with the mass expected for a star of their spectral type. In general, this indicates that more observations are required to determine the orbit.

However, Sebastian Daemgen pointed out during the workshop that this could also be the result of an overestimated distance to the systems. In particular, RX J0444.4+1952 might not be a member of the Taurus-Auriga star-forming region, but a young foreground star. Since the dynamical mass is proportional to the third power of the semi-major axis (which is proportional to the distance of the system), a change in distance by a factor of 2 results in a mass that is off by almost an order of magnitude.

From the spectral type of RX J0444.4+1952, we would expect the system mass to be about $0.86 M_{\odot}$ (Daemgen, priv. comm.). The mass depends only weakly on the age and is nearly the same for an age between 2 and 20 Myr. Our

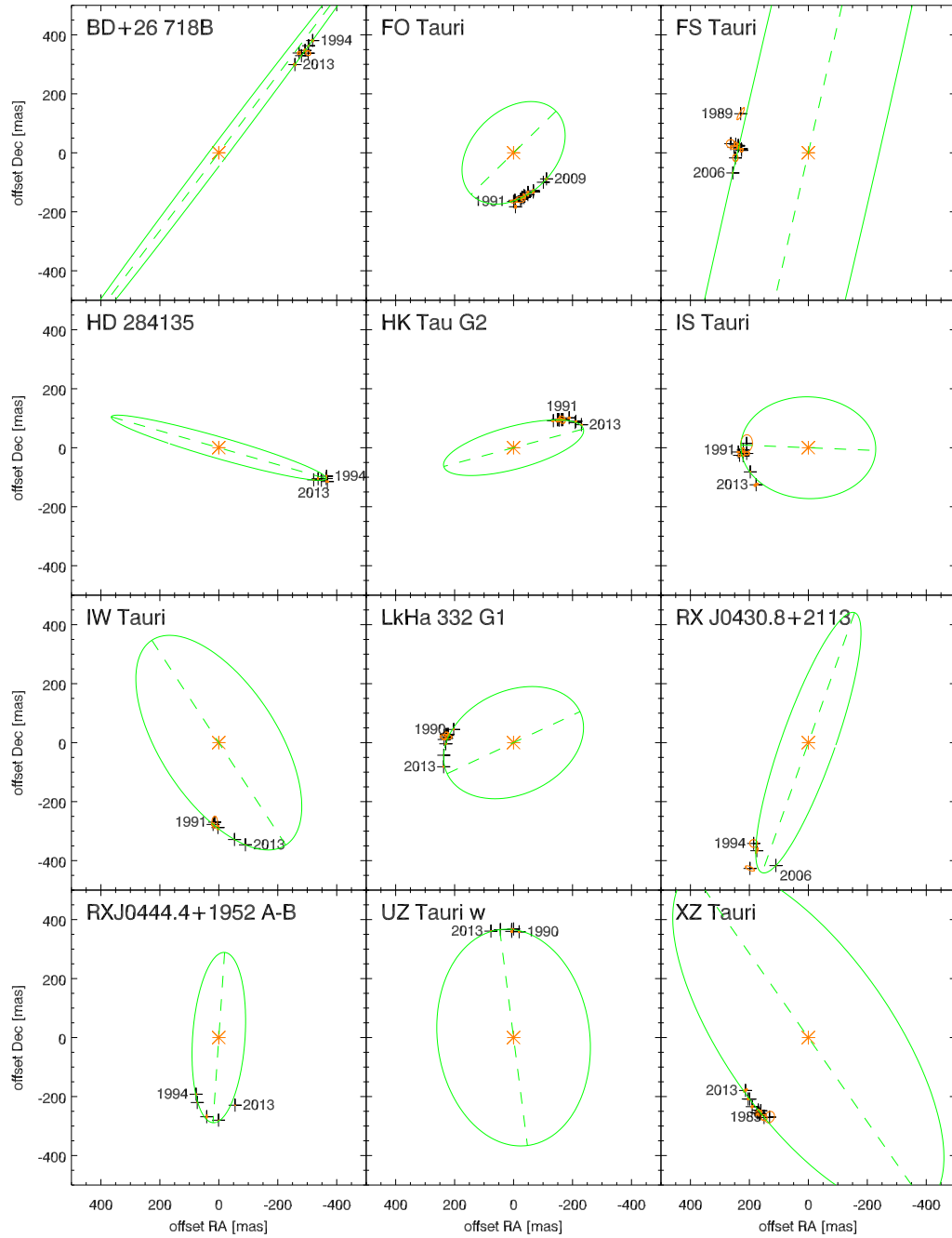


Figure 2.: Orbits of the stars that have moved far enough to solve for a preliminary orbit. The observed positions are marked by their error ellipses. The year of the first and latest observation is given. The green ellipse shows the best-fitting circular orbit. The dashed line marks the line of nodes.

dynamical mass estimate would also be $0.86 M_{\odot}$ if the distance to the binary was only about 55 pc instead of the canonical distance to Taurus-Auriga of 140 pc.

The spectral type of the second star with an implausible large mass, RX J0430.8+2113, is G8 (Wichmann et al. 1996). At this spectral type, the mass depends strongly on the age. It is about $3.5 M_{\odot}$ at 1 Myr, but only about $1.2 M_{\odot}$ at 20 Myr. At a distance of 55 pc, our dynamical mass would be $3.6 M_{\odot}$. However, a star of this mass would be much brighter than observed. The star is either even closer than 55 pc, or our orbit fit is still far from the true orbit (which we consider to be the more likely explanation).

4. Outlook

We will continue to monitor the close young binaries in Taurus-Auriga and other star-forming regions. The next AstraLux observations are scheduled for November 2014. With astrometric measurements collected in a few more years, we expect to be able to carry out full orbit fits for some of our targets. By then, *Gaia* will have provided precise parallaxes, which will resolve the uncertainty of the distance.

Acknowledgements. We thank the staff at Lick, Paranal, and Calar Alto observatory for carrying out the observations.

References

- Bauman, B. J., Gavel, D. T., Waltjen, K. E., et al. 2002, in Proc. SPIE, Vol. 4494, Adaptive Optics Systems and Technology II, ed. R. K. Tyson, D. Bonaccini, & M. C. Roggemann, 19–29
- Close, L. M., Puglisi, A., Males, J. R., et al. 2012, ApJ, 749, 180
- Ghez, A. M., Neugebauer, G., & Matthews, K. 1993, AJ, 106, 2005
- Hillenbrand, L. A. & White, R. J. 2004, ApJ, 604, 741
- Hormuth, F., Hippler, S., Brandner, W., Wagner, K., & Henning, T. 2008, in Proc. SPIE, Vol. 7014, Ground-based and Airborne Instrumentation for Astronomy II, ed. I. S. McLean & M. M. Casali, 48
- Köhler, R. & Leinert, C. 1998, A&A, 331, 977
- Köhler, R., Ratzka, T., Petr-Gotzens, M. G., & Correia, S. 2013, A&A, 558, A80
- Leinert, C., Zinnecker, H., Weitzel, N., et al. 1993, A&A, 278, 129
- Lenzen, R., Hartung, M., Brandner, W., et al. 2003, in Proc. SPIE, Vol. 4841, Instrument Design and Performance for Optical/Infrared Ground-based Telescopes, ed. M. Iye & A. F. M. Moorwood, 944–952
- Rousset, G., Lacombe, F., Puget, P., et al. 2003, in Proc. SPIE, Vol. 4839, Adaptive Optical System Technologies II, ed. P. L. Wizinowich & D. Bonaccini, 140–149
- Simon, M. 2008, in The Power of Optical/IR Interferometry: Recent Scientific Results and 2nd Generation Instrumentation, ed. A. Richichi, F. Delplancke, F. Paresce, & A. Chelli, 227
- Wichmann, R., Krautter, J., Schmitt, J. H. M. M., et al. 1996, A&A, 312, 439

Chapter 18

Star-planet interactions

A. F. Lanza

*INAF-Osservatorio Astrofisico di Catania,
Via S. Sofia, 78 – 95123 Catania, Italy*

Abstract. Stars interact with their planets through gravitation, radiation, and magnetic fields. I shall focus on the interactions between late-type stars with an outer convection zone and close-in planets, i.e., with an orbital semi-major axis smaller than ≈ 0.15 AU. I shall review the roles of tides and magnetic fields considering some key observations and discussing theoretical scenarios for their interpretation with an emphasis on open questions.

1. Introduction

Stars interact with their planets through gravitation, radiation, and magnetic fields. I shall focus on the case of main-sequence late-type stars and close-in planets (orbit semimajor axis $a \lesssim 0.15$ AU) and limit myself to a few examples. Therefore, I apologize for missing important topics in this field some of which have been covered in the contributions by Jardine, Holtzwarth, Grissmeier, Jeffers, and others at this Conference.

The space telescopes CoRoT (Auvergne et al. 2009) and Kepler (Borucki et al. 2010) have opened a new era in the detection of extrasolar planets and the study of their interactions with their host stars because they allow us, among others, to measure stellar rotation in late-type stars through the light modulation induced by photospheric brightness inhomogeneities (e.g., Affer et al. 2012; McQuillan et al. 2014; Lanza et al. 2014). Moreover, the same flux modulation can be used to derive information on the active longitudes where starspots preferentially form and evolve (e.g., Lanza et al. 2009a; Bonomo & Lanza 2012)^a. Combining all the information together, we can study the correlation between

^aDetailed tests of the capability of spot modelling to recover the actual distributions of the active regions have been performed, e.g., for the Sun as a star (Lanza et al. 2007), CoRoT-2, using

stellar rotation, spot activity, and close-in planets as well as investigate the relationships between different stellar and orbital parameters as derived by follow-up observations. A recent result obtained by studying the rotation of Kepler planetary candidates is the paucity of close-in planets around fast-rotating stars. I shall discuss models to account for this intriguing phenomenon in Sect. 2.

Optical spectroscopy allows us to study the emission of stellar chromospheres in lines such as Ca II H&K or H α . Some indication of chromospheric features associated to close-in planets have been reported. Stellar coronae can be monitored through X-ray observations and also in that case there have been reports concerning possible planetary effects. Therefore, I shall consider interactions potentially leading to chromospheric and coronal features in Sect. 3. The high-energy radiation emitted by stellar coronae plays a fundamental role in the evaporation of the atmospheres of close-in planets, but other kinds of interactions can play a role as well (cf. Sect. 4.). The presence of close-in planets may affect the evolution of the stellar angular momentum and this aspect will be briefly discussed in Sect. 5. Finally, circumstantial evidence for photospheric starspot activity related to close-in planets will be introduced in Sect. 6., while some general conclusions will be reported in Sect. 6.

2. Some tidal effects in star-planet systems

A general introduction to tides in stars and planets is provided by, e.g., Zahn (2008), Mathis et al. (2013), Zahn (2013), and Ogilvie (2014). A remarkable observational result that has been connected to the action of tides is the dearth of close-in planets, i.e. with orbital period $P_{\text{orb}} \lesssim 3 - 5$ d, around rapidly rotating stars, i.e. with a rotation period $P_{\text{rot}} \lesssim 3 - 5$ d, among Kepler candidates (see Fig. 1 and McQuillan et al. 2013; Walkowicz & Basri 2013).

Teitler & Königl (2014) proposed an interpretation based on the tidal evolution of the orbits of close-in planets. Their model included the evolution of the rotation of the host stars under the action of tides, stellar wind and internal coupling between the radiative interior and the convection zone. In their model, the tidal interaction between stars and planets is quite strong with a stellar modified tidal quality factor $Q'_* \simeq 10^5 - 10^6$, leading a remarkable fraction of close-in planets to end their evolution by falling into their hosts.

A different explanation was proposed by Lanza & Shkolnik (2014) by considering that most of the Kepler planetary candidates have radii $R_p \lesssim 3 - 4 R_{\oplus}$ and are probably members of multi-planet systems. In such systems secular chaotic interactions generally develop. They can induce large excursions in the orbital eccentricity of the innermost planet, while its semimajor axis stays nearly constant (Laskar 1997, 2008; Wu & Lithwick 2011). When those systems reach a stationary dynamical regime, the distribution function of the eccentricity of the innermost planets $f(e)$ is predicted to follow a Rayleigh distribution, i.e.:

$$f(e) \propto e \exp\left(-\frac{e^2}{2\sigma^2}\right), \quad (18.1)$$

starspot occultations during transits (Silva-Valio & Lanza 2011), and HR 1099, using Doppler imaging (Lanza et al. 2006).

where the standard deviation σ depends on the mass of the planets and their perturbers. In Fig. 2 we plot the observed eccentricity distribution for planets with a projected mass $\geq 0.1 M_J$, i.e., massive enough to allow a sufficiently accurate determination of the eccentricity from their spectroscopic orbits. Only values of $e > 0.07$ have been considered because lower values may be spurious and result from errors or noise in radial velocity measurements. To reduce the effects of tides that circularize the orbits, only planets with a periastron distance between 0.1 and 10 AU have been considered as in Wu & Lithwick (2011). Fig. 2 shows that a Rayleigh distribution function with $\sigma \simeq 0.2$ is not too a bad approximation to the observed eccentricity distribution. Of course, it includes systems with very different ages, i.e., for which secular perturbations have acted for different time intervals, so the stationary theoretical distribution is not expected to match it accurately.

When the periastron distance of the innermost planet becomes small enough ($\lesssim 0.05 - 0.07$ AU), the planet experiences a strong tidal encounter with its host star and its orbit is shrunk and circularized on a timescale of the order of a few tens of Myr thanks to tidal dissipation inside the planet itself. Considering a simple model for the probability of such a tidal encounter, Lanza & Shkolnik (2014) can account for the observed distribution of the orbital periods of the planets in the range $3 \lesssim P_{\text{orb}} \lesssim 15$ d around main-sequence stars of different ages as estimated from gyrochronology (Barnes 2007). In their model, the probability of finding a planet on a close orbit is higher for older stars because there has been more time for the secular chaos to excite a higher eccentricity of the planetary orbit before the tidal encounter. Since older stars are slower rotators owing to magnetic braking, the probability of finding closer planets is higher around slowly rotating stars.

A limitation of both Königl & Teitler's and Lanza & Shkolnik's models is that the predicted frequency of systems on very close orbits ($P_{\text{orb}} \lesssim 1 - 2$ d) is noticeably different from the observed one. This may indicate that both models are missing some important process that shapes the distribution of such systems, e.g., secular perturbations in the case of Königl & Teitler, or a final decay of the orbits due to tides inside the stars for Lanza & Shkolnik.

The two models require rather different tidal dissipation efficiencies inside the host stars. A value of $Q'_* \sim 10^5 - 10^6$ as considered by Teitler & Königl (2014), is expected to produce a detectable orbital period variation ($O - C \sim 5 - 80$ s) in one or two decades in the case of systems with transiting hot Jupiters such as Kepler-17 (Bonomo & Lanza 2012), CoRoT-11 (Lanza et al. 2011a), or WTS-2 (Birkby et al. 2014). Therefore, a long-term timing of a sample of transiting hot Jupiters should constrain the efficiency of tidal dissipation in their host stars, indirectly testing the assumptions of Teitler & Königl's model. It is important to observe a sufficiently large sample of systems to be able to disentangle the tidal orbital evolution from perturbations induced by possible third bodies in the systems themselves.

In addition to the distribution of the orbital eccentricity of planets with periastron distance $\gtrsim 0.1$ AU, another test of secular chaos may be provided by the distribution of the projected obliquity of the planetary orbits that can be measured through the Rossiter-McLaughlin effect. Thanks to the high precision of the HARPS and HARPS-N spectrographs, this has become feasible also for planets orbiting slowly rotating, old stars with orbital periods of several days

(cf. Esposito et al. 2014) for which secular chaos is expected to induce a significant fraction of highly inclined or even retrograde orbits (e.g., Wu & Lithwick 2011). Considering a sufficiently large sample of such systems, in principle the predictions of the secular chaotic model for the orbital evolution can be tested^b.

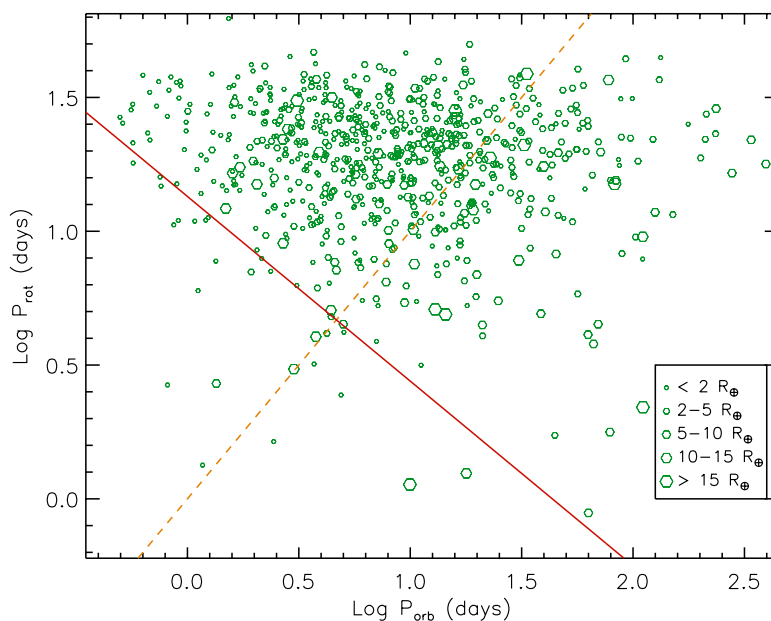


Figure 1.: Rotation period vs. the orbital period of the innermost planet for the sample of candidate transiting planets considered by McQuillan et al. (2013). The size of the green symbols indicates the radius of the planet as specified in the legend. The red solid line indicates the lower boundary of the distribution as determined by McQuillan et al. (2013), while the dashed orange line marks the locus of synchronized stellar rotation ($P_{\text{rot}} = P_{\text{orb}}$).

3. Magnetic interactions in stellar chromospheres and coronae

I shall focus on a few observations and the models proposed for their interpretation. Then I shall briefly consider the star-planet magnetic interactions from a more general perspective with the help of some recent magnetohydrodynamic (MHD) models.

3.1 Some selected observations

Chromospheric hot spots rotating in phase with the orbit of a hot Jupiter rather than with the stellar rotation have been reported by, e.g., Shkolnik et al. (2003, 2005, 2008), and Gurdemir et al. (2012). The power emitted by those spots can

^bThis possibility has been suggested by Dr. K. Poppenhaefer in a comment to my talk.

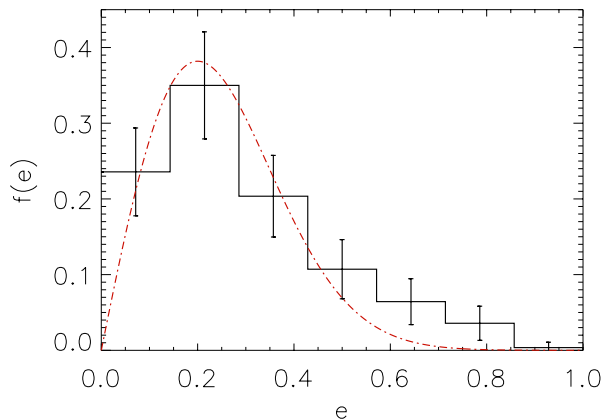


Figure 2.: Distribution of the eccentricity of the planets with mass $> 0.1 M_J$, periastron distance between 0.1 and 10 AU, and $e \geq 0.07$. The histogram is based on the data extracted on July 21 2014 from the Exoplanets Data Explorer (<http://exoplanets.org>). The semiamplitudes of the error bars correspond to twice the square root of the number of planets in each bin. The red dot-dashed line is proportional to a Rayleigh function with $\sigma = 0.2$ (cf. Eq. (18.1) in the present paper and Fig. 6 in Wu & Lithwick 2011).

reach $\sim 10^{20} - 10^{21}$ W, i.e., a few percent of the entire chromospheric flux and they are not stationary phenomena because they are observed only in 30 – 50 percent of the seasons in the case of HD 179949 and v And, the systems with the best evidence to date. The spots are not at the subplanetary longitude, but are shifted up to $\sim 170^\circ$ in the case of v And. Several studies have questioned the reality of the phenomenon, possibly owing to its non-stationary nature (cf. Poppenhaeger et al. 2011; Miller et al. 2012; Scandariato et al. 2013). Nevertheless, the consideration of those hot spots has greatly stimulated the development of theoretical models for the interaction between stellar and planetary magnetic fields (see Sects. 3.2 and 3.3).

Another intriguing observation has been reported by Fossati et al. (2013) who found a very low level of chromospheric emission in WASP-12, WASP-18, and a few other systems with transiting hot Jupiters as observed in the Ca II H&K resonance lines. Not only the Ca II H&K lines, but also the Mg II h&k lines of WASP-12 show no detectable emission in their cores (Haswell et al. 2012). The explanation proposed by Haswell et al. (2012) and Fossati et al. (2013) is that the lack of flux in the cores of the chromospheric resonance lines is due to absorption by circumstellar material probably evaporated from the very close hot Jupiter having $P_{\text{orb}} \sim 1.1$ d in WASP-12. However, the possibility that the star has a very low intrinsic level of chromospheric activity, even lower than the basal level generally observed in stars of the same spectral type without hot Jupiters, cannot be completely excluded in view of the lack of detection of photospheric magnetic fields (Fossati et al. 2010a). Similarly, Pillitteri et al. (2014a) found a very low level of coronal X-ray emission in WASP-18 that is unlikely to be due to

circumstellar absorption and suggests a very low magnetic heating of the outer stellar atmosphere.

The observations of the transit of the hot Jupiter WASP-12 with HST in the near ultraviolet ($\approx 254 - 280$ nm) show an earlier ingress and a deeper transit than in the optical passband, suggesting absorption by some unevenly distributed circumplanetary gas, with a density enhancement preceding the planet along its orbit (Fossati et al. 2010b).

Observations of HD 189733, a K-type main-sequence star with a transiting hot Jupiter on a $P_{\text{orb}} \sim 2.2$ d orbit, have detected coronal flares occurring immediately after the egress of the planet from the stellar occultation, i.e. in the phase range $0.55 - 0.65$, in three different seasons (Pillitteri et al. 2011, 2014b). Although the statistics is still limited, such observations suggest a possible connection between the frequency of stellar flares and the orbital phase of the planet, something possibly reminiscent of the chromospheric hot spot phenomenon, although much more transient in nature (cf. Shkolnik et al. 2008, in particular their Sect. 3.2).

In view of the above observations, the main questions to be addressed by theoretical models can be summarized as follows:

- a) what is the physical process responsible for the energy dissipated in the chromospheric hot spots ?
- b) why are they shifted with respect to the subplanetary longitude ?
- c) what is producing the low level of chromospheric emission in some stars with transiting hot Jupiters ?
- d) What is producing the asymmetric transit profile in the UV in the case of WASP-12 ?
- e) Is there any mechanism to account for preferential orbital phases for flaring activity as suggested by the observations of HD 189733 ?

3.2 Analytic models of chromospheric and coronal interactions

The first, seminal work on the possibility of star-planet interaction was that of Cuntz et al. (2000). Since that time, more detailed investigations have been performed, also pointing out similarities and differences with the Sun-planet interactions. In the Solar system, planets are located in a region where the velocity of the solar wind v_w is greater than the local Alfvén velocity $v_A = B/\sqrt{\mu\rho}$, where B is the magnetic field in the interplanetary space, μ the permeability of the plasma, and ρ its density. In this regime, a bow shock forms at the magnetospheric boundary in the case of a planet having an intrinsic magnetic field, as for the Earth. On the other hand, most close-in planets are probably located in a region where the velocity of the stellar wind is smaller than the local Alfvén velocity (Preusse et al. 2005), leading to a rather different regime.

The first models proposed to account for chromospheric hot spots were based on the analogy with the Jupiter-Io system. Io orbits inside the magnetosphere of Jupiter and is a continuous source of Alfvén waves that propagate inward and reach Jupiter’s atmosphere where they dissipate energy producing a hot spot that rotates in phase with the orbital motion of the satellite. Io is very likely

not possessing an intrinsic magnetic field, but it has an electrically conducting body. In this regime, the excitation and propagation of Alfvén waves along the magnetic field lines of Jupiter’s magnetosphere is described by the so-called unipolar inductor model (for a review see Saur et al. 2013).

The same model has been applied to account for the stellar chromospheric hot spots and is capable of explaining the large phase lag between a planet and the associated hot spot thanks to the travel time needed for the waves to propagate from the planet to the star (Preusse et al. 2006; Kopp et al. 2011). The location of the planet inside the sub-Alfvénic wind region is a fundamental requisite for this model because in the super-Alfvénic domain any Alfvén wave excited close to the planet is blown away by the wind moving faster than its phase velocity and cannot propagate down to the star. Saur et al. (2013) find that about 30 percent of hot Jupiters can excite Alfvén waves that may reach their host stars with an available power up to $10^{18} - 10^{19}$ W. Those estimates are based on the typically measured stellar fields as derived from spectropolarimetry (e.g. Moutou et al. 2007; Fares et al. 2012; Vidotto et al. 2014b) and adopted planetary fields of the order of that of Jupiter ($\approx 10 - 20$ G), and are insufficient by 2 – 3 orders of magnitude to account for the emission of the hot spots as observed in, e.g., HD 179949.

A different approach has been introduced by Lanza (2008, 2009, 2012, 2013). It assumes that in the domain from the outer stellar atmosphere up to the distance of the planet: a) gravity and plasma pressure are negligible in comparison to the Lorentz force; and b) the velocities of the plasma and of the planet are much smaller than the Alfvén velocity. Therefore, the system can be assumed to be in a stationary, magnetohydrostatic equilibrium. In this regime, the equilibrium is everywhere characterized by the force-free condition, i.e., the Lorentz force $\mathcal{L} = \mathbf{J} \times \mathbf{B} = 0$, where $\mathbf{J} = \mu^{-1}(\nabla \times \mathbf{B})$ is the current density. In other words, $(\nabla \times \mathbf{B}) \times \mathbf{B} = 0$. This means that the curl of the field is everywhere parallel to the field itself and we can write $\nabla \times \mathbf{B} = \alpha \mathbf{B}$, where α is a scalar that is constant along each field line as immediately follows by taking the divergence of both sides of the previous equation and considering that \mathbf{B} is solenoidal: $\mathbf{B} \cdot \nabla \alpha = 0$.

In general, two different magnetic topologies are possible, if the planet has an intrinsic magnetic field (cf. Fig. 3). When the boundary conditions at the base of the stellar corona are such that $\alpha \neq 0$ along the field lines that reach the planet, the coronal field and the planetary field are topologically separated because the planetary field is potential, so that $\alpha = 0$ along its field lines (cf. Fig. 3, left panel). In other words, if there were a field line interconnecting the star and the planet, α would be constant along it, but this is not possible given that $\alpha \neq 0$ on the star, while $\alpha = 0$ on the surface of the planet because currents are not allowed to propagate through its mostly neutral atmosphere. Therefore, the stellar and the planetary fields are allowed to interact only at the boundary of the planetary magnetosphere where magnetic reconnection takes place if the field lines have different directions.

The radius of the planetary magnetosphere R_m is determined by magnetic pressure equilibrium between the stellar and planetary fields because the ram pressure of the stellar wind is assumed to be negligible (Lanza 2009). In this regime, the power dissipated by the reconnection process is:

$$P_d \simeq \gamma \frac{\pi}{\mu} \left[B_* \left(a, \frac{\pi}{2} \right) \right]^2 R_m^2 v_{\text{rel}}, \quad (18.2)$$

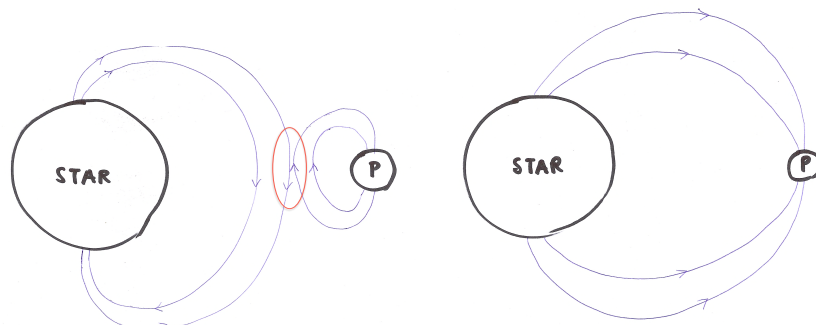


Figure 3.: Left: Magnetic topology consisting of two separated flux line systems for the stellar coronal field and the planetary field. The red oval marks the domain where oppositely directed magnetic field lines of the two systems reconnect. Right: Magnetic topology with a loop interconnecting the star and the planet (P).

where $0 < \gamma < 1$ is an efficiency parameter depending on the relative orientation of the interacting field lines, $B_*(a, \frac{\pi}{2})$ the coronal field at the distance a of the planet's orbit assumed to be circular and on the equatorial plane of the star (colatitude $\theta = \frac{\pi}{2}$), and v_{rel} the relative velocity between the coronal and the planetary field lines that corresponds to the orbital velocity of the planet for a slowly rotating star. Considering typically measured fields in active planetary hosts, $B_*(R_*) = 10 - 40$ G at the surface of the star ($r = R_*$), and a planetary field at its poles $B_p = 10$ G, we obtain for a typical hot Jupiter around a sun-like star with $v_{\text{rel}} = 100 - 200$ km/s, $R_m \sim 4 - 5 R_p$ and $P_d \sim 10^{17} - 10^{19}$ W, where R_p is the radius of the planet (cf. Lanza 2012)^c. This is insufficient by 2 - 3 orders of magnitudes to account for the power emitted by hot spots, although a twisted stellar force-free field can easily account for the observed phase lag between the spot and the planet (cf. Lanza 2008, 2009).

Lanza (2012) proposed that the perturbation of the stellar coronal field induced by the motion of the planet may trigger a release of the energy previously stored in the coronal field itself by reducing the magnetic helicity of its configuration. Previous order-of-magnitude calculations by Lanza (2009) showed that the reduction of magnetic helicity associated with the motion of the planet is a promising mechanism to account for the power released in hot spots. More-

^cThe given power range accounts for different stellar field configurations with the lower values associated with a potential field and the higher ones with non-linear force-free fields.

over, a periodic modulation of the magnetic helicity is possible in a long-lived magnetic loop that reaches to the orbit of the planet. This may trigger flares with the characteristic periodicity of the orbital period as suggested by Pillitteri et al. (2014b) in the case of HD 189733. The conjectured mechanism is analogous to that proposed for solar flares where the minimum-energy configuration, corresponding to a potential magnetic field for the given photospheric boundary conditions, can be reached only when the magnetic helicity of the coronal field is substantially reduced as a result of the emergence of new magnetic flux, motions at the boundary, or a loss of magnetic flux associated with a coronal mass ejection.

The reduction of the magnetic helicity associated with the orbital motion of the planet will in general drive the field toward a linear force-free configuration, that is a field with a constant α along all the different field lines (see Lanza 2009, 2012). Some linear configurations are particularly interesting because they have a rope of azimuthal flux that encircles the star with closed field lines that do not intersect the surface of the star (see Fig. 4)^d. If the planet is inside the flux rope, the energy released by magnetic reconnection cannot reach the star and no hot spot is produced. Nevertheless, the intense stellar ultraviolet radiation and the energy made available by magnetic reconnection can power the evaporation of the planetary atmosphere (Lanza 2013) that fills the flux rope with a hot plasma that subsequently cools and condenses into clumps with a typical temperature of the order of 10^4 K. They may effectively absorb in the core of the Mg II h&k or Ca II H&K lines, accounting for the extremely low flux level in the cores of those lines in the case of some systems with close-in massive planets (see Sect. 3.1). The formation of an azimuthal flux rope depends on the boundary conditions and the value of the helicity of the stellar field in the stationary configuration. This depends, in turn, on the processes that change magnetic helicity and the dissipation induced by the planet (see Lanza 2009, for details).

On the other hand, when the magnetic helicity of the stellar field is low, the field is close to a potential configuration and there can be field lines interconnecting the base of the stellar corona with the surface of the planet (cf. Fig. 3, right panel). These interconnecting loops are continuously stressed by the orbital motion of the planet, storing energy in excess of the minimum energy corresponding to the potential field. If such an energy can be dissipated at the same rate it is stored into the loop, the field can attain a stationary configuration and the interconnecting loop becomes a persistent feature of the system. The dissipated power can be easily calculated from the flux of the Poynting vector across the base of the interconnecting loop at the pole of the planet (Lanza 2013) and is:

$$P_{\text{int}} \simeq \frac{2\pi}{\mu} f_{\text{AP}} R_{\text{p}}^2 B_{\text{p}}^2 v_{\text{rel}}, \quad (18.3)$$

where f_{AP} is the fraction of the planetary surface crossed by the interconnecting field lines (typically $f_{\text{AP}} \sim 0.1 - 0.2$, cf. Adams 2011). The dissipated power reaches $10^{20} - 10^{21}$ W for the typical parameters adopted above, easily accounting for the emission of hot spots. The probability of having a stellar axisymmetric

^dAlso non-linear axisymmetric force-free configurations can have an azimuthal flux rope, but for simplicity here we shall limit ourselves to the linear case that represents the minimum energy configuration for a given total helicity.

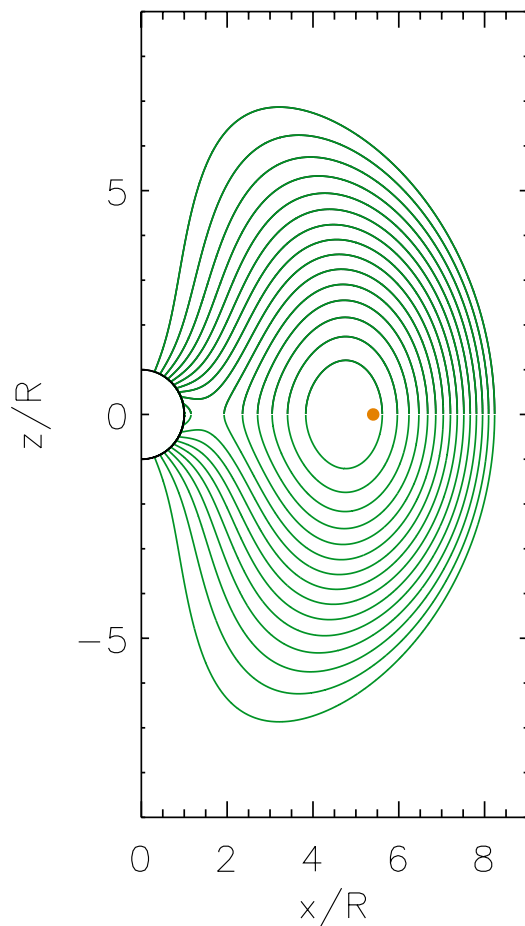


Figure 4.: Meridional section of an axisymmetric coronal force-free field with an azimuthal magnetic flux rope consisting of closed field lines that encircle the star. The projections of the field lines onto the meridional plane are shown as green solid lines, while the projection of the stellar surface is given by the black semicircle centered at the origin of the reference frame. The unit of measure is the radius R of the star with the Cartesian coordinates x and z measured from the origin at the center of the star in the equatorial plane and along the spin axis, respectively. The filled orange circle marks the position of a planet orbiting in the equatorial plane inside the azimuthal flux rope.

potential field is higher when the magnetic helicity is low, that is in the phases of minimum of the stellar cycle when the large-scale field is mainly poloidal according to solar-like dynamo models^e. This could explain why chromospheric

^eNote that a non-axisymmetric field would produce a chromospheric hot spot with a periodicity different from the orbital period of the planet (see Lanza 2012, for details).

hot spots are not stationary features since they can be preferentially produced during the minima of a stellar activity cycle. Note that in the case of F-type stars magnetic cycles can be as short as a couple of years as observed in the case of τ Bootis (Fares et al. 2009).

Finally, it is interesting to mention models proposed to explain the asymmetric and deeper transits of WASP-12 in the ultraviolet. Since the planet is close to filling its Roche lobe, Lai et al. (2010) proposed that a stream of matter flowing toward the star through the inner Lagrangian point and tilted in the direction of the orbital motion by the conservation of the angular momentum could absorb light in the UV just before the transit when its column density is the highest. Alternatively, a bow shock may develop in front of the planet due to its orbital motion inside the stellar corona or wind. This idea has been further explored by Vidotto et al. (2010), Llama et al. (2011), and Vidotto et al. (2011) and can in principle provide an estimate of the strength of the planetary field, if the stellar coronal field intensity is known by extrapolating the field observed on the photosphere through spectropolarimetric techniques.

3.3 Numerical models

Several results of analytic models have been confirmed by numerical MHD models. They can include the effects of finite plasma pressure and gravity, and simulate non-stationary configurations going beyond the very simple assumptions of analytic models. On the other hand, numerical models cannot fully resolve all the physically relevant lengthscales of the systems, therefore they include simplified (sometimes even crude) parameterization of the processes over sub-grid scales. Nevertheless, the recent progress in the field of stellar MHD simulations (e.g., Brun et al. 2014) makes them truly promising to explore star-planet magnetic interactions as well (e.g., Strugarek et al. 2012, 2014).

Interesting results were obtained by Cohen et al. (2009, 2011a,b) who confirmed the possibility of forming interconnecting magnetic loops that can be stressed by the orbital motion of the planet and suggested that enough energy is available to account for the chromospheric hot spots in the case of HD 179949 or v And. Those simulations included a realistic large-scale field geometry as obtained by extrapolating the field measured on the stellar photosphere through spectropolarimetric techniques. They were not limited to simple, stationary configurations and were extended to treat time-dependent events such as the interaction of a coronal mass ejection with a planet.

Recent work focussed on M-type dwarf stars whose habitable zones are closer than in the case of the brighter sun-like stars. By extrapolating spectropolarimetric field observations, it has become possible to study the large-scale geometry of their Alfvén surfaces, i.e., the transition surfaces separating the sub-alfvenic wind regions from the super-alfvenic ones (e.g., Vidotto et al. 2014a). Cohen et al. (2014) showed that the formation of a bow shock in the super-alfvenic wind regime helps to protect the planet from the effect of mass loss, even when the evaporation induced by stellar irradiation is strong, because most of the planetary field lines along which the evaporating plasma flows are bent and closed back in the magnetospheric tail. On the other hand, in the sub-alfvenic regime, a substantial fraction of the field lines are open and connected to the wind field lines, thus the evaporating plasma is free to escape from the planet producing a significantly larger mass loss. Since the Alfvén surface, as reconstructed by

photospheric field extrapolation, is generally irregular and far from a spherically symmetric shape, the MHD regime can switch from sub- to super-alfvenic and viceversa several times along the orbit of the planet. Adding the time variability of the stellar field (long-term activity evolution and/or short-term stellar activity cycles) this makes a planet experience rather different regimes during its lifetime.

4. Evaporation of planetary atmospheres

Vidal-Madjar et al. (2003, 2004, 2008), Linsky et al. (2010), and others found evidence of a deeper transit in the Lyman- α and other far-ultraviolet lines (e.g., of SiIII λ 120.65 nm, CII λ 133.45 and λ 133.57 nm) with depths 2–3 times greater than in the optical bandpass for HD 209458, HD 189733, and WASP-12. A remarkable time variability has been reported by Lecavelier des Etangs et al. (2012) in the case of HD 189733. The absorbing material extends beyond the planetary Roche lobe and has velocities ranging from several tens to $\approx 100 - 150$ km/s. These observations are interpreted as evidence of evaporation of planetary atmospheres. Haswell et al. (2012) extended the approach to the near-ultraviolet lines finding evidence of evaporation in WASP-12b.

The stellar extreme-ultraviolet (EUV) flux ($\lambda \lesssim 91$ nm) has been identified as the main source of energy to power the evaporation. It depends on the spectral type and the rotation rate of the star that determine the overall heating level of the transition region and the corona emitting in that passband. The flux can vary remarkably along a stellar activity cycle (at least by a factor of 2–3 in the Sun) and be enhanced during flares. Owing to absorption by interstellar Hydrogen, it is difficult to measure the EUV flux, so different estimates of it have been proposed for stars of various ages and spectral types (e.g., Ribas et al. 2005; Lecavelier Des Etangs 2007; Sanz-Forcada et al. 2011; Linsky et al. 2013).

Recently, Buzasi (2013) and Lanza (2013) proposed an additional source to power evaporation, i.e., the energy released by magnetic reconnection between stellar and planetary fields at the boundary of the planetary magnetosphere (cf. Sect. 3.2 and Eq. 18.2). Reconnection accelerates electrons that are conveyed down along the magnetic field lines reaching the base of the planetary exosphere, where they induce evaporation and chemical reactions. An estimate of the minimum available power in units of that of the EUV flux (Lecavelier Des Etangs 2007) is shown in Fig. 5 as a function of the orbital semimajor axis for different configurations of the stellar magnetic field. Specifically, we assume that the coronal field depends on the radial distance r from the center of the star as $B_*(r) = B_*(R_*)(r/R_*)^{-s}$, where $B_*(R_*)$ is the field at the surface of the star ($r = R_*$) and $2 \leq s \leq 3$ is a parameter depending on the field geometry, ranging from $s = 2$ for a purely radial field to $s = 3$ for a potential field; intermediate values are associated with force-free fields (cf. Lanza 2012, 2013). Assuming a planetary field comparable with that of Jupiter ($B_p = 10$ G), a stellar field $B_*(R_*) = 10$ G, as indicated by spectropolarimetric observations (Moutou et al. 2007; Fares et al. 2012), and $\gamma = 0.5$, we find that planets closer than 0.03–0.05 AU experience a magnetic heating greater than the estimated stellar EUV flux. The corresponding mass loss is therefore significantly increased, although the effect is generally not large enough to completely ablate the closest planets during the main-sequence lifetime of their host stars (see Lanza 2013).

Given the remarkable time variability of stellar magnetic fields, we expect that magnetically powered evaporation is not constant. Kawahara et al. (2013) suggest that the evaporation rate in the very close transiting object KIC 12557548 ($P_{\text{orb}} \sim 0.6536$ d) be modulated by the rotation of its spotted star. This could arise from the rotational modulation of the EUV flux coming from its active regions, but also a magnetically-induced evaporation may be invoked because the stellar magnetic field at the boundary of the planetary magnetosphere is modulated as well.

Energetic electrons accelerated by reconnection and conveyed into the planetary exosphere can produce chemical reactions that lead to the formation of molecules such as C_2H_2 , C_2H_4 , NH_3 , C_6H_6 . They have potential astrobiological relevance and may not be produced with the same efficiency by EUV radiation because photons have no electric charge (cf. Rimmer et al. 2014a,b; Stark et al. 2014).

5. Star-planet interaction and evolution of stellar rotation

Pont (2009), Brown et al. (2011), and Bolmont et al. (2012), among others, proposed that tides can spin up planet-hosting stars, especially in the case of giant planets orbiting slowly rotating late-type stars. A quantitative study, however, is made difficult by our limited knowledge of the tidal coupling in star-planet systems and its dependence on the stellar rotation rate (see Sect. 2. and Ogilvie & Lin 2007). Moreover, some theoretical models predict that the braking of stellar rotation in late-type stars produced by their magnetized winds can be reduced thanks to the interaction with a close-in planet (e.g., Cohen et al. 2010; Lanza 2010).

Brown (2014) compared the ages estimated for stars with close-in planets by means of gyrochronology and isochrone fitting, but the large intrinsic errors prevented him from reaching definite conclusions. Some progress should be possible by applying asteroseismology to improve the determination of stellar ages (cf. Angus 2014), independently of the rotation rate.

Another approach exploits the presence of a distant, presumably co-eval, visual companion whose age can be estimated from its X-ray coronal flux. Poppenhaeger & Wolk (2014) summarize the results obtained so far and find that CoRoT-2 and, to a lesser extent, HD 189733, appear to rotate faster than expected from gyrochronology on the basis of the estimated ages of their visual companions, respectively.

6. Evidence of star-planet interaction in photospheric activity ?

The possibility that photospheric active regions be associated with close-in planets has also been considered. Santos et al. (2003) reported the intriguing case of HD 192263, a K2V star accompanied by a planet with an orbital period of 24.35 d and a projected mass of $0.72 M_{\text{J}}$, that showed during some seasons a photometric modulation with the same period of its planet. This led Henry et al. (2002) to question the planetary nature of the radial velocity modulation, but its long-term stability supports the reality of the planet. The coincidence $P_{\text{rot}} \simeq P_{\text{orb}}$ would be easily understood in terms of tidal synchronization of the stellar rotation with the orbital motion, but the long orbital period makes the

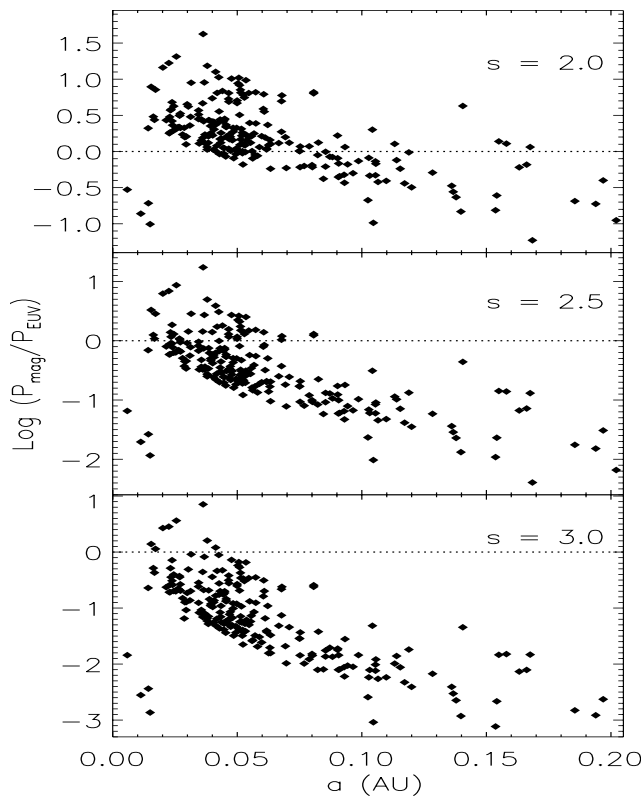


Figure 5.: Upper panel: ratio of the power delivered by magnetic reconnection into the planetary atmosphere to the power of the stellar EUV irradiation vs. the orbital semimajor axis. The parameter $s = 2.0$ corresponds to a stellar magnetic field having radially directed field lines (see the text). The horizontal dotted line marks $P_{\text{mag}} = P_{\text{EUV}}$, i.e., the two sources of evaporation having the same power. Middle panel: the same as the upper panel, but for a force-free field with $s = 2.5$. Lower panel: the same as the upper panel, but for a potential coronal field ($s = 3.0$).

tidal interaction remarkably weak in this system. Of course, the possibility that the stellar rotation period is close to the orbital period of the planet by chance cannot be excluded, but an alternative exotic interpretation is that the formation and evolution of starspots are in some way coupled with the orbital motion of the planet. Further similar cases have been reported.

Walker et al. (2008) studied the case of τ Bootis, an F-type star rotating synchronously with the orbital period of its massive planet ($P_{\text{rot}} \sim P_{\text{orb}} \sim 3.3$ d). It showed a long-lived active region that has maintained an approximately constant phase lag of $\approx 75^\circ$ with respect to the planet for at least ≈ 5 years.

Lanza et al. (2009b) found that in the F-type dwarf star CoRoT-4 the rotation of the photospheric starspots was approximately synchronous with the

orbital period of the planet ($P_{\text{orb}} \sim 9.2$ d) and there was a spot close to the subplanetary longitude during most of the CoRoT observations covering a time span of ~ 60 d. Tides are weak in the CoRoT-4 system because of the long orbital period and the relatively low mass of the planet ($\sim 0.75 M_{\text{J}}$).

Another interesting case is that of CoRoT-6, a F9V star that has a planet with a mass of $\sim 3 M_{\text{J}}$ and $P_{\text{orb}} = 8.89$ d, while the mean stellar rotation period is $P_{\text{rot}} \sim 6.35$ d. Lanza et al. (2011b) found that starspot activity was enhanced in the active regions when they crossed a longitude that was trailing the subplanetary longitude by $\sim 200^\circ$ during the ~ 150 d of CoRoT observations.

A phenomenon reminiscent of such a behaviour was found by Béky et al. (2014) in the transiting systems HAT-P-11 and Kepler-17. The rotation periods of those stars are not synchronized with the orbital periods of their planets, respectively, but are close to an integer multiple of them. Precisely, $P_{\text{rot}} \sim 6P_{\text{orb}}$ in the case of HAT-P-11 and $P_{\text{rot}} \sim 8P_{\text{orb}}$ in Kepler-17. The intriguing phenomenon is that, in spite of the imperfect commensurability of the mean rotation and orbital periods, there are starspots that rotate with an almost perfect commensurable period in both systems. This is demonstrated by the recurrence of their occultations by the planets at the same orbital phases along datasets spanning more than ≈ 800 days. The observed recurrence rates of those starspots are about 2.3 times the values expected in the case of a random distribution of their rotation rates.

Although a global estimate of the probability that the coincidences reported above occurred by chance has not been given yet, the cases based on CoRoT and especially Kepler long-term observations suggest that a close-in massive planet may in some way modulate the starspot activity in the photosphere of its host star. Other intriguing observations refer to preferential orbital phases for an enhancement of the stellar flux variability (Pagano et al. 2009) and a short-term starspot cycle in CoRoT-2 with a period close to ten times the synodic period of the planet with respect to the mean stellar rotation period (Lanza et al. 2009a). A similar short-term spot cycle was observed in Kepler-17, but no commensurability with the synodic period was found in that case (Bonomo & Lanza 2012).

From the theoretical side, it is difficult to find a physical mechanism to account for a starspot activity phased to the orbital motion of a close-in planet. In the case of close active binaries, the strong tides in the almost synchronized component stars might interact with large scale convection and lead to active longitudes that rotate almost in phase with the orbital motion (cf. Weber et al. 2013, for the role of large-scale convection in the formation of active longitudes). Magnetic flux tubes close to the base of the convection zone could also be de-stabilized by the tidal deformation of the stars producing active longitudes (Holzwarth & Schüssler 2003a,b). However, it is unclear whether those mechanisms may account for the phenomena observed in planetary systems because the mass of a hot Jupiter is of the order of 10^{-3} of the mass of a stellar companion, so tidal effects are dominated by stochastic convective motions inside the star. However, numerical simulations of the dynamo action in systems affected by tides are beginning to be performed and they have the potential to shed light on those effects (cf. Cébron & Hollerbach 2014).

It has also been conjectured that the interaction between the planetary and the stellar magnetic fields may modulate the total magnetic helicity of the stellar field that, in turn, affects the operation of the stellar dynamo (cf. Brandenburg

& Subramanian 2005). Helicity is mainly dissipated by eruptive processes in the corona such as mass ejections and large flares, so it is conceivable that a planet moving close to its star may modulate the occurrence of those phenomena and indirectly affect the stellar dynamo (see Lanza 2008, 2009, 2011, for details).

7. Conclusions

Star-planet interactions are a fascinating field. I have reviewed some topics that have mostly impressed me and that are promising for further investigations both observationally and theoretically. Planetary systems offer the opportunity to test tidal theories in previously unexplored regimes with extreme mass ratio between the two bodies, eccentric orbits, and stellar rotation far away from synchronization. Tides in multi-body systems can also be investigated. I have discussed in some detail one application of the tidal models to account for the intriguing distribution of Kepler candidate systems in the $P_{\text{rot}} - P_{\text{orb}}$ plane.

Magnetic interactions in systems with close-in planets can take place in a regime characterized by a local Alfvén speed smaller than the plasma (stellar wind) speed. This allows a perturbation excited by the planet to propagate down to its host star in a regime not observed in our Solar system. Simple MHD models predict different magnetic configurations in star-planet systems. Configurations characterized by an azimuthal magnetic flux rope may store the plasma evaporating from a close-in planet possibly accounting for the presence of circumstellar absorption as suggested by the observations of some systems. On the other hand, magnetic loops interconnecting the star with the planet may be stressed by the orbital motion of the planet and dissipate powers up to $10^{20} - 10^{21}$ W that may account for chromospheric hot spots moving in phase with the planet rather than with stellar rotation. The energy dissipated by magnetic reconnection can play a relevant role in the evaporation of planetary atmospheres, especially for close-in ($\lesssim 0.05$ AU) planets.

Photospheric spots and coronal flares associated with a close-in planet have been suggested by recent observations. Moreover, the magnetic and tidal interactions between a planet and its host may affect the angular momentum evolution and the activity level of the star making standard gyrochronology difficult to apply.

New observations and theoretical models are mandatory for making progress in this field. A long-term monitoring of an extended sample of targets is necessary to confirm the phenomena suggested by the observations discussed above. The most severe limitation in the case of CoRoT and Kepler is the scarcity of bright stars with close-in massive planets, the only systems for which these subtle effects can be detected. The recently selected space mission PLATO is therefore particularly interesting because it is dedicated to the detection, characterization, and long-term (at least 2 – 3 yr) monitoring of planetary systems orbiting bright stars (Rauer et al. 2014). For those stars, asteroseismology can allow us to determine the age with typical errors of 10 – 15 percent, thus allowing to test and calibrate gyrochronology for planetary hosts (cf. Sect. 5.).

Acknowledgements. I wish to thank the Scientific Organizing Committee of Cool Stars 18 for their kind invitation to review star-planet interactions and for the organization of such

a stimulating meeting. I am grateful to Drs. Airapetian and Shkolnik for interesting discussions.

References

- Adams, F. C. 2011, *ApJ*, 730, 27
- Affer, L., Micela, G., Favata, F., & Flaccomio, E. 2012, *MNRAS*, 424, 11
- Angus, R. 2014, this meeting
- Auvergne, M., Bodin, P., Boissard, L., et al. 2009, *A&A*, 506, 411
- Barnes, S. A. 2007, *ApJ*, 669, 1167
- Béky, B., Holman, M. J., Kipping, D. M., & Noyes, R. W. 2014, *ApJ*, 788, 1
- Birkby, J. L., Cappetta, M., Cruz, P., et al. 2014, *MNRAS*, 440, 1470
- Bolmont, E., Raymond, S. N., Leconte, J., & Matt, S. P. 2012, *A&A*, 544, A124
- Bonomo, A. S., & Lanza, A. F. 2012, *A&A*, 547, A37
- Borucki, W. J., Koch, D., Basri, G., et al. 2010, *Science*, 327, 977
- Brandenburg, A., & Subramanian, K. 2005, *Physics Reports*, 417, 1
- Brown, D. J. A. 2014, *MNRAS*, 442, 1844
- Brown, D. J. A., Collier Cameron, A., Hall, C., Hebb, L., & Smalley, B. 2011, *MNRAS*, 415, 605
- Brun, A. S., Browning, M. K., Dikpati, M., Hotta, H., & Strugarek, A. 2014, *Space Sci.Rev.*, in press; doi: 10.1007/s11214-013-0028-0
- Buzasi, D. 2013, *ApJ*, 765, L25
- Cébron, D., & Hollerbach, R. 2014, *ApJ*, 789, L25
- Cohen, O., Drake, J. J., Kashyap, V. L., et al. 2009, *ApJ*, 704, L85
- Cohen, O., Drake, J. J., Kashyap, V. L., Sokolov, I. V., & Gombosi, T. I. 2010, *ApJ*, 723, L64
- Cohen, O., Kashyap, V. L., Drake, J. J., et al. 2011a, *ApJ*, 733, 67
- Cohen, O., Kashyap, V. L., Drake, J. J., Sokolov, I. V., & Gombosi, T. I. 2011b, *ApJ*, 738, 166
- Cohen, O., Drake, J. J., Gloer, A., et al. 2014, *ApJ*, 790, 57
- Cuntz, M., Saar, S. H., & Musielak, Z. E. 2000, *ApJ*, 533, L151
- Esposito, M., Covino, E., Mancini, L., et al. 2014, *A&A*, 564, L13
- Fares, R., Donati, J.-F., Moutou, C., et al. 2009, *MNRAS*, 398, 1383
- Fares, R., Donati, J.-F., Moutou, C., et al. 2012, *MNRAS*, 423, 1006
- Fossati, L., Haswell, C. A., Froning, C. S., et al. 2010, *ApJ*, 714, L222

- Fossati, L., Bagnulo, S., Elmasli, A., et al. 2010, *ApJ*, 720, 872
- Fossati, L., Ayres, T. R., Haswell, C. A., et al. 2013, *ApJ*, 766, L20
- Gurdemir, L., Redfield, S., & Cuntz, M. 2012, *PASA*, 29, 141
- Haswell, C. A., Fossati, L., Ayres, T., et al. 2012, *ApJ*, 760, 79
- Henry, G. W., Donahue, R. A., & Baliunas, S. L. 2002, *ApJ*, 577, L111
- Holzwarth, V., & Schüssler, M. 2003a, *A&A*, 405, 291
- Holzwarth, V., & Schüssler, M. 2003b, *A&A*, 405, 303
- Kawahara, H., Hirano, T., Kurosaki, K., Ito, Y., & Ikoma, M. 2013, *ApJ*, 776, L6
- Kopp, A., Schilp, S., & Preusse, S. 2011, *ApJ*, 729, 116
- Lai, D., Helling, C., & van den Heuvel, E. P. J. 2010, *ApJ*, 721, 923
- Lanza, A. F. 2008, *A&A*, 487, 1163
- Lanza, A. F. 2009, *A&A*, 505, 339
- Lanza, A. F. 2010, *A&A*, 512, A77
- Lanza, A. F. 2011, *Ap&SS*, 336, 303
- Lanza, A. F. 2012, *A&A*, 544, A23
- Lanza, A. F. 2013, *A&A*, 557, A31
- Lanza, A. F., Piluso, N., Rodonò, M., Messina, S., & Cutispoto, G. 2006, *A&A*, 455, 595
- Lanza, A. F., Bonomo, A. S., & Rodonò, M. 2007, *A&A*, 464, 741
- Lanza, A. F., Pagano, I., Leto, G., et al. 2009a, *A&A*, 493, 193
- Lanza, A. F., Aigrain, S., Messina, S., et al. 2009b, *A&A*, 506, 255
- Lanza, A. F., Damiani, C., & Gandolfi, D. 2011a, *A&A*, 529, A50
- Lanza, A. F., Bonomo, A. S., Pagano, I., et al. 2011b, *A&A*, 525, A14
- Lanza, A. F., Das Chagas, M. L., & De Medeiros, J. R. 2014, *A&A*, 564, A50
- Lanza, A. F., & Shkolnik, E. L. 2014, *MNRAS*, 443, 1451
- Laskar, J. 1997, *A&A*, 317, L75
- Laskar, J. 2008, *Icarus*, 196, 1
- Lecavelier Des Etangs, A. 2007, *A&A*, 461, 1185
- Lecavelier des Etangs, A., Bourrier, V., Wheatley, P. J., et al. 2012, *A&A*, 543, L4
- Linsky, J. L., Yang, H., France, K., et al. 2010, *ApJ*, 717, 1291
- Linsky, J. L., France, K., & Ayres, T. 2013, *ApJ*, 766, 69

- Llama, J., Wood, K., Jardine, M., et al. 2011, *MNRAS*, 416, L41
- Mathis, S., Alvan, L., & Remus, F. 2013, *EAS Publications Series*, 62, 323
- McQuillan, A., Mazeh, T., & Aigrain, S. 2013, *ApJ*, 775, L11
- McQuillan, A., Mazeh, T., & Aigrain, S. 2014, *ApJS*, 211, 24
- Miller, B. P., Gallo, E., Wright, J. T., & Dupree, A. K. 2012, *ApJ*, 754, 137
- Moutou, C., Donati, J.-F., Savalle, R., et al. 2007, *A&A*, 473, 651
- Ogilvie, G. I. 2014, *ARA&A*, in press, arXiv:1406.2207
- Ogilvie, G. I., & Lin, D. N. C. 2007, *ApJ*, 661, 1180
- Pagano, I., Lanza, A. F., Leto, G., et al. 2009, *Earth Moon and Planets*, 105, 373
- Pillitteri, I., Günther, H. M., Wolk, S. J., Kashyap, V. L., & Cohen, O. 2011, *ApJ*, 741, L18
- Pillitteri, I., Wolk, S. J., Sciortino, S., & Antoci, V. 2014a, *A&A*, 567, A 128
- Pillitteri, I., Wolk, S. J., Lopez-Santiago, J., et al. 2014b, *ApJ*, 785, 145
- Pont, F. 2009, *MNRAS*, 396, 1789
- Poppenhaeger, K., & Wolk, S. J. 2014, *A&A*, 565, L1
- Poppenhaeger, K., Lenz, L. F., Reiners, A., Schmitt, J. H. M. M., & Shkolnik, E. 2011, *A&A*, 528, A58
- Preusse, S., Kopp, A., Büchner, J., & Mutschmann, U. 2005, *A&A*, 434, 1191
- Preusse, S., Kopp, A., Büchner, J., & Mutschmann, U. 2006, *A&A*, 460, 317
- Rauer, H., Catala, C., Aerts, C., et al. 2014, *Experimental Astronomy*, in press, arXiv:1310.0696
- Ribas, I., Guinan, E. F., Güdel, M., & Audard, M. 2005, *ApJ*, 622, 680
- Rimmer, P. B., Helling, C., & Bilger, C. 2014a, *International Journal of Astrobiology*, 13, 173
- Rimmer, P. B., Walsh, C., & Helling, C. 2014b, *IAU Symposium*, 299, 303
- Santos, N. C., Udry, S., Mayor, M., et al. 2003, *A&A*, 406, 373
- Sanz-Forcada, J., Micela, G., Ribas, I., et al. 2011, *A&A*, 532, A6
- Saur, J., Grambusch, T., Duling, S., Neubauer, F. M., & Simon, S. 2013, *A&A*, 552, A119
- Scandariato, G., Maggio, A., Lanza, A. F., et al. 2013, *A&A*, 552, A7
- Shkolnik, E., Walker, G. A. H., & Bohlender, D. A. 2003, *ApJ*, 597, 1092
- Shkolnik, E., Walker, G. A. H., Bohlender, D. A., Gu, P.-G., Kürster, M. 2005, *ApJ*, 622, 1075
- Shkolnik, E., Bohlender, D. A., Walker, G. A. H., & Collier Cameron, A. 2008, *ApJ*, 676, 628

- Silva-Valio, A., & Lanza, A. F. 2011, *A&A*, 529, A36
- Stark, C. R., Helling, C., Diver, D. A., & Rimmer, P. B. 2014, *International Journal of Astrobiology*, 13, 165
- Strugarek, A., Brun, A. S., & Matt, S. 2012, SF2A-2012: Proceedings of the Annual meeting of the French Society of Astronomy and Astrophysics, 419
- Strugarek, A., Brun, A. S., Matt, S. P., & Reville, V. 2014, *IAU Symposium*, 300, 330
- Teitler, S., Königl, A. 2014, *ApJ*, 786, 139
- Vidal-Madjar, A., Lecavelier des Etangs, A., Désert, J.-M., et al. 2003, *Nature*, 422, 143
- Vidal-Madjar, A., Désert, J.-M., Lecavelier des Etangs, A., et al. 2004, *ApJ*, 604, L69
- Vidal-Madjar, A., Lecavelier des Etangs, A., Désert, J.-M., et al. 2008, *ApJ*, 676, L57
- Vidotto, A. A., Jardine, M., & Helling, C. 2010, *ApJ*, 722, L168
- Vidotto, A. A., Jardine, M., & Helling, C. 2011, *MNRAS*, 411, L46
- Vidotto, A. A., Jardine, M., Morin, J., et al. 2014a, *MNRAS*, 438, 1162
- Vidotto, A. A., Gregory, S. G., Jardine, M., et al. 2014b, *MNRAS*, 441, 2361
- Walker, G. A. H., Croll, B., Matthews, J. M., et al. 2008, *A&A*, 482, 691
- Walkowicz, L. M., & Basri, G. S. 2013, *MNRAS*, 436, 1883
- Weber, M. A., Fan, Y., & Miesch, M. S. 2013, *ApJ*, 770, 149
- Wu, Y., & Lithwick, Y. 2011, *ApJ*, 735, 109
- Zahn, J.-P. 2008, *EAS Publications Series*, 29, 67
- Zahn, J.-P. 2013, *Lecture Notes in Physics*, Berlin Springer Verlag, 861, 301

Chapter 19

Determining the stellar spin axis orientation

Anna-Lea Lesage¹, Günter Wiedemann²

¹*Leiden Observatory, P.O. Box , Leiden, The Netherlands*

²*Hamburg Observatory, Gojenbergsweg 112, 21029 Hamburg, Germany*

Abstract.

We present an observing method that permits the determination of the absolute stellar spin axis position angle based on spectro-astrometric observations for slowly-rotating late-type stars. This method is complementary to current interferometric observations that determine the orientation of stellar spin axis for early-type fast-rotating stars.

Spectro-astrometry enables us to study phenomena below the diffraction limit, at the milli-arcsecond scale. It relies on the wavelength dependent variations of the centroid position of a structured source in a long-slit spectrum. A rotating star has a slight tilt in its spectral lines, which induces a displacement of the photocentre's position. By monitoring the amplitude of the displacement for varying slit orientations, we can infer the absolute position angle of the stellar spin axis.

Finally, we present first observational results on Aldebaran obtained with the Thüringer Landesternwarte high resolution spectrograph. We were able to retrieve Aldebaran's position angle with less than 10° errors.

1. Motivation

1.1 Introduction

In their earliest variations, stellar formation theory, directly inspired by our own solar system, predicted that during its formation the star conserved its angular

momentum, and consequently the spin axis orientation and kept a perfect spin-orbit alignment if the system happened to host planets. Nowadays, the large number of misaligned system discovered in the last decades, be it spin-orbit misalignment in cases of exoplanets (Fabrycky et al 2009), or spin-axis misalignment in cases of binaries (Albrecht et al 2009), imply that stellar formation is more chaotic than imagined before. Finally, recent simulations converge towards a state of random distribution of stellar spin axes (Bate et al 2010) in open clusters.

Recent interferometric observations have managed to determine the spin axis orientation for a handful of early-type fast-rotating stars (Monnier et al (2007) and deSouza et al (2003)). Indeed, fast rotating stars are theorized to present cases of gravitation-darkening, i.e. the equatorial latitude of the star is cooler than the polar latitude. By imaging the oblateness of those stars and the brightness distribution, it is possible to retrieve the absolute orientation of the stellar spin axes.

However, this method would not work for slowly-rotating late-type stars as they neither present gravitational darkening nor oblateness strong enough to be measured. Hence, we propose an alternative method relying on spectro-astrometric observations, to determine the absolute position angle of the stellar spin axis for those late-type slowly rotating stars.

1.2 Spectro-astrometry

Spectro-astrometry is an observing technique relying on long-slit spectra. Taking advantage of the conservation of the spatial information along the slit spatial axis, this technique resolves spatial features in the milli-arcsecond scale, well below the diffraction limit of the telescope. Since each slit orientation delivers only one-dimensional content along that orientation, it is necessary to probe several slit orientations on sky to unravel the full spatial information. Finally, it is common to probe anti-parallel slit orientations. By doing so, instrumental artefacts are identified and can be strongly reduced when subtracting both orientations (Brannigam et al 2006).

In practice, the spatial information is extracted by measuring the wavelength dependence of the photocentre of the spectral order. This is either done via Gaussian fit or arithmetic weighted mean. Both methods are valid and yield similar results, assuming the spectra were properly corrected for bad pixels. As a result, the position of the photocentre is measured with sub-pixel precision, enabling the milli-arcsecond scale information.

Nonetheless the analysis of the position spectrum still requires a proper understanding of the features one wishes to observe. For instance, spectro-astrometry was used successfully for mapping the surfaces of giant stars (Voigt and Wiedemann 2009).

2. The Method

We use in the method the angle conventions defined in the figure 1. The absolute stellar position angle is deduced from: $PA_{\text{star}} = PA_{\text{slit}} + \psi$. Since the orientation of the slit on sky is known, the determination of the stellar position angle is directly linked to the measurement of the angle ψ .

The star is no longer considered as an unresolved point source on the slit, which means that Doppler effects due to the star's rotation can no longer be

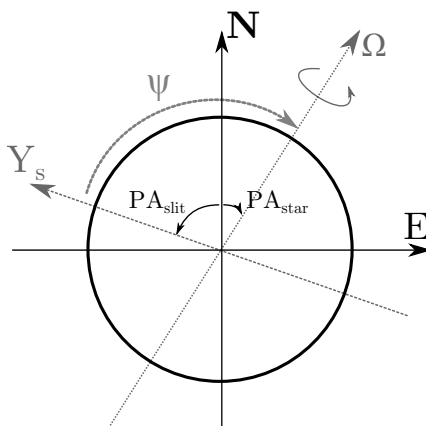


Figure 1.: Angle conventions used for the method.

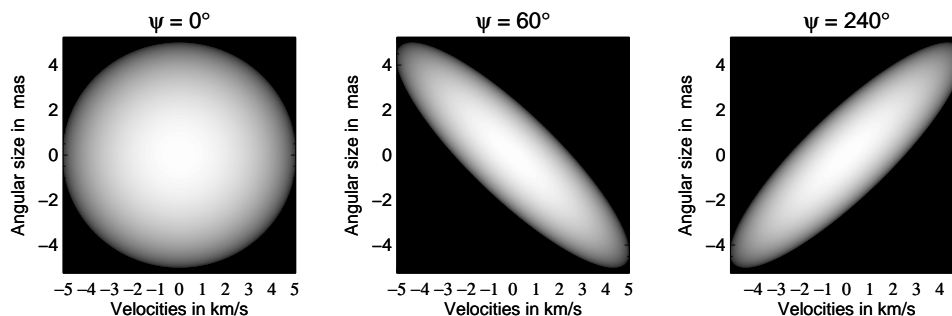


Figure 2.: Stellar profile in the wavelength-spatial referential taking into account the Doppler shifts cause by the stellar rotation, and the angle between slit and spin axis.

neglected. The part of the star coming towards us is blue shifted, and the portion of the star moving away from the observer is red shifted. While the spatial axis of the slit conserves the spatial information, the dispersion axis translates these Doppler shifts into wavelength displacements. Once the two informations are combined, it is possible to model the star in the wavelength-spatial referential proper to the spectrograph. As seen on the figure 2, in the wavelength-spatial referential, the star is no longer a round object, but a slanted ellipse whose inclination is linked to the angle ψ . As a result, the stellar lines, which are the result of the convolution of the intrinsic stellar spectrum with the two-dimensional model of the star in the spectrograph's referential, are tilted with the angle ψ .

The tilt of the stellar lines follows a sine function of the form : $\sin(\psi - \text{PA}_{\text{star}})$. It is measured as a displacement in the position spectrum at the position of the stellar lines, i.e. the photocentre of the spectral order is displaced from the continuum. By monitoring the amplitude of this displacement as a function of the slit orientation, it is possible to retrieve the absolute position angle of the star, as illustrated step-by-step in figure 3.

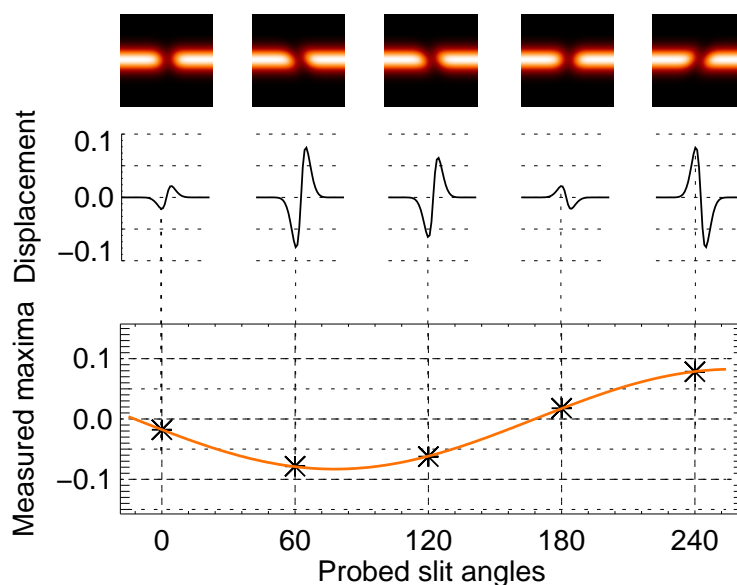


Figure 3.: Working principle of the method: The stellar rotation induces a line tilt whose inclination is correlated to the angle ψ as seen in the upper row. The line tilt is translated in the position spectrum as a displacement from the continuum as shown in the middle row. The amplitude of the displacement with probed slit orientation follow a sine curve whose phase yields the absolute stellar position angle.

2.1 Retrieving the signal in the position spectrum

In some cases, e.g. when the seeing and the spectrograph plate scale are small, the displacement of the photocentre in the position spectrum at the line position is visible with the naked eye, and can be directly measured. However, in most cases, we expect the signal to be drown in a sea of noise. Then retrieving the displacement amplitude becomes a challenge. As a solution, we propose to proceed to a cross-correlation analysis between position spectrum and the derivative of the intensity spectrum, i.e. a function of the contrast of the spectrum. By doing so, we combine the information of multiple stellar lines to enhance the signal. We then monitor the amplitude of the cross-correlation function as a function of slit orientation.

2.2 Seeing and instrumental noise

Seeing and instrumental profile are the two main error sources in this method. The instrumental profile can induce a distortion of the stellar wavelength-spatial profile, causing a tilt which is no longer correlated to the slit orientation. Furthermore, seeing acts similarly on a shorter timescale. While the instrumental profile may change over an hour, seeing profile fluctuate in less than a second.

The influence of profile distortions caused by seeing can be kept minimal by choosing relatively large exposure times. As a result the effects of seeing are smeared over the spectrum without influencing the stellar profile over that

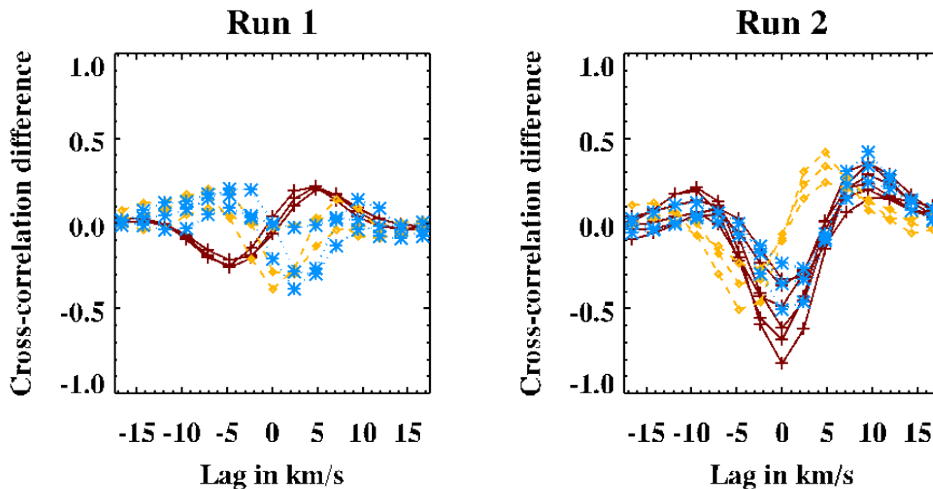


Figure 4: Two observing runs of Aldebaran for two different orientations. In red, the cross-correlation signal from the target star Aldebaran. In blue and yellow, the cross-correlation signal measured before and after respectively of the telluric lines in a reference star. Run 1 and 2 probed respectively slit orientations 202° and 130° .

time scale. On the other hand, disentangling the displacement caused by the instrumental profile from the one generated by the stellar rotation requires a special observing technique and additional instrument.

We have developed a differential image rotator, a small instrument to be inserted between the telescope output and the slit, which splits the input beam along two polarisations, rotates both beams to anti-parallel orientations, and projects them both on the slit (Lesage et al 2012). The resulting spectrum features the same orders twice, one for each beam orientation. As such, the anti-parallel orientations are taken simultaneously and have seen same seeing and instrumental profile. With this instrument, it becomes possible to compare directly the two anti-parallel orientation and be seeing independent.

Additionally we recommend to observe an early-type star before and after the observing run, while keeping the latter short. By measuring the line tilt displacement along the telluric lines and comparing it to the line tilt displacement of the target star, we disentangle the stellar signal from the instrumental profile. As illustrated in figure 4, when the stellar signal is the strongest, i.e. when the angle ψ is close to 90° or 270° , the stellar signal (here is continuous red) diverges from the signal measured in the telluric lines (in blue and yellow stars). However, if the stellar signal is minimal, i.e. when the angle ψ is either 0° or 180° , then the signal measured in the telluric lines dominates.

3. Observations of Aldebaran

Aldebaran is one of the very few cool giants whose position angle has already been measured by Lagarde et al (1995). As such it is an ideal candidate to test the validity of the method and the instrument. We observed Aldebaran during a 2

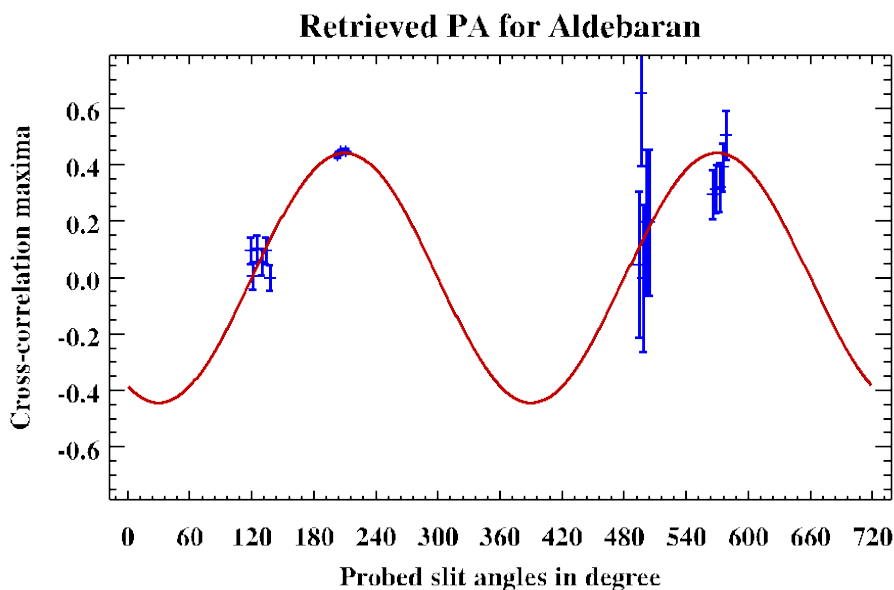


Figure 5.: The amplitude of the photocentre displacement as measured from the cross-correlation functions for the four slit orientations probed during the 2 nights observation of Aldebaran. In red, the best sine fit. The second night was characterised by degrading seeing conditions which are reflected by the important scatter of the points compared to the previous night.

nights observing runs on the Coudé high resolution ($R = 60\,000$) Spectrograph of the Thüringer Landessternwarte Tautenburg. We used the natural field rotation of the Coudé spectrograph to probe four different slit orientations on sky during the two nights. With a pixel scale of 0.51 arcseconds, we expected a photocentre displacement of the order of 2 to 5% of a pixel for Aldebaran. From each observing run, spanning about 5° on sky, we extracted 10 independent displacement measurements.

We applied the method described earlier to disentangle the signal from Aldebaran from the instrumental induced signal. In addition, the exposure time was kept relatively high, around 200 seconds, considering that Aldebaran is a $Vmag = 0.8$ star. Figure 5 shows the final step of the analysis, where we fitted a sine curve to the measured displacements. We retrieved a position angle of $115^\circ \pm 4^\circ$ which is in agreement with the angle of $110^\circ \pm 5^\circ$ measured by Lagarde et al (1995).

4. Conclusion

To conclude, we have presented here a method which enables the determination of the position angle of the stellar spin axis. The method was successfully tested on Aldebaran, despite non-optimal seeing and instrumental conditions. Applied to a larger sample of stars, this method would provide a first step in confirming the chaotic aspects of stellar formation which cannot be measured yet.

Acknowledgements. A.-L. Lesage would like to acknowledge the precious help to the instrumental team of the Thüringer Landessternwarte Tautenburg, and the possibility to test the method on their telescope.

References

- Bate, M. R., Lodato, G. and Pringle, J. E., 2010, MNRAS, 401, 1505
- Fabrycky, D. C. and Winn, J. N. 2009, ApJ, 696, 1230
- Albrecht, S., Reffert, S., Snellen, I. A. G. and Winn, J. N. 2009, Nature, 461, 373
- Monnier, J., Zhao, M., Pedretti, E., Thureau, N., Ireland, M., Muirhead, P., Berger, J.-P., Millan-Gabet, R., Van Belle, G., ten Brummelaar, T., McAlister, H., Ridgway, S., Turner, N., Sturmann, L., Sturmann, J. and Berger, D. 2007, Science, 317, 342
- Domiciano de Souza, A., Kervella, P., Jankov, S., Abe, L., Vakili, F., di Folco, E. and Paresce, F. 2003, A&A, 407, L47
- Brannigan, E., Takami, M., Chrysostomou, A. and Bailey, J. 2006, MNRAS, 367, 315-
- Voigt, B., and Wiedemann, G., 2009, 15th Cambridge Workshop on Cool Stars, Stellar Systems, and the Sun, 1094, 896
- Lesage, A.-L., Schneide, M., and Wiedemann, G., 2012, SPIE Proceedings, 8446
- Lagarde, S., Sanchez, L. J. and Petrov, R. G., 1995, IAU Colloq. 149: Tridimensional Optical Spectroscopic Methods in Astrophysics, 71, 360

Chapter 20

Predicting the Extreme-UV and Lyman- α Fluxes Received by Exoplanets from their Host Stars

Jeffrey L. Linsky¹, Kevin France², Thomas Ayres²

¹*JILA, University of Colorado and NIST, Boulder, CO 80309-0440 USA*

²*CASA, University of Colorado, Boulder, CO 80309-0593 USA*

Abstract.

Extreme-UV (EUV) radiation from the chromospheres, transition regions, and coronae of host stars (spectral types F, G, K, and M) ionize and heat the outer atmospheres of exoplanets leading to mass loss that is observed during transits and can change the exoplanet's atmosphere. Lyman- α emission from host stars controls the photochemistry in the upper layers of planetary atmospheres by photodissociating important molecules including H₂O, CO₂, CH₄, thereby increasing the oxygen and ozone mixing ratios important for habitability. Both the EUV and strong Lyman- α radiation are largely absorbed by the interstellar medium and must be reconstructed or estimated to understand the radiation environment of exoplanets. In two recent papers, Linsky et al. (2013) and Linsky et al. (2014), we have presented robust methods for predicting the intrinsic Lyman- α and EUV fluxes from main sequence cool stars. Solar models and satellite observations (HST, FUSE, and EUVE) provide tests for the feasibility of these methods.

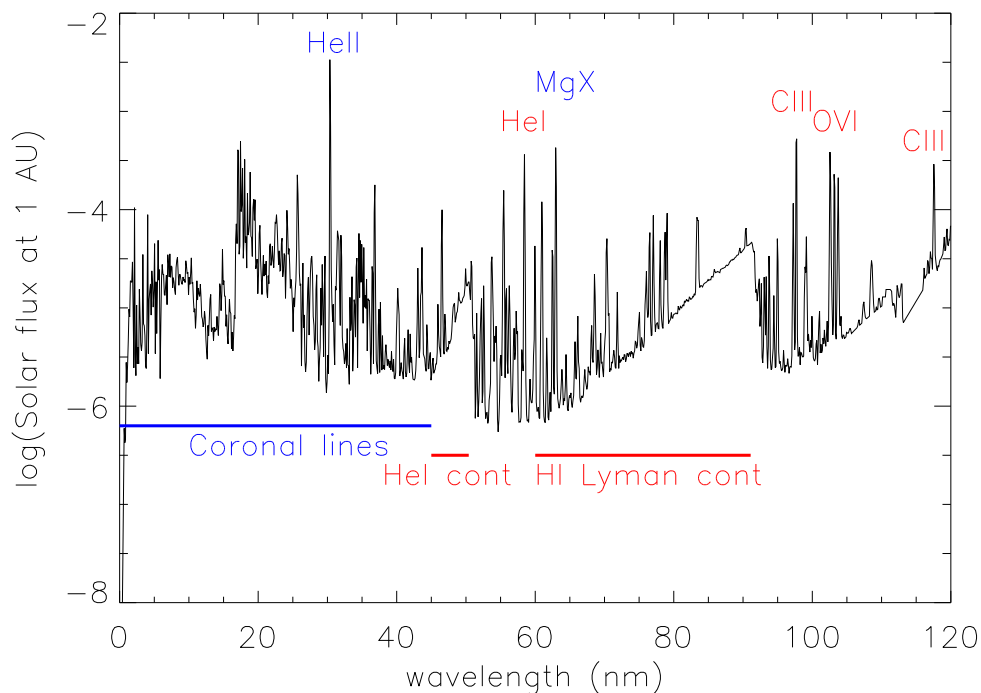


Figure 1.: The Solar Irradiance Reference Spectrum (SIRS) obtained at solar minimum (March–April 2008) (Woods et al. 2009). Flux units are $\text{Wm}^{-2}\text{nm}^{-1}$ at 1 AU.

1. Estimating the Host Star’s EUV Flux

The solar EUV spectrum (Figure 1) contains emission features produced in the chromosphere (e.g., H I Lyman and He I continua) and emission lines from the transition region and corona. Late-type stars should contain the same features, but the ISM absorbs all of the 40–91.2 nm flux and most of the flux at shorter wavelengths. The EUVE satellite obtained fluxes at $\lambda < 40$ nm for a few nearby stars.

Semi-empirical models of portions of the solar atmosphere with different heating rates (e.g., Fontenla et al. 2014) show that the EUV to Lyman- α flux ratios vary smoothly with the Lyman- α flux. We show these flux ratios in different wavelength bands in Figures 2-4. These figures also show the available flux ratios obtained from the EUVE satellite and reconstructed Lyman- α fluxes. These figures show that: the EUVE/Lyman- α flux ratios have a linear dependence on the Lyman- α flux for F-K stars and the ratios are constant for the M stars. The flux ratios for the F-K stars are similar to the solar flux ratios for the same Lyman- α fluxes.

Figure 5 shows the solar EUV/Lyman- α flux ratios for the 40–70 nm region where there are no stellar observations for comparison. Not shown are solar flux ratio plots for the 70–91.2 nm region and the 91.2–117 nm region where there is good agreement with FUSE satellite observations of 5 stars.

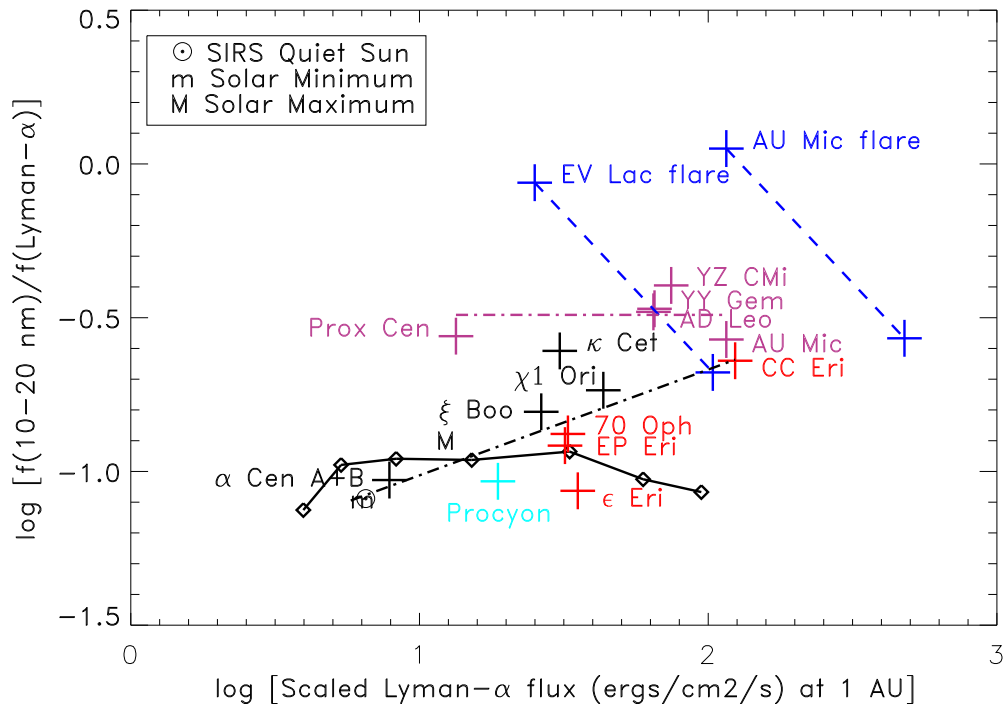


Figure 2.: Ratios of the 10–20 nm intrinsic flux (corrected for interstellar absorption) divided by the reconstructed Ly α flux vs. the reconstructed Ly α flux at 1 AU scaled by the ratio of stellar radii squared. The solid line-connected diamonds are the flux ratios in this passband for the Fontenla et al. (2014) semiempirical models 13x0 to 13x8 (from left to right). Flux ratios for one F star (cyan), four G stars (black), four K stars (red), and five M stars (plum) based on *EUVE* spectra are shown as ± 15 error bar symbols. The dash-dot (black) line is the least-squares fit to the solar and F, G, and K star ratios. The plum dash-dot line is the mean of the M star ratios excluding the EV Lac flare and AU Mic flare data. Flux ratios for EV Lac and AU Mic during flares (blue) are plotted two ways. The upper left symbols are ratios of EUV flare fluxes to quiescent Ly α fluxes. Dashed lines extending to the lower right indicate the ratios for increasing Ly α flux. The symbols at the lower end of the dashed lines are ratios obtained using the most likely values of the Ly α fluxes during flares.

2. Estimating the Star’s Lyman- α Flux

Photodissociation of H₂O, CH₄, CO₂ and other important molecules in exoplanet atmospheres is controlled by radiation from the host star at wavelengths shortward of 170 nm. The brightest emission line in this spectral region, the H I Lyman- α line at 121.6 nm, contains as much flux as the 116–169 nm spectrum of the Sun and as much flux as the whole ultraviolet spectrum (116–305 nm) of M dwarfs (France et al. 2013). Reconstructing the intrinsic Lyman- α line flux to correct for interstellar H I absorption is feasible for nearby stars but requires high-resolution Lyman- α line spectra with the HST/STIS instrument (see Wood et al. 2005; France et al. 2013).

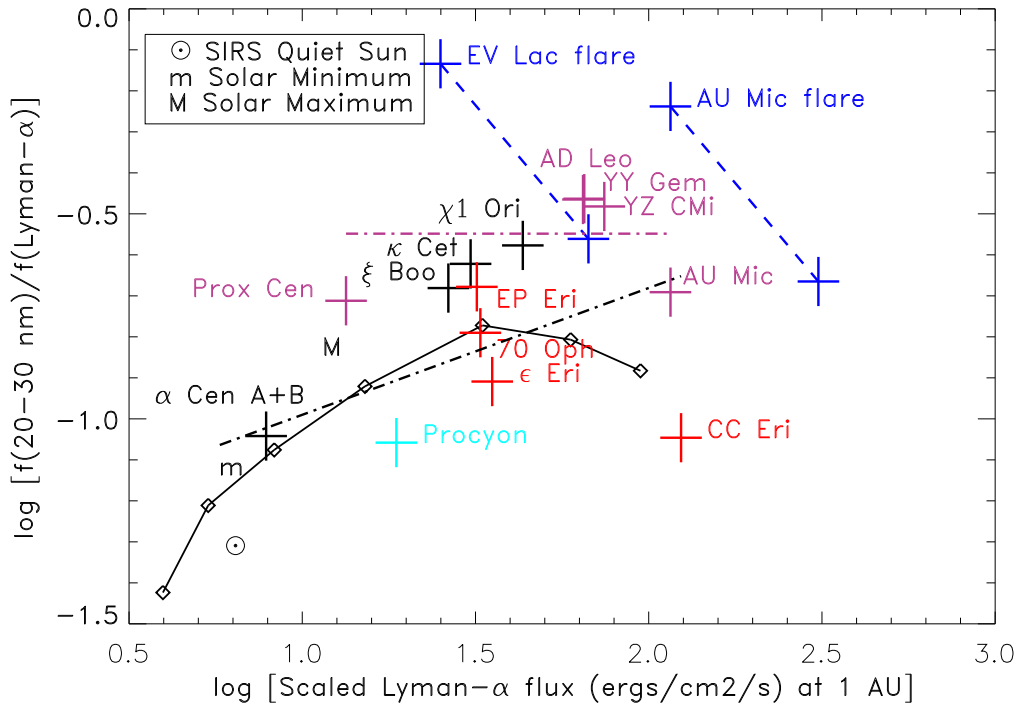


Figure 3.: Same as Figure 2 except for the 20–30 nm wavelength interval.

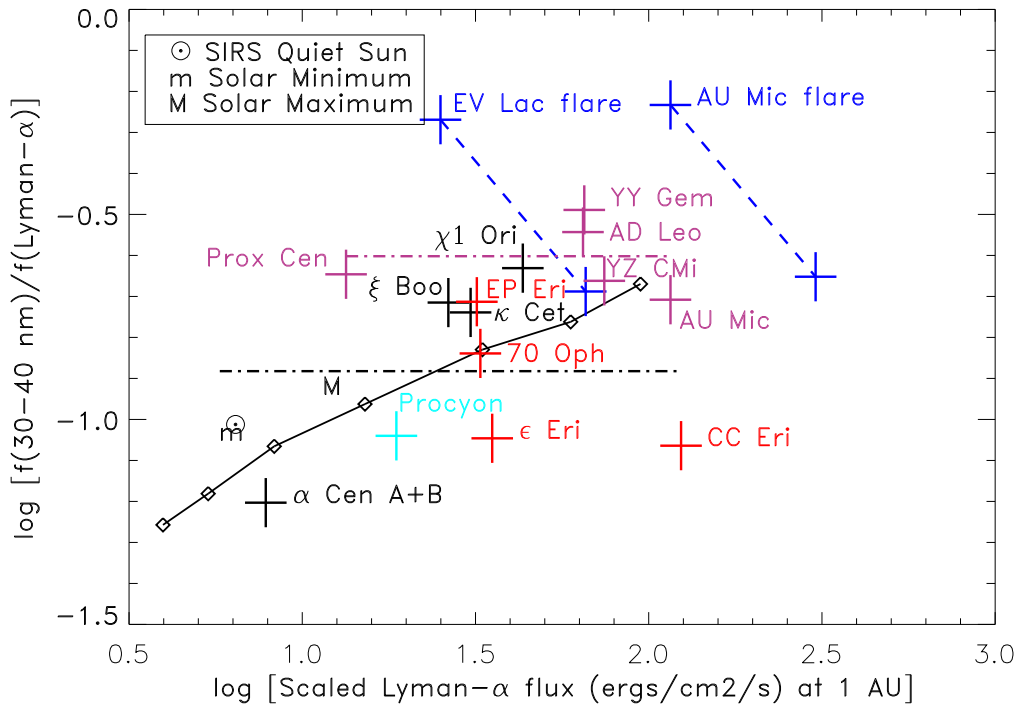


Figure 4.: Same as Figure 2 except for the 30–40 nm wavelength interval.

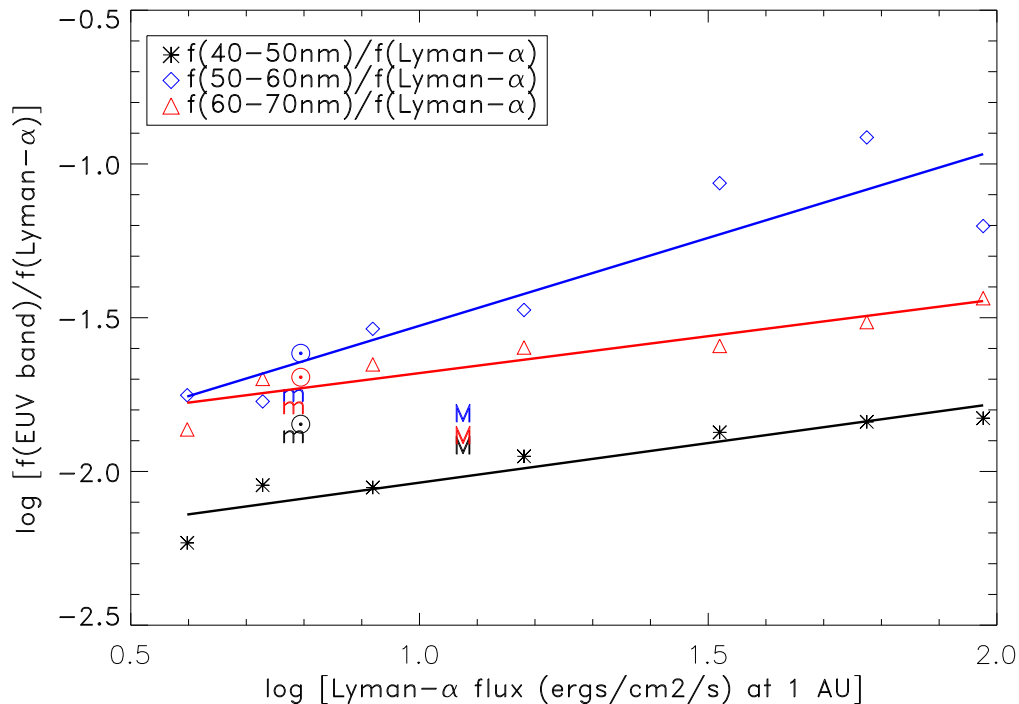


Figure 5.: Same as Figure 2 except for the 40–50 nm, 50–60 nm, and 60–70 nm wavelength bands.

From Wood et al. (2005) and France et al. (2012), we now have intrinsic Lyman- α fluxes for 45 F5 V to M5 V stars. We first study how accurately one can estimate the intrinsic Lyman- α flux from the T_{eff} of a star. Figure 6 shows that the range in intrinsic Lyman- α flux is more than an order of magnitude at a given T_{eff} . We can narrow this range considerably by including an activity indicator such as the rotation period (P_{rot}). The scatter about least-squares fit lines is generally less than a factor of 2 but larger for M dwarfs. The scatter is further reduced by plotting the Lyman- α flux in the habitable zone rather than at a standard distance of 1 AU. Note that the intrinsic Lyman- α flux in the habitable zone for M dwarfs is about 10 times larger than for the Sun.

One can obtain more accurate estimates of the intrinsic Lyman- α flux by comparison to other emission lines formed in the stellar chromosphere and transition region. Figure 7 shows the ratio of Lyman- α to the C IV 154.8+155.0 nm lines. If changes in the magnetic heating rate in a stellar chromosphere mainly alter the densities but not the thermal structure, then we anticipate that line ratios will depend gradually on line flux with little scatter about the least-squares fit lines. Figure 7 shows this to be the case for F5 V to K5 V stars but not the M stars. We believe that the large scatter for the variable M stars is due to observations of Lyman- α and the UV lines at different times. We find similar results when plotting ratios of Lyman- α to lines of C II, O I, and Mg II.

Figure 8 shows the correlation of the intrinsic Lyman- α flux with the flux of the Ca II H and K lines formed in the lower chromosphere. This correlation provides a tool for inferring the flux of the strongest ultraviolet emission line from optical spectra. Other UV emission lines and the EUV flux in different

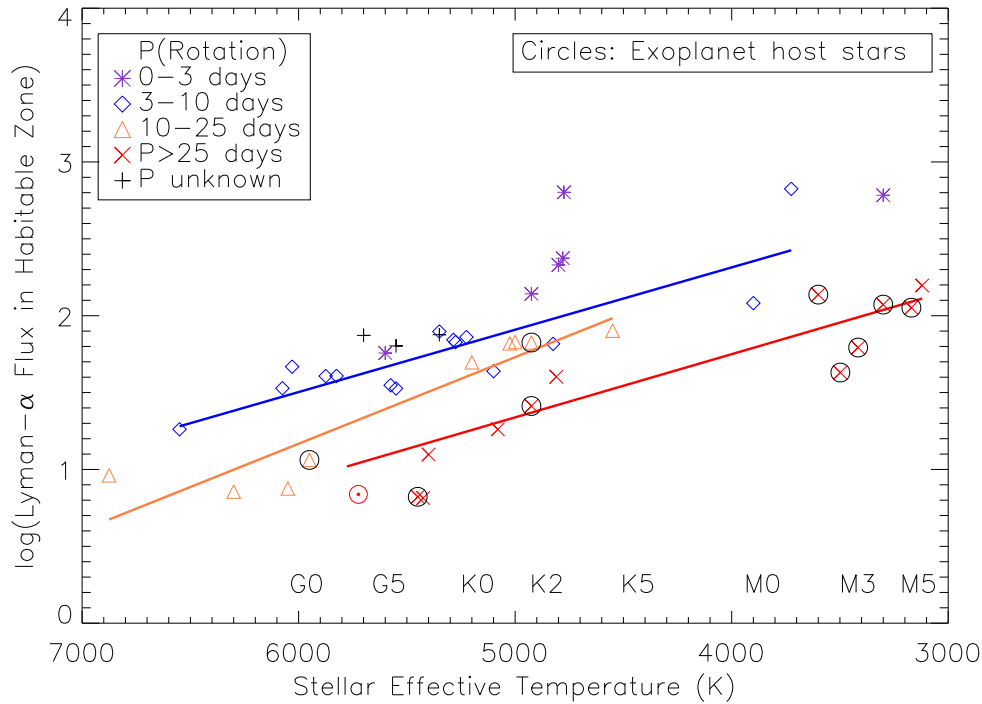


Figure 6.: Lyman- α flux at 1 AU vs. stellar effective temperature. The stars are grouped according to stellar rotation period: ultrafast rotators ($P_{\text{rot}} < 3$ days), fast rotators (3–10 days), moderate rotators (10–25 days), and slow rotators (> 25 days). Rotation period is a rough measure of the magnetic heating rate in the star’s chromosphere and corona. Host stars of exoplanets are circled and the quiet Sun is marked as a circled dot. Least-squares fit lines are shown for the fast, moderate, and slow rotators.

wavelength bands can then be inferred indirectly from the Ca II emission line fluxes.

3. Future Work

Our objective is to provide accurate fluxes required for computing the photochemistry and mass loss from exoplanet atmospheres. The reconstructed Lyman- α fluxes in the Linsky et al. (2013) paper are being used to construct new atmosphere models of terrestrial and mini-Neptune planets by Rugheimer et al. and by Miguel et al. We are also writing a paper that will present the complete spectra (X-rays to IR) for a representative sample of K and M stars including exoplanet host stars.

Acknowledgements. This work is supported by grants from the Space Telescope Science Institute to the University of Colorado. STScI is operated by the Association of Universities for Research in Astronomy, Inc., under NASA contract NAS 5-26555.

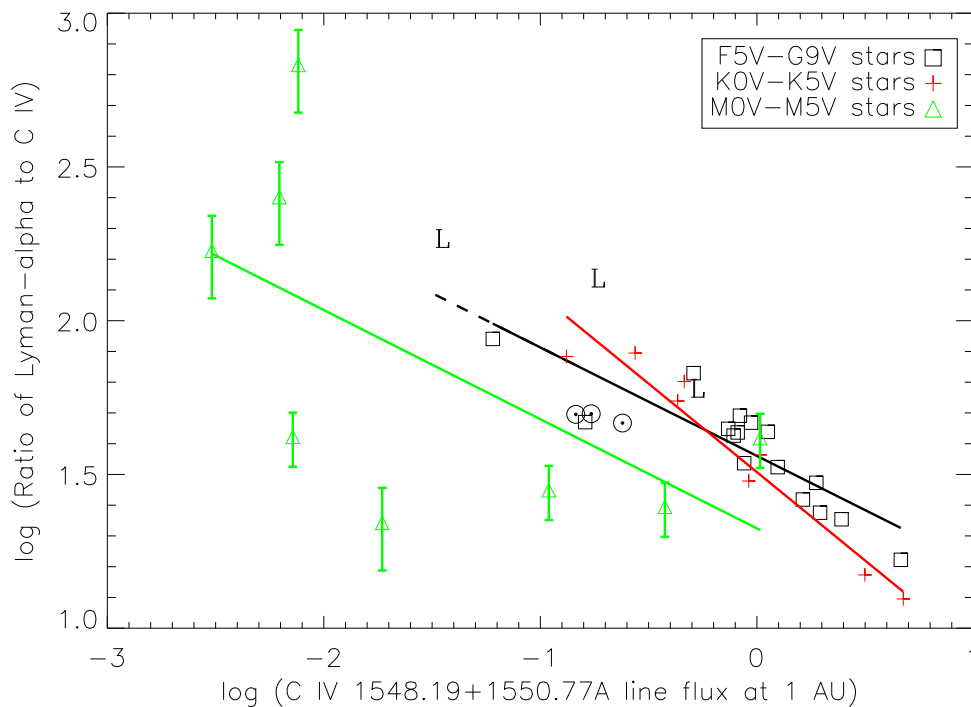


Figure 7.: Plot of the ratio of the Lyman- α to C IV 154.8+155.0 nm line flux vs. the C IV line flux at 1 AU. Included are stars between spectral types F5 V and M5 V, divided into three spectral type bins, the quiet Sun and the active Sun at two different times. The solar data are indicated by Sun symbols, and the L symbol refers to a star with low metal abundance $[\text{Fe}/\text{H}] < -0.30$. The solid lines are least-squares fits for each spectral type bin excluding the L stars and the Sun. The ratio for α Cen A is closest to the solar ratios. The errors bars are 20% for stars using the Wood et al. (2005) correction for missing Lyman- α flux or 30% for stars using the France et al. (2012) correction for missing Lyman- α flux.

References

- Fontenla, J. M., Landi, E., Snow, M., & Woods, T. 2014, *Solar Phys.*, 289, 515
- France, K., Linsky, J. L., Feng, T., Froning, C. S., & Roberge, A. 2012a, *ApJ*, 750, 32
- France, K., Froning, C. S., Linsky, J. L., Roberge, A., Stocke, J. T., Yian, F., Bushinsky, R., Désert, J.-M., Mauas, P., Vieytes, M., & Walkowitz, L. M. 2013, *ApJ*, 763, 149
- Linsky, J. L., France K., & Ayres, T. R. 2013, *ApJ*, 766, 69
- Linsky, J. L., Fontenla, J., & France, K. 2014, *ApJ*, 780, 61
- Wood, B. E., Redfield, S., Linsky, J. L., Müller, H.-R., & Zank, G. P. 2005, *ApJS*, 159, 118
- Woods, T. N., et al. 2009, *J. Geophys. Res.*, 36, L01101

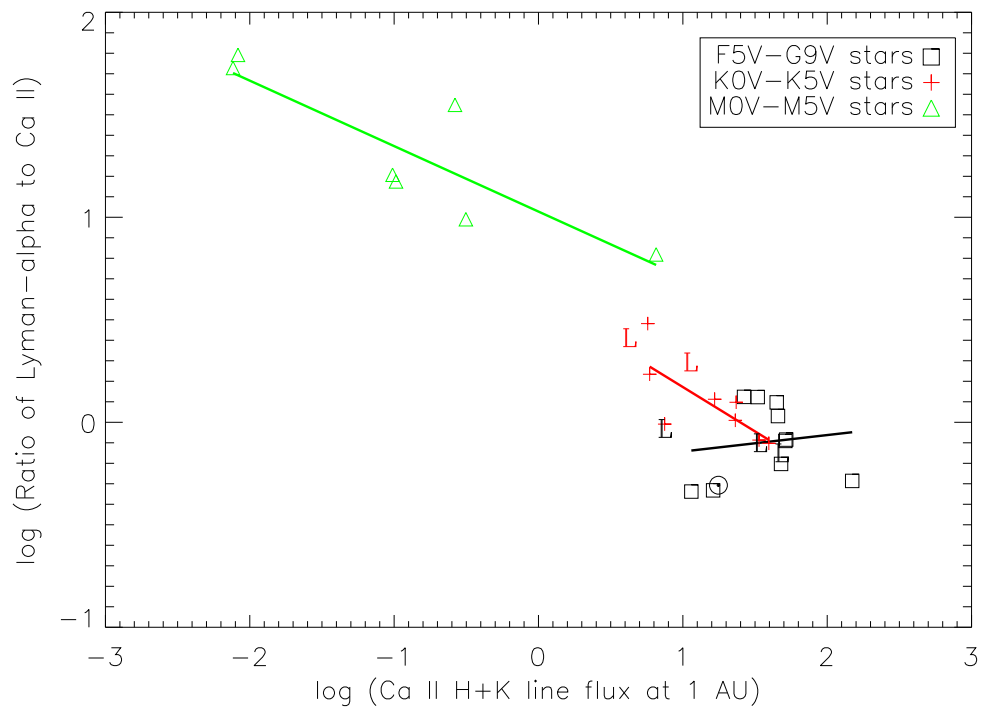


Figure 8.: Plot of the Lyman- α to Ca II 3933 + 3968 \AA line flux ratio vs. the Ca II line flux at 1 AU for the M0 to M5 stars. The solar data are indicated by the Sun symbol, and the L symbol refers to a star with low metal abundance $[\text{Fe}/\text{H}] < -0.30$. The solid lines are least-squares fits for each spectral type bin excluding the L stars and the Sun.

Chapter 21

The extension of the corona in classical T Tauri stars

J. López-Santiago¹, E. Flaccomio², S. Sciortino²

¹*Facultad de Ciencias Matemáticas, Universidad Complutense de Madrid, E-28040 Madrid, Spain*

²*INAF-Osservatorio Astronomico di Palermo, Piazza del Parlamento 1, I-90134 Palermo, Italy*

Abstract. The extension of the corona of classical T Tauri stars (cTTS) is under discussion in the Astrophysical community. The standard model of magnetic configuration of cTTS predicts that coronal magnetic flux tubes connect the stellar atmosphere to the inner region of the disk. Gas accretion from the disk to the star takes place along those magnetic tubes. Flaring events have been detected in cTTS. The weakest flares are assumed to have their origin in solar-like magnetic loops. However, strong, long-duration flares may be related to those long structures connecting the star and the disk. Such scenario is supported by some past result based on the use of hydrodynamic models with the assumption that those strong flares take place in single or small groups of loops. This assumption is still controversial. To disentangle this controversy, new independent measurement of the loop length are needed. We present an approach for determining the length of flaring loops based on the quasi-periodic MHD oscillations of loop emission after strong flares.

1. Model for magnetic tube oscillations

A longitudinal wave that propagates along a tube of length L with a velocity c_t (tube velocity) shows a period P such that $P = 2L/c_t$. In the magnetohydrodynamic (MHD) approximation, the tube velocity satisfies the relation

$$\frac{1}{c_t^2} = \frac{1}{c_s^2} + \frac{1}{c_A^2} \quad (21.1)$$

where $c_A = B/(4\pi n_i m_i)^{1/2}$ (in the c.g.s.) is the Alfvén velocity and $c_s = (2\gamma k_B T/m_p)^{1/2}$ is the sound velocity for an ideal gas. Here, n_i and m_i are, respectively, the ion number density and the ion mass and B is the magnetic field strength. In the

sound velocity equation, γ is the adiabatic index, m_p is the proton mass (assuming total ionization for the gas), k_B is the Boltzmann constant and T is the plasma temperature.

MHD oscillations may be caused by different processes, including spontaneous reconnection (e.g. Nakariakov et al. 2010). A particularly interesting process is that proposed by Zaitsev & Stepanov (1989). According to the authors, the evaporation of chromospheric material during the flare produces a centrifugal force that causes, alternatively, stretch and contraction of the magnetic tube and triggers Alfvén oscillations of the magnetic flux tube that are damped. The relative amplitude of the oscillation follows the relation for slow magnetoacoustic waves

$$\frac{\Delta I}{I} = \frac{4\pi n T}{B^2} \quad (21.2)$$

being n the plasma density, T its temperature, B the magnetic field strength, I the oscillation intensity and $\Delta I/I = \Delta B/B$.

The existence of a relation between the magnetic field and the relative amplitude of the oscillation permits to determine the strength of the magnetic field at the top of the coronal loop by measuring the damping of the intensity of the oscillation and the parameters of the plasma (temperature and density). This approach was applied by Mitra-Kraev et al. (2005) for the oscillations observed in an X-ray flare of the M dwarf AT Mic, obtaining $B \sim 100$ G and a loop length $L \sim 10^{10}$ cm, consistent with the value obtained assuming radiative cooling and pressure balance (Shibata & Yokoyama 2002). Recently, Pillitteri et al. (2014) used the same model to determine the length of a flaring loop in the hot-jupiter host star HD 189733. The authors obtained a length of $\sim 2-4 R_\star$, suggesting the probable interaction between the star and the planet.

In a purely hydrodynamic (HD) scenario, the warming of the chromosphere at the loop base is very brief and the loop is not completely filled up with hot material. Blobs of hot dense material ascend long the tube at supersonic velocities ($v > c_t$) from both sides of the loop until they encounter at the top and descend again. The process is periodic until final dissipation and produces oscillations in density detected in HD modeling. In this case, there is no way to determine the length of the flaring loop, but a lower limit can be determined assuming the wave is propagating at the velocity of sound in the tube ($v = c_t$).

2. Application to cTTS in Orion

Figure 1 shows oscillations detected in the X-ray band in some classical T Tauri stars (cTTS) in the Orion Nebula Cluster (ONC). Light curves are from the COUP (Favata et al. 2005). Rapidly damped slow oscillations are observed in each case. Table 1 lists results on the loop lengths determined by using Zaitsev & Stepanov (1989)'s method. Our results are compared to those obtained by Favata et al. (2005) from HD modeling (Reale et al. 2004). The observed similarity with results from Favata et al. (2005) suggests that the oscillations are related to Alfvén waves propagating along the reconnected tube.

3. Discussion and conclusions

By using the simple model of Zaitsev & Stepanov (1989) for explaining the appearance of oscillations in reconnected magnetic loops in cTTS, we determined loop lengths for those stars that are in agreement with the results obtained by Favata et al. (2005) from hydrodynamic modeling. In their work, Favata et al. (2005) assumed that the observed flare light curves come from the ignition of a single loop, according to Reale et al. (2004). This approach is quite controversial and many authors disagree with it and prefer to use scaling laws to determine the parameters of the flaring loop (e.g. Aschwanden et al. 2008). The assumption of the single loop scenario yields to long loops in strong flaring events, with magnetic field strengths similar to those found in similar loops in the Sun.

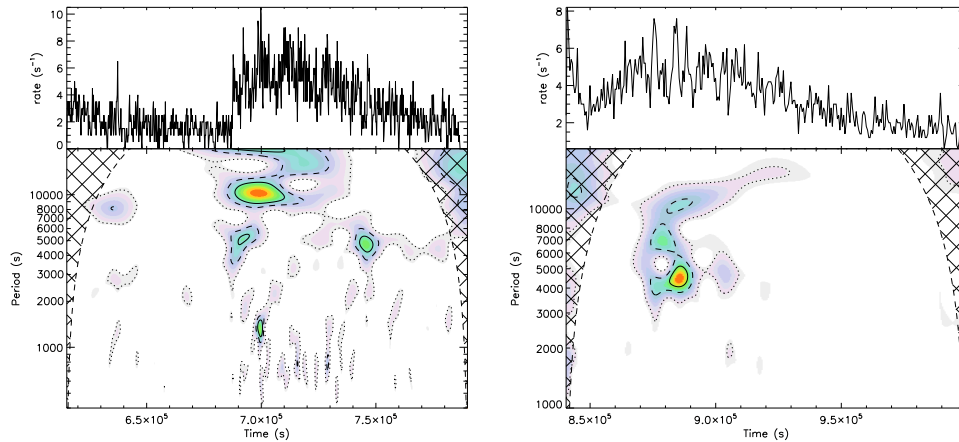


Figure 1.: Two examples of oscillations detected in some cTTS in the ONC (Favata et al. 2005). In both cases, oscillations occur at the top of the rise phase of the flare’s light curve, but the period of the oscillation differs.

Table 1.: Results of applying the Zaitsev & Stepanov (1989)’s model to several cTTS in the COUP sample (Favata et al. 2005).

ID	Favata et al. (2005)			This work	
	T_{peak} (MK)	L (10^{10} cm)	L/R_{\star}	L (10^{10} cm)	L/R_{\star}
43	142	112 (75 - 134)	5.5	100.0	5.0
597	87	22 (0 - 75)	1.6	26.0	1.9
976	270	76 (...)	12.0	30.0	4.7
1608	258	82 (0 - 99)	6.7	108	9.0

Instead, the using scaling laws shorter loops with stronger magnetic fields are predicted. To disentangle this dichotomy is important in the case of cTTS, in order to validate or disprove the canonical scenario of the interaction between star and disk (Camenzind 1990). The use of an independent method to measure the length of the reconnecting magnetic loops can deeply improve in the knowledge of the structure of the corona of cTTS. In particular, analyzing oscillations like the ones studied in this work we will be able to determine parameters from flaring loops and compare results with those obtained by different methods.

Acknowledgements. J.L.-S. acknowledges the Spanish Ministerio de Economía y Competitividad for support under grant AYA2011-29754-C03-01.

References

- Aschwanden, M. J., Stern, R. A., Güdel, M. 2008, ApJ, 672, 659
 Camenzind, M. 1990, Reviews in Modern Astronomy, 3, 234

Favata, F., Flaccomio, E., Reale, F., et al. 2005, *ApJS*, 160, 469

Mitra-Kraev, U., Harra, L. K., Williams, D. R., & Kraev, E. 2005, *A&A*, 436, 1041

Nakariakov, V. M., Inglis, A. R., Zimovets, I. V., et al. 2010, *Plasma Physics and Controlled Fusion*, 52, 124009

Pillitteri, I., Wolk, S. J., Lopez-Santiago, J., et al. 2014, *ApJ*, 785, 145

Reale, F., Güdel, M., Peres, G., & Audard, M. 2004, *A&A*, 416, 733

Shibata, K., & Yokoyama, T. 2002, *ApJ*, 577, 422

Zaitsev, V. V., & Stepanov, A. V. 1989, *Soviet Astronomy Letters*, 15, 66

Chapter 22

X-Shooter Medium Resolution Brown Dwarfs Library

E. Manjavacas, B. Goldman, J. M. Alcalá, M. Bonnefoy, F. Allard, R. L. Smart, V. Béjar, M. R. Zapatero-Osorio, T. Henning, H. Bouy.
Max Planck Institute für Astronomie, Königstuhl, 17.
D-69117 Heidelberg, Germany
manjavacas@mpia.de

Abstract. We obtain medium-resolution spectra in the optical (550-1000 nm, $R \sim 5400$) and the near-infrared (1000-2500 nm, $R \sim 3300$) using the *Wideband ultraviolet-infrared single target spectrograph* (X-Shooter) at the Very Large Telescope (VLT). Our sample is compound of 22 brown dwarfs binary candidates with spectral types between L1 and T7. We aim to empirically confirm or refute the binarity of our candidates, comparing them to spectral templates and to other brown dwarfs in a color-magnitude diagram, for targets that have published parallaxes. We use X-shooter at the VLT to obtain medium resolution spectra of the targets. We develop a slightly different analysis depending of the type of binaries we search for. To find L plus T brown dwarf binaries candidates, we compute spectral indices to select L-brown dwarfs plus T-brown dwarf binaries, and then we compare them to single and composite template spectra. To find potential L plus L or T plus T brown dwarf binaries, we first simulate their spectra creating synthetic binaries using combination of single template spectra. Then we compare them to our set of spectral libraries and composite of them to test if our method is able to find these binaries. Using spectral indices, we select four possible candidates to be combination of L plus T brown dwarfs: SIMP 01365662+0933473, 2MASSI J0423485-041403 (T0, known binary), DENIS-P J0255.0-4700 and 2MASS J13411160-3052505. We compare these candidates to single brown dwarf template spectra and combinations of them, and we select the best matches. All candidates beside SIMP 01365662+0933473 have decent matches to composite of two single template spectra. DENIS-P J0255.0-4700 have also good agreements to several late L and early T single template spectra. To find L plus L or T plus T brown dwarfs candidates, test the comparison to templates method use

before to find L plus T brown dwarf binaries. The test consist on finding synthetic L plus L and T plus T binaries by comparing with spectral templates. We conclude that we cannot find L plus L and T plus T binaries using comparing to single and composite spectral templates, because the main difference between different L or T spectral types is just the spectral energy distribution. Optical and near infrared spectra report in this paper will serve as templates for future studies in any of these wavelengths. In the near future, Gaia satellite will release high precision parallaxes of more than one billion of objects in the Milky Way, including hundred of brown dwarfs. These parallaxes will allow us to detect the overluminosity of brown dwarf binaries.

1. Introduction

Stars are social celestial bodies. They are normally born in nurseries of several entities. After childhood they leave their birth place and settle on the main sequency. A majority of stars remain in couples or hierarchical systems. Multiplicity has long been used as a powerful constrain on the star formation process, and they provide contrains in fundamental parameters, such of dynamical masses, essential to test atmospheric models. It is well known that the binary fraction decreases when decreasing mass. This fraction decreases from 80%-60% for O, A, B and G, K stars to 40% for the M dwarfs (??).

The decreasing trend for binarity seems to be prolonged to the substellar regime. ?, ?, ?, ?, ?, ?, ?, ?, ? and ? estimate the fraction of binarity of about 20% for L and T brown dwarfs.

? determined that 98% of the brown dwarfs have separations smaller as 20 AU. The peak of the separation distribution of brown dwarfs is ~ 3 UA, which is very close to the resolution limit of the high resolution imaging surveys, as ? pointed out. ? searched for low-mass stars and brown dwarfs binaries in Chamaleon using the radial velocity method, and concluded that the percentage of brown dwarfs binary systems with separations below 1 AU are less than $\sim 10\%$. ? determined that the binary frequency of very tight systems is $2.5^{+8.6}_{-1.6}\%$. The fraction of very wide systems, i.e. systems with separations higher than 100 AU, was estimated by ? and ? among others, to be quite small $\sim 1\%$.

Mass is the parameter that determines the evolution of an object. As brown dwarfs do not burn hidrogen due to their low masses, age for objects is difficult to estimate. Monitoring binary systems orbits we are able to measure the dynamical masses empirically. Since the discovery of brown dwarfs, there have been several programs aiming to derive dynamical masses (????????). These programs provide feedback to constrain fundamental parameters of their components, such as age, mass, radius, temperature, etc. and test evolutionary and atmospheric models.

Atmospheric models allow us to disentangle the effect of varying T_{eff} , $\log g$, and (metallicity) M/H on the spectral features. Below $T_{eff} \sim 2600$ K, models predict that clouds of iron and silicate grains begin to form, changing the opacity (?, ?, ?, ?, ?, ?, ?).

? estimated that a fraction of $\sim 6-7\%$ of brown dwarf binary systems have not been detected yet, as a consequence of observational biased. In this paper, we aim to find tight brown dwarf binary systems among a sample of 24 objects which were found to have different spectral classification in the optical and in the near-infrared or peculiar spectra in comparison with objects of the same spectral type. We intent to contribute to the improvement of the brown dwarf binaries statistics, classify our objects in the optical and in the near-infrared as the same time.

2. Sample selection

We selected a sample of 24 brown dwarfs found in the literature with optical spectral types between L2 and T7, which have discrepant optical and near-infrared classification or peculiar spectra. Some of those unresolved binaries can probably already be guessed from this discrepancy, based on the optical or near-infrared schemes. Furthermore, we added some know brown dwarfs binary systems, LHS 102B (L4.5) and SDSS J042348.56-041403.4 (T0) [hereafter SD0423] to calibrate the results and confirm the reliability of our analysis. Two of our objects had noisy spectra, so we decided not to use them for our analysis. Therefore, we finally count with a sample of 22 optical and near-infrared spectra. Our list of candidates and their physical properties reported in the literature and their references can be found in Table 1.

3. Observations and data reduction

Our targets were observed using X-Shooter (Wideband ultraviolet-infrared single target spectrograph) on the Very Large Telescope (VLT) between October 2009 and June 2010, under programs 084.C-1092(A), 085.C-1062(A) and 085.C-1062(A). X-Shooter covers a range between 300-2500 nm. The instrument is separated into three arms: UVB (300-550 nm), optical (550-1000 nm) and near-infrared (1000-2500 nm). It was operated in echelle slit nod mode, using the 1.6" slit for the UVB arm, and the 1.5" for the optical and the near-infrared arms. This setup provides resolutions of ~ 3300 in the UVB and NIR, and ~ 5400 in the VIS. We moved the object along the slit between two positions following an ABBA pattern. Flux detected in the UVB arm is extremely weak, so that we do not use spectra taken in this range. Telluric standards are observed before or after every target at the same airmass. Bias, darks and flats are taken at the beginning of every night. Arc frames are taken every second day.

The spectra were reduced using the ESO X-Shooter pipeline in version 1.3.7. In the reduction cascade, the pipeline delete the non-linear pixels and subtracts bias in the optical or dark frames in the near-infrared. It generates the guess order from a format-check frame, a reference list of arc line and a reference spectral format table. It refines the order guess table into an order table from an order definition frame obtained by illuminating the X-Shooter pinhole with a continuum lamp. The master flat frame and the order tables tracing the flat edges are created. Finally, the pipeline determines the instrumental response and science data are reduced in slit nodding mode. In the case of the data taken in the near infrared, the pipeline did not product

Table 1.: List of observed targets. Magnitudes are given in 2MASS system.

Name	d_{trig} (pc)	SpT OPT	SpT NIR	Remarks
LHS 102B	13.2±0.7	L5	L4.5	Binary
2MASS J00361617+1821104	8.8±0.1	L3.5	L4	No binarity
2MASS J00531899-3631102		L3.5	L4	
SIMP 01365662+0933473	6.0±0.1		T2.5	
2MASS J01443536-0716142		L5		Red
2MASS J02182913-3133230		L3	L5.5	
DENIS-P J0255.0-4700	4.9±0.1	L8	L9	
2MASS J02572581-3105523	10.0±0.7	L8	L8.5	
2MASS J03480772-6022270			T7	
2MASS J03552337+1133437	9.1±0.1	L5	L3	Young
2MASSI J0423485-041403	13.9±2.1	L7.5	T0	Binary
2MASS J04390101-2353083	9.1±0.3	L6.5		
2MASS J04532647-1751543		L3pec		Young?
2MASS J05002100+0330501		L4	L4	
2MASS J05395200-0059019	12.2±4.5	L5	L5	No binarity
2MASS J06244595-4521548	11.9±0.6	L5pec	L5	
G1 229B	5.8±0.4		T7pec	MP&Young
2MASS J10043929-3335189	17.0±1.6	L4	L5	
2MASS J11263991-5003550		L4.5	L6.5	Blue L
2MASS J13411160-3052505		L2pec	L2	
2MASS J18283572-4849046	11.9±1.1		T5.5	
2MASS J21513839-4853542			T4	

a satisfactory response function. In these case, we utilized the telluric star of the corresponding to every science target in that night to obtain the response function. We use the non-response calibrated spectrum of the target and the non-response calibrated spectra of the telluric star. We remove cosmetics and cosmics from the telluric stars, as well as the H and He absorption lines, using a Legendre polynomial fit of the pseudocontinuum around the line. Then we divide the telluric by a black body synthetic spectra with the same temperature as the telluric star (?). Finally, to calibrate in response, we use the package *noao.onedspec.telluric* from the software *Image Reduction and Analysis Facility*, (IRAF).

To make sure that the flux in the whole near-infrared spectra was correctly scaled, we calibrated flux of our near-infrared spectra using fluxes given by 2MASS (Two Micron All Sky Survey). We convolved our near-infrared spectra with J, H and K filter transmission curves of 2MASS. The resulting spectra were integrated. Then we calculate the flux in 2MASS for our targets in the J, H and K bands using 2MASS magnitudes (?). Finally, we calculate the scaling factor for J, H and K bands and we multiply our near-infrared spectra in J, H and K filters to have the same flux as the given by 2MASS. We need to scale the flux from the optical spectra to be continue with the flux in the near-infrared spectra. In the overlapping wavelengths of the optical and near-infrared spectra, we calculate a scaling factor. This factor is

calculated as the median of the flux in the overlapping wavelengths of the near-infrared spectra, divided by the median of the flux in the overlapping wavelengths of the optical spectra.

4. Empirical analysis

4.1 Finding L plus T brown dwarf binaries

Brown dwarf spectral binaries that are combinations of a L and a T brown dwarf have been in the past years widely studied (??). The combined spectra of these type of binaries are expected to show peculiar characteristics, as they are a combination of two quite different spectra, with different molecules absorptions (?). In L brown dwarf spectra we find NaI, and two KI doublets in the J-band. In the H-band, appear the FeH absorption from 1.59 to 1.75 μm and in the K-band, we find the first overtone of band heads of ^{12}CO . In contrast, in T brown dwarf spectra we find also NaI and KI alkali lines like in the L-sequence, plus CH_4 bands in the range 1.15-1.25 μm . In the H-band there is CH_4 feature at 1.67 μm , and in the K-band we find CH_4 at 2.2 μm . ? describe differences of L plus T binaries in comparison with single template spectra: in general, they show bluer spectral energy distribution in the near-infrared, and in particular, some spectral features vary, like the CH_4 and H_2O at 1.1 μm which are deeper for binaries and the CH_4 feature at 1.6 μm is stronger in comparison to the 2.2 μm band. Using the differences found, ? and ? define some spectral indices which help to detect L plus T brown dwarf binaries regarding these peculiar spectral characteristics. Objects that satisfy two criteria, are considered weak brown dwarf binary candidates, and objects that satisfy three or more criteria are strong binary candidates.

Calculating these indices was the first step of our empirical analysis, because just with eight plots we can select those objects from our sample that are candidates to be L plus T binaries. In Fig. 1 we show the result of calculating ? and ? indices. Regarding the result of these plot, object 2MASS J01365662+0933473 [hereafter SIMP0136] satisfy four criteria, objects 2MASS J0423485-041403 [hereafter SD0423], which is a known binary, DENIS-P J0255.0-4700 [hereafter DE0255] and 2MASS J13411160-3052505 [hereafter 2M1341], satisfy two criteria. In Section 5., taking into account the whole analysis and the bibliography, we will further discuss whether, these objects are strong candidates to be binaries or not.

The next step in the empirical analysis consists on compare our spectra with several libraries of template spectra. We degrade our X-Shooter spectra to the resolution of each template before compare and we reinterpolated library spectra and X-Shooter spectra to the same grid. We used medium resolution template spectra of L and T field dwarfs ($R \sim 2000$??). We also compared our spectra to low resolution templates ($R \sim 120$) of the SpeX Prism Spectral Library^a. From this analysis we find the best matches to single and composite spectra, previously calibrated in flux to the same distance. To identify the best matches we use a χ^2 as explained in ? and visual inspection. We show the best match to potential L plus T objects in Appendix 7..

^a<http://pono.ucsd.edu/~adam/browndwarfs/spexprism/>

After compare to single and composite spectra, we find best matches to these selected objects. Plots to the following results are available in Appendix 7.. The best match to object SD0423 is a composite spectra formed by 2MASS15150083+4847416 (L6) and SDSS125453.90-012247.4 (T2). The best match to SIMP0136 spectra is the spectrum of SDSS152103.24+013142.7, which is a single T2 template. Object DE0255 is well reproduced by several single SpeX late L and early T template spectra: SDSS085234.90+472035.0 (L9.5), SDSS105213.51+442255.7 (T0.5) and 2MASS0328426+230205 (L9.5), among others. Nevertheless, there are also good agreements of these spectra to composite spectra: SDSS103931.35+325625.5 (T1) and SDSS163030.53+434404.0 (L7) and SDSS035104.37 (T1) and SDSS104409.43+042937.6 (L7). Object 2M1341 is classified as L2 with peculiar spectra. The best matches to this object are actually combinations of L plus T brown dwarfs templates: SDSS 175805.46+463311.9 (T6.5) and GJ1048B (L1) and 2MASS 1217110-031113 (T7) and GJ1048B (L1). Nonetheless, none of the matches are able to fully reproduce features in the H and K bands.

4.2 Finding L plus L or T plus T brown dwarf binaries

Spectroscopy search of brown dwarf binary pairs L plus L and T plus T has not been as developed as for L plus T binaries. Differences between L or T brown dwarfs of different spectral types is mainly in the spectral energy distribution, but the difference in spectral features is almost negligible, therefore the search of pairs of binaries with similar spectral types becomes challenging.

Before comparing to the set of libraries used in Section 4.1, we first test the effectivity of our method using synthetic binaries. For this we choose several L and T single and not peculiar brown dwarfs from the SpeX library. Then we calibrate their fluxes to the same distance, using the absolute magnitude-spectral type relation published by ?. We combine different pairs of L brown dwarfs with L brown dwarfs and different pairs of T brown dwarfs with T brown dwarfs, creating L plus L and T plus T synthetic binaries. We produce several L plus L brown dwarf binary pairs: 2MASS01303563-4445411B (L6) [hereafter 2M1303-4445] and DENIS-PJ220002.05-303832.9B (L0) [hereafter DE2200-3038], SDSSJ111320.16+343057.9 (L3) [hereafter SD1113+3430] and DE2200-3038 (L0) , and SDSSJ121951.45+312849.4 (L8) [hereafter SD1219+3128] and SDSSJ111320.16+343057.9 (L3) [hereafter SD1113+3430]. We create two T plus T brown dwarf binary pairs: 2MASSJ1553022+153236 (T7) [hereafter 2M1553+1532] and 2MASSJ11220826-3512363 (T2) [hereafter 2M11220-3512], and SDSSJ015141.69+124429.6 (T1) [hereafter SD0151+1244] 2MASSJ04070885+151456 (T5) [hereafter 2M0407+1514] and a L plus T pair: SDSSJ104409.43+042937.6 (L7) [hereafter SD1044+0429] and 2M11220-3512 (T2).

We compare L plus L, T plus T and L plus T brown dwarf binaries pairs mention before to single SpeX templates and find best matches. Our objective is to test if synthetic L plus L and T plus T binaries can be found by comparing to spectral library spectra. Figures showing best matches are shown in Appendix 7.. For L plus L pairs, 2M1303-4445 (L6) and DE2200-3038 (L0),

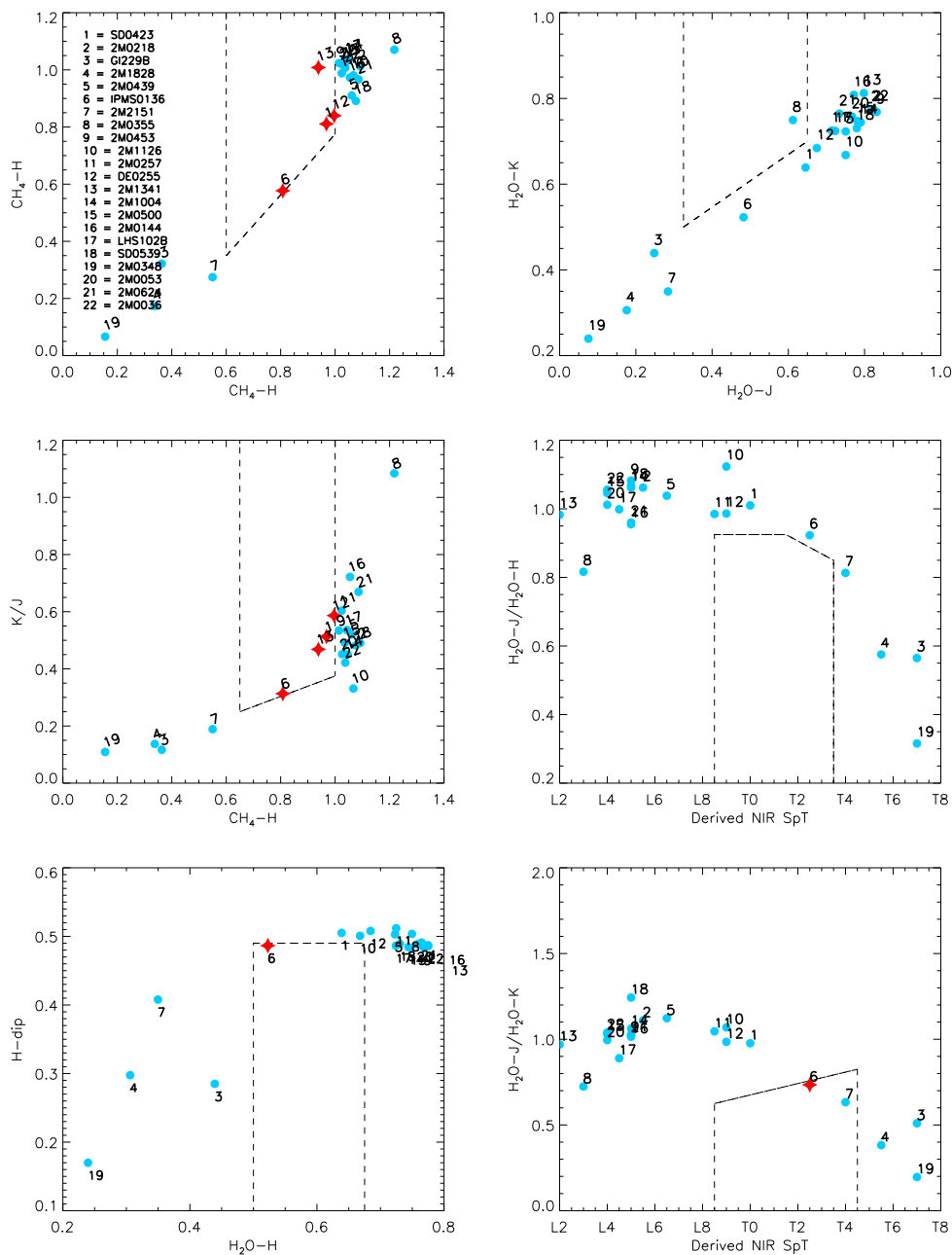


Figure 1.: Spectral index selection. We compare H_2O-J vs H_2O-K , CH_4-H vs CH_4-K , CH_4-H vs K/J , H_2O-H vs $H-dip$, and finally the estimated spectral type using SpeX template spectra vs H_2O-J/H_2O-H and H_2O-J/CH_4-K . Numbers 1-22 correspond to the name of our objects.

SD1113+3430 (L3) and DE2200-3038 (L0), and SD1219+3128 (L8) and SD1113+3430 (L3), best matches are: 2MASS0345432+254023 (L1) and 2MASS2130446-084520 (L1.5) for L0+L6, 2MASS2130446-084520 (L1.5) and HD89744B (L early) for L3+L0 and DENIS-PJ1228-1547 (L6±2) and 2MASSJ14283132+5923354 (L4) for L3+L8, Spex single templates. In Appendix 7. we show two best matches for every synthetic binary. For T plus T synthetic binary pairs, 2M1553+1532 (T7) and 2M11220-3512 (T2), and SD0151+1244 (T1) and 2M0407+1514 (T5), the best matches are: SDSSJ120602+281328 (T3) and SDSS175032+175903 (T3.5) for T2+T7, SDSSJ102109-030420 (T3) and SDSS143945+304220 (T2.5) for T1+T5. Spex single templates. The best match found for the synthetic spectra composed by SD1044+0429 (L7) and 2M11220-3512 (T2) is 2MASS J22541892+3123498 [hereafter 2M2254+3123]. 2M2254+3123 is a strong brown dwarf binary candidate (?) with T4 spectral type.

From this analysis, we conclude that L plus L and T plus T brown dwarfs binaries may not be straightforward to detect just by comparing with single or composite spectral libraries. Therefore, additional data will be necessary to find these binaries, i.e. parallaxes or high resolution imaging. From our 22 objects sample, there are distances for 12 of the objects, with precisions around 10%. Color-magnitude diagrams (CMD) showing J-H and J-K in the MKO (Mauna Kea Observatory) system versus absolute magnitude in J are presented for these objects (Fig. 2). In Fig. 2, the two known binaries from our sample stand out over objects with their same spectral types, together with Gl229B. Nevertheless, photometry of Gl229B it may not be reliable enough, because of the proximity of the companion. For the rest of the objects in the same, it is difficult to extract conclusions, as there are not clear outliers.

In Table 2 we show all best matches of our objects to spectral libraries ?, ? and Spex libraries. We show the best matches plots in Section 7.. In Table 2 we do not include those objects for which we did not find a match to spectra from spectral libraries. For objects 2M0348 (T7), Gl229B (T7), 2M1828 (T5.5) and 2M2151 (T4) we did not find lots of late T template spectra in ? and ? libraries and in SpeX, which can explain the lack of decent matches to these objects. Objects 2M0624 (L5:) and 2M1126 (L6.5:) have peculiar spectra, so we can expect not to find a acceptable match. Object 2M0355 (L5) is a young object (?), therefore we can expect not to find a decent match to spectra from field brown dwarfs in ?, ? and SpeX.

5. Revised properties

In this section we aim to revise properties of some of our objects taking into account our results from Section 4..

5.1 SIMP 01365662+0933473

Object SIMP 0136 was discovered by ? in the SIMP (Sondage Infrarouge de Movement Propre) near infrared proper motion survey, and it was classified as a T2.5. ? searched for companions using high resolution imaging with NACO at VLT with sensitivity of 0.2" (1-40 AU), but no companions were found. ? detected photometric variability in J and K band with a modulation

Table 2.: Best matches spectra coming from spectral libraries

Name	Best match	Library
LHS 102B	SDSS 083506.16+195304.4 (L4.5)	SpeX
2MASS J00361617+1821104	2MASS 02081833+2542533 (L1)	?
2MASS J00531899-3631102	2MASS 15074769-1627386 (L5)	?
2MASS J01443536-0716142	2MASS 22244381-0158521 (L4.5)	?
2MASS J02182913-3133230	Kelu-1 (L2)	?
2MASS J04390101-2353083	2MASS 15150083+4847416 (L6)	?
2MASS J04532647-1751543	2MASS 15150083+4847416 (L6)	?
2MASS J05002100+0330501	2MASS 15065441+1321060 (L3)	?
2MASS J05395200-0059019	2MASS 18131803+5101246 (L5)	SpeX
2MASS J10043929-3335189	2MASS 11463449+2230527AB (L3)	?

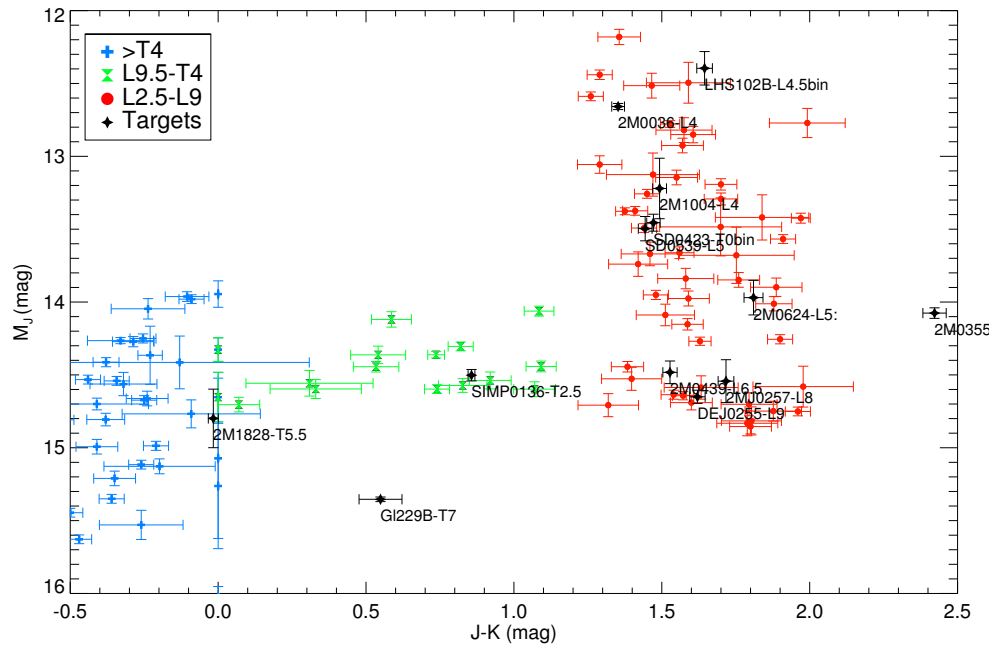


Figure 2.: Color magnitude diagram showing brown dwarfs with measured parallax from ? together with our targets.

of ~ 2.4 h and an amplitude of 50 mmag. ? calculated the amplitude of the variability for a object similar to SIMP 0136 (2MASS J21392676+0220226, T1.5) if it were produced by a companion, but the variability in that case would be much smaller than the variability found. ? explain this variability with a mixture of thick and thin patchy iron and silicate clouds covering the surface of the object.

In Section 4.1 we utilized indices by ? and ? to select potential L plus T brown dwarf binary candidates. Object SIMP 0136 was selected as

a strong brown dwarf binary candidate, as it appears in the selected area of four of the plots in Figure 1. These indices are made to select peculiar spectral characteristics that appear usually in binary L plus T brown dwarf spectra. Nevertheless, if variability is produced by a mixture of thick and thin clouds in the brown dwarf atmosphere, similar peculiar spectral characteristics would appear in brown dwarf spectra. We also compare our X-Shooter spectra with several single and composite of brown dwarf spectra of several spectral libraries (?, ? and Spex) and we found a best match with SDSS152103.24+013142.7 (T2) (see Fig. 5.1), which contradicts also possibility of being binary.

Parallax for SIMP 0136 is known, but not published (Smart, private comm.). Utilizing parallax we place the object in a CMD diagram together with objects published in ? (see Fig. 2) and we compare this object with objects of similar spectral type. We do not find overluminosity indicating similar spectral types binaries (see Fig. 2).

5.2 DENIS-P J0255.0-4700

Object DE0255 was discovered by ? and it was classified as a peculiar L6. ? reported evidence of variability in the optical with a frequency of $6.7 d^{-1}$. ? reported absolute parallax for this object: $\pi = 201.37 \pm 3.89$ mas. ? classified this object in the optical as a L8 and in the near infrared as a L9. Finally, ? searched for multiplicity for this object using NICMOS NIC1 camera on the Hubble Space Telescope and obtain high-resolution, but the result was negative.

In Section 4.1 was selected as a weak candidate to be brown dwarf L plus T binary by ? and ? indices. We compared DE0255 near infrared X-Shooter spectra to single and composite spectra from ?, ? and Spex libraries. We found decent matches to both single late L early T spectra and to composite spectra of late L plus early T spectra.

? published parallax for this object, we plot this object in a CMD diagram together with objects published in ? (see Fig. 2), as done for SIMP0136 previously, and no overluminosity is found. Therefore, either DE0255 is not a binary or it is a very unequal binary system.

5.3 2MASS J13411160-3052505

Object 2M1341 is the less studied object from our sample. It was discovered by ? using 2MASS data. ? classified as a L2 with a peculiar spectrum. Finally, ? found also variability of 67 mmag in I-band in a period of two days.

In Section 4.1 was selected as a weak candidate to be brown dwarf L plus T binary by ? and ? indices. We compared 2M1341 X-Shooter near infrared spectrum to ?, ? and Spex libraries. Best matches to this object were composite spectra of L plus T brown dwarf spectra. The best match were SDSS 175805.46+463311.9 (T6.5) and GJ1048B (L1) and 2MASS 1217110-031113 (T7) and GJ1048B (L1). Nonetheless, none of the matches are able to fully reproduce features in the H and K bands. Parallax for this object has not been yet published. Therefore, we can not confirm or refute if this object is a binary.

5.4 Gl229B

Object Gl229B was discovered by ?, and it was the first T brown dwarf discovered. It is companion of Gl229A. ? provided spectral types for Gl229A (M1V). ? classified Gl229B as a T7 brown dwarf with peculiar spectra. Parallax for this object was published by ? using Hipparcos data ($\pi = 173.81 \pm 0.99$ mas). ? confirmed that the system Gl229A and Gl229B is metal-poor, as ? found before.

We did not find a best match to this object to other object in ?, ? and Spex libraries. There is no photometry in H band for this object in 2MASS, due to the proximity of Gl229A. Therefore, we can only plot in the J-K vs M_J CMD (see Fig. 2). In Fig. 2 Gl229B is found together with much brighter objects. This could be an indicative of binarity. Nonetheless we cannot rely on this result as the photometry for Gl229B is contaminated by the photometry of Gl229A.

6. Conclusions

Peculiar brown dwarf spectra or the divergence in optical and near-infrared spectral type classification may indicate tight brown dwarfs binary systems. A proper characterization of these peculiar spectra may help either to understand the formation mechanisms of brown dwarfs and to calculate the binarity fraction for brown dwarfs with better precision.

We observed and analyzed 22 optical and near infrared medium resolution spectra of brown dwarfs with spectral types between L2 and T7. Our sample of objects had peculiar spectral characteristics or different classifications in the optical and in the near infrared. Two objects from our sample are known binaries, that allow us to test our analysis. We performed observations using VLT/X-Shooter between October 2009 and June 2010. Spectral resolution of our spectra is $R \sim 5400$ in the optical and $R \sim 3300$ in the near infrared.

Among the whole sample, we aim to find first potential L plus T brown dwarf binaries, because their peculiar spectral characteristics have been broadly studied. ?? developed a set of spectral indices that allow to identify potential L plus T binary candidates. We used his method to identify this objects in our sample. We selected four objects as potential L plus T binary candidates: SIMP0136 (T2.5), SD0423 (T0, known binary), DE0255 (L9) and 2M1341 (L2, peculiar spectra). Afterward, we compared these four selected objects with spectral libraries of field brown dwarfs (?, ? and Spex) and composite spectra of these libraries. We select the best match for every of this objects with exception of SD0423. Best match for SIMP0136 is object 2MASS J21392676+0220226 (T1.5) and parallax do not reveal overluminosity. Nevertheless, DE0255, is well reproduced for several single late L and early T brown dwarfs and composite of them, but parallax do nor reveal any overluminosity. Finally, the spectrum of object 2M1341 is just reproduced by a combination of the spectra from SDSS 175805.46+463311.9 (T6.5) and GJ1048B (L1) and the combination of the spectrum of 2MASS 1217110-031113 (T7) and GJ1048B (L1).

We studied if it is possible to find also L plus L or T plus T brown dwarfs binaries using the method of comparing to several spectral libraries. We created several synthetic binaries of L plus L spectra and several synthetic binaries of T plus T spectra, previously calibrated to the same distance. We compared all synthetic binaries to *?*, *?* and Spex libraries and look for the best matches to single and composite spectra. Best matches for all the synthetic binaries created were single spectra, with an intermediate spectral type between the primary and the secondary from the binary. We result can be expected, because the main difference between a L0 and a L8 brown dwarf is the SED, as well as for T1 and T7. As there are not different spectral characteristics beside the difference in SED, peculiarities in L plus L and T plus T brown dwarf spectra are difficult to find. In these cases, we need supplementary parallax measurements or high resolution imaging to confirm or discard binarity. We also compared the rest of the objects in our sample to *McLean*, *?* and Spex libraries. In these case, when we find a match is usually with a single spectra from one of these libraries.

Optical and near infrared spectra reported in this paper will serve as templates for future studies in any of these wavelengths. In the near future, Gaia satellite will release high precision parallaxes of more than one billion of objects in the Milky Way, including hundred of brown dwarfs. These parallaxes will allow us to detect the overluminosity of brown dwarf binaries.

Acknowledgments. We gratefully acknowledge ESO allocation time committee and Paranal Observatory staff for allowing the performance of these observations. We thank Adam Burgasser for providing and maintain The SpeX Prism Spectral Libraries: <http://pono.ucsd.edu/~adam/browndwarfs/spexprism/>. We thank Adam Burgasser, Daniella Bardalez Gagliuffi, Jackie Radigan and Esther Buenzli for their help in the development of this paper.

7. Appendix

7.1 Synthetic L plus L or T plus T best matches to template spectra

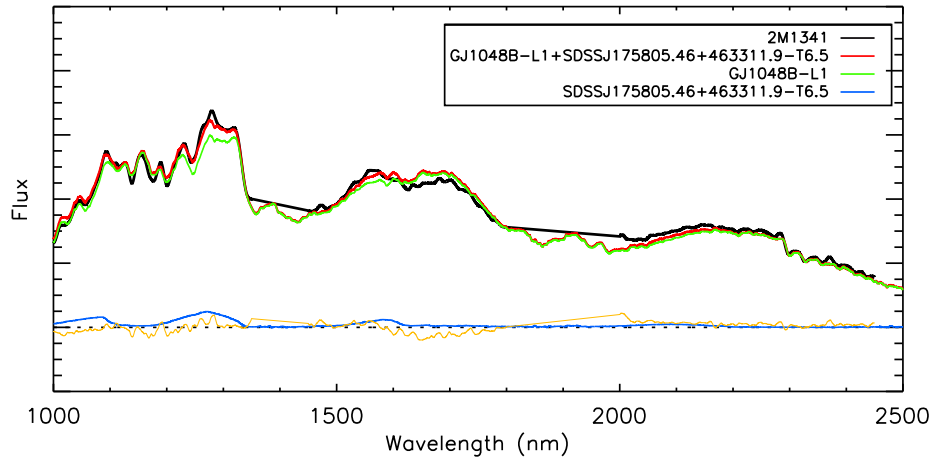


Figure 3.: Best matches for object 2M1341 (L2, peculiar). Object SDSS175805.46+463311.9 has T6.5 spectral type, GJ1048B is a L1 and 2MASS1217110-031113 is a T7. In black we show the synthetic T2+T7 spectrum, in blue the single best match object and in green residuals.

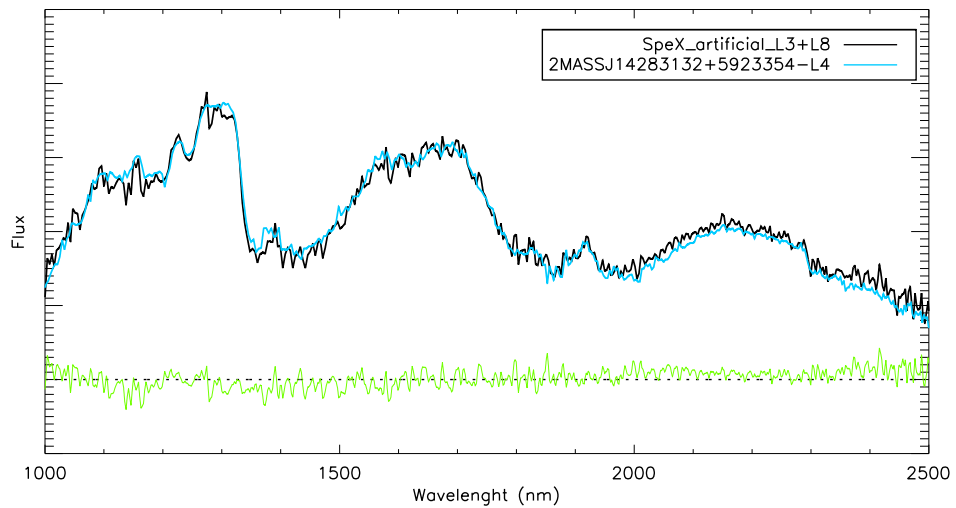


Figure 4.: Best matches for a L3 (SDSSJ111320.16+343057.9) + L8 (SDSSJ121951.45+312849.4) synthetic binary.

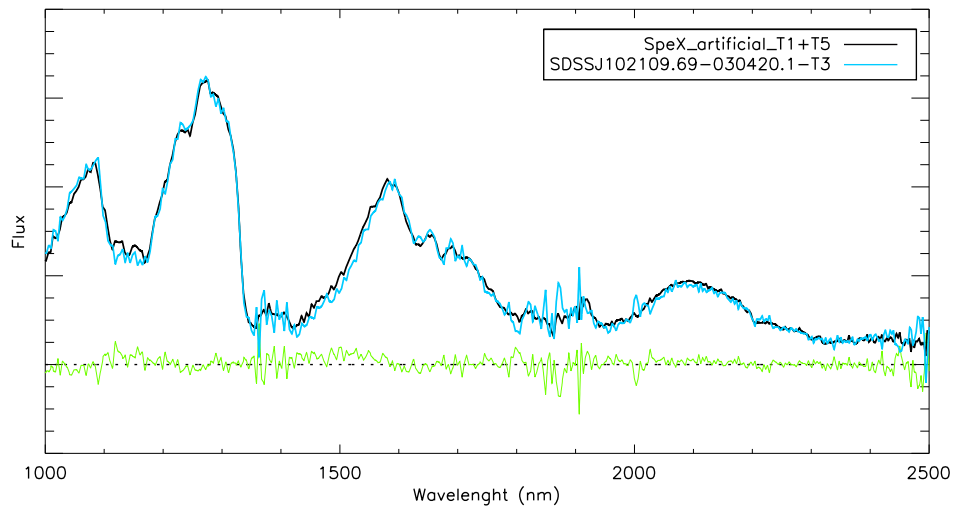


Figure 5.: Best matches for a T1 (SDSSJ015141.69+124429.6) + T5 (2MASSJ04070885+1514565) synthetic binary.

Chapter 23

First results of the TIGRE chromospheric activity survey

M. Mittag¹, A. Hempelmann¹, J. N. González-Pérez¹, J. H. M. M. Schmitt¹ and K-P Schroeder²

¹*Hamburger Sternwarte, Gojenbergsweg 112, 21029 Hamburg*

²*Department of Astronomy, University of Guanajuato, Mexico*

Abstract. We present the first results of the stellar activity survey with TIGRE (Telescopio Internacional de Guanajuato, Robótico-Espectroscópico). This long term program was started in August 2013 with the monitoring of a larger number of stars. We aim at measuring the short- and long-term variability of stellar activity for stars of different spectral types and luminosity classes, using indicators of different spectral lines (mainly Ca II S-Index, Ca II IR triplet, H $_{\alpha}$ and sodium D). A transformation equation of the TIGRE S-Index into the Mount Wilson S-index was derived in order to compare our results to the vast body of existing S-index measurements. Furthermore, the correlation between the S-index and the lines of the Ca II IR triplet has been studied, based on strictly simultaneous observations.

1. Introduction

Ca II H+K line emission is a very sensitive indicator of stellar activity. Therefore, this resonance line doublet at 3934 and 3968 Å has become the work horse for investigating the chromospheric stellar activity of cool stars. However, this spectral region is difficult to observe for stars of very late spectral type, since it is quite faint in the spectra of late K and M type stars. From that practical point of view, it is much more efficient to use some other stronger lines at longer wavelengths. One possibility is offered by the Ca II IR triplet, since it is known that the Ca II IRT line depths are indeed

Table 1.: This set of calibration stars was used to derive the transformation of the TIGRE S-index onto the Mount Wilson S-index.

Objects and references: (0) Interpolate from time series from Baliunas et al. (1995), (1) Baliunas et al. (1995), (2) Hall (private communication)

HD6920 ¹	HD23249 ¹	HD42807 ²	HD100563 ¹	HD129333 ¹
HD10307 ²	HD25998 ¹	HD45067 ¹	HD101501 ¹	HD131156A ¹
HD10700 ¹	HD26923 ¹	HD61421 ¹	HD106516 ¹	HD137107 ¹
HD13421 ¹	HD30495 ¹	HD72905 ¹	HD142373 ¹	HD142373 ¹
HD16673 ¹	HD32923 ²	HD75332 ¹	HD115043 ¹	HD158614 ¹
HD17925 ¹	HD35296 ²	HD75528 ²	HD115383 ¹	HD201091 ⁰
HD19373 ²	HD37394 ¹	HD89744 ¹	HD115617 ¹	HD207978 ¹
HD22049 ¹	HD39587 ²	HD95735 ¹	HD124570 ¹	HD216385 ¹
HD22072 ¹	HD41330 ²	HD97334 ¹	HD124850 ¹	HD217014 ¹

correlated with the Ca II H+K emission, (Busà et al. 2007; Martínez-Arnáiz et al. 2011).

In our study we started with investigating the question, how good and how sensitive are the Ca II IRT lines as a stellar activity indicator. For such studies the TIGRE instrumentation and its double-channel (red & blue) spectrograph is ideally suited, because both the Ca II H+K and IRT lines are observed strictly simultaneously (Schmitt et al. 2014).

2. Transformation from the TIGRE S-index into the Mount Wilson S-index

The Mount Wilson S-index (hereafter S_{MWO} -index) is the most commonly used and most important activity index in the optical spectral range, thanks to the decades-long efforts of the "Mount Wilson HK-Project". This project was a long-term monitoring effort to search for chromospheric variations in solar-type stars (Wilson 1978; Duncan et al. 1991; Baliunas et al. 1995). Basically, the S_{MWO} -index is defined as the ratio of the sum (i) of the counts in the Ca II H+K line centre in a triangular bandpasses with a FWHM of 1.09 Å over (ii) two 20 Å pseudo-continuum bandpasses centred at 3901.07 Å and 4001.07 Å (Vaughan et al. 1978; Duncan et al. 1991).

The TIGRE S-index (hereafter S_{TIGRE} -index) is calculated from the blaze-normalised and echelle-order-merged spectra. Here a rectangular 1.0 Å bandpass is used to represent the flux in the Ca II H+K line centres (instead of the classical triangular bandpass with a FWHM of 1.09 Å; cf. Vaughan et al. (1978)).

In general, any type of S-index measured with an instrumentation other than the original instrument has to be transformed to the Mount Wilson scale by measuring the original set of calibration stars to allow a direct comparison. This calibration procedure and the linear least-square correlation between

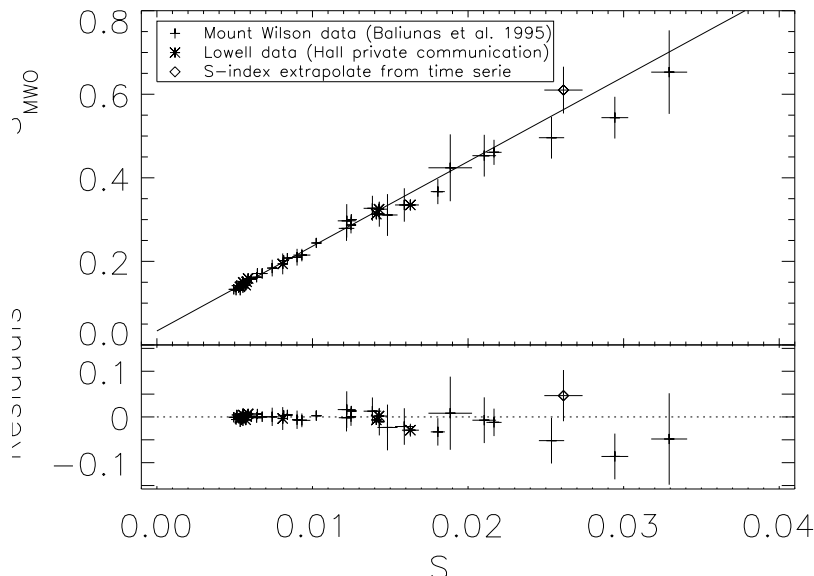


Figure 1.: S_{MWO} -index vs. S_{TIGRE} -index. Upper panel: S_{MWO} -index vs. S_{TIGRE} -index, the solid line shows the best linear fit to convert the S_{TIGRE} -index into S_{MWO} -index. Lower panel: Fit residuals.

our and the original S-index measurements results in a linear equation which then transforms any S_{TIGRE} -index measurement into the respective S_{MWO} -index values. The calibration stars with very well known S_{MWO} values were selected from Baliunas et al. (1995) and Hall et al. (2007). More importantly, these stars are known to be relatively constant in their activity levels and do not show any periodic activity behaviour either (with the only exception of HD201091 (see Tab. 1).

All calibration stars have been observed more than ten times with TIGRE to obtain a robust average S_{TIGRE} value. In Fig. ??, S_{MWO} -index values are plotted vs. the respective S_{TIGRE} -index measurements. A tight, linear correlation between S_{MWO} and S_{TIGRE} is evident. The least-square fit is represented by the solid line, which defines the transformation:

$$S_{\text{MWO}} = (0.033 \pm 0.003) + (20.3 \pm 0.4)S_{\text{TIGRE}}. \quad (23.1)$$

The standard deviation of the residuals is very small (0.02) and the mean scatter of the residuals between the transformed S_{TIGRE} -index and the corresponding reference S_{MWO} -index is 3.6%.

3. Correlation between the S_{MWO} -index and the Ca II IRT 8542 line of HD131977

To investigate the correlation between the S_{MWO} -index and the Ca II IRT lines, suitable activity indicator must first be defined for the Ca II IRT lines. For this purpose, the same definition is used as for the S_{MWO} . Consequently, we again use "S" as the name for this indicator, but with the index "IRT 8542" for the Ca II IRT 8542 line. S_{IRT8542} is defined as the ratio of the counts

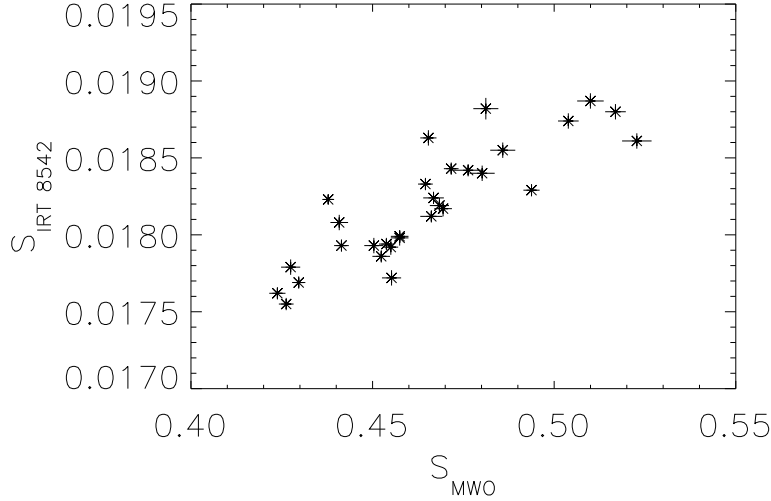


Figure 2.: Correlation between the S_{IRT8542} -index vs. S_{MWO} -index.

in a 1 \AA bandpass centred on the line core over a 20 \AA continuum bandpass centred at 8580 \AA . In Fig. 2, the S_{IRT8542} -index values are plotted over the respective S_{MWO} -index measurements and a clear correlation between both indicators is evident. However, this graph also illustrates the fact that the Ca II IRT 8542 line is not as sensitive as the Ca II H&K lines, since it varies by about a factor of 2 less.

4. Variation in the S_{MWO} -index and the Ca II IRT 8542 line time series of HD131977

In Fig. 3a, a time series of TIGRE S_{MWO} -index values is shown for HD131977. The time series was detrended and a Fourier analysis has been performed using the Lomb-Scargle periodogram. As a result, a periodic variation of 33.0 ± 0.4 days was found, (see Fig. 3b). In Fig. 3c, the detrended time series is plotted phase-folded with that period. We interpret the main peak as the rotation period of that star.

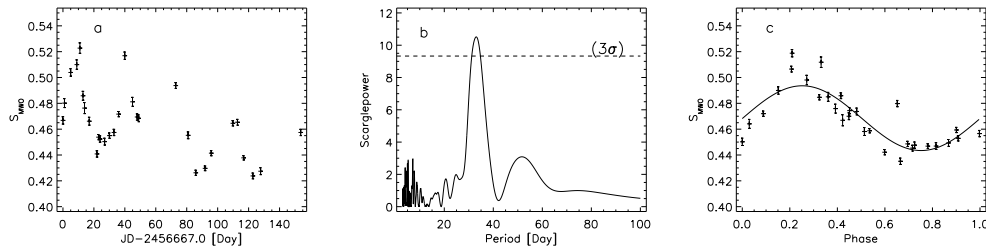


Figure 3.: Left panel: S_{MWO} -index time series. Medium panel: Periodogram of the detrended time series. Right panel: Phase folded detrended time series.

The same investigation was performed for the Ca II IRT 8542 line S-index, see Fig. 4a. In Fig. 4b, the periodogram is shown and again we find a clear peak at the period of 33.3 ± 0.5 days, showing that these two activity indicators vary with the same period.

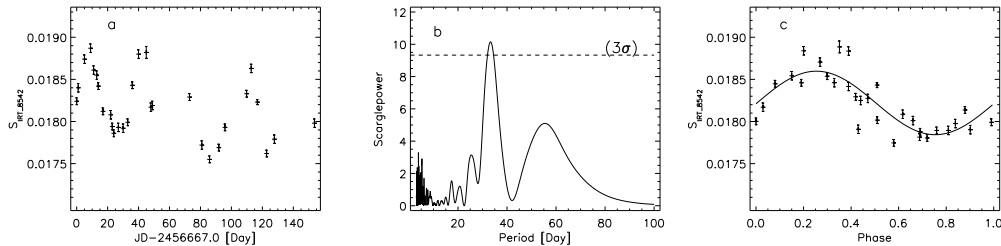


Figure 4.: Left panel: S_{IRT8542} -index time series. Medium panel: Periodogram of the detrended time series. Right panel: Phase folded detrended time series.

5. Summary and conclusions

In the first year of TIGRE observations at La Luz Observatory La Luz we were able to take the first time series for a stellar sample of more than 100 stars. This sample includes $\approx 90\%$ of the stars listed in Baliunas et al. (1995). One result of this initial observing season is the calibrated equation to transform our S_{TIGRE} -index measurements into S_{MWO} -index values. With this transformation onto the Mount Wilson scale, it is possible to compare our results with data covering a time-span of several decades and several thousands of stars.

Furthermore, we have investigated the correlation between the S_{MWO} -index and the Ca II IRT lines and show that the rotation periods measured in the S_{MWO} -index series and in the Ca II IRT lines is the same for the case of HD 131977. Thus we can estimate how the sensitivity of the Ca II IRT lines to stellar activity compares with that of the Ca II H+K based S_{MWO} -index. Furthermore, we find that the sensitivity of S_{IRT8542} -index compared to S_{MWO} is a factor of ≈ 2 lower, nevertheless, Ca II IRT lines are usable to measure rotation periods. Through this possibility, a new observation window can be open to measure the rotation period of very late type stars (late K and M type stars) since these objects are much easier to observe in the near IR.

Acknowledgements. We are grateful to Jeffrey C. Hall for the Mt. Wilson S-index time series, which we used for the derivation of the transformation equation from TIGRE S-index into the Mount Wilson S-index. This project was funded by DFG grant No. SCHM 1032/49-1

References

Baliunas, S. L., Donahue, R. A., Soon, W. H., et al. 1995, ApJ, 438, 269

Busà, I., Aznar Cuadrado, R., Terranegra, L., Andretta, V., & Gomez, M. T. 2007, *A&A*, 466, 1089

Duncan, D. K., Vaughan, A. H., Wilson, O. C., et al. 1991, *ApJS*, 76, 383

Hall, J. C., Lockwood, G. W., & Skiff, B. A. 2007, *AJ*, 133, 862

Martínez-Arnáiz, R., López-Santiago, J., Crespo-Chacón, I., & Montes, D. 2011, *MNRAS*, 414, 2629

Schmitt, J. H. M. M., et al. 2014, accepted, *Astronomische Nachrichten*

Vaughan, A. H., Preston, G. W., & Wilson, O. C. 1978, *PASP*, 90, 267

Wilson, O. C. 1978, *ApJ*, 226, 379

Chapter 24

Molecular outflows driven by young brown dwarfs and VLMS. New clues from IRAM interferometer observations

Monin, J.-L.^{1,2}, Whelan, E.³, Lefloch, B.^{1,2}, Dougados, C.^{1,2,4}

¹*Univ. Grenoble Alpes, IPAG, F-38000 Grenoble, France*

²*CNRS, IPAG, F-38000 Grenoble, France*

³*Institut für Astronomie und Astrophysik, Kepler Center for Astro and Particle Physics, Eberhard Karls Universität, 72076 Tübingen, Germany*

⁴*Laboratoire Franco-Chilien d'Astronomie, UMI 3386 CNRS, 1515 Camino el observatorio, Casilla 36-D correo central, Santiago, Chile*

Abstract. The outflow phenomenon is ubiquitous in star forming regions and is now known to play an important role in the formation of both young stellar objects (YSOs) and brown dwarfs (BDs) (Whelan et al., 2012). Observations of outflows from both stars and BDs are thus essential to our understanding of the overall star & planet formation process. In 2011 and 2012 we conducted a survey with the IRAM 30 m telescope of the CO emission in the vicinity of a large sample of BDs and VLMSs to check for molecular outflows. We followed up three of the most remarkable sources namely MHO 5, BD Tau 6 and FU Tau A with high angular resolution observations with the Plateau de Bure Interferometer (PdBI). These sources were chosen because their associated CO emission showed clear evidence of an outflow and / or their spectral energy distributions (SEDs) showed strong evidence of a massive accretion disk, that we postulate to be associated with an outflow. In this paper, we present the first results of our CO(1-0) PdBI investigations

of the molecular outflows of 2 of these sources, MHO5 and BD Tau 6. The signal to noise ratio on FU Tau is 3 times less than on the other sources and the results need more investigation.

1. Observations

Observations have been performed on the IRAM interferometer on a shared tracks basis from July to November 2012, with 5 or 6 antennas in a rather compact configuration, yielding a spatial resolution of $2.5''$. The cumulated time on tracks for the 2 sources presented here was 4.8 hours with 5 antennas and 3.2 hours with 6 antennas. The median sensitivities are for 0.192 MHz channels and 2 polarisations. The sensitivity reached in 156 kHz channels is 16.8 mJy. For MHO5, the best sensitivity is achieved in the 5.3 to 3.8 km/s range, and for BD Tau 6, in the 8.8 to 7.3 km/s range.

2. Results and Discussion

In figure 1 and 2, we show velocity integrated maps of the emission of the $^{12}\text{CO}(1-0)$ line observed on MHO5 and BD Tau 6. On each image, the central star symbol is placed at the position of the BD, and we show in the upper right corner the CO line at the central position to emphasise the velocity ranges where we have integrated the blue & red emission.

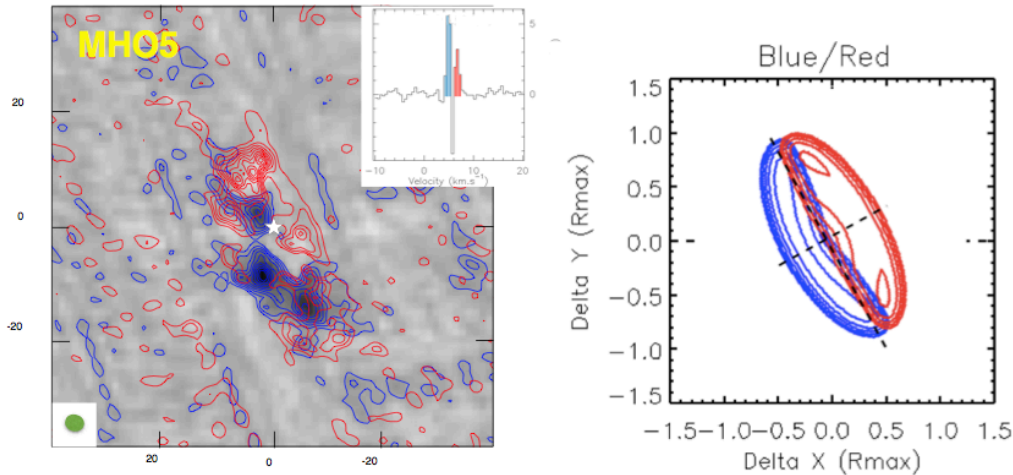


Figure 1.: Left: image of the integrated emission in the velocity range Blue: 4 - 5.5 km/s and Red: 6 - 7.5 km/s for MHO5. In each colour, the contours are from 20% to 90% of the max (Blue: 0.15 Jy/beam; Red: 0.17 Jy/beam) by 10%; Right: Optically thin, density scalable model of the MHO5 flow, using a 85° opening angle cone oriented at 65° toward the observer. North is up, East is to the left.

MHO5: the source line shows at a velocity close to the one of the surrounding extended cloud emission (≈ 6 km/s), and the central velocity channel is suppressed by the interferometer. This is not a real problem as the signal we are looking for is the one in the wings, well outside from the cloud emission. The velocity integrated blue and red emission appear distributed on an ellipsis with lobes symmetrical with respect to the central source. This result is more complex although apparently consistent with the one of Phan-Bao (2011). The estimated mass in each of the blue / red lobes is $\approx 2 \cdot 10^{-5} M_{\odot}$. We model the MHO5 emission in the form of a cone oriented at 65 degree in the plane of the sky. Such an almost edge-on situation could explain why MHO5 is so dim, and it could also explain the low radial (blue-shifted) velocity of the OI6300 line of ≈ 20 km/s. We downloaded this HIRES spectra from the Keck Observatory Archive (KOA), and the spectra were reduced using standard IRAF routines. This spectra was originally discussed in Muzerolle et al. 2003, and we discuss here for the first time the radial velocity of [OI]6300 line.

Many questions remain concerning the validity of our model, as we use a cone with an opening angle $\approx 80 - 90^{\circ}$, i.e. almost along the plane of the disk.

BD Tau 6: the integrated blue and red emission lobes are almost superimposed at $\approx 10''$ to the SW from the central source. This result is surprising, and is already visible on our lower spatial resolution results obtained during our 30 m observations. The geometry of the emission is difficult to reconcile with an outflow originating from the central source. We have estimated the integrated column density present in each of the blue / red emission on BD Tau 6, and find $\approx 6 \cdot 10^{-6} M_{\odot}$ of H_2 gas in each lobe. Such a value is of the order of what was observed in FU Tau by Monin et al. (2013).

In none of the two sources we detect the continuum emission. The upper limit reached from the sensitivity of these observations is consistent with the one published by Schaefer et al. 2009 (7.8 mJy @ 2.6 mm).

More complete results will be published in a forthcoming paper (Monin et al., 2014).

Acknowledgements. We thank the Operators of the IRAM interferometer for their help during the observations. E.T. Whelan acknowledges financial support from the Deutsche Forschungsgemeinschaft through the Research Grant Wh 172/1-1

References

- Monin et al, 2013, A&A 551, L1
- Monin et al., 2014, in prep.
- Phan-Bao et al., 2011, ApJ 735, 14
- Whelan et al., 2012, ApJ 761, 120
- Schaefer et al., 2009, ApJ 701, 698

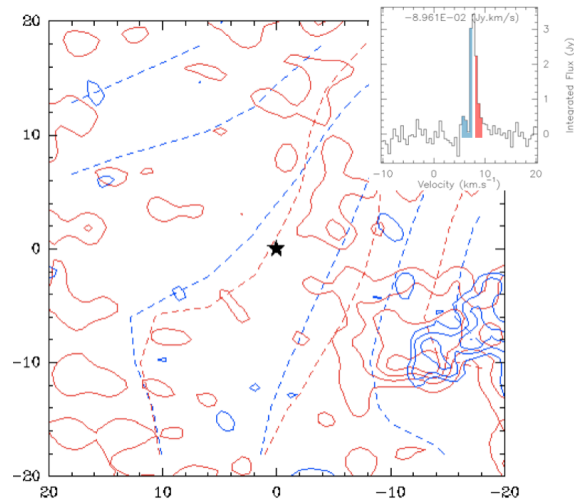


Figure 2.: Superimposition of 30 m (dashed lines) and PdBI (solid lines) integrated emission in the same velocity range: Blue 6 - 7.5 km/s and Red 8 - 9 km/s for BD Tau 6. In each colour, the contours are from 30% to 90% of the max (Blue: 0.05 Jy/beam; Red: 0.09 Jy/beam) by 20%.

Chapter 25

Preparation of the CARMENES Input Catalogue: Mining public archives for stellar parameters and spectra of M dwarfs with master thesis students

D. Montes¹, J. A. Caballero², F. J. Alonso-Floriano¹,
M. Cortés-Contreras¹, E. González-Álvarez¹, D. Hidalgo¹,
G. Holgado¹, M. Llamas¹, H. Martínez-Rodríguez¹, J. Sanz-Forcada²,
J. López-Santiago¹

¹*Dpto. Astrofísica, Facultad de CC. Físicas, Universidad Complutense de Madrid, E-28040 Madrid, Spain*

²*Centro de Astrobiología (CSIC-INTA), Campus ESAC, PO Box 78, E-28691 Villanueva de la Cañada, Madrid, Spain*

Abstract. We help compiling the most comprehensive database of M dwarfs ever built, CARMENCITA, the CARMENES Cool dwarf Information and daTa Archive, which will be the CARMENES ‘input catalogue’. In addition to the science preparation with low- and high-resolution spectrographs and lucky imagers (see the other contributions in this volume), we compile a huge pile of public data on over 2100 M dwarfs, and analyze them, mostly using virtual-observatory tools. Here we describe four specific actions carried out by master and grade students. They mine public archives for additional high-resolution spectroscopy (UVES, FEROS and HARPS), multi-band photometry (*FUV-NUV-u-B-g-V-r-R-i-J-H-Ks-W1-W2-W3-W4*), X-ray data (*ROSAT*, *XMM-Newton* and *Chandra*), periods, rotational

velocities and $H\alpha$ pseudo-equivalent widths. As described, there are many interdependences between all these data.

1. Contributing to the CARMENES ‘input catalogue’

The main goal of the CARMENES^a instrument is to find exoearths around M dwarfs by the radial velocity technique (see Quirrenbach et al. 2012, 2014a,b). To ensure an efficient use of CARMENES guaranteed time, and the highest chances of success, it is necessary first to select the most promising targets. To achieve this, we are compiling the most comprehensive database of M dwarfs ever built, CARMENCITA, the CARMENES Cool dwarf Information and daTa Archive, which will be our ‘input catalogue’ (Caballero et al. 2013). As part of the target science preparation, we carry out low-resolution spectroscopy with CAFOS, high resolution spectroscopy with FEROS, CAFE and HRS (Alonso-Floriano et al. 2014) and direct image to identify M dwarfs at close and wide physical separations (Cortés-Contreras et al. 2014). With the help of master and grade students at the Universidad Complutense de Madrid^b, we are mining public archives for additional high-resolution spectra and compiling additional information from the literature on photometry, rotational periods, projected rotational velocity and chromospheric and coronal activity of these M dwarfs.

2. Photometry of M dwarfs

During his MSc thesis, Gonzalo Holgado compiled photometric data in the bands *FUV-NUV-u-B-g-V-r-R-i-J-H-Ks-W1-W2-W3-W4* from *GALEX*, SDSS, Tycho-2, UCAC4, CMC14, 2MASS and *WISE* archives by using the Aladin Virtual Observatory tool. He have developed a software with the Python programming language in order to study the spectral energy distributions (SEDs) of our potential targets. Each star was studied individually. We discarded photometric data that clearly deviated from the general trend of the stellar SED and of template SEDs of the same spectral type. As a result of the analysis, we generated cleansed SEDs for almost 400 M dwarfs (see an example in Fig. 1).

For further characterization, he studied color-spectral type and color-color relations, and compared them with those tabulated by Bochanski et al. (2007) and Davenport et al. (2014). In addition, he also studied the quality of the photometric filters by contrasting the proportion of data erased in the cleansed data, as well as the relevance of the different color indices in order to assign a spectral sub-type to the stars. Finally, he also quantified the ultraviolet-excess emission comparing the *GALEX* near ultraviolet band (*NUV*) with the visible band (*V*) and identified active early M dwarfs, such as FF And, HD 79211, LP 787–52, OT Ser and GSC 02187–00512 (Fig. 2).

^a<http://carmenes.caha.es>

^b<http://www.ucm.es/masterastrofisica/>

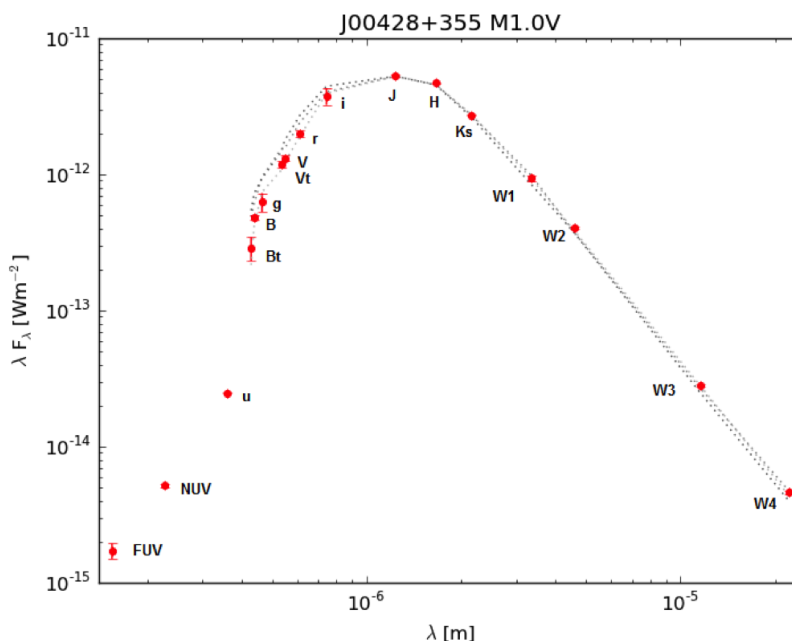


Figure 1.: Example of SED for the M1.0 V star FF And. The three dotted lines are the template SEDs for spectral types M0.5, 1.0 and 1.5 V.

3. Mining public archives for high-resolution spectra of M dwarfs

During his MSc thesis, Héctor Martínez-Rodríguez downloaded 128 UVES/VLT spectra from the ESO archive (advanced data products)^c of 61 CARMENCITA stars in eight channels (see representative spectra of channel BLU437 in Fig. 3) and measured pseudo-equivalent widths (pEW s) of $H\alpha$ to $H\eta$, Ca II H&K, Na I D₁&D₂ and He I D₃. He measured $pEW(H\alpha)$ of 27 M dwarfs for the first time and studied its relation to other lines in emission (see $pEW(H\beta)$ vs. $pEW(H\alpha)$ in Fig. 4). He applied a cross-correlation technique to determine rotational velocities ($v \sin i$). M stars with low $H\alpha$ emission and slow rotation were used as templates and to calibrate the relation between the cross-correlation function (CCF) width and $v \sin i$ (see Montes et al. 2000; López-Santiago et al. 2003, 2010). By using this method, the student measured $v \sin i$ of 24 stars (7 new) and identified wrong values published in the literature.

A grade student (Manuel Llamas) continued this work by downloading 67 FEROS + 2 HARPS spectra from the ESO archive of 59 CARMENCITA stars determining also $pEW(H\alpha)$ and $v \sin i$ in the same way. In his CCF analysis, he has identified double and triple peaks in some stars that result to be double-line spectroscopic binaries (GJ 1284, G 272–145, LP 675–076, HG 7–206 and G 050–001) or even spectroscopic triples (LP 653–008). Of them, only one (GJ 1284) was previously known to be an SB2 (Torres et al. 2006).

^chttp://archive.eso.org/eso/eso_archive_adp.html

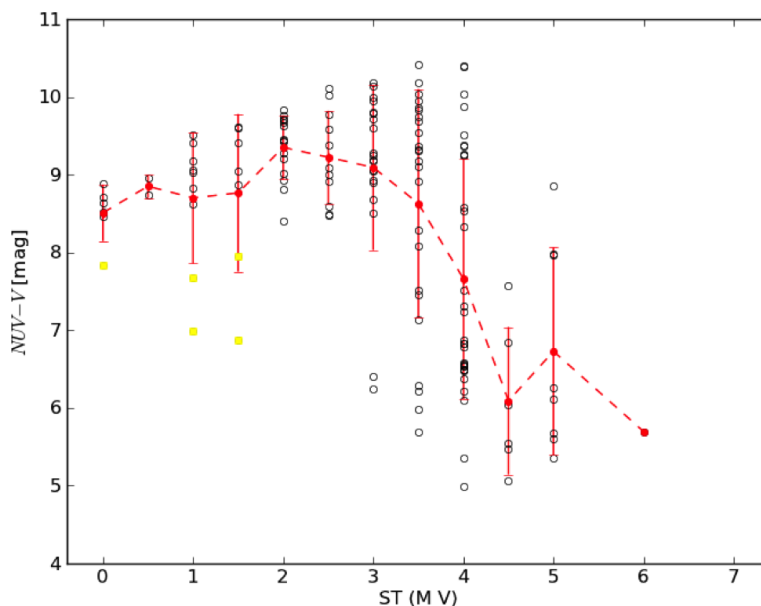


Figure 2.: $NUV-V$ vs. spectral type diagram. Red dots are the mean value for each spectral sub-type. Yellow squares are the early M dwarfs with $NUV-V$ excess.

4. X-rays emission in M dwarfs

During her MSc thesis, Esther González-Álvarez searched for information from X-ray data (*ROSAT*, *XMM-Newton* and *Chandra*) using the NASA HEASARC archive (High Energy Astrophysics Science Archive Research Center)^d, the SIMBAD astronomical data base and several publications (e.g. Hünsch et al. 1999; Sanz-Forcada et al. 2011). She studied each star individually to avoid assigning the X-ray emission to a wrong source. Many cases had nearby contaminant sources that hampered the identification of the emitting source. After this detailed study, she added new X-ray count-rate and hardness-ratio data of 188 M dwarfs to CARMENCITA. She calculated X-ray fluxes and luminosity ratios L_X/L_J for 770 stars in total and investigated its variation with spectral type (see Fig. 5) and rotational velocity (see Fig. 6). She corroborated with a large sample that close binaries (red dots in Figs. 5 and 6) are more active than single stars and that X-ray saturation starts at $v \sin i \approx 5 \text{ km s}^{-1}$.

5. Activity and rotational periods of M dwarfs

During his MSc thesis, Diego Hidalgo ransacked dozens of publications and compiled rotational photometric periods for 217 CARMENCITA stars (e.g. the

^d<http://heasarc.nasa.gov/docs/archive.html>

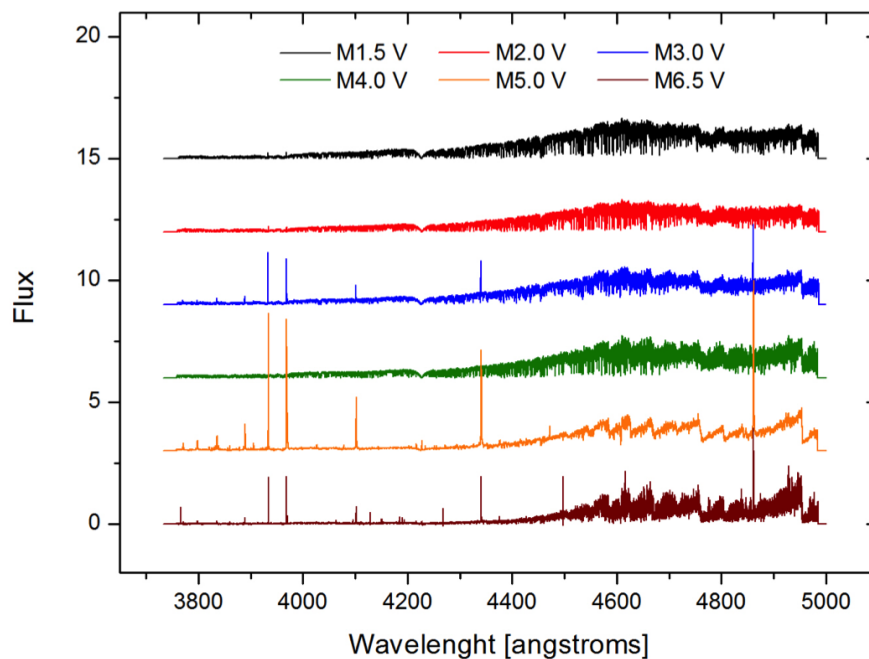
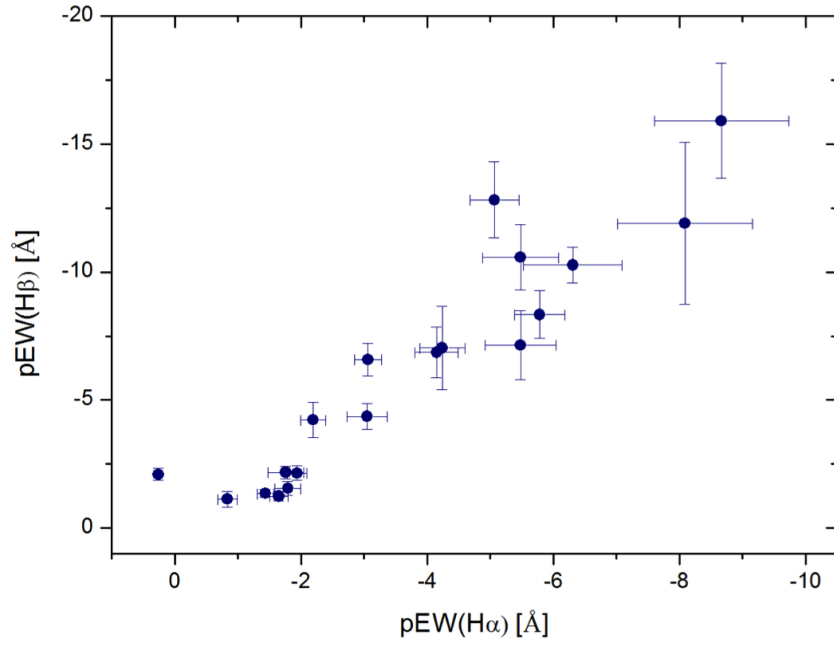
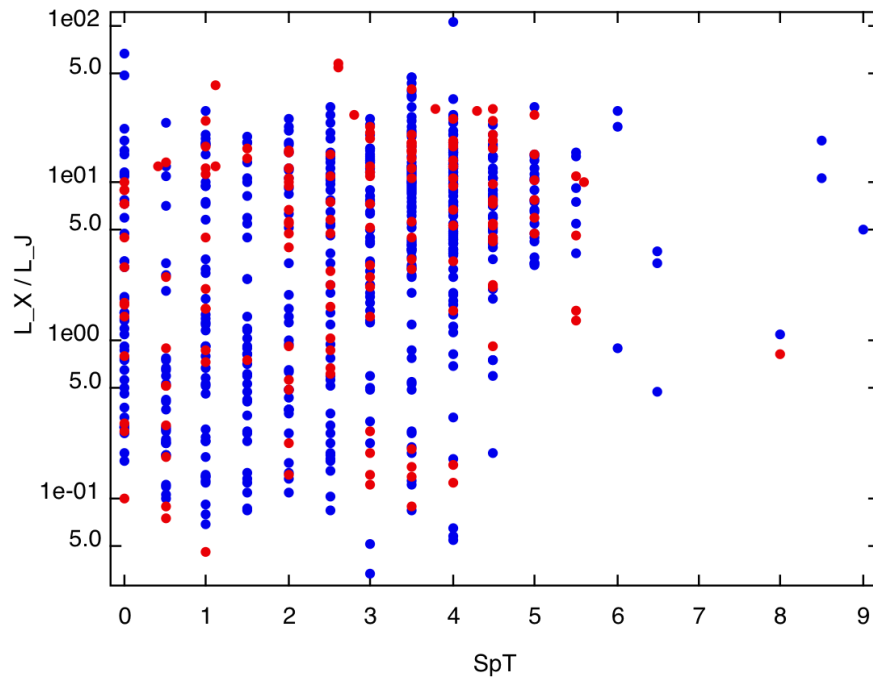


Figure 3.: Representative UVES/VLT spectra (from M1.5 V to M6.5 V) of channel BLU437.

MEarth^e project, Irwin et al. 2011), rotational velocities ($v \sin i$) for 420 (e.g. Jenkins et al. 2009; Reiners et al. 2012), $pEW(H\alpha)$ s for 1766 (e.g. Hawley et al. 1996; Lépine et al. 2013; Alonso-Floriano et al. 2014), and membership in young moving groups (e.g. Montes et al. 2001; Torres et al. 2008; Shkolnik et al. 2012) for 44. He studied the relation between spectral type, $H\alpha$ activity level (see Fig. 7), close multiplicity, rotational period (see Fig. 8) and $v \sin i$, from where he identified three stars with large inclination angles $i = 79^{\circ}.3$ to $81^{\circ}.6$: DT Vir AB, BD-21 1074 A and FFAnd.

^e<http://www.cfa.harvard.edu/MEarth/>

Figure 4.: $pEW(H\beta)$ vs. $pEW(H\alpha)$ diagram.Figure 5.: L_X/L_J vs. spectral type diagram (M0 V to M9 V). Blue dots are single stars and red dots binaries with separations less than 5 arcsec.

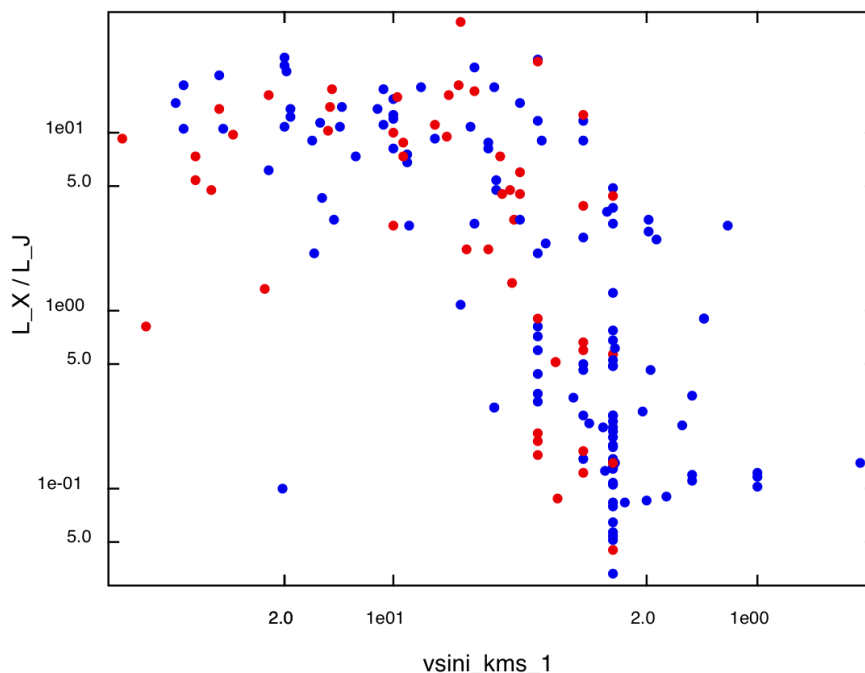


Figure 6.: Same as Fig. 5, but for L_X/L_J vs. rotational velocity ($v \sin i$) diagram.

Acknowledgements. Based on data obtained from the ESO Science Archive Facility. This research has made use of the SIMBAD database, the Aladin Sky Atlas operated at CDS, Strasbourg, France, and data provided by the High Energy Astrophysics Science Archive Research Center (HEASARC), which is a service of the Astrophysics Science Division at NASA/GSFC and the High Energy Astrophysics Division of the Smithsonian Astrophysical Observatory. Financial support was provided by the Spanish Ministerio de Ciencia e Innovación under grants AYA2011-30147-C03-02 and AYA2011-30147-C03-03.

References

- Alonso-Floriano, F. J., Montes, D., Caballero, J. A., et al. 2014, this volume
- Barrado y Navascués, D., & Martín, E. L. 2003, *AJ*, 126, 2997
- Bochanski, J. J., West, A. A., Hawley, S. L., & Covey, K. R. 2007, *AJ*, 133, 531
- Caballero, J. A., Cortés-Contreras, M., Alonso-Floriano, F. J., et al., 2013, *Protostars and Planets VI*, Heidelberg, July 15-20, 2013. Poster #2K020
- Cortés-Contreras, M., Béjar, V. J. S., Caballero, J. A. et al. 2014, this volume
- Davenport, J. R. A., Ivezić, Ž., Becker, A. C., et al. 2014, *MNRAS*, 440, 3430
- Hawley, S. L., Gizis, J. E., & Reid, I. N. 1996, *AJ*, 112, 2799
- Hünsch, M., Schmitt, J. H. M. M., Sterzik, M. F., & Voges, W. 1999, *A&AS*, 135, 319
- Irwin, J., Berta, Z. K., Burke, C. J., et al. 2011, *ApJ*, 727, 56

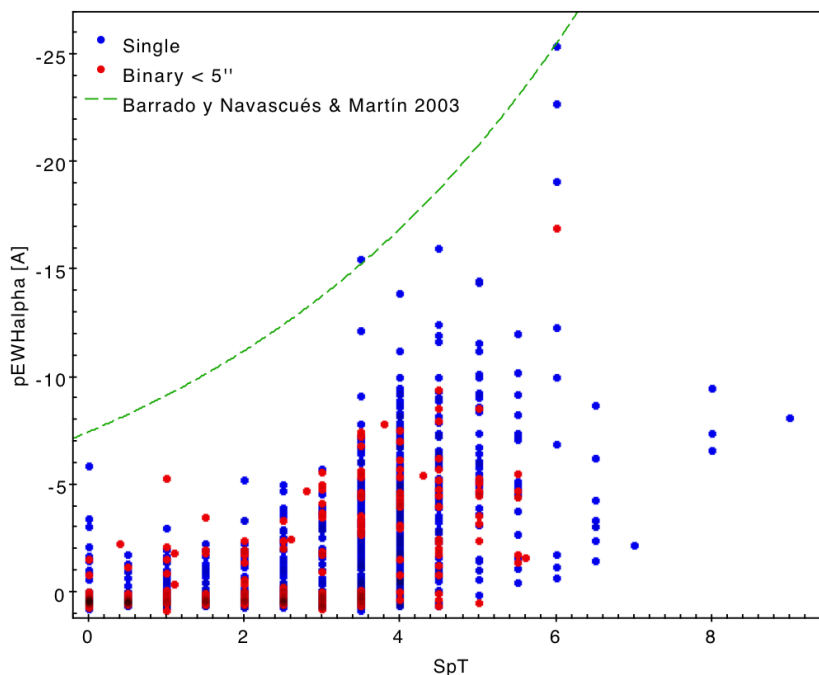


Figure 7.: $pEW(H\alpha)$ vs. spectral type diagram (M0 V to M9 V). The green dashed line is the empirical boundary between accreting and non-accreting objects based on the saturation limit of chromospheric activity of (Barrado y Navascués & Martín 2003).

Jenkins, J. S., Ramsey, L. W., Jones, H. R. A., et al. 2009, *ApJ*, 704, 975

Lépine, S., Hilton, E. J., Mann, A. W., et al. 2013, *AJ*, 145, 102

López-Santiago, J., Montes, D., Fernández-Figueroa, M. J., & Ramsey, L. W. 2003, *A&A*, 411, 489

López-Santiago, J., Montes, D., Gálvez-Ortiz, M. C., et al. 2010, *A&A*, 514, A97

Montes, D., Fernández-Figueroa, M. J., De Castro, E., et al. 2000, *A&AS*, 146, 103

Montes, D., López-Santiago, J., Gálvez, M. C., et al. 2001, *MNRAS*, 328, 45

Quirrenbach, A., Amado, P. J., Seifert, W., et al. 2012, *SPIE Proceeding*, 8446, 84460R

Quirrenbach, A., Amado, P. J., Caballero, J. A., et al. 2014, *SPIE Proceeding*, 9147, 91471F

Quirrenbach, A., Caballero, J. A., Amado, P. J., et al. 2014, this volume

Reiners, A., Joshi, N., & Goldman, B. 2012, *AJ*, 143, 93

Sanz-Forcada, J., Micela, G., Ribas, I., et al. 2011, *A&A*, 532, A6

Torres, C. A. O., Quast, G. R., da Silva, L., et al. 2006, *A&A*, 460, 695

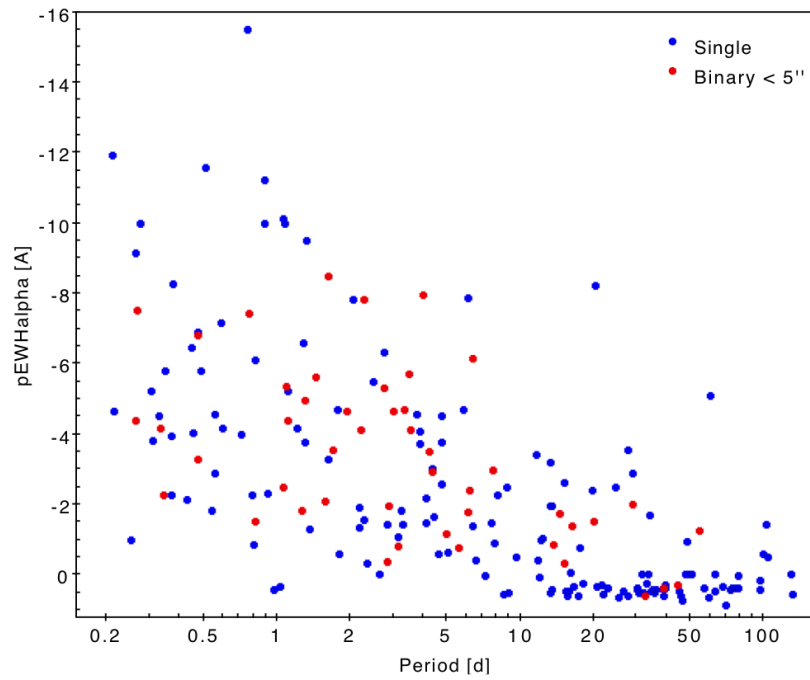


Figure 8.: $pEW(H\alpha)$ vs. rotational period (in logarithmic scale) diagram.

Torres, C. A. O., Quast, G. R., Melo, C. H. F., & Sterzik, M. F. 2008, Handbook of Star Forming Regions, Volume II, 757

Shkolnik, E. L., Anglada-Escudé, G., Liu, M. C., et al. 2012, ApJ, 758, 56

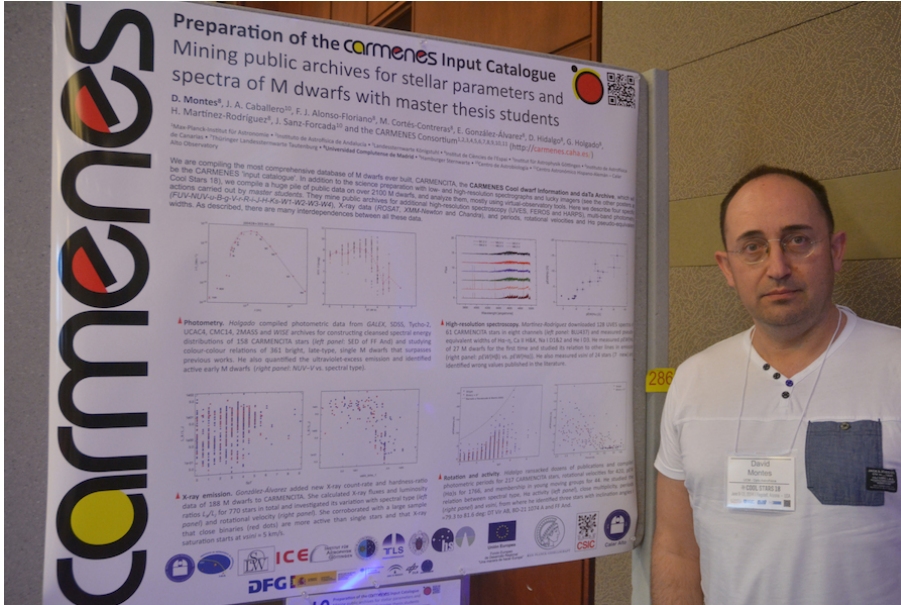


Figure 9.: David Montes in front of his CARMENES poster during the CS18 meeting.

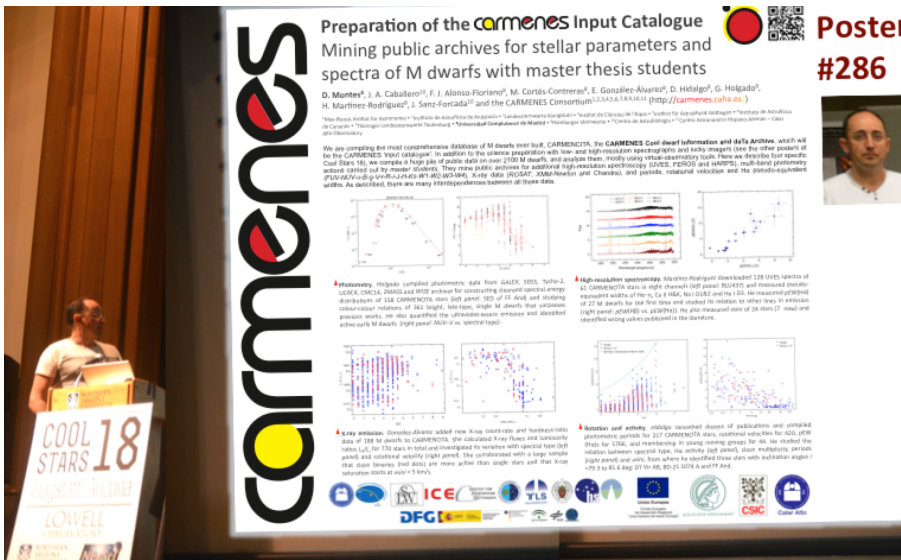


Figure 10.: David Montes during the poster pop-up presentation of the splitter session: “Portraying The Hosts: Stellar Science From Planet Searches”.

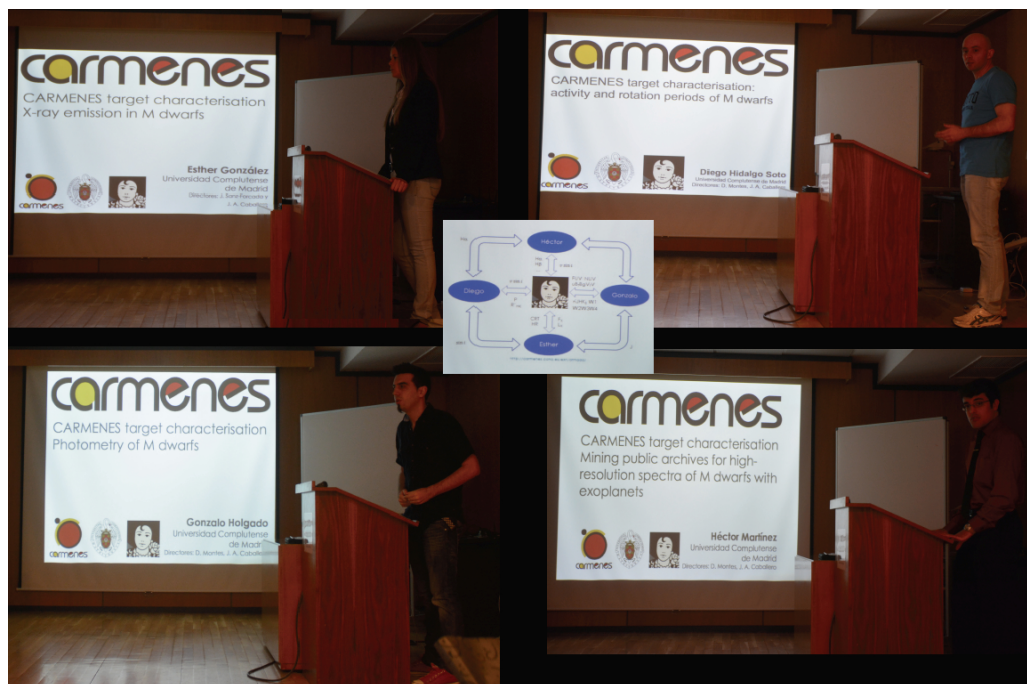


Figure 11.: The four master students (E. González-Álvarez, D. Hidalgo, G. Holgado and H. Martínez-Rodríguez) during the presentation of their MSc theses at the Universidad Complutense de Madrid, Master in Astrophysics.

Chapter 26

New Results from the GALEX Nearby Young-Star Survey

David R. Rodriguez¹, B. Zuckerman², Joel H. Kastner³, Laura Vican²,
David Principe³, Jacqueline K. Faherty⁴, Simon J. Murphy⁵, Mike S.
Bessell⁶

¹*Department of Astronomy, Universidad de Chile*

²*University of California, Los Angeles*

³*Rochester Institute of Technology*

⁴*Carnegie Department of Terrestrial Magnetism*

⁵*Astronomisches Rechen-Institut, University of Heidelberg*

⁶*Australian National University*

Abstract.

The last few decades have seen the discovery of many 10–100 Myr-old stars in moving groups within 100 parsecs of Earth. The present membership of these groups, however, is still incomplete at the lowest masses. We have initiated a program, the GALEX Nearby Young-Star Survey, or GALNYSS, to search for the missing low-mass stars. GALNYSS has combined ultraviolet data with near-IR surveys, as well as kinematic information, in order to identify over 2000 candidate young low-mass stars near Earth. Spectroscopic followup is ongoing, and results thus far confirm the youthful nature of many stars among the GALNYSS sample. This suggests that our technique is capable of revealing the populations of low-mass stars that are presently missing from the nearby young moving groups. We present an overview

of our survey to date and highlights from the latest contributions to our knowledge of the low-mass membership of nearby, young stellar associations.

1. The GALEX Nearby Young-Star Survey

Over the last few decades, many young (10–100 Myr-old) stars have been identified in moving groups located close to Earth (<100 pc). For direct imaging searches of extrasolar planets these stars represent excellent targets and as such they will be continuously observed during the coming decades as new imaging systems and larger telescopes are commissioned. However, the census of young stars among these groups is still incomplete at the lowest masses. To find the missing population of young stars in young moving groups near Earth, we have initiated the GALEX Nearby Young-Star Survey (GALNYSS). With ultraviolet (GALEX) and near-infrared (WISE & 2MASS) color selection criteria, estimated photometric distances, proper motions, and a UVW velocity analysis we have identified over 2000 candidate young, low-mass stars spread across most of the sky (see Figure 1). Our methodology and sample is discussed in Rodriguez et al. (2013). We have thus far published low-mass candidates to several nearby moving groups: TW Hydrae (Rodriguez et al. 2011), Tucana-Horologium (Rodriguez et al. 2013), and β Pictoris (Rodriguez et al. 2014). On-going work is being carried out to determine radial velocities and measure signatures of youth for additional candidates to these and other young moving groups.

2. LDS 5606: A Dusty M-dwarf Binary in the β Pictoris Moving Group

One of the latest GALNYSS results has been the identification of LDS 5606 as a β Pic moving group member (Rodriguez et al. 2014; Zuckerman et al. 2014). This is a wide pair of M5 dwarfs with a kinematic distance estimate of 65 pc. Radial velocity measurements place the stars in the β Pic moving group and both stars show signatures of youth, such as Li absorption.

Spectroscopic observations of LDS 5606 revealed a large number of emission lines, particularly for the A component (see Figure 2). Very strong Hydrogen and Helium lines can be seen and indicate on-going accretion. We also detected [OI] emission that likely traces OH photodissociation and disk photoevaporation by UV and/or soft X-ray photons from the central star (Zuckerman et al. 2014). LDS 5606 is one of several GALNYSS M-dwarfs that will be observed with our XMM GO program (D. Principe, PI) to characterize its X-ray properties.

In addition to rich optical emission-line spectra, LDS 5606 shows infrared excesses due to dusty circumstellar disks. The SEDs of both components reveal warm dust (200 K) around both stars and very warm dust (900 K) around the A component. In this and other respects, LDS 5606 appears to represent an older analog to the wide M-dwarf binary TWA 30 (Looper et al. 2010a,b). However, the components of TWA 30 show weaker H and He emission lines, and their spectra are instead dominated by forbidden transitions. Sharply contrasting viewing geometries — nearly edge-on for both TWA 30A and 30B, vs. more nearly pole-

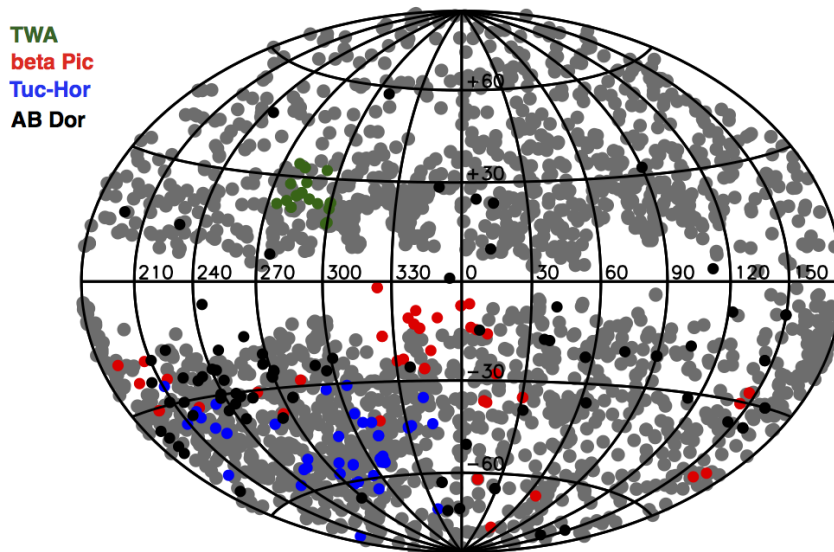


Figure 1.: GALNYSS stars (grey) in Galactic coordinates compared to several known moving groups (Torres et al. 2008).

on for the two components of LDS 5606 — can explain the differences between these two binaries (Zuckerman et al. 2014).

Acknowledgements. This work is supported by NASA Astrophysics Data Analysis Program award NNX12AH37G to RIT and UCLA and Chilean FONDECYT grant 3130520 to D.R.R. at Universidad de Chile.

References

- Looper et al. 2010a, ApJ, 714, 45
 Looper et al. 2010b, AJ, 140, 1486
 Rodriguez et al. 2011, ApJ, 727, 6
 Rodriguez et al. 2013, ApJ, 774, 101
 Rodriguez et al. 2014, A&A, 567, A20
 Torres et al. 2008, Handbook of Star Forming Regions, Volume II, 757
 Zuckerman et al. 2014, ApJ, 788, 102

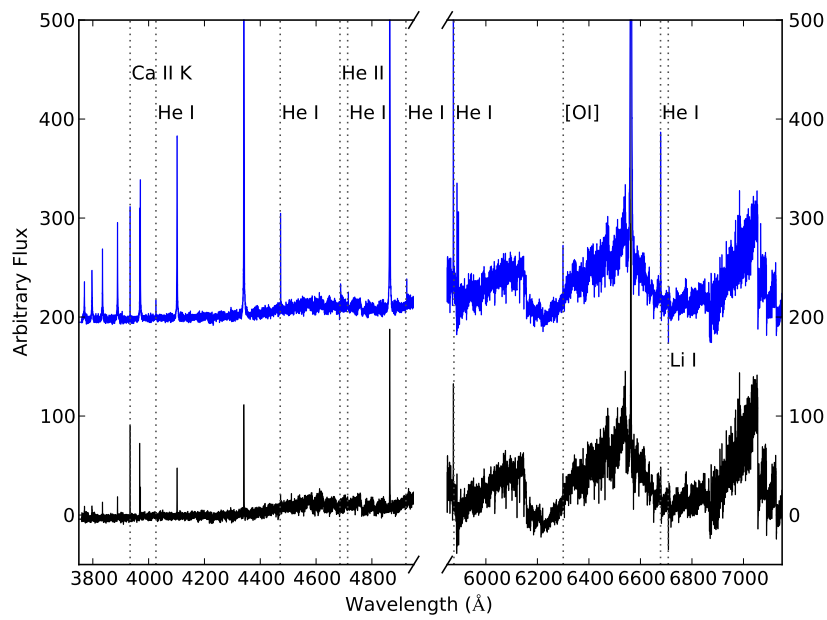


Figure 2.: VLT-UVES spectra of LDS 5606 A (top) and B (bottom) from Rodríguez et al. (2014).

Chapter 27

M dwarfs search for pulsations and flare studies within Kepler GO program

C. Rodríguez-López¹, J. E. Gizis², J. MacDonald², P. J. Amado¹

¹*Instituto de Astrofísica de Andalucía (IAA-CSIC), Glorieta de la Astronomía s/n, 18008 Granada, Spain*

²*University of Delaware. Dep. of Physics and Astronomy, Newark, Delaware 19716, USA*

Abstract.

We have done time-series analysis to search for pulsations in a sample of four M dwarfs -plus one M giant that seeped in our selection criteria - observed in short-cadence within Kepler (Koch et al. 2010) Guest Observer (GO) program. High-cadence sampling (Gilliland et al. 2010) is essential to detect the shortest pulsations predicted theoretically in the 20 min range and to enable high time-resolution analysis of flares. Three of the targets present stellar activity and two rotational modulation. We find that white light flares are present in the M dwarfs with rotational periods less than 20 days, and that their energy-frequency relations are comparable to traditional flare stars. The rapidly rotating M4 GJ1243 shows the strongest and more frequent flares. Pulsations have not been found to a detection limit of several parts per million.

1. Pulsations Analysis

Kepler SAP short-cadence light curves of our targets (see Table 1) were detrended with a 3σ clipping to a point-to-point deviation of the two point difference function to remove outliers, following García et al. (2011). The SAP flux in e-/s was converted to relative flux in ppm and a 1-degree polynomial was fitted. Then, the

light curves were appropriately binned to perform a cubic spline interpolation to remove the variations caused by activity and obtain a zero-centered flux.

The Fourier Transform analysis was performed with Period04 (Lenz & Breger 2005). A frequency was considered significant if its amplitude SNR ≥ 4 in a 2 c/d box around the considered peak.

Table 1.: Targets

KIC ID	Other ID	KEP mag	Sp. Type Rot. Period (d)
002424191		11.880	M giant
004142913	GJ 4099	10.910	M1 ; 30 d
004743351		13.806	M0 ; 10 d
008607728	LP 230-6	13.410	M1 ; 30 d
009726699	GJ 1243	12.738	M4 ; 0.593 d

1.1 Results

Most of the frequencies found significant are matched to some of the artifacts described in Baran (2013) (see Table 2) or to the artifacts caused by the long cadence (LC) sampling. Frequencies found in the 320-500 c/d range, equivalently periods in the 3-5 min range, significantly change amplitude with time and thus cannot be attributable neither to pulsations, or to Solar-like oscillations as they lack their characteristic Gaussian profile. KIC 9726699, or GJ 1243, is a well known active M4 dwarf whose rotational period has been measured to be 0.593 d (Savanov & Dmitrienko 2011) and that we recover here, along with its 2 to 6 harmonics.

We encourage further searches for very low amplitude oscillations in M dwarfs, as supported by theory (Rodríguez-López et al. 2014). More short cadence high-precision photometry within Kepler K2 mission and spectroscopic variability searches as those carried out by the *Cool Tiny Beats Survey* (see Anglada-Escudé et al. (2014) and Berdiñas et al. (2014) in these proceedings) are essential to unveil M dwarfs pulsations.

1.2 Flares Analysis

Kepler's precision and broad filter allows hot white light flares to be detected in M dwarfs against the red photosphere. Figure 1 shows four days of data for the fully convective star GJ 1243. White light flares are frequent. We identify and measure the strength of the flares by subtracting a running median light curve consisting of five rotation periods. For the slower rotating stars, a simple polynomial suffices to model the underlying rotational light curve. Figure 2 shows the cumulative flare frequency for the three M dwarfs with meaningful numbers of detected flares. The much higher flare rate of the fully convective M4 GJ 1243 is due to its rapid rotation.

The main uncertainty in comparing the flare rates of the stars is systematic errors in the flare energy calibration. GJ 1243 is well studied with a trigonometric parallax (11.8 +/- 0.4 pc; Harrington & Dahn (1980)), but the other M dwarfs have uncertain distances and correspondingly uncertain energy calibrations. Gaia parallaxes and improved spectroscopy will allow the energy scale of the flares to be better constrained.

Table 2.: Spurious frequencies

Freq. (c/d)	Artifact	KIC ID
8.48	0.5*16.98 (spurious)	2424101
19.92	'wide 20+ artifact'	2424101
31.42	'wide 20+ artifact'	2424101, 8607728
31.68	'wide 20+ artifact'	2424101, 8607728
153.46	'W artifact?'	8607728
219.52	0.5* 8/LC	2424101
293.63	6/LC	8607728
342.56	7/LC	4743351, 8607728
391.54	8/LC	2424101, 4142913, 8607728
440.48	9/LC	2424101, 47, 8607728
644.81	'U artifact' U17b	9726699
680.58	U18b	9726699
716.25	U19b	9726699

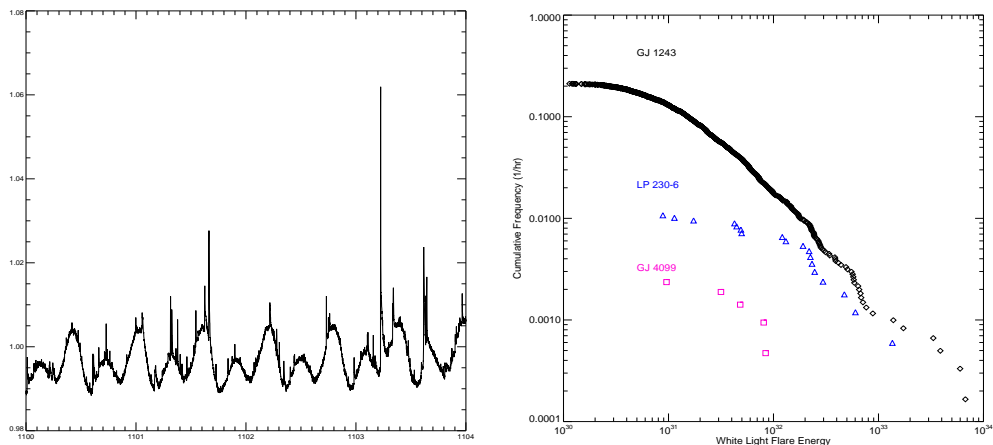


Figure 1.: Left: A four day time series for GJ 1243. Note the white light flares and periodic spot rotation. Kepler short cadence photometry allows the flares to be resolved in time. Right: Frequency of observed white flares as a function of their energy for three M dwarfs.

Acknowledgements. CR-L has a post-doctoral contract of the JAE-Doc program (CSIC) co-funded by the European Social Fund (FSE) and also acknowledges financial support provided from the *Annie Jump Cannon* fund of the Department of Physics and Astronomy of the University of Delaware. JEG and JM acknowledge support from NASA under award No. NNX12AC90G. PJA and CR-L acknowledge the funding provided by projects AYA2011-30147-C03-01 of the Spanish MINECO and 2011 FQM 7363 of Junta de Andalucía.

References

Anglada-Escudé, G., Arriagada, P., Tuomi, M., et al. 2014, arXiv:1406.0818

Baran, A. S. 2013, *Acta Astron.*, 63, 203

García, R. A., Hekker, S., Stello, D., et al. 2011, *MNRAS*, 414, L6

Gilliland, R. L., et al. 2010, *ApJ*, 713, L160

Harrington, R. S., & Dahn, C. C. 1980, *AJ*, 85, 454

Koch, D. G., et al. 2010, *ApJ*, 713, L79

Lenz, P., & Breger, M. 2005, *Communications in Asteroseismology*, 146, 53

Rodríguez-López, C., MacDonald, J., Amado, P. J., Moya, A., & Mullan, D. 2014, *MNRAS*, 438, 2371

Savanov, I. S., & Dmitrienko, E. S. 2011, *Astronomy Reports*, 55, 890

Chapter 28

Solar cycle 24 UV radiation: lowest since more than 6 decades

Klaus-Peter Schröder^{1,2}, Marco Mittag², Jürgen Schmitt²

¹*Dept. Astronomia, Univ. of Guanajuato (MEX)*

²*Hamburger Sternwarte, Universität Hamburg (GER)*

Abstract. Using spectra taken by the robotic telescope "TIGRE" (see Fig. 1 and the TIGRE-poster presented by Schmitt et al. at this conference) and its mid-resolution (R=20.000) HEROS double-channel echelle spectrograph, we present our measurements of the solar Ca II H&K chromospheric emission. Using moonlight, we applied the calibration and definition of the Mt. Wilson S-index, which allows a direct comparison with historic observations, reaching back to the early 1960ies. At the same time, coming from the same EUV emitting plage regions, the Ca II H&K emission is a good proxy for the latter, which is of interest as a forcing factor in climate models.

Our measurements probe the weak, asynchronous activity cycle 24 around its 2nd maximum during the past winter. Our S-values suggest that this maximum is the lowest in chromospheric emission since at least 60 years – following the longest and deepest minimum since a century. Our observations suggest a similarly long-term (on a scale of decades) low of the far-UV radiation, which should be considered by the next generation of climate models. The current, very interesting activity behaviour calls for a concerted effort on long-term solar monitoring.



Fig. 1: TIGRE, formerly the Hamburg robotic telescope, with its $R \approx 20,000$ double-channel (red&blue) spectrograph is now operating from Guanajuato, Mexico. “TIGRE” (Telescopio Internacional de Guanajuato, Robotico Espectroscopico) is a joint project of the Universities of Hamburg, Guanajuato and Liège.

1. S-index: A way to bridge the decades

Most measurements, whether space- or ground-based, suffer shifts or drifts whenever the instrumentation or calibration equipment is changed. In that respect, Olin Wilson’s S-index of the chromospheric activity, seen as emission in the Ca II H&K line cores, is a perfect choice. Our solar S-values, taken from lunar spectra, are calibrated by the same list of stars used by the Mt. Wilson team (see e.g. Duncan et al. 1991). For a more detailed description of this process, see Schröder et al. (2012) and the poster on first TIGRE-results presented at this conference by Mittag et al.

While Baliunas et al. (1995) never saw the Sun in any of its minima touch the basal flux S-level of inactive (“flat”) main sequence stars (visible in the survey of Duncan et al. 1991 as a cut-off at around $S=0.150$), in 2008/9 the Sun did! In the minima of the 1970ies and 1980ies the smoothed S-values hovered above 0.160, distinctly larger than the S-values of “flat activity” stars with only basal chromospheric emission. By contrast in 2008/9 it averaged around 0.155 and on

some plage-free days even got down to 0.150 (see Fig. 2 here and Schröder et al. 2012 for more details)!

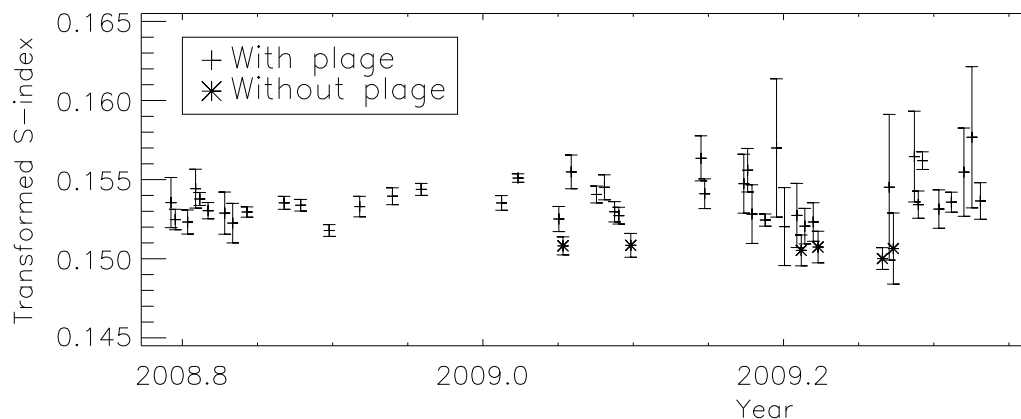


Fig. 2: The extraordinary minimum of 2008/09 had a number of very inactive, even plage-free days, during which the Sun reached its basal flux level of $S \approx 0.150$.

2. The dismal activity of cycle 24

Hence, the present cycle no. 24 was anticipated with much interest. The installation of TIGRE (formerly the Hamburg robotic telescope) in Guanajuato, Mexico (see poster on TIGRE by Schmitt et al.) last year allowed us to spectroscopically monitor the Sun (using the Moon) over the period of autumn 2013 to spring 2014, which covers the 2nd maximum of this cycle. This activity maximum was driven by the southern solar hemisphere and came 2 years later and out of phase with the peak of northern activity. It brought the largest sunspot groups and the strongest flare activity of the current cycle, slightly exceeding the activity of the sharp first maximum in December 2011 driven by the northern solar hemisphere.

Fig. 3 illustrates the active appearance of the solar chromosphere in the Helium line at 304 nm on a typical day in May 2014 (right, by SDO), contrasting with an entirely inactive day without even a plage as in February 2009 (SOHO-EIT). Indeed, our S-values from the past winter should about represent the strongest chromospheric emission of cycle 24. Nevertheless, in the spectrum of the entire Sun, Ca II H&K emission has not really increased that much:

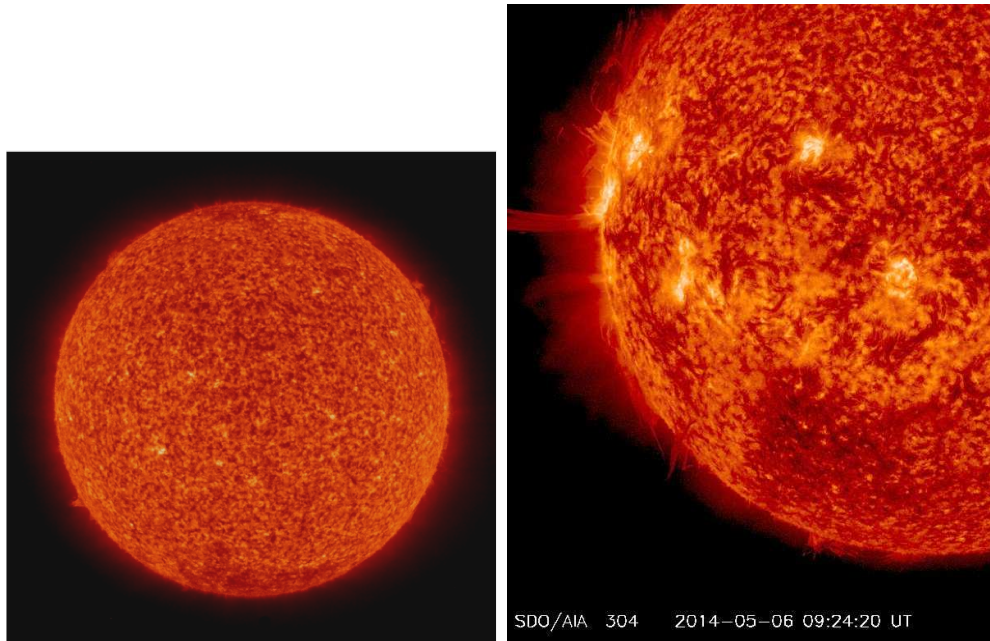


Fig. 3: Several times, the solar chromosphere in the extraordinary minimum showed no sign of activity (left, SOHO-EIT, 304 nm), not even a plage, and the solar S-index reached its basal level of 0.150. Compare this to the rich chromospheric appearance in January 2014 (right, SDO, 304 nm)! Nevertheless, the S-index then rose to only between 0.170 and ≈ 0.175 .

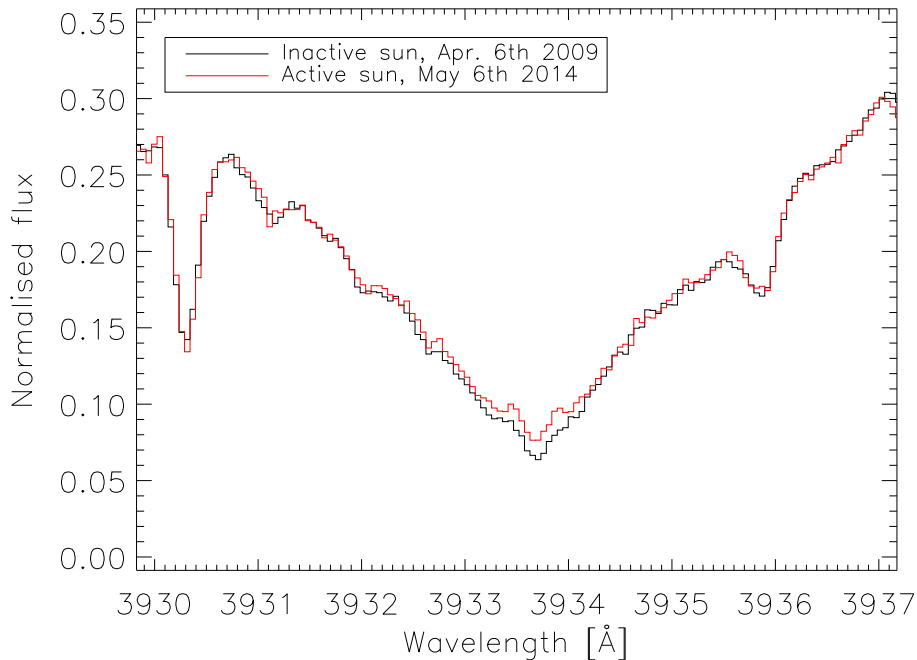


Fig. 4: The solar chromospheric emission in the core of the Ca II K line at basal flux level ($S \approx 0.15$, as several times in 2008 and 2009) and at modest activity ($S \approx 0.17$) typical for the maximum of cycle 24.

In Fig. 4 we compare the hardly visible chromospheric emission in the core of the Ca II K line of such an inactive day ($S \approx 0.15$) with a typical active day ($S \approx 0.17$) in the past winter. Smoothed over a month or so, our S-values of those months (see Fig 5) peak around only 0.172. That was the average over the whole previous cycle 23 (Hall et al. 2007), which saw a smoothed peak about $S \approx 0.19$.

3. Climate consequences of a historic underachiever?

The relatively weak past cycle 23 compared in strength to cycle 20 of the 1960ies, which was the first solar activity cycle recorded by S-values from the Mt. Wilson team (see Fig. 6 from Baliunas et al. 1995). By contrast, cycles 21 and 22 of the 1970ies and 1980ies were about the strongest of the whole past century. They seem to compare only with cycle 19 of the 1950ies and so represent the solar output around the past Gleissberg (or “grand”) maximum.

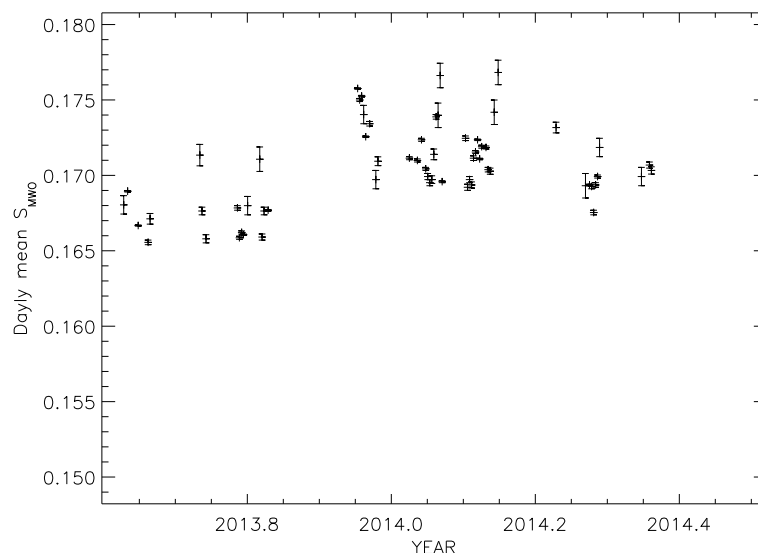


Fig. 5: The second maximum of cycle 24 in 2013/14 produced the best display of sunspots and flares. Nevertheless, our smoothed, well-calibrated S-values peak around only 0.172.

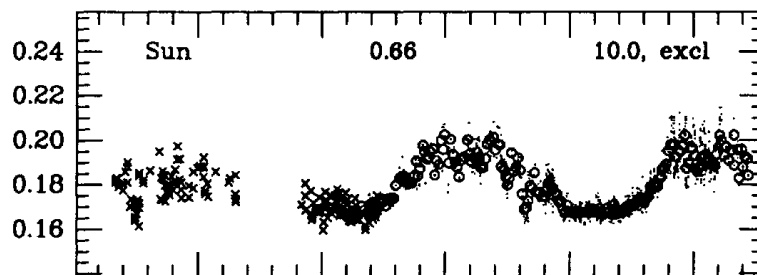


Fig. 6: S-values of cycles 20-22 reported by Baliunas et al. 1995: averages of cycle 21 and 22 exceeded 0.20. By comparison the current chromospheric emission is extraordinarily low, well underscoring the weak cycle 20.

Compared to those cycles 21 and 22, the chromospheric emission around the maximum of present cycle 24 is closer to the solar minimum emission of the 1980ies (compare Fig. 5 with Fig. 6)!

The Ca II H&K emission of the active Sun stems from the same plages and hotter plasma as does the EUV and near-UV radiation. The latter and its variation is of much impact to stratospheric conditions and plankton growth and so constitutes a climate forcing factor.

We regard Ca II H&K emission as a valuable proxy to the chromospheric UV and EUV radiation. While the latter can nowadays be observed with space-based instruments like SOLSTICE, such observations do not offer any direct comparison with data from 50 years ago.

Looking ahead, an average $\langle S \rangle$ value for the whole cycle 24 will probably fall between 0.160 and 0.165 (minimum years: 0.150-0.160, maximum years: 0.165-0.175). Consequently, we must regard the current decade as being under “eternal solar minimum conditions” by 1980ies solar UV radiation standards. See Schmidt et al. (2010) for such climate models with the HARMONIA code. Approaching a new “grand” minimum, *even lower UV forcing* must be expected for the next 1-3 decades.

Obviously, here is an urgent need to study amplification mechanisms, mainly known as “top-down” for the stratospheric impact and “bottom-up” for the ocean surface water warming. These seem to give UV forcing, despite its small share of total irradiation, an impact on local climate patterns, i.e. the Jet stream and North-Atlantic Oscillation (NAO), and the southern El-Niño-la-Niña Oscillation.

Certainly, the 1980ies solar UV spectrophotometry still used by most climate models is now outdated. Consequently, a concerted effort by the solar-stellar community is required to provide up-to-date solar data for future climate models.

Acknowledgements: This work was supported by the mexican Conacyt international mobility grant (proposal no. 207662) and by the german DFG.

References:

- S.L. Baliunas, R.A. Donahue, W.H. Soon, et al. 1995, ApJ, 438, 269
D.K. Duncan, A.H. Vaughan, O.C. Wilson, et al. 1991, ApJS, 76, 383
J.C. Hall, G.W. Lockwood, B.A. Skiff 2007, AJ, 133, 862
H. Schmidt, G.P. Brasseur, M.A. Giorgetta 2010, J. Geophys. Res., 115, 1029
K.-P. Schröder, M. Mittag, M.I. Pérez Martínez, M. Cuntz, J.H.M.M. Schmitt 2012, A&A 540, A130 (Research Note)

Chapter 29

The Surface Brightness Contribution of II Peg: A Comparison of TiO Band Analysis and Doppler Imaging

H. V. Şenavcı¹, D. O’Neal², G.A.J. Hussain³, J.R. Barnes⁴

¹*Ankara University, Faculty of Science, Department of Astronomy and Space Sciences, TR-06100, Tandoğan, Ankara, Turkey*

²*Keystone College, Natural Science and Mathematics, La Plume, PA, 18440, USA*

³*ESO, Karl-Schwarzschild-Str. 2, 85748, Garching bei München, Germany*

⁴*Center for Astrophysics Research, University of Hertfordshire, College Lane, Hateld, Hertfordshire AL10 9AB*

Abstract. We investigate the surface brightness contribution of the very well known active SB1 binary II Pegasi, to determine the star spot filling factor and the spot temperature parameters. In this context, we analyze 54 spectra of the system taken over 6 nights in September - October of 1996, using the 2.1m Otto Struve Telescope equipped with SES at the McDonald Observatory. We measure the spot temperatures and spot filling factors by fitting TiO molecular bands in this spectroscopic dataset, with model atmosphere approximation using ATLAS9 and with proxy stars obtained with the same instrument. The same dataset is then used to also produce surface spot maps using the Doppler imaging technique. We compare the spot filling factors obtained with the two independent techniques in order to better characterise the spot properties of the system and to better assess the limitations inherent to both techniques. The results obtained from both techniques show that the variation of spot filling factor as a function of

phase agree well with each other, while the amount of TiO and DI spot filling factors disagree by an order of magnitude.

1. Introduction

II Peg is a very well known active SB1 type RS CVn binary that has been classified by Rucinski (1977) and Vogt (1981). Berdyugina et al. (1998) determined that the primary component of the system is a K2IV sub-giant, while the unseen secondary component is an M-dwarf. They also obtained the orbital period, inclination, and the projected rotational velocity of the system as $P = 6.72$ days, $i = 60$, and $v \sin i = 22.6$ km/s, respectively. Regarding the activity behavior of II Peg, several studies have been performed by means of photometry, Zeeman Doppler Imaging, Doppler Imaging (hereafter DI), and molecular band analyses techniques, the most recent one by Xiang et al. (2014). These studies have revealed that the system has a large cool star-spot coverage showing complex migration behavior.

Among the techniques mentioned above, molecular band analyses have remarkable advantages as being more sensitive to cooler spots and detecting these features regardless of their distribution, even on slowly rotating stars (O'Neal et al. 2004). In this study, we investigate the surface brightness contribution of II Peg using TiO band analysis and DI, and present the results together with the comparison of these techniques.

2. Data

For both DI and TiO band analyses of II Peg, we used 54 time-series spectra obtained between the nights September 28 and October 3, taken from 2.1m Otto Struve Telescope equipped with SES (McCarthy et al. 1993) at the McDonald Observatory. These data are also used by O'Neal et al. (1998), in which the details can be found. We obtained the spectral resolution using the FWHM values from arc spectrum as around $R \sim 54000$, which corresponds to the value of 5.5 km/s per pixel.

3. TiO Band Analysis

The TiO analysis is simply based on the determination of spot filling factors (f_s) and spot temperatures (T_S) by fitting the depths of the TiO bands near 7055\AA and 8860\AA . The whole point of the technique is to simultaneously determine spot filling factor and temperature, so both are left as variables. In order to perform the modeling, we construct empirical models to represent the unspotted (quiet) photosphere and spots. The construction of these models are carried out in two different ways. First by fitting them using model atmospheres (ATLAS9) and the second using proxy (template) spectra of standard inactive G-K type (photosphere) and M type (spot) stars. Samples of the models together with observed spectra of II Peg for 7050\AA and 8860\AA band heads are given in the left and right panels of Fig. 1, respectively. The

systematic difference between spot filling factors determined from proxies vs. models might come from using very low gravity red giants as spot proxies. The (non-existent) M subgiants would have smaller TiO band depth for the same effective temperature, so would need more area on the star to give the same TiO band depth in the combined spectrum.

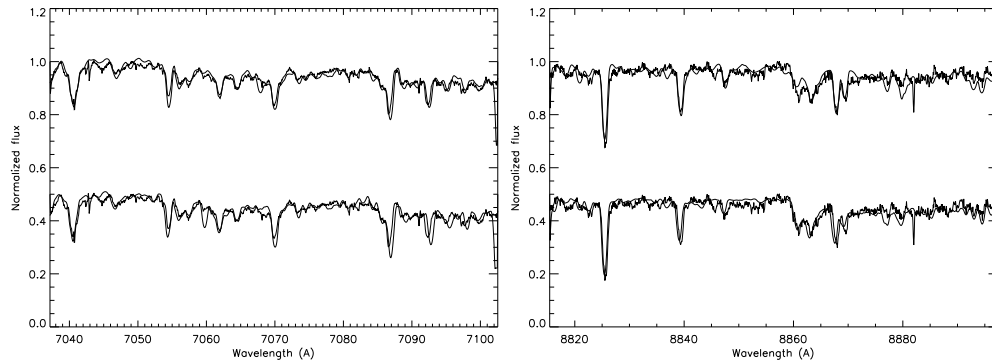


Figure 1.: Left Panel: Fits to 7055Å region of II Peg spectrum #21 using proxy stars (top) and ATLAS9 models (bottom). In both cases, assumed $T_S = 3425$ K and assumed $T_Q = 4750$ K. Right Panel: Same as left panel but for 8860Å region of II Peg spectrum #41.

To model each II Peg spectrum, we used different nonspot and spot comparison stars (proxies and models from ATLAS9) spanning the temperature range ($3000 \text{ K} \leq T_S \leq 4000 \text{ K}$) over which the TiO-band technique is valid. Each possible pair of comparison stars was used to fit the active star spectrum, and an f_S was computed assuming those two temperature components. For each nonspot comparison star used (i.e., each assumed T_Q), we plot the relation between each assumed T_S and the resultant f_S for both the 7055Å and 8860Å bands (a sample is shown in Figure 2). Therefore, the certain T_S and f_S values are determined, where the two relations intersect.

4. Doppler Imaging

We applied the LSD routine (see Donati et al. 1997 for details) to obtain high S/N profiles of each spectrum in the time series. We used the linelist extracted from the Vienna Atomic Line Database (VALD) (Kupka et al. 1999). During the preparation of the linelist, several wavelength regions were removed. These correspond to strong chromospheric emission lines (e.g. H_α , Na D), the artefact and excess illumination (see Şenavcı et al. 2011), and strong telluric regions. We obtained S/N values between 700 - 800, which are lower than expected. This may be due to our spectral range (6500Å - 8900Å) including several telluric lines and molecular bands, rather than photospheric absorption lines. In addition, due to the lack information of molecular bands in VALD database (e.g. depth), we couldn't take into account the molecular bands in our linelist.

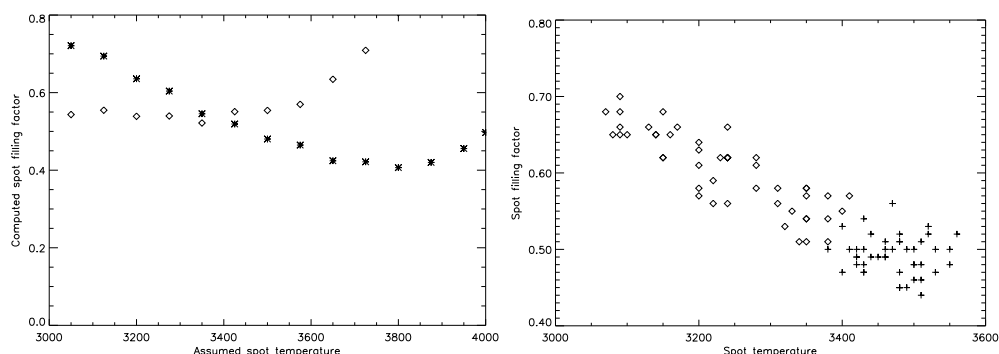


Figure 2.: Left Panel: Fits with ATLAS9 models for II Peg spectrum #41. Asterisks: fits to 7055\AA TiO bands with given spot temperature models. Diamonds: fits to 8860\AA TiO bands. The computed T_S and f_S values are taken where the two curves cross. T_Q was assumed to be 4750 K for these fits. Right Panel: Spot filling factor f_S vs. spot temperature T_S for all II Peg spectra. Plus signs: fits with proxy stars. Diamonds: fits with ATLAS9 models. Uncertainties for spot filling factor and spot temperature are about $0.05 - 0.08$ and 125 K , respectively.

The surface maps of II Peg were obtained using the imaging code, DoTS (Collier Cameron 1997). DoTS implements a maximum entropy regularised iterative algorithm to obtain fits to the observed time series spectra. Images with spot filling factors are derived from a two-temperature model. To produce accurate spot surface maps of stars, it is necessary to fine-tune the fundamental system parameters (see Şenavcı et al. 2011 for details). Inaccurate system parameter measurements introduce artefacts into the surface reconstructions (Unruh 1996). In this context, we used preliminary system parameters derived by Berdyugina et al. (1998) and Xiang et al. (2014), which are in accordance with the LSD profiles we obtained. We then fine tune some of the parameters (e.g. EW , R , V_γ) to obtain the most accurate maps of II Peg. Best fit system parameters are listed in Table 1.

Table 1.: System parameters

T_0 (HJD-2400000)	P (days)	q (M_2/M_1)	i (deg)	V_γ (km/s)	R_1 (M_\odot)	K_1 (km/s)	$v \sin i$ (km/s)
43033.47	6.72422	0.5	60	-29.3 ± 0.5	3.25 ± 0.03	38.66	22.6

During the preparation of line intensity (EW) lookup tables, we used the photospheric temperature as $T_{Ph} = 4750\text{ K}$ and spot temperature as $T_S = 3425\text{ K}$, together with the corresponding limb darkening coefficients. The resultant map (left panel) and fits to some LSD profiles (right panel) are given in Figure 3. The final chi-squared value after MEM iterations is $\chi^2 = 1.0$.

The pixel resolution of 5.5 km/s provides us the minimum resolvable spot size as around 22 deg , which is in accordance with our resultant map. As can be seen from Figure 3, there is a strong polar spot and 3 prominent spot regions

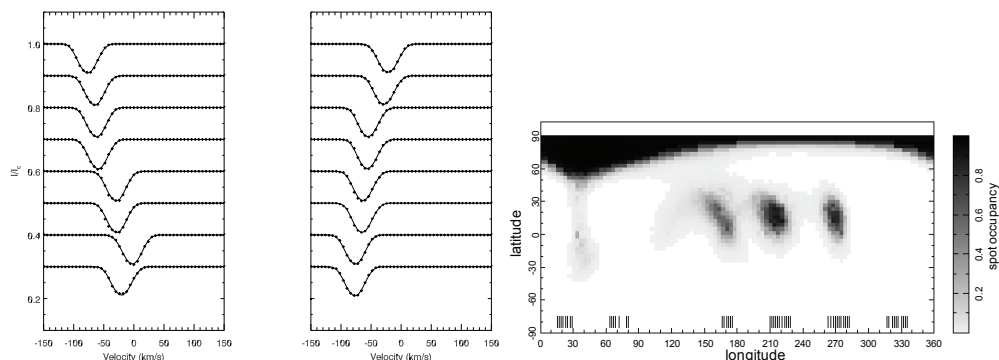


Figure 3.: Left Panel: 16 sample LSD profiles covering the full orbital phase (0.067 - 0.957). Right Panel: Surface brightness distribution of II Peg, using 54 time series spectra of the system.

located around the equator. This map, is very similar to that obtained by Xiang et al. (2014). We obtain a spot filling factor of 6.2% for the spot map of II Peg as shown in Figure 3. In the next section we compare this value with those obtained from TiO band fitting.

5. Results and Discussion

We investigate the surface inhomogeneities of the RS CVn type system II Peg, using TiO analysis and DI. TiO analysis yields an average spot filling factor of 0.5 and 0.6 with proxy stars and model atmosphere approximation, respectively. Doppler maps, on the other hand, is in accordance with other DI studies of the system and give a spot filling factor of 0.062. Our value is also typical of spot filling factors obtained for other active cool stars using Doppler imaging (typical spot filling factors < 0.1). However, DI is only sensitive to the inhomogeneously distributed spots with sizes larger than the resolution limit of the technique. TiO band fitting reveals the underlying level of cool spots that cannot be detected using DI alone (Solanki 1999).

We also compare the variation of spot filling factors with phase, in order to look for a correlation of f_S value obtained using two techniques. To do this, we first estimate the average phases of observations and then calculate the corresponding spot filling factors from TiO analysis and DI. Since the f_S value obtained from TiO analysis (convolved synthetic spectra) is nearly 10 times greater than that is obtained from DI, we normalized the spot filling factor values to unity, in order to perform a better comparison of two techniques (Fig. 4). It is clear from Figure 4 that the variation of spot filling factor with phase from two techniques are quite compatible with each other. This indicates that the most spotted phases are the same regardless of the technique, so the large spots detected by DI are also associated with an underlying larger filling factor of small, cool spots below the resolution limit of the DI technique. As a result, it can be said that, a considerable amount of spot coverage is hidden in a spot map from DI. However, performing TiO analysis together with the DI give a

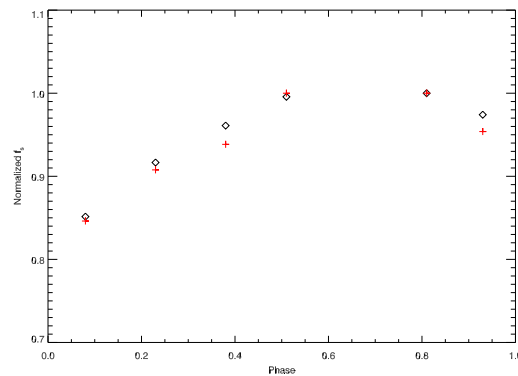


Figure 4.: Spot filling factor f_S vs. phase for the average phases of II Peg spectra. Red plus signs: f_S values from DI. Diamonds: f_S values from TiO analysis using ATLAS9 models.

more complete picture of the spot properties as well as the brightness distributions on the surfaces of cool stars.

Acknowledgements. H.V. Şenavcı acknowledge the support by Scientific Publications and Participation Incentives Department (BEYÖD) of Ankara University. D. O’Neal’s participation in this research was funded by a grant from the National Science Foundation’s Research at Undergraduate Institutions program. McDonald Observatory is owned and operated by the University of Texas at Austin.

References

- Berdyugina, S. V., Jankov, S., Ilyin, I., Tuominen, I., & Fekel, F. C. 1998, *A&A*, 334, 863
- Collier Cameron, A. 1997, *MNRAS*, 287, 556
- Donati, J.-F., Semel, M., Carter, B. D., Rees, D. E., & Collier Cameron, A. 1997, *MNRAS*, 291, 658
- Kupka, F., Piskunov, N., Ryabchikova, T. A., Stempels, H. C., & Weiss, W. W. 1999, *A&AS*, 138, 119
- McCarthy, J. K., Sandiford, B. A., Boyd, D., & Booth, J. 1993, *PASP*, 105, 881
- O’Neal, D., Saar, S. H., & Neff, J. E. 1998, *ApJ*, 501, L73
- O’Neal, D., Neff, J. E., Saar, S. H., & Cuntz, M. 2004, *AJ*, 128, 1802
- Rucinski, S. M. 1977, *PASP*, 89, 280
- Şenavcı, H. V., Hussain, G. A. J., O’Neal, D., & Barnes, J. R. 2011, *A&A*, 529, A11
- Solanki, S. K. 1999, *Solar and Stellar Activity: Similarities and Differences*, 158, 109

Unruh, Y. C. 1996, *Stellar Surface Structure*, 176, 35

Vogt, S. S. 1981, *ApJ*, 247, 975

Xiang, Y., Gu, S.-h., Cameron, A. C., & Barnes, J. R. 2014, *MNRAS*, 438, 2307

Chapter 30

UCAC4 Nearby Star Survey: A Search for Our Stellar Neighbors

John P. Subasavage¹, Charlie T. Finch², Norbert Zacharias², Todd J. Henry³, & Adric R. Riedel^{4,5}

¹*U. S. Naval Observatory Flagstaff Station, Flagstaff, Arizona, USA 86005*

²*U. S. Naval Observatory, Washington, DC, USA 20392*

³*RECONS Institute, Chambersburg, Pennsylvania, USA 17201*

⁴*Hunter College, New York, New York, USA 10065*

⁵*American Museum of Natural History, New York, USA 10024*

Abstract.

We present 16 photometric color- M_K relations using the U. S. Naval Observatory Fourth CCD Astrograph Catalog (UCAC4). These relations estimate distances to nearby red dwarfs at the $\sim 15\%$ accuracy level using photometry from the Two-Micron All-Sky Survey (2MASS) and the AAVSO Photometric All-Sky Survey (APASS). A sample of nearby stars from the Research Consortium On Nearby Stars (RECONS) group along with a supplemental list of very red stars all having accurate trigonometric parallaxes are used to generate the relations. Color, proper motion, and existing literature sources are used in an attempt to attain a clean sample of red dwarfs while limiting the amount of contamination from background giants. From this sample, we find 1761 candidate nearby M dwarfs estimated to be within 25 pc. Of this sample, 339 have no previously known published parallax or distance estimate and five of these are estimated to be within 10 pc. The nearest distance estimate of 5.9 pc was found for a star with V magnitude of 10.5. That several hundred new stars

have been revealed so close to the Sun illustrates once again that there is considerable work yet to be done to map the solar neighborhood.

1. Introduction

Nearby stars represent the best candidates for detailed studies of stellar luminosity and mass functions, as well as stellar activity, ages, multiplicity, and exoplanets because they are the brightest members of their classes of stars. Candidate nearby stars are often selected by proper motion for follow-up studies to confirm proximity. One primary goal of the Research Consortium On Nearby Stars (RECONS) effort is to identify and characterize all stars within 25 pc of the Sun. This work represents an initial phase of candidate identification that permits trigonometric parallax investigations by, e.g., the Cerro Tololo Inter-American Observatory Parallax Investigation (CTIOPI; Riedel et al. 2014, and references therein).

The U. S. Naval Observatory Fourth CCD Astrograph Catalog (UCAC4; Zacharias et al. 2013) contains more than 100 million sources and has incorporated photometric data from both the American Association of Variable Star Observers (AAVSO) Photometric All Sky Survey (APASS) and the Two Micron All-Sky Survey (2MASS). The astrometric data in the catalog is a compilation of original observations coupled with results from large proper motion surveys (e.g., Lépine & Shara 2005). In this work, we search the UCAC4 to identify candidate nearby stars where a full discussion can be found in (Finch et al. 2014).

2. Photometric Distances

To obtain photometric distances for UCAC4 sources, we generated a new set of 16 photometric color- M_{K_s} relations using (a) $BVgr_i$ optical photometry from APASS, (b) JHK_S near-infrared photometry from 2MASS, (c) nearby red dwarfs with high-quality trigonometric parallaxes from the RECONS effort, and (d) a set of M dwarfs with spectral types M6.0 V to M9.5 V within 25 pc that is referred to as the supplemental sample in Henry et al. (2006). M_{K_s} magnitudes were calculated for all calibration stars and compared to the suite of photometric colors available ($BVgr_iJHK_S$). A minimum color range of one magnitude was required for a given color to be reliable thus reducing the 28 possible relations to 16. A second-order fit was used for all relations and the coefficients of these fits, as well as the applicable color range, are listed in Table 1. Not all calibration stars had useful data in all wavebands so the number of stars used is different for each color relation and ranges from 102 to 141.

3. UCAC4 Trawl for Nearby Stars

A series of cuts were applied to the UCAC4 catalog to identify 25 pc candidate members.

Table 1.: Details of the 16 Photometric Distance Relations

Color	Color Range [mag]	Stars Used [number]	Coeff. 1 [\times color ²]	Coeff. 2 [\times color]	Coeff. 3 [constant]	rms [mag]
V-J	3.1 – 7.0	118	-0.14260	+2.551	-1.0870	0.40
V-H	3.5 – 7.7	118	-0.13910	+2.657	-2.3950	0.41
V-K	4.0 – 8.0	118	-0.12390	+2.523	-2.4720	0.42
V-i	1.4 – 3.9	113	-0.33800	+3.663	+0.9571	0.38
B-J	4.2 – 9.0	140	-0.08928	+2.188	-2.6330	0.37
B-H	4.9 – 10.0	141	-0.09372	+2.347	-4.0930	0.39
B-K	5.0 – 10.0	141	-0.08031	+2.174	-3.8580	0.39
B-i	2.8 – 6.0	102	-0.13570	+3.091	-1.6910	0.38
g-J	3.9 – 7.8	113	-0.13290	+2.693	-2.8800	0.39
g-H	4.2 – 8.4	113	-0.11760	+2.796	-4.2560	0.41
g-K	4.5 – 8.8	108	-0.13480	+2.637	-4.2120	0.41
g-i	2.2 – 4.5	105	-0.13340	+3.619	-1.0110	0.39
r-J	2.9 – 6.2	107	-0.11530	+2.383	+0.2988	0.41
r-H	3.4 – 6.8	107	-0.28630	+2.502	-0.9758	0.42
r-K	3.5 – 7.1	102	-0.19210	+2.353	-1.0590	0.42
r-i	1.0 – 3.0	105	-0.26210	+3.237	+2.9860	0.41

- Target must have photometry in at least two filters in the APASS catalog, with photometry errors (apase) ≤ 0.10 mag.
- Target must have photometry in all three JHK_S filters in the 2MASS catalog, with photometry errors (e2mpho) ≤ 0.10 mag.
- Target must not have a UCAC object flag (objt) = 1 or 2, indicating it is near an over-exposed star or a streaked object.
- Target must have a valid, non-zero proper motion.
- Target must have a Lyon-Meudon Extragalactic DAtabase (LEDA) galaxy flag (leda) = 0 and a 2MASS extended source flag (2mx) = 0 – both indicate a point source.

The remaining number of candidates after the cuts was 25,865,591. The photometric distance relations were then applied to these candidates requiring that (a) at least seven of the 16 relations were used, and (b) distances were estimated to be within 25 pc to produce a list of candidates numbering 381,054. This candidate list was then cross-checked with literature sources to find spectral types and previous distance estimates (either via trigonometric parallax or photometric). Dozens of known giants were extracted via this literature search and were used as empirical checks for the next two constraints imposed on the sample to minimize giant contamination.

We implemented the $J - K_S$ vs. $V - K_S$ color-color diagram coupled with the boundary constraints defined in Riedel (2012) that isolate regions of suspected dwarfs vs. those of giants. Figure 1 illustrates these boundaries with known dwarfs and giants overplotted in the left panel and the entire unknown sample of 381,054 (as a surface density plot) in the right panel. Box 1 contains candidates that are most likely M dwarfs while Box 2 contains M dwarfs with significant giant contamination. The number of candidates within both boxes was reduced to 4424.

As a second constraint to minimize giant contamination, we implemented a reduced proper motion cut using the proper motions from UCAC4. Reduced

proper motion is a useful tool for separating dwarfs from giants and takes the following form.

$$H_V = V + 5 \log \mu, \quad (30.1)$$

where μ is given in arcseconds per year. The reduced proper motion diagram with our known giants and dwarfs is plotted in the left panel of Figure 2 as well as the empirical boundary between the two samples. The unknown sample is plotted in the right panel of Figure 2. Once this criterion was implemented, another 2408 candidates from the sample of 4424 were removed yielding a sample of 2016 candidate nearby stars. After removing duplicate entries from this sample, a total of 1761 candidates remained.

From this sample of 1761 candidates, 669 have published trigonometric parallaxes, 749 have published photometric/spectroscopic distance estimates, and 4 are known giants. The remaining 339 candidates are new potential 25 pc members. A by-eye examination of these 339 candidates was performed using Aladin and revealed that 101 did not show any detectable proper motion. Further investigation of the epoch spreads of the plates indicated that all but six of the 101 targets had less than one arcsecond of total proper motion between the two epochs.

Finally, as is evident in Figures 1 and 2 a handful of bona fide M dwarfs have been eliminated by our selection criteria. Of the 181 known M dwarfs, a total of eight were omitted thus resulting in a $\sim 4\%$ loss. This loss is acceptable given that we aim to obtain a clean sample of M dwarfs with minimal giant contamination.

4. Results

A total of 339 candidate nearby stars within 25 pc have been identified by this effort, including five estimated to be within 10 pc. A sky distribution plot is shown in Figure 3 and illustrates that the majority of the new discoveries are in

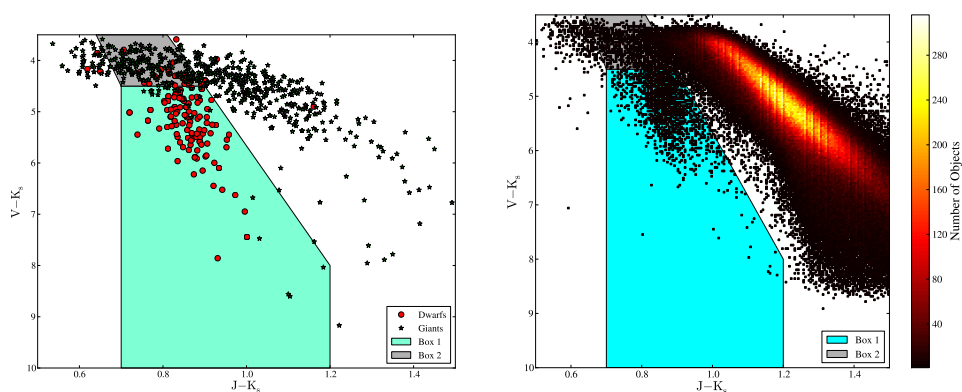


Figure 1.: **Left:** Color-color plot showing the regions (shaded boxes) where dwarfs are expected vs. those of giants and overplotted are the known giants (*stars*) and the known dwarfs (*circles*). **Right:** Same plot as left except now overplotting the sample of 381,054 candidates (as a surface density plot).

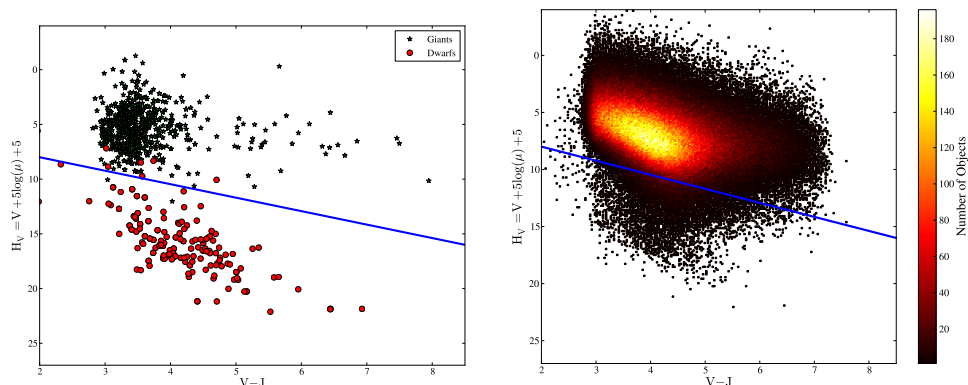


Figure 2.: **Left:** Reduced proper motion diagram illustrating the dividing line between the sample of known giants (stars) vs. that of known dwarfs (circles). **Right:** Same plot as left except now overplotting the 381,054 candidates (as a surface density plot).

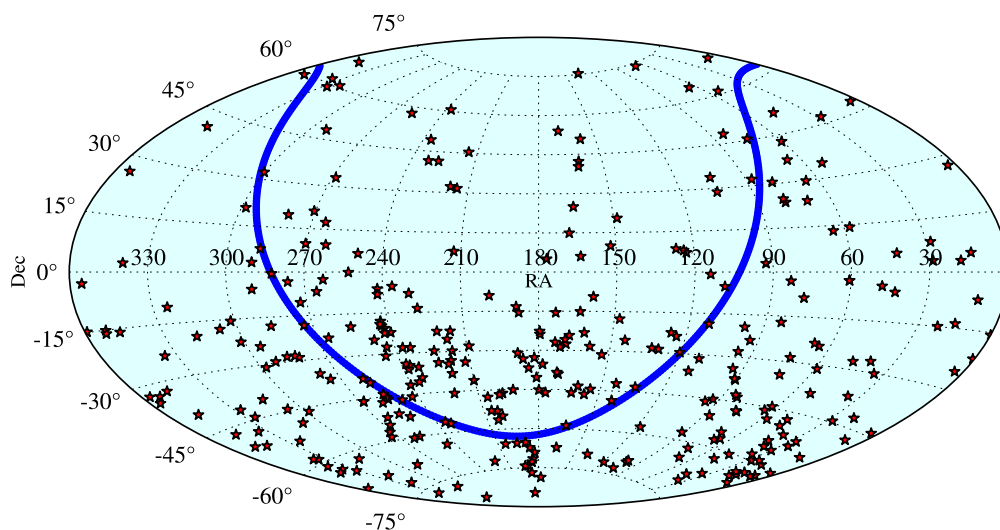


Figure 3.: Aitoff sky projection illustrating the 339 new nearby candidates (stars). The Galactic Plane (blue curve) is also shown for reference.

the southern hemisphere, likely the result of historical undersampling relative to the north. Follow-up trigonometric parallax efforts are needed to confirm proximity.

4.1 Local Statistics

By evaluating the sample of 669 candidates recovered in this work that have previous trigonometric parallaxes, we find that 532 have distances within 25 pc and 110 are beyond 25 pc – a success rate of 84%. We then infer that ~ 285 of the 339 new candidates are likely within 25 pc. To estimate the impact this new nearby candidate sample has on the local statistics, we use the RECONS 25 pc Database. As on 01 January 2014, there are 2169 systems known within 25 pc

based on accurate trigonometric parallaxes (i.e., parallax errors less than 10%). Therefore, 285 new members of the 25 pc sample represent an increase of 13%. We expect ongoing astrometric efforts (e.g., USNO, CTIOPI) as well as European Space Agency's Gaia astrometric mission will verify proximity for these targets as well as to better populate the sample of M dwarfs within 25 pc overall.

5. Conclusions

We use the UCAC4 catalog, which compiles previous astrometric efforts in addition to original astrometric results as well as the photometric catalog of the APASS, to identify new nearby M dwarfs within our 25 pc horizon of interest. To aid in this effort, we developed color- M_{K_S} relations using the UCAC4 catalog cross-matched with known M dwarfs that have accurate trigonometric parallaxes. We also utilize color-color and reduced proper motion diagrams to better permit giant discrimination. The final sift revealed 339 candidate new nearby stars within 25 pc, including five within 10 pc. All tabular data from this survey, as well as additional details related to the survey, can be found in Finch et al. (2014).

Acknowledgements. The authors would like to thank the organizers of this workshop for an exciting and content-rich meeting. We thank the entire UCAC team for providing the database from which this survey was gleaned. We thank members of the RECONS group for their support and the use of the RECONS database. This work has made use of the SIMBAD, VisieR, and Aladin databases operated at the CDS in Strasbourg, France. This work has also made use of the data from 2MASS, APASS, and the ADS service.

References

- Finch, C. T., Zacharias, N., Subasavage, J. P., Henry, T. J., & Riedel, A. R. 2014, submitted
- Henry, T. J., Jao, W.-C., Subasavage, J. P., et al. 2006, *AJ*, 132, 2360
- Lépine, S., & Shara, M. M. 2005, *AJ*, 129, 1483
- Riedel, A. R. 2012, Ph.D. Thesis,
- Riedel, A. R., Finch, C. T., Henry, T. J., et al. 2014, *AJ*, 147, 85
- Zacharias, N., Finch, C. T., Girard, T. M., et al. 2013, *AJ*, 145, 44

Chapter 31

Characterizing the Parents: Exoplanets Around Cool Stars

Kaspar von Braun¹, Tabetha S. Boyajian², Gerard T. van Belle³,
Andrew Mann⁴, Stephen R. Kane⁵

¹*Max-Planck-Institute for Astronomy (MPIA), Königstuhl 17, 69117
Heidelberg, Germany; braun@mpia.de*

²*Yale University, P.O. Box 208101, New Haven, CT 06520-8101, USA*

³*Lowell Observatory, 1400 West Mars Hill Road, Flagstaff, AZ 86001, USA*

⁴*University of Texas, 2515 Speedway, Stop C1400, Austin, TX 78712-1205,
USA*

⁵*San Francisco State University, 1600 Holloway Ave., San Francisco, CA
94132, USA*

Abstract. The large majority of stars in the Milky Way are late-type dwarfs, and the frequency of especially low-mass exoplanets in orbits around these late-type dwarfs appears to be high. In order to characterize the radiation environments and habitable zones of the cool exoplanet host stars, stellar radius and effective temperature, and thus luminosity, are required. It is in the stellar low-mass regime, however, where the predictive power of stellar models is often limited by sparse data quantity with which to calibrate the methods. We show results from our CHARA survey that provides directly determined stellar parameters based on interferometric diameter measurements, trigonometric parallax, and spectral energy distribution fitting.

1. “Why?” and “How?": Introduction and Methods

Essentially every astrophysical parameter of any exoplanet is a function of its equivalent host star parameters (radius, surface temperature, mass, etc.). **You**

Figure 1.: Habitable zones are calculated based on our empirical values of stellar radii and effective temperatures. This plot shows the system architecture of the GJ 876 system. The HZ is shown in grey. Planets b and c spend most or all of their orbital durations in the HZ. For scale: the size of the box is $0.8 \text{ AU} \times 0.8 \text{ AU}$. Adapted from von Braun et al. (2014).

only understand any exoplanet as well as you understand its respective parent star. The main purpose of the presented research is to directly characterize exoplanets in orbits around their hosts and to produce empirical constraints to stellar models. We use infrared and optical interferometry, coupled with spectral energy distribution fitting and trigonometric parallax values, to get estimates of stellar radii and effective temperatures that are as model-independent as possible. For more details, see, e. g., Boyajian et al. (2013) and von Braun et al. (2014). For transiting planets, using literature photometry and spectroscopy time-series data allows for the determination of model-independent planetary and stellar masses, radii, and bulk densities (e. g., von Braun et al. 2012).

2. “So What?”: Results

Our results provide empirically determined values for stellar radii, effective temperatures, and luminosities. They confirm the well-documented discrepancy between predicted and empirical radii and temperatures (e.g., Torres et al. 2010; Boyajian et al. 2012, 2013) and can thus provide constraints to improvements to stellar models. They can furthermore be used to establish relations to predict stellar sizes based on observable quantities, like stellar broad-band colors, for stars too faint and/or small to be studied interferometrically (Boyajian et al. 2014). In addition, any individual system’s circumstellar habitable zone (HZ) is a function of stellar radius and effective temperature (Fig. 1).

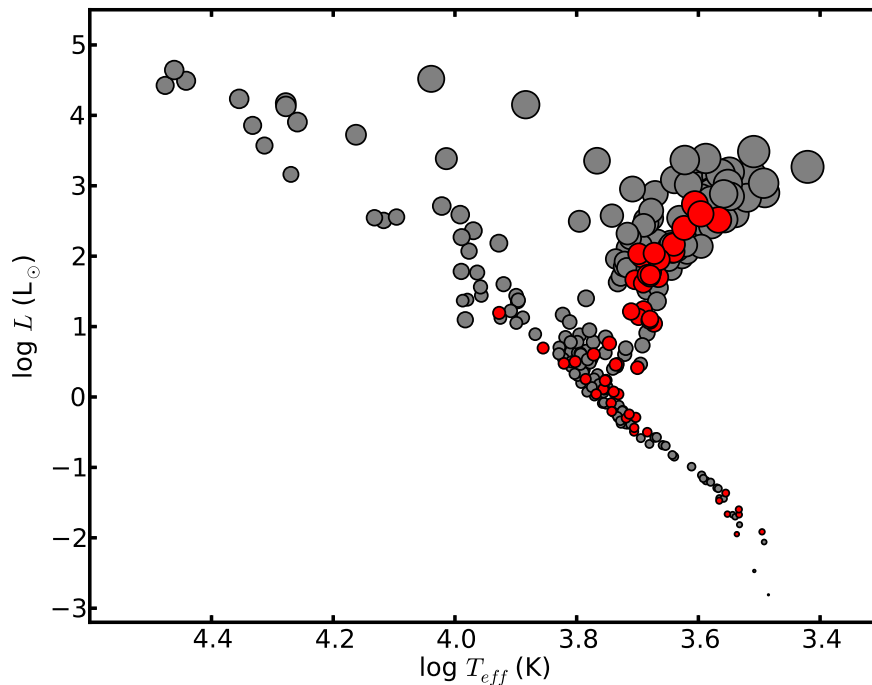


Figure 2.: Empirical H-R Diagram for all stars with interferometrically determined stellar radii whose random uncertainties are smaller than 5%. The diameter of each data point is representative of the logarithm of the corresponding stellar radius. Error bars in effective temperature and luminosity are smaller than the size of the data points. Exoplanet host stars are shown in red; stars that are not currently known to host any exoplanets are shown in grey. Stellar radii data are taken from Baines et al. (2008, 2012, 2013); Bigot et al. (2006); Boyajian et al. (2008, 2012, 2013); di Folco et al. (2004, 2007); Henry et al. (2013); Kervella et al. (2003); Ligi et al. (2012); Richichi et al. (2005); van Belle et al. (1999); van Belle & von Braun (2009); von Braun et al. (2011a,b, 2012, 2014); White et al. (2013).

3. “And what have you done for me lately?”: Status

Over the course of the last 5+ years, we have been using the CHARA interferometric array to directly determine the stellar parameters of over 100 main-sequence stars and of around 30 exoplanet host stars, with a particular emphasis on cool stars (Fig. 2).

Acknowledgements. We would like to sincerely thank the organizers for a phantastic conference. We furthermore express our gratitude to the poster judges for their thumbs up on our work. This research has made use of the Habitable Zone Gallery at hzglory.org (Kane & Gelino 2012).



Figure 3.: Thank you, organizers and poster judges!

References

- Baines, E. K., McAlister, H. A., ten Brummelaar, T. A., et al. 2008, *ApJ*, 680, 728
- Baines, E. K., White, R. J., Huber, D., et al. 2012, *ApJ*, 761, 57
- Baines, E. K., McAlister, H. A., ten Brummelaar, T. A., et al. 2013, *ApJ*, 772, 16
- Bigot, L., Kervella, P., Thévenin, F., & Ségransan, D. 2006, *A&A*, 446, 635
- Boyajian, T. S., McAlister, H. A., Baines, E. K., et al. 2008, *ApJ*, 683, 424
- Boyajian, T. S., von Braun, K., van Belle, G., et al. 2012, *ApJ*, 757, 112
- Boyajian, T. S., von Braun, K., van Belle, G., et al. 2013, *ApJ*, 771, 40
- Boyajian, T. S., van Belle, G., & von Braun, K. 2014, *AJ*, 147, 47
- di Folco, E., Thévenin, F., Kervella, P., et al. 2004, *A&A*, 426, 601
- di Folco, E., Absil, O., Augereau, J.-C., et al. 2007, *A&A*, 475, 243
- Henry, G. W., Kane, S. R., Wang, S. X., et al. 2013, *ApJ*, 768, 155
- Kane, S. R., & Gelino, D. M. 2012, *PASP*, 124, 323

- Kervella, P., Thévenin, F., Ségransan, D., et al. 2003, *A&A*, 404, 1087
- Ligi, R., Mourard, D., Lagrange, A. M., et al. 2012, *A&A*, 545, A5
- Richichi, A., Percheron, I., & Khristoforova, M. 2005, *A&A*, 431, 773
- Torres, G., Andersen, J., & Giménez, A. 2010, *A&A Rev.*, 18, 67
- van Belle, G. T., Lane, B. F., Thompson, R. R., et al. 1999, *AJ*, 117, 521
- van Belle, G. T., & von Braun, K. 2009, *ApJ*, 694, 1085
- von Braun, K., Boyajian, T. S., Kane, S. R., et al. 2011, *ApJ*, 729, L26
- von Braun, K., Boyajian, T. S., ten Brummelaar, T. A., et al. 2011, *ApJ*, 740, 49
- von Braun, K., Boyajian, T. S., Kane, S. R., et al. 2012, *ApJ*, 753, 171
- von Braun, K., Boyajian, T. S., van Belle, G. T., et al. 2014, *MNRAS*, 438, 2413
- White, T. R., Huber, D., Maestro, V., et al. 2013, *MNRAS*, 433, 1262

Index

active region, 32
activity, 30
asymmetry, 29

bisector, 30

C-shape, 32
CARMENES, 204
chromospheric activity, 72
coronal emission, 13

EUV, 167

host stars, 167
hyperfine, 32

ISS, 29

line asymmetry, 30
lithium, 22, 23
Lyman-alpha, 167

M dwarfs, 204
magnetic, 32

NISP, 33

photoshchemistry, 167
photospheric activity, 72

RECONS, 233
rotation, 13, 21

solar analogs, young, 71
solar cycle, 30
SOLIS, 29
stellar flares, 72
stellar flickering, 72

UCAC4, 233

velocity span, 30

X-ray emission, 13